

University of St Andrews



Full metadata for this thesis is available in
St Andrews Research Repository
at:

<http://research-repository.st-andrews.ac.uk/>

This thesis is protected by original copyright

Frequency Comb Generation in a Pump Enhanced Optical Parametric Oscillator



University
of
St Andrews

Michael B. Spurr, MSci (Hons)

A thesis submitted to the University of St Andrews in
application for the degree of Doctor of Philosophy

August, 2005



TH
FIII

Declarations

I, Michael Barrie Spurr, hereby certify that this thesis, which is approximately 58200 words in length, has been written by me, that it is the record of work carried out by me and that it has not been submitted in any previous application for a higher degree.

Date: 29/11/05 Signature of Candidate:

I was admitted as a research student in September 2001 and as a candidate for the degree of PhD in September 2002; the higher study for which this is a record was carried out in the University of St Andrews between 2001 and 2005.

Date: 29/11/05 Signature of Candidate:

I hereby certify that the candidate has fulfilled the conditions of the Resolution and Regulations appropriate for the degree of PhD in the University of St Andrews and that the candidate is qualified to submit this thesis in application for that degree.

Date: 29/11/05 Signature of Supervisor:

Copyright Declaration

In submitting this thesis to the University of St Andrews I understand that I am giving permission for it to be made available for use in accordance with regulations of the University Library for the time being in force, subject to any copyright vested in the work not being affected thereby. I also understand that the title and abstract will be published, and that a copy of the work may be made and supplied to a *bona fide* library or research worker.

Date: 29/11/07 Signature of Candidate:

Abstract

This thesis describes the development and characterisation of a device for the generation of a wide spanning comb of frequencies, based upon a pump enhanced optical parametric oscillator. The frequency comb, consisting of thousands of equally spaced modes, has several potential applications in the field of optical communications. By exploiting the high circulating field created by the pump enhanced scheme, a compact device, operating at a level compatible with current telecommunications systems can be realised.

Through careful resonator design and optimisation, an OPO with a threshold of 30 - 50mW and optimum pumping level of 120mW was developed. The OPO was pumped at 800nm, producing a degenerate signal and idler wavelength of 1600nm. By modulating the internal signal/idler field at a depth of 0.5 rad, a frequency comb spanning up to 50nm (5.9 THz), with a mode spacing of 520 MHz was generated.

In an attempt to increase the width of the frequency comb and improve the overall stability of the device, dispersion compensation was implemented by way of a pair of intra-cavity chirped mirrors. With full compensation for the positive intra-cavity dispersion, a frequency comb spanning 70nm (8.2 THz) was generated – a 20nm increase over the uncompensated case. A significant increase was also observed in the lifetime of the comb.

The frequency comb output was mixed with the output from a narrow-linewidth DBR laser. Through the generation of beat frequencies, this confirmed the existence of sharp frequency modes under the comb envelope, with a linewidth below 13.5 MHz.

Acknowledgements

In the eventful four years that have preceded the submission of this thesis, I have become indebted to a number of people. Firstly, I must thank my supervisor, Professor Malcolm Dunn, for initially piquing my interest in the area of laser physics and nonlinear optics during my senior honours project and then offering me the PhD position. His knowledge of lasers, optics and physics in general is something to aspire to and without his guidance, this project could not have been completed.

My thanks also go to the members of the OPO Group, both past and present. Their advice, humour and downright cynicism have made my time as a PhD student most enjoyable. Special mention must go to two gentlemen in particular. Dr David Stothard was the first member of the OPO group that I met during my honours project and he left a lasting impression! His unsurpassed skill with electronics has helped me out on a number of occasions and he is never too busy to lend a hand. Sadly, Dr Ian Lindsay has now moved on to new challenges in the Netherlands. However, he will certainly be remembered for a long time within the OPO group. His knowledge and experience, particularly at the beginning of my project, made sure that I stayed on the right track. Also, his ability to invent new and inventive swear words, often whilst working on the computer, provided an endless source of amusement within the office.

I owe a debt of gratitude to a number of other people within the physics department. I thank the workshop and electronics staff for creating a number of custom-designed pieces of equipment without laughing at my drawings, Scott in stores for letting me in the building in the morning and supplying me with the niggly pieces of equipment that I always seemed to run out of, the secretarial staff for taking care of my most inane requests with a smile and finally the members of the Photonics Innovation Centre (PIC) for letting me share their office and labs during the last year. Particular thanks must go to Dr Cameron Rae, the technical manager of PIC, for providing lots of sound advice and never turning down a request to borrow expensive equipment.

During my time at St Andrews, both as an undergraduate and postgraduate, I have met a number of amazing people. There are probably too many to name individually (and I'd only end up forgetting someone) so, to all my friends I'd like to say thanks. Thanks for all those nights sitting in the warmth of the pub, sampling some of the

finest ales in Britain. Thanks for making a great team for the weekly Cellar Bar music quiz. Thanks for humiliating me at various sports in the nicest way possible. Thanks for sharing the experiences, trials and tribulations of university life and being the greatest bunch of friends that anyone could wish for.

Of course, I can't write these acknowledgements without thanking the people responsible (perhaps 'guilty' is a better word) for attempting to nurture me into the mature and sensible person that I should be at this age. My parents and family have always supported me in everything that I have done and regularly provide essential services such as cooking and cleaning!

My final thanks go to the one special person in my life who, despite my many bad habits, will soon become my wife - Christina. Despite causing the occasional distraction, she has always been there throughout my PhD and the writing of this thesis. Her support and willingness to listen to my ranting when everything seemed to be going wrong has helped me get to this stage. I am also grateful for her gentle pushes towards the computer on the numerous sunny days when thesis writing was the last thing I wanted to do. And so, with all my love, I dedicate this thesis to Christina and the new life that we will soon bring into this world.

Table Of Contents

<i>Declarations</i>	I
<i>Abstract</i>	III
<i>Acknowledgements</i>	IV
<i>Glossary of Abbreviations</i>	X
<i>1. Introduction & OPO Background</i>	1
<hr/>	
1.1. Optical Parametric Generation	4
1.2. The Manley-Rowe Relations	11
1.3. Phasematching	12
1.4. Optical Parametric Oscillation	16
1.5. Oscillation Thresholds	19
1.6. Tuning Behaviour	24
1.7. Chapter Summary & References	28
<i>2. Frequency Comb Generation</i>	34
<hr/>	
2.1. The Electro-Optic Effect	34
2.2. Phase Modulation	39
2.3. Comb Generation in a Passive Cavity	43
2.4. Comb Generation with an Active Medium	45
2.5. FM Lasers	47
2.6. Frequency Comb Generation & Optical Communications	51
2.7. Chapter Summary & References	55

3. *Pump Enhanced OPOs* 60

3.1. The Pump Enhanced Cavity	60
3.2. Split Cavity Configuration	63
3.3. Measuring the Enhancement Factor	64
3.4. Optimum Pumping Level	72
3.5. Stabilisation of Pump Cavity	80
3.6. Chapter Summary & References	82

4. *System Design & Optimisation* 87

4.1. Nonlinear Crystal	87
4.2. Requirements for Optical Resonator	93
4.3. Resonator Configurations	97
4.4. Final Design	100
4.5. EOM Set-up	106
4.6. Optimisation – Pumping Level & Input/Output Coupling	109
4.7. Chapter Summary & References	116

5. *Comb Generation in a Dispersive Cavity* 120

5.1. Modelling of Comb Bandwidths	120
5.2. Experimental Comb Generation 1 (Proof of Principle)	123
5.3. Experimental Comb Generation 2 (Optimum Pumping Level)	128
5.4. Problems with Dispersive Cavity	131
5.5. Experimental Comb Generation 3 (Uncompensated)	135
5.6. Chapter Summary & References	142

6. Dispersion Compensation	146
<hr/>	
6.1. Dispersion in the FCG System	149
6.2. Consequences for OPOs & FCG	153
6.3. Compensation Methodologies	161
6.4. Chapter Summary & References	168
7. Comb Generation in a Dispersion Compensated Cavity	173
<hr/>	
7.1. Incorporating Dispersion Compensation into OPO-FCG	175
7.2. Dispersion Compensated OPO	182
7.3. Characterisation of Dispersion Compensated FCG	190
7.4. Experimental Comb Generation 4 (Dispersion Compensated)	196
7.5. Heterodyne Experiments	200
7.6. Chapter Summary & References	202
8. Conclusions & Further Work	205
<hr/>	
8.1. Overall Summary	205
8.2. Further Work	208
8.3. Concluding Remarks & References	214

<i>Appendix I</i>	- <i>Publications & Conference Proceedings</i>	216
<i>Appendix II</i>	- <i>Derivation of Optimisation Equations for PE-SRO</i>	217
<i>Appendix III</i>	- <i>MathCad Programs</i>	221

Glossary of Abbreviations

The following is a list of abbreviations used within this thesis:

BPM	Birefringent Phasematching
CW	Continuous-Wave
DBR	Distributed Bragg Reflector
DFG	Difference Frequency Generation
DP	Double Pass
DRO	Doubly-Resonant Oscillator
DWDM	Dense Wavelength Division Multiplexing
EF	(Pump) Enhancement Factor
EM	Electro-Magnetic/Magnetism
EOM	Electro-Optic Modulator
FCG	Frequency Comb Generation/Generator
FM	Frequency Modulation/Modulated
FSR	Free Spectral Range
FWHM	Full Width at Half Maximum
GDD	Group Delay Dispersion
GVD	Group Velocity Dispersion
IC	Intra-Cavity
IR	Infra-Red
ITU-T	International Telecommunications Union – Telecommunication
NL	Nonlinear
OPA	Optical Parametric Amplification/Amplifier
OPG	Optical Parametric Generation
OPO	Optical Parametric Oscillator
OPO-FCG	Frequency Comb Generator based on an Optical Parametric Oscillator
OSA	Optical Spectrum Analyser
PE	Pump Enhanced
PE-DRO	Pump Enhanced Doubly-Resonant Oscillator
PE-OPO	Pump-Enhanced Optical Parametric Oscillator

PE-SRO	Pump Enhanced Singly-Resonant Oscillator
P.I.D	Proportional Gain, Integration, Differentiation
PMB	Phasematching Bandwidth
PZT	Piezo-Electric Transducer
QPM	Quasi-Phasematching
RF	Radio Frequency
RFSA	Radio Frequency Spectrum Analyser
SHG	Second Harmonic Generation
SRO	Singly-Resonant Oscillator
TEM	Transverse Electric Mode
Ti:S	Titanium Sapphire (Laser)
TRO	Triply-Resonant Oscillator
WDM	Wavelength Division Multiplexing

Chapter 1

Introduction & OPO Background

The birth of the laser in 1960 heralded a revolution in the field of optics. Properties such as high spatial and spectral coherence, large power densities and near diffraction-limited focusing meant that several phenomena, previously accessible only to the pen and paper of a theorist, could subsequently be explored in the laboratory. One such phenomenon, which now encompasses a wide range of topics, is the area of nonlinear optics. Within this area lie a group of devices known as optical parametric oscillators (OPOs), whose operation is based on the nonlinear optical effect known as difference frequency generation. In basic terms, an OPO takes an input laser frequency and splits it into two new frequencies, which sum to the original frequency. The output from an OPO has the same properties as laser light, without the constraint of being determined by a particular atomic or molecular transition. This means that OPOs can generate radiation that is tunable over a broad frequency/wavelength range. In particular, OPOs are capable of accessing wavelengths, such as in the mid-IR, which cannot be reached by available laser systems.

Optical parametric oscillation was first demonstrated by Giordmaine and Miller in 1965 [1]. Subsequent research was of a fairly fundamental nature, with the high power laser systems required to reach oscillation threshold precluding OPOs from finding uses in many applications. However, in the last two decades a mini-revolution has taken place in the field of OPOs. The discovery of several new types of nonlinear crystal, based on arsenate and phosphate compounds, coupled with the development of quasi-phasematching (see section 1.3) and novel resonator designs (see section 1.4) has led to OPO systems with much lower power requirements. This has coincided with the emergence of diode pumped solid-state lasers, whose high efficiency and compact nature makes an ideal pump source for the new generation of OPOs. Today, the combination of OPO and diode pumped solid-state laser (or even a diode laser on its own) results in a highly efficient, compact device capable of producing widely tunable laser radiation ranging between the UV and mid-IR parts of the EM spectrum. Alongside the growth of OPO technology, the past decade has also seen a substantial volume of research into the area of frequency metrology and particularly the

1. Introduction & OPO Background

generation of optical frequency combs. Indeed, the application of frequency comb generation to metrology was the subject of the 2005 Nobel Prize for Physics. As the name suggests, a frequency comb consists of a series of precisely spaced, phase-locked frequencies, usually over a bandwidth of several THz. Within the comb, the individual frequency separation is generally in the region of a GHz. Therefore; the comb spacing can be locked to a precision microwave/RF oscillator, providing a highly stable source of optical frequencies that can be linked back to a single well-defined electronic frequency.

The advantages of such a source for frequency metrology and spectroscopy are clear to see. The frequency comb provides a set of exact frequencies against which an unknown optical frequency can be measured with great accuracy. Even greater potential lies with the application of frequency comb generation to the field of optical communications and the technique known as wavelength division multiplexing. This method for sending multiple communication channels down a single optical fibre requires an equally spaced series of well-defined, stable frequencies - all properties that are satisfied by an optical frequency comb.

To complement existing telecommunications technology, a frequency comb generator must be compact and efficient, with low power requirements. If all three criteria are to be met, a laser diode pump source is a necessity. In a previous experiment [2], the technologies of optical parametric oscillation and frequency comb generation were combined in a single, elegant device. Whilst compact in size, prohibitively high power requirements meant that this device was not suitable for telecommunications.

This thesis describes the work carried out in a project whose aim was to develop a combined optical parametric oscillator and frequency comb generator that would be suitable for telecoms-based applications. Through careful design and modelling, a dual cavity resonator was developed for the OPO. This allowed the input pump light to be resonated entirely separate from the comb generation process in a scheme known as pump enhancement. The high pump field circulating in the resonant cavity significantly reduced the power requirements of the system. After optimisation a threshold of 30 – 50mW was measured, with an optimum pumping level at 150mW corresponding to a 10-fold enhancement of the pump field. This level can be easily accessed by a single-mode laser diode.

With a pump wavelength of 800nm, a frequency comb was generated around 1600nm by modulating the downconverted field within the OPO at a frequency equal to the

1. Introduction & OPO Background

longitudinal mode spacing. For a modulation depth of 0.5 rad, a comb spanning up to 50nm was observed, comparable to that predicted by the theory. However, these experiments also highlighted a number of problems relating to the stability and maximum width of the comb. One of the main causes was found to be dispersion within the intra-cavity media and this was confirmed by theoretical calculations and computer modelling.

Whilst not originally considered at the outset of the project, the problems due to dispersion could not be ignored. As a result, a dispersion compensation scheme was implemented. Congruent with the aim of developing a compact device, a pair of chirped mirrors was used to provide sufficient negative dispersion to cancel out the positive intra-cavity dispersion. An initial characterisation of the system showed a large but predictable change in behaviour. In particular, the OPO was found to switch off for long periods as the cavity length was changed, which confirmed the effectiveness of the dispersion compensation scheme. Under similar conditions to the uncompensated case a frequency comb was again generated around 1600nm, but with a 20nm increase in width, an increased lifetime and a reduction in power fluctuations. In a final experiment, the dispersion-compensated frequency comb was mixed with the output from a narrow-linewidth DBR laser. The resulting observation of specific beat frequencies proved the existence of sharp, equally spaced modes underneath the comb envelope.

The layout of this thesis and ordering of topics generally follows the timeline of the project. In chapter 2, the technique of frequency comb generation is described in detail, beginning with the underpinning theory and then discussing the various methods employed and prior research in the field. Chapter 3 introduces the novel pump-enhancement cavity and various related quantities such as the enhancement factor and the optimum pumping level. The design and optimisation of the frequency comb generator is covered by chapter 4. In particular, the various criteria and options for cavity design are discussed, followed by the reasons for choosing the final design. This chapter also summarises the results of experiments undertaken to find the optimum pumping level for the device. The first proof-of-principle comb generation experiments are detailed in chapter 5, followed by similar experiments that were undertaken at the optimum pumping level. Subsequent problems with the latter experiments and their explanation naturally established dispersion as an important factor. In chapter 6, a detailed exploration of dispersion in the frequency comb

1. Introduction & OPO Background

generator is described, ending with a discussion of the various compensation methodologies that are currently employed. Chapter 7 continues the dispersion theme, describing the incorporation of dispersion compensation into the frequency comb generator and subsequent comb generation experiments. These final experiments mark the end of the project, which is summarised in the last chapter, along with a discussion of possible further work and directions in which the project could be taken. However, before delving into the world of frequency comb generation it is first necessary to introduce the device that forms the basis for the entire project, the OPO. The physics behind the operation of an OPO has been described in a number of seminal research papers and theses (see for example [3-7]). Rather than repeat much of the analysis, which has already been concisely recorded in the mentioned manuscripts, the rest of this chapter will simply give the main and pertinent results. The accompanying text will seek to explain the context of these results and prepare the reader with the necessary theoretical background to understand the discussions and results in later chapters.

1.1) Optical Parametric Generation

When a material is placed within an electric field, the electrostatic forces associated with the field produce a physical separation of the positive and negative charges within the atoms/molecules of the material. This effect is known as *polarisation*. If the electric field is oscillating, such as in the case of incident electromagnetic radiation, the induced polarisation must also oscillate. In theoretical terms, this results in an extra term being added to Maxwell's equation, which is given below for the case of plane waves propagating along the z-axis.

$$\frac{\partial^2 E(z,t)}{\partial z^2} = \mu_0 \epsilon_0 \epsilon_r \frac{\partial^2 E(z,t)}{\partial t^2} + \mu_0 \frac{\partial^2 P(z,t)}{\partial t^2} \quad (1.1)$$

In order to solve Maxwell's equation, the polarisation term must first be related to the incident electric field. In the case when a linear relationship can be assumed, this is described by:

$$P(t) = \epsilon_0 \chi E(t) \quad (1.2)$$

1. Introduction & OPO Background

In equation (1.2), P and E are both vector quantities. The electric susceptibility, χ , is the physical mechanism through which the interaction between polarisation and electric field takes place. A linear relationship between P and E applies in the case of low optical powers only, where the incident electric field is much smaller than the intra-atomic field between electron and nucleus. This governs the area of *linear optics*, which encompasses phenomena such as refraction and absorption.

However, when the incident electric field approaches the intra-atomic field ($\sim 10^7 \text{V/m}$), the linear relationship between P and E breaks down. Instead, the polarisation must be expanded as a power series in terms of the electric field, as shown by equation (1.3)

$$P(t) = \epsilon_0 \left[\chi^{(1)} E(t) + \chi^{(2)} E(t) E(t) + \chi^{(3)} E(t) E(t) E(t) + \dots \right] \quad (1.3)$$

Here, the first term on the right-hand side represents the linear polarisation as in equation (1.2). Subsequent terms represent the 2nd, 3rd order polarisation and so on, each governed by a separate susceptibility. Typically, $\chi^{(2)}$ is several orders of magnitude smaller than $\chi^{(1)}$, with a similar difference between $\chi^{(2)}$ and $\chi^{(3)}$. Hence, the effects of the higher order polarisation terms only manifest at very large optical power densities, restricting the source to a focussed laser beam.

The crystal structure of the material in which the polarisation is induced also has an important role to play. Due to the symmetry properties of the polarisation, even order terms are only exhibited by crystals that can be described as *non-centrosymmetric* i.e. crystals that do not have a centre of symmetry within the unit cell of their lattice structure. Since the relationship between P and E is no longer linear, effects due to higher order polarisation terms are grouped into the field of nonlinear optics.

The effect of each polarisation order can be obtained by examining the associated term from equation (1.3) on its own. For the 2nd order polarisation, the required term is:

$$P^{(2)}(t) = \epsilon_0 \chi^{(2)} E(t) E(t) \quad (1.4)$$

If the incident field consists of a single frequency, ω_1 , then it is simple to show that the resulting polarisation term in equation (1.4) will oscillate at $2\omega_1$. A more

1. Introduction & OPO Background

interesting case occurs when the electric field consists of two components, oscillating at ω_1 and ω_2 respectively i.e.

$$E(t) = E_1 \cos(\omega_1 t) + E_2 \cos(\omega_2 t) \quad (1.5)$$

Substituting the electric field described by equation (1.5) into equation (1.4) yields the following polarisation term,

$$P^{(2)}(t) = \epsilon_0 \chi^{(2)} \left(\begin{array}{l} \frac{E_1}{2} [\cos(2\omega_1 t)] + \frac{E_2}{2} [\cos(2\omega_2 t)] + \frac{E_1}{2} + \frac{E_2}{2} \\ + E_1 E_2 [\cos(\omega_1 + \omega_2)t + \cos(\omega_1 - \omega_2)t] \end{array} \right) \quad (1.6)$$

Equation (1.6) shows that the resulting polarisation contains terms with frequencies equal to the sum and difference of the two incident frequencies as well as terms at twice the incident frequencies and DC. Since this polarisation will consist of a series of oscillating dipoles within the material, EM radiation will be emitted with frequencies equal to $2\omega_1$, $2\omega_2$, $\omega_1 + \omega_2$ and $\omega_1 - \omega_2$.

Each of these frequencies represents a different nonlinear optical process. Second harmonic generation (SHG) corresponds to $2\omega_1$ and $2\omega_2$, whilst $\omega_1 + \omega_2$ and $\omega_1 - \omega_2$ refer to sum and difference frequency mixing respectively. Finally, the appearance of a DC electric field across the material is known as optical rectification.

For optical parametric generation (OPG), the underlying nonlinear optical process is difference frequency mixing. OPG usually occurs in a crystalline material and involves the interaction of a strong optical field at ω_3 , known as the *pump*, with a weak optical field at ω_2 , via the $\chi^{(2)}$ susceptibility. This generates a field at the difference frequency, $\omega_1 = \omega_3 - \omega_2$, which can then interact with ω_3 by the same process, increasing the field at ω_2 . As a result, the pump is depleted whilst the weak fields at ω_1 and ω_2 , collectively known as the *downconverted* waves, experience gain. If OPG is considered in terms of particles rather than waves, then the process can be pictured as a pump photon of energy E_p splitting into two lower frequency photons, whose energies sum to E_p .

To see exactly how gain/depletion occurs for each of the three interacting fields, it is necessary to solve the coupled wave equations. These equations, which can be derived

1. Introduction & OPO Background

separately from Maxwell's electromagnetic wave equation, describe the change in amplitude of the fields as they propagate through the crystal medium (usually chosen to be the z-direction):

$$\frac{\partial E_1(z)}{\partial z} = j \frac{d_{\text{eff}} \omega_1}{cn_1} E_3(z) E_2^*(z) e^{j(\Delta kz)} \quad (1.7)$$

$$\frac{\partial E_2(z)}{\partial z} = j \frac{d_{\text{eff}} \omega_2}{cn_2} E_3(z) E_1^*(z) e^{j(\Delta kz)} \quad (1.8)$$

$$\frac{\partial E_3(z)}{\partial z} = j \frac{d_{\text{eff}} \omega_3}{cn_3} E_1(z) E_2(z) e^{-j(\Delta kz)} \quad (1.9)$$

In the three coupled wave equations above, d_{eff} is known as the effective nonlinear optical coefficient and is defined as $\frac{\chi_{\text{eff}}}{2}$. At this point, it should be noted that χ_{eff} refers to a particular value of $\chi^{(2)}$, which is dependent on the direction of propagation with respect to the crystal axes. In the general situations described by equations (1.4) and (1.6), $\chi^{(2)}$ is represented by a 3x3x3 tensor, with d , the piezo-electric tensor, equal to $\frac{\chi^{(2)}}{2}$. To solve equations such as Maxwell's equation and the coupled wave equations, it is necessary to write $\chi^{(2)}$ in the form of a two-dimensional matrix. Whilst this is possible, a matrix representation of $\chi^{(2)}$ in its complete form is difficult to use in practice. Fortunately, there are several ways in which the matrix can be simplified to a readily useable form. Firstly, from equation (1.6) in particular, it is clear that interchanging E_1 and E_2 will make no difference to the expression. This is because the polarisation term, as given by equation (1.4), is only dependent on the product of the two fields. As a result, an element in the matrix, χ_{ijk} is equivalent to χ_{ikj} and this allows the use of a contracted notation with suffices j and k replaced by a single suffix m . This new suffix takes values between 1 and 6 and therefore, the matrix is reduced to a 3x6 array with 18 independent elements. Since the suffix ranging from 1 to 6 was originally used in piezoelectricity, this simplification of the $\chi^{(2)}$ matrix is known as the *piezoelectric contraction*.

1. Introduction & OPO Background

A further reduction in the number of independent matrix elements can be achieved by applying the various crystal symmetry operations that are allowed for the particular crystal class. If a crystal remains physically unchanged after a symmetry operation is performed, then the $\chi^{(2)}$ matrix should also be left unchanged. This requirement means that certain elements in the matrix must be zero, whilst others must be equal or equal in magnitude with opposite sign. As a result of performing many symmetry operations, the number of independent matrix elements is drastically reduced from the maximum of 18.

The final simplification to the $\chi^{(2)}$ matrix arises from the *Kleinman symmetry condition*. This is applicable when the interacting optical fields are at frequencies far away from resonances in the medium i.e. well within the transparency range (this is almost always the case, since the crystal will be chosen to be transparent at the optical frequencies of interest). This means that the frequency dependence of the d coefficients is negligible (zero dispersion). Under this condition, the components of the piezoelectric tensor will remain the same for any permutation of the suffices i , j and k i.e. $d_{ijk} = d_{ikj} = d_{jik}$ etc. Regardless of the piezoelectric contraction and crystal symmetry operations, Kleinman symmetry always reduces the number of independent elements in the piezoelectric tensor to a maximum of 10.

By combining the piezoelectric contraction, crystal symmetry and Kleinman symmetry, the number of independent, non-zero elements in the piezoelectric tensor is reduced to only a few for all non-centrosymmetric crystal classes. It is then usually a simple matter to obtain the correct value of d_{eff} from the reduced form of the tensor for the chosen propagation direction through the crystal.

Returning to the coupled wave equations, (1.7) to (1.9), whose solutions show the evolution of the three interacting fields as they propagate through the crystal during the OPG process. The method for obtaining these solutions has been covered in great detail by the reviews of Boyd, Ashkin and Byer [6, 7] and in the theses of Colville [4] and Lindsay [5]. The main points will be summarised here. Firstly, it is common to work with Gaussian beams rather than plane waves, since the former represents a physically realistic description of the three fields. It is also useful to convert to a new variable, α , which is defined such that $|\alpha|^2$ is equivalent to the normalised photon flow. Finally, it is usually assumed that the amplitude of each field remains roughly constant over the length of the crystal. Whilst this may seem paradoxical at first, it

1. Introduction & OPO Background

must be remembered that the changes described by equations (1.7) - (1.9) are small and the gain/depletion experienced by each field on a single pass through the crystal is very low. As a result of this approximation, the coupled wave equations simplify to linear differential equations, which can be easily integrated to give:

$$\alpha_1(L) = \alpha_1(0) + 2\tau\alpha_3(0)\alpha_2^*(0) \quad (1.10)$$

$$\alpha_2(L) = \alpha_2(0) + 2\tau\alpha_3(0)\alpha_1^*(0) \quad (1.11)$$

$$\alpha_3(L) = \alpha_3(0) - 2\tau\alpha_1(0)\alpha_2(0) \quad (1.12)$$

In the equations above, $\alpha_{1,2,3}(0)$ represent the fields at the input face of the crystal, which is of length L . Initially, equations (1.10) - (1.12) appear to show gain at the weak fields, α_1 and α_2 , and depletion at the strong pump field, α_3 . However, the crucial factor is in fact τ , which is defined in equation (1.13) below:

$$\tau = \kappa L \operatorname{sinc}\left(\frac{\Delta k L}{2}\right) e^{j\left(\frac{\Delta k L}{2}\right)} \quad (1.13)$$

Here, κ is a constant factor that is determined by d_{eff} , the spatial coupling between the three Gaussian beams and the frequency and refractive index of each beam. In the context of gain/depletion, the most important part of τ is $\operatorname{sinc}\left(\frac{\Delta k L}{2}\right)$. In the argument of the sinc function, Δk is known as the wavevector mismatch and represents the difference in k-vector between the three waves i.e.

$$\Delta k = k_3 - k_2 - k_1 = \frac{n_3\omega_3}{c} - \frac{n_2\omega_2}{c} - \frac{n_1\omega_1}{c} \quad (1.14)$$

Figure 1.1 shows the sinc function plotted against $\frac{\Delta k L}{2}$.

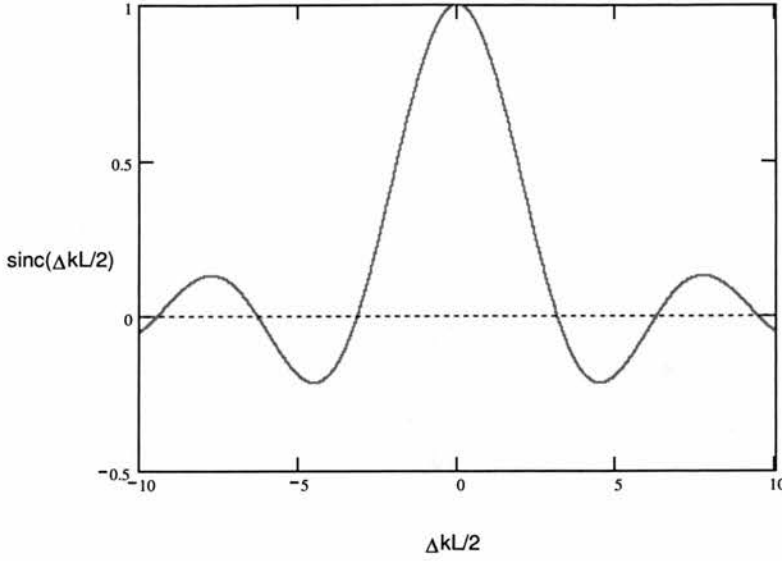


Figure 1.1 – Plot of $\text{sinc}\left(\frac{\Delta kL}{2}\right)$ function

From figure 1.1, there are two important observations to be made. Firstly, a maximum in the sinc function (thereby giving maximum gain at α_1 and α_2) requires Δk to be zero. For any small non-zero value of Δk , the value of the sinc function and hence the gain rapidly decreases as either Δk or L increases. Secondly, if Δk is non-zero, then as L increases (i.e. beams propagate through the crystal) there comes a point $\left(\frac{\Delta kL}{2} = \pi\right)$ at which the sinc function becomes negative. Going back to equations (1.10) - (1.12), it can be seen that this will result in depletion for α_1 and α_2 and gain at α_3 . In other words, energy will be transferred back into the pump from the downconverted waves. If L is increased further, then figure 1.1 shows that this process reverts back to gain at α_1 , α_2 and depletion at α_3 when $\frac{\Delta kL}{2} = 2\pi$. Hence, for OPG with wavevector mismatch between the three interacting fields, power will oscillate periodically between the pump and downconverted waves. The energy in α_1 and α_2 will reach a maximum when $L = \frac{\pi}{\Delta k}$. This is known as the *coherence length* and is a measure of the useful crystal length for OPG. It is usually equal to a few tens of microns. To ensure maximum gain and the continual flow of energy from α_3 to α_1 and α_2 over the entire length of the crystal, it is clear that Δk must be set equal to zero. Methods for

1. Introduction & OPO Background

achieving this condition, known as *phasematching*, will be discussed in section 1.3. However, it is first prudent to introduce a set of relations that give further insight into the transfer of energy between the three fields.

1.2) The Manley-Rowe Relations

Returning once again to equations (1.7) - (1.9) and multiplying by E_1^* , E_2^* , E_3^* gives

$$\frac{\partial |E_1(z)|^2}{\partial z} = j \frac{d_{\text{eff}} \omega_1}{cn_1} E_3(z) E_2^*(z) E_1^*(z) e^{j(\Delta kz)} \quad (1.15)$$

$$\frac{\partial |E_2(z)|^2}{\partial z} = j \frac{d_{\text{eff}} \omega_2}{cn_2} E_3(z) E_2^*(z) E_1^*(z) e^{j(\Delta kz)} \quad (1.16)$$

$$\frac{\partial |E_3(z)|^2}{\partial z} = -j \frac{d_{\text{eff}} \omega_3}{cn_3} E_3(z) E_2^*(z) E_1^*(z) e^{j(\Delta kz)} \quad (1.17)$$

Note that to obtain equation (1.17), the complex conjugate of each side of the expression is taken (after multiplying (1.9) by E_3^*). From the three equations above, it can be seen that:

$$\frac{n_1}{\omega_1} \frac{\partial |E_1(z)|^2}{\partial z} = \frac{n_2}{\omega_2} \frac{\partial |E_2(z)|^2}{\partial z} = -\frac{n_3}{\omega_3} \frac{\partial |E_3(z)|^2}{\partial z} \quad (1.18)$$

For an electromagnetic wave of amplitude, E , the associated intensity is given by:

$$I = \frac{1}{2} \epsilon_0 cn |E|^2 \quad (1.19)$$

Utilising equation (1.19) to substitute for $|E_1|^2$, $|E_2|^2$, $|E_3|^2$ in equation (1.18) and cancelling out any repeating terms results in the most common form of the Manley-Rowe relations,

$$\frac{\partial}{\partial z} \left(\frac{I_1}{\omega_1} \right) = \frac{\partial}{\partial z} \left(\frac{I_2}{\omega_2} \right) = -\frac{\partial}{\partial z} \left(\frac{I_3}{\omega_3} \right) \quad (1.20)$$

1. Introduction & OPO Background

In the equation (1.20), $\frac{I_i}{\omega_i}$ effectively represents photon flux. Therefore, the Manley-Rowe relations show that the destruction of any single pump photon results in the creation of exactly one photon at each of the downconverted frequencies. This interpretation assumes that the three waves have the correct phase relationship for energy to flow from the pump to the downconverted waves. Furthermore, if the total intensity is defined as the sum of I_1 , I_2 and I_3 and remembering that $\omega_3 = \omega_2 + \omega_1$ then,

$$\frac{\partial I_T}{\partial z} = \frac{\partial I_1}{\partial z} + \frac{\partial I_2}{\partial z} + \frac{\partial I_3}{\partial z} = 0 \quad (1.21)$$

This shows that the total intensity in the OPG process is conserved.

In most applications of OPG, it is usual for only one of the downconverted waves to be used. Since the Manley-Rowe relations detail the flow of energy between pump and downconverted waves, they can also be interpreted as measure of the fundamental efficiency of the conversion process from pump to useful output. No external factors are involved in this efficiency and hence it is the theoretical 'best' that can be achieved.

1.3) Phasematching

Phasematching is a crucial part of many nonlinear optical processes, particularly those utilising continuous-wave sources. As explained in section 1.1, phasematching in OPG involves setting the wavevector mismatch, Δk , to zero. This allows the maximum gain for the process to be achieved and ensures the continual flow of energy from the pump wave to the downconverted waves. Examining equation (1.14), it is clear that $\Delta k = 0$ requires the refractive indices of all three waves to be equal i.e. $n_3 = n_2 = n_1$. However, when operating within the transparency range of a material, normal dispersion will apply. Broadly, this means that refractive index will increase with frequency (see chapter 6 for more details) and, in general, $n_3 > n_2 > n_1$ for the OPG process. Had a solution to this problem not been found, then it is likely that the area of nonlinear optics would have been reduced to a large volume of theory with

1. Introduction & OPO Background

little practical value. Fortunately, there now exist two well-established methods for achieving phasematching.

The first, *birefringent phasematching* (BPM) utilises the anisotropic properties of many of the crystals used in nonlinear processes. In such crystals, the experienced refractive index is dependent on the polarisation and direction of propagation of the incident waves. In particular, the refractive index associated with each crystal axis will not be the same in all cases. For materials with this property, called *birefringence*, the refractive index can be represented by a 3-D construction known as the *index ellipsoid* or *optical indicatrix* (for information on the origin of this construct, see chapter 2, section 2.1). The index ellipsoid for the simplest type of birefringent crystals is shown in figure 1.2.

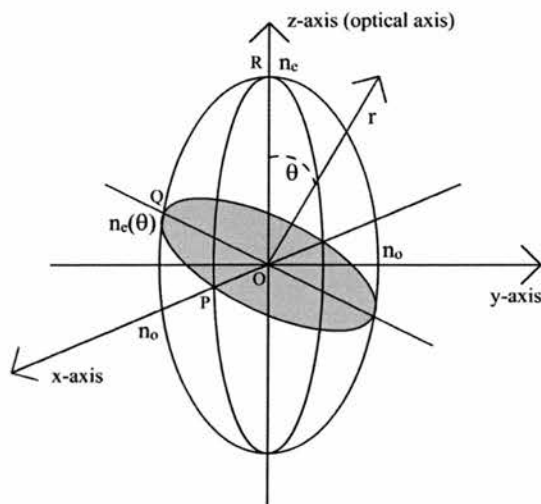


Figure 1.2 – Index ellipsoid for uniaxial crystal

Uniaxial birefringent crystals have two associated refractive indices. By convention, the refractive indices of the x and y -axes are both equal to the ordinary refractive index, $n_x = n_y = n_o$, whilst the refractive index of the z -axis is equal to the extraordinary refractive index, $n_z = n_e$. In figure 1.2, \mathbf{r} represents an arbitrary direction through the crystal. The shaded ellipse shows the intersection of the plane perpendicular to \mathbf{r} with the ellipsoid. Hence, the semi-major (OQ) and semi-minor (OP) axes of the shaded ellipse correspond to the two orthogonal polarisations of a wave whose normal is in the \mathbf{r} direction. Due to the isotropy of the crystal in the xy -plane, a wave polarised parallel to OP will always experience n_o . This is known as the ordinary wave. On the other hand, a wave polarised along OQ will experience a refractive index, $n_e(\theta)$ that is a combination of n_o and n_e . Crucially, as shown by figure

1. Introduction & OPO Background

1.2, the refractive index for the OQ polarisation (extraordinary wave) will change as the angle between \mathbf{r} and the z -axis is varied. Therefore, the refractive index of the extraordinary wave depends on the propagation direction through the crystal. Note that if a wave propagates along the z -axis, then the refractive index is n_o for any polarisation direction. The isotropic nature of the z -axis means that it is usually defined as the optic axis.

There also exists a second class of birefringent crystals known as *biaxial*, with $n_x \neq n_y \neq n_z$. Such crystals can also be represented by an index ellipsoid. However, with two isotropic planes rather than one, the optic axis will not, in general, lie along one of the crystal axes.

The variable refractive index of the extraordinary wave provides a means to set $n_3 = n_2 = n_1$ and achieve phasematching. Consider the simple case where $\omega_1 = \omega_2 = \frac{\omega_3}{2}$. If the downconverted waves are polarised such that they are ordinary waves and experience n_o , then the pump should be polarised as an extraordinary wave. This allows a propagation direction to be chosen such that $n_3 = n_e(\theta) = n_o$. Note that the choice of the downconverted waves as ordinary or extraordinary will depend on whether $n_e > n_o$ (positive uniaxial) or $n_o > n_e$ (negative uniaxial). The case where both downconverted waves have the same polarisation is known as type I phasematching. In type II phasematching, the downconverted waves have orthogonal polarisations – one ordinary and one extraordinary.

Since BPM was not employed in this project, the discussion of this type of phasematching will go no further. For more information and details of the calculations involved see [8, 9].

It was previously mentioned that for non-phasematched OPG, the power generated in the downconverted waves reaches a maximum after one coherence length. Beyond this point, power is transferred back into the pump. This can be interpreted as being due to destructive interference between the propagating fields and the fields newly created by the oscillating polarisation in the crystal. This in turn is due to the fact that the pump wave, which drives the polarisation, travels at a different speed to the downconverted waves. However, if a π phase shift could be applied to the oscillating polarisation every coherence length, the phase difference between propagating and created fields would be reset to zero. Therefore, constructive interference between the

1. Introduction & OPO Background

two would always occur and the downconverted power would increase through the entire length of the crystal. This is the concept behind *quasi-phasematching* (QPM) and was demonstrated as early as 1966 [10]. Today, QPM is achieved by a technique known as *periodic poling*, which inverts ferro-electric domains in the nonlinear material to produce the required phase shift. Periodic poling was first demonstrated by Yamada et al [11] and can now be applied to many types of nonlinear crystal.

In terms of the wavevector mismatch, the effect of QPM is quite different to BPM. Instead of setting the refractive indices equal, QPM introduces an extra term into the equation for Δk to make up for any shortfall in the wavevector difference:

$$\Delta k = k_3 - k_2 - k_1 - K = 2\pi \left(\frac{n_3}{\lambda_3} - \frac{n_2}{\lambda_2} - \frac{n_1}{\lambda_1} - \frac{1}{\Lambda} \right) \quad (1.22)$$

In equation (1.22), Λ represents the poling period (also known as the grating period) of the quasi-phasematching i.e. the length between each domain inversion. Since Λ is an engineered quantity and therefore independent of inherent properties of the crystal, QPM allows any propagation direction to be utilised. Typically, the direction will be chosen to exploit the maximum available d_{eff} coefficient and will normally be along one of the crystal axes to negate unwanted birefringent effects such as beam walkoff. This is the major advantage of QPM over BPM.

A Fourier analysis of the QPM process [12] shows that the nonlinear coefficient is reduced by a factor of $\frac{\pi}{2}$ compared to the perfectly phasematched case i.e.

$$d_{\text{QPM}} = \frac{2}{\pi} d_{\text{eff}} \quad (1.23)$$

This fits with the picture given by figure 1.1, which shows that the sinc function has a value of $\frac{2}{\pi}$ after a coherence length (the point at which a domain inversion takes place), compared to a value of 1 in the perfectly phasematched case. It is worth noting that despite this reduction, QPM allows nonlinear coefficients that are typically at least twice their birefringent counterparts to be accessed. As a result, nonlinear processes that employ QPM can experience a much higher gain than the equivalent birefringent system. This is of particular importance if the d_{eff} associated with BPM is

1. Introduction & OPO Background

small. In such cases, the use of QPM can drastically reduce the size and power requirements of the pump source.

A further advantage of QPM lies with the fact that it can be employed for isotropic nonlinear crystals. Such crystals, e.g. gallium arsenide, often have high nonlinear coefficients but cannot be used with BPM due to their lack of anisotropy. The main drawback of QPM is down to the method used to invert the domains, rather than any fundamental issues with the phasematching process. The standard poling method of inverting ferro-electric domains requires the application of a large pulsed electric field across the crystal. Due to the spreading out of electric field lines, accurate domain inversion is typically limited to thin crystals (around 0.5 – 1mm). This results in a small aperture at the input face of the crystal, limiting the size of the beams in the crystal and requiring tight focussing of the pump and downconverted waves. Problems may also arise if the breakdown voltage of the crystal is close to the voltage required for periodic poling.

1.4) Optical Parametric Oscillation

The process of optical parametric generation, coupled with one of the phasematching methods described in the previous section forms the basis of an optical parametric amplifier (OPA). Given that the beams travelling through such devices only perform a single-pass through the nonlinear crystal, significant power in the downconverted waves can only be generated when the initial gain is extremely high. The resulting high power required of the pump wave can only be achieved practically by short-pulse systems. Therefore, the OPA is generally restricted to use in the pulsed regime.

When the pump beam consists of a continuous wave (CW), the gain achieved on a single pass through the nonlinear crystal is invariably too small to produce any significant downconverted power. Hence, it is necessary for at least one of the downconverted waves to be resonant in an optical cavity surrounding the crystal. Such a configuration is described as an optical parametric oscillator (OPO). The basic OPO design, which has remained relatively unchanged since its inception in 1965 [1], is shown in figure 1.3 below.

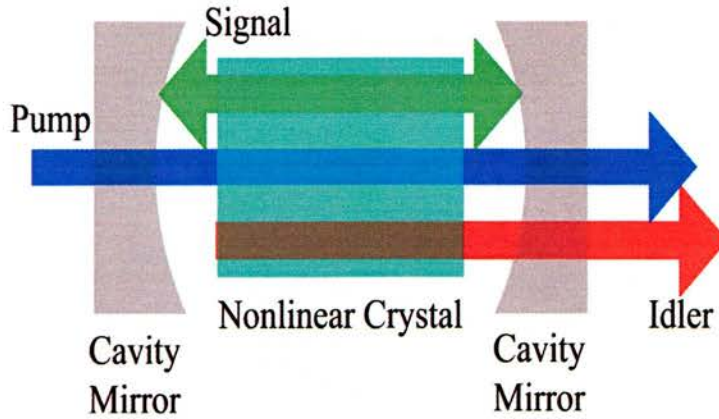


Figure 1.3 – Basic OPO cavity

When discussing the three waves involved in an OPO, the convention is to describe ω_3 as the *pump*. Of the two downconverted waves, ω_2 is usually defined as the higher of the two frequencies and is called the *signal*, leaving ω_1 as the lower frequency *idler*. Figure 1.3 shows the simplest type of OPO, known as a singly resonant oscillator (SRO). In this case, the cavity is designed so that the signal (or idler) is resonant, as shown by the double-headed arrow in the diagram. The pump and idler, on the other hand, exit the cavity after a single pass through the nonlinear crystal.

When introducing the concept of OPG, it was stated that the process involves the interaction of a strong field at ω_3 with a weak field at ω_2 to produce ω_1 via DFG. As shown by figure 1.3, the initial ω_2 need not be provided by an external source. Rather, it arises from quantum mechanical vacuum fluctuations, which, on average, produce half a photon in each available mode [13]. The mode with the correct phase (determined by the phasematching conditions) is amplified by the DFG process, generating ω_1 and ω_2 .

Since only one wave is required to be resonant, the SRO is easy to set-up and does not require complex mirror coatings with high reflectivity at multiple wavelengths. This also leads to well-behaved tuning of the downconverted frequencies as the pump frequency or crystal temperature is altered (see section 1.5). However, the fact that the pump and idler waves pass through the crystal only once means that the input pump power required for the OPO to begin oscillating, the threshold power (see section 1.4), is typically very large. Pump thresholds for SROs tend to be in the region of a few Watts [14, 15], requiring large and expensive laser sources.

1. Introduction & OPO Background

The drive to reduce the pump threshold to a more practical level has led to the development of several different types of OPO. Some are nothing more than modifications to the SRO cavity shown in figure 1.3, whilst in others, the cavity design is significantly different. Table 1.1 below summarises the different types of OPO, each with a diagram for illustration. The colouring of pump, signal and idler waves is the same as that used in figure 1.3.

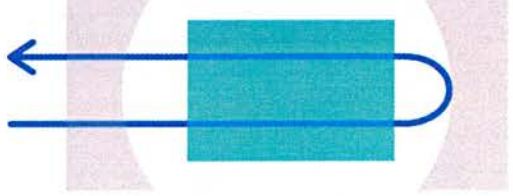
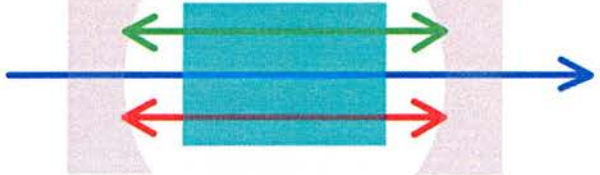
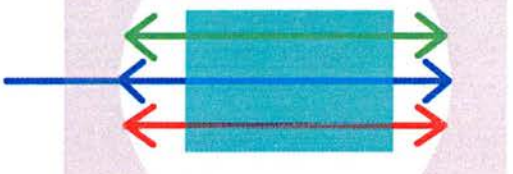
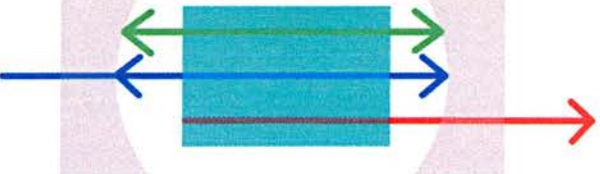
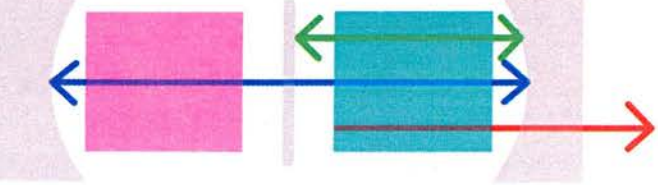
OPO Type & Description	Diagram
<p><u>Double Pass (DP)</u> – Pump and/or nonresonant wave reflected by output mirror for 2nd pass through crystal.</p>	
<p><u>Doubly Resonant Oscillator (DRO)</u> – Both downconverted waves resonated.</p>	
<p><u>Triply Resonant Oscillator (TRO)</u> – All three waves resonated.</p>	
<p><u>Pump Enhanced (PE)</u> – Pump and one of downconverted waves resonated.</p>	
<p><u>Intra-Cavity (IC)</u> – Nonlinear crystal placed inside pump laser cavity. Separate OPO cavity created by beamsplitter.</p>	

Table 1.1 – Types of OPO

1. Introduction & OPO Background

Each of the OPO cavities summarised in table 1.1 has its own advantages and disadvantages. Those relating to pump threshold and tuning behaviour will be discussed at greater length in the following two sections. For the moment it suffices to say that increasing the number of double passed or resonant waves will reduce the threshold. However, these schemes also increase the number of constraints on the system, particularly with regard to optical coatings and the length of the cavity. Further reduction in threshold can be achieved by employing the pump enhancement or intra-cavity approaches. In the context of this project, pump enhancement is very important, being the overall design on which the frequency comb generator was based (see chapter 4). Consequently, chapter 3 is devoted entirely to the method of pump enhancement and no further discussion need take place here.

The intra-cavity OPO has recently been the subject of much research [16-18] and hence deserves some further explanation. With this type of OPO, the nonlinear crystal is placed within the cavity of the pump laser, with a beamsplitter used to create a separate cavity for the resonant downconverted waves. Since the circulating laser field can often reach tens or hundreds of Watts, the pump threshold for the OPO can be reduced by several orders of magnitude. This allows small and efficient laser sources to be used. In particular, the IC-OPO is often combined with a diode-pumped solid-state laser system (such as Nd:YAG or Nd:YVO₄) to produce a very compact device with high electrical to optical efficiency.

1.5) Oscillation Thresholds

The oscillation threshold of an OPO is defined as the input pump power at which the production of coherent output power in the downconverted waves begins. At this point the unsaturated gain (i.e. the gain with no fields at α_1 and α_2) is just equal to the round-trip loss within the OPO cavity. A further increase of the pump power causes the device to oscillate with fields α_1 and α_2 being generated. These fields in turn cause the gain to saturate and, under steady-state conditions, to remain fixed at the threshold value. Therefore, the gain in an OPO operating above threshold is always equal to the round-trip loss. As well as being an important parameter in establishing the minimum pump power required for a particular OPO to work, the oscillation

1. Introduction & OPO Background

threshold also plays an important role in determining the optimum operating point for the OPO (see chapter 3, section 3.4 for more detail).

The preceding definition of the oscillation threshold suggests that a mathematical expression for the threshold power should be obtained by equating the gain and loss for each of the three interacting waves on a single round trip of the OPO cavity. This is indeed the method used in the detailed derivations of threshold expressions (see for example [4]). As with the rest of this chapter, the derivations will not be repeated here. Instead, the final expressions for the pump threshold in each of the cases listed in table 1.1 will be given, with the accompanying discussion concentrating on how the threshold is affected by the identifying features of the particular OPO type.

It should be noted that the expressions to follow give the minimum pump threshold in each case. Therefore, perfect phasematching ($\Delta k = 0$) is assumed and no phasematching parameters appear in the expressions. Also, the pump volume is assumed to be minimised within the nonlinear crystal, creating an ideal balance between having a small spot size and reducing beam divergence. This is known as confocal focussing and, in general, results in the lowest pump thresholds. The alternate case, where the effects of pump focussing are considered in greater detail, is discussed alongside confocal focussing in chapter 4, section 4.2.

Starting with the simplest type of OPO, the threshold expression for an SRO is given below:

$$P_{p,th,min}^{in} = \frac{n_p^2 \epsilon_0 c^4}{\pi L d_{eff}^2 (1 - \delta^2)^2 v_p^3 \mathfrak{F}_{s/i}} \quad [SRO] \quad (1.24)$$

In equation (1.24), the superscript and subscripts on the left hand side simply relate to the fact that this expression gives the minimum external pump power that should be coupled into the OPO to reach threshold. It can be seen that the expression for the SRO threshold contains both crystal parameters (length L and d_{eff}) and pump beam parameters (n_p and v_p). However, the two most important factors are δ and $\mathfrak{F}_{s/i}$. The finesse of the cavity for the resonant wave (signal or idler) is given by $\mathfrak{F}_{s/i}$. The finesse is effectively a measure of the quality of the resonant cavity and is related to the round-trip loss, $\gamma_{s/i}$, by:

$$\mathfrak{F}_{s/i} = \frac{2\pi}{\gamma_{s/i}} \quad (1.25)$$

1. Introduction & OPO Background

Hence, from equations (1.24) and (1.25), decreasing the losses in the resonant cavity (and increasing the finesse) will reduce the pump threshold. The second factor, δ , is a parameter defining how far from degeneracy $\left(\omega_s = \omega_i = \frac{\omega_p}{2}\right)$ the OPO is being operated,

$$\delta = \frac{2\omega_s - \omega_p}{\omega_p} = \frac{\omega_p - 2\omega_i}{\omega_p} \quad (1.26)$$

Equation (1.26) shows that $\delta = 0$ exactly at degeneracy. If all other values are fixed, then this will give the lowest possible pump threshold.

Perhaps the most straightforward modification to the SRO is to double-pass the pump and/or non-resonant downconverted wave by converting the output mirror into a high reflector at the relevant wavelengths. As shown by the first diagram in table 1.1, this is equivalent to doubling the crystal length for each wave that is double-passed. Therefore, the threshold for an SRO with double-passed pump is simply half that of the single pass case:

$$P_{p,th,min}^{in} = \frac{n_p^2 \epsilon_0 c^4}{2\pi L d_{eff}^2 (1 - \delta^2)^2 v_p^3 \mathfrak{F}_{s/i}} \quad [SRO - DP P] \quad (1.27)$$

Note that this assumes that the output mirror has 100% reflectivity at the pump wavelength. Given that high reflectors are generally specified as being >99.9% reflecting during design, this is a reasonable assumption to make.

If the non-resonant downconverted wave were double-passed on its own then the interaction between signal and idler on the backward pass through the crystal would be in the absence of the pump field. Hence, conversion from signal and idler to pump would occur, known as backconversion and reducing the downconverted power. This problem can be overcome by double passing both the pump and non-resonant wave to ensure that the pump field is always present in the crystal. As might be expected, this results in a reduction of the threshold by a further factor of 2 (again assuming 100% reflectivity and, additionally, correct phasing between the interacting fields):

1. Introduction & OPO Background

$$P_{p,th,min}^{in} = \frac{n_p^2 \epsilon_0 c^4}{4\pi L d_{eff}^2 (1-\delta^2)^2 v_p^3 \mathfrak{F}_{s/i}} \quad [SRO - DP P, S / I] \quad (1.28)$$

The next type of OPO to consider is the doubly resonant oscillator (DRO), where both the signal and idler wave are resonant in the OPO cavity. In this case the pump threshold is given by:

$$P_{p,th,min}^{in} = \frac{n_p^2 \epsilon_0 c^4}{2L d_{eff}^2 (1-\delta^2)^2 v_p^3 \mathfrak{F}_s \mathfrak{F}_i} \quad [DRO] \quad (1.29)$$

As shown by equation (1.29), the expression for the DRO threshold is very similar to that of the SRO, but with an additional factor of $\frac{\pi}{2\mathfrak{F}_{s/i}}$. This can also be compared to the case of double-passing the non-resonant downconverted wave on its own in an SRO (ignoring the issue of backconversion). The additional factor contains the finesse of the cavity for this wave and therefore accounts for the fact that it is resonant in the DRO. Taking a typical round-trip loss of 4%, equation (1.25) gives a finesse of ~ 150 . Hence, the threshold of a DRO is generally two orders a magnitude less than its SRO counterpart with figures in the mW range [19, 20].

As with the SRO, there exists the opportunity to double-pass the pump wave in a DRO. In this case, the pump wave will be able to interact with both resonant downconverted waves for twice the crystal length. Given the previous discussion on double passing in an SRO, the logical conclusion is that the DRO threshold is reduced by a factor of 4 (2 for each resonant wave). This is supported by the threshold analysis, which yields equation (1.30):

$$P_{p,th,min}^{in} = \frac{n_p^2 \epsilon_0 c^4}{8L d_{eff}^2 (1-\delta^2)^2 v_p^3 \mathfrak{F}_s \mathfrak{F}_i} \quad [DRO - DP P] \quad (1.30)$$

Equations (1.27), (1.28) and (1.30) have shown that a significant threshold reduction can be achieved by reflecting the pump wave back through the nonlinear crystal before exiting the cavity. Taking this idea one step further leads to the prospect of resonating the pump wave in either an SRO or a DRO, with the latter becoming a triply resonant oscillator (TRO) as a result. Before considering the threshold expressions in each case, it should first be pointed out that, as far as the OPO is

1. Introduction & OPO Background

concerned, a resonant pump wave is no different to the double-pass case. This is due to the fact that the resonant pump wave will pass through the crystal twice on any single round trip. Therefore, the threshold pump power at the input face of the nonlinear crystal, commonly known as the *internal threshold*, will be the same as that achieved by double-passing the pump. Of course, the big difference is that, with a resonant pump, the internal threshold power can build up over a number of round trips. As a result, the pump power coupled into the cavity, the *external threshold*, is significantly reduced. Since, in the case of a resonant pump, the external threshold is only a fraction of the internal threshold (if the pump is double-passed the internal and external thresholds are equal), such a set-up is known as *pump enhancement*.

The concept and application of pump enhancement will be discussed in detail in chapter 3. For now, the relevant threshold expressions are considered. In the preceding discussion, the similarity between pump enhancement and double passing was noted. A natural hypothesis would be to expect this similarity to be repeated in the threshold expressions, which are given below:

$$P_{p,th,min}^{in} = \frac{n_p^2 \epsilon_0 c^4}{2\pi L d_{eff}^2 (1-\delta^2)^2 \nu_p^3 \tilde{\mathfrak{F}}_{s/i} E_{p,max}} \quad [SRO-PE] \quad (1.31)$$

$$P_{p,th,min}^{in} = \frac{n_p^2 \epsilon_0 c^4}{8L d_{eff}^2 (1-\delta^2)^2 \nu_p^3 \tilde{\mathfrak{F}}_s \tilde{\mathfrak{F}}_i E_{p,max}} \quad [DRO-PE (TRO)] \quad (1.32)$$

The hypothesis is shown to be correct. Equations (1.31) and (1.32) are identical to their double-pass counterparts (equations (1.27) and (1.30)), except for a new factor in the denominator, $E_{p,max}$. This is known as the enhancement factor (see chapter 3, section 3.1) and is defined by equation (1.33):

$$E_{p,max} = \frac{T_1 \tilde{\mathfrak{F}}_p^2}{\pi^2} \quad (1.33)$$

It can be seen from the above expression, that the enhancement factor is dependent on the finesse of the cavity at the pump wavelength and the transmission of the input mirror, T_1 , through which pump light enters the OPO cavity. Hence, the enhancement factor is directly linked to the cavity resonance at the pump wavelength. Note that the

1. Introduction & OPO Background

second cavity mirror is assumed to be 100% reflecting, giving the maximum enhancement factor in equation (1.33). Given a typical cavity finesse of around 100 and a 10% transmission at the input mirror, the resulting enhancement factor would be around 25. From the threshold expressions, this would also be the reduction in pump threshold from the case of double-pass pumping. Therefore, pump enhancement has the potential for very low external thresholds with values less than 10mW for the DRO and less than 100mW for the SRO [21].

The final type of OPO to be covered is the intra-cavity OPO (IC-OPO). As shown by the diagram in table 1.1, the nonlinear crystal in this case is situated within the cavity of the pump laser. This allows the large pump field circulating within the laser cavity to be utilised. In this respect, the IC-OPO is similar to an OPO with pump enhancement. At first glance, it might be expected that the threshold expressions for an SRO or DRO with double-pass pump (equations (1.27) and (1.30)) can be applied here. Of course, the subsequent threshold value must be equated with circulating pump field rather than the output of the pump laser itself. As a result, the power requirement of the pump laser is significantly reduced compared to the standard SRO or DRO. The problem with this first approximation to the IC-OPO threshold is that it ignores any effect the OPO might have on the pump laser itself via interactions with the internal laser field. This issue is complicated by the fact that the OPO is a dynamic device and therefore the interaction will be different below and above threshold. A more detailed discussion of the IC-OPO threshold is beyond the scope of this thesis. However, several publications have reported on the study of IC-OPO operation with the observation of effects such as power clamping and relaxation oscillations [22, 23].

1.6) Tuning Behaviour

The signal and idler frequencies upon which a particular OPO will operate are determined by a number of factors. Perhaps the most important is the requirement for phasematching within the nonlinear crystal. In sections 1.1 and 1.3, methods for achieving perfect phasematching, such that $\Delta k = 0$, were discussed. However, it is more common to specify a range of Δk values over which the phasematching is considered acceptable. This results in a phasematch bandwidth, which by consensus is

1. Introduction & OPO Background

defined between $\Delta k = \pm \frac{\pi}{L}$. At these points, the sinc function shown by figure 1.1 has a value that is approximately two thirds of the peak and the gain at α_1 and α_2 is reduced by the same amount. In terms of the intensity gain for the signal and idler, the corresponding reduction is just over half of the peak value. With the phasematch bandwidth defined, the phasematching condition (equation (1.22)) can be rewritten as:

$$|\Delta k| = |k_3 - k_2 - k_1 - K| \leq \frac{\pi}{L} \quad (1.34)$$

The phasematch bandwidth can be viewed in similar terms to the gain bandwidth of a laser. However, the important distinction and advantage of the phasematch bandwidth is that its centre wavelength can be shifted, often over a wide range. Methods for doing this include varying the pump wavelength [24], crystal temperature [25], crystal angle (BPM) [26] and poling period (QPM) [27].

Changing the position of the phasematch bandwidth can generally be considered as coarse tuning. For finer tuning it is necessary to look at frequency selection factors within a fixed bandwidth. These can be summarised by the two equations below:

$$\nu_p = \nu_s + \nu_i \quad (1.35)$$

$$\nu_j - pFSR_j \leq \frac{\Delta\nu_{c,j}}{2} \quad (1.36)$$

Equation (1.35) simply represents the requirement for energy conservation, which underpins the entire parametric generation process. In equation (1.36), j corresponds to a resonant wave, be it pump, signal or idler, p is a large integer and FSR is the cavity free spectral range. This equation shows that the difference between the frequency of the resonant wave and the nearest cavity mode must be less than half the cavity linewidth, $\Delta\nu_c$ i.e. the resonant wave must lie within the linewidth of a cavity mode. So, equations (1.35) and (1.36) show that the signal and idler frequencies must satisfy energy conservation and, if resonant, must coincide with a cavity mode frequency.

1. Introduction & OPO Background

Beginning with the SRO, where only one of the signal or idler is resonant, the optimum frequency for the resonant wave will be that of the cavity mode closest to the maximum of the phasematch bandwidth. The non-resonant wave, under no constraint with regard to the OPO cavity, is free to adopt any frequency that satisfies the conservation of energy. Fine tuning can be achieved by varying either the pump frequency or the cavity length and consequently, the stability of the resonant wave is dependent on the stability of these two factors.

Taking the idler to be the non-resonant wave and looking at tuning by pump frequency first, it is clear that there are two cases. In the first case, the pump frequency is changed such that the maximum of the phasematch bandwidth shifts by less than half a FSR at the signal. Since the cavity mode closest to the phasematch maximum has not changed, the idler frequency will change to maintain equation (1.35) whilst the signal frequency remains fixed. The second case involves the phasematch maximum shifting by at least half a signal FSR. This causes the signal frequency to hop to an adjacent cavity mode. The maximum idler tuning range before a mode hop occurs can be calculated from:

$$|\Delta\nu_{i,\max}| = \left(\frac{\Delta\nu_p}{\Delta\nu_s} - 1 \right) FSR_s \quad (1.37)$$

In equation (1.37), $\Delta\nu_s$ is the change in signal frequency that occurs for a change in pump frequency of $\Delta\nu_p$.

If tuning is instead achieved by varying the cavity length then, as before, the largest shift in the maximum of the phasematch bandwidth before a mode hop occurs is plus or minus half a signal FSR. This gives a total tuning range of one FSR. Since the pump frequency is now fixed, any change in the signal frequency will be repeated by the idler frequency, but in the opposite direction, due to energy conservation. Hence, the maximum mode-hop-free tuning range can be written as:

$$|\Delta\nu_{s,\max}| = |\Delta\nu_{i,\max}| = FSR_s \quad (1.38)$$

The frequency shift, $\Delta\nu$, for a change in cavity length, Δl , within this range can be obtained by differentiating the standard equation for FSR,

$$v_{FSR} = \frac{c}{2nL+l} \quad (1.39)$$

with respect to l (length of empty cavity) giving:

$$\Delta v_s = -\Delta v_i = \frac{v_s}{nL+l} \Delta l \quad (1.40)$$

If pump enhancement is implemented within the SRO cavity, then the further requirement of pump resonance must be included when considering the tuning characteristics of the OPO. Clearly, tuning by variation of the cavity length is limited to the range over which the pump remains resonant within the cavity. This is determined by the cavity linewidth at the pump wavelength and will generally be much smaller than the range given by equation (1.38) for an SRO with single-pass pump.

As discussed in chapter 3, section 3.5, it is normal to employ some form of stabilisation to ensure that the pump wave remains on resonance. Assuming that the pump source can also be stabilised to a high degree, the utilisation of such a scheme can result in an OPO with high frequency stability in the downconverted waves. Should the pump wavelength change; there will be a shift in the maximum of the phasematch bandwidth as described in the single-pass pump case. In addition, the subsequent change in cavity length to ensure pump resonance will produce a change in the signal and idler frequencies. This results in an overall change to the resonant signal frequency given by:

$$\Delta v_s = \frac{v_{s,0} FSR_s}{v_{p,0} FSR_p} \Delta v_p \quad (1.41)$$

Here, $v_{p,0}$ and $v_{s,0}$ are the initial pump and signal frequencies before the any shifts occur. As in the case of an SRO with single-pass pump, a mode hop will occur if the shift in the phasematch maximum away from the resonant signal frequency is greater than half a FSR. However, it is necessary to take into account the fact that the signal frequency also changes, as previously mentioned. Therefore, the criteria for a mode-hop is given by the following:

$$\Delta v_{s,pm} - \Delta v_s = \pm \frac{FSR_s}{2} \quad (1.42)$$

1. Introduction & OPO Background

Equation (1.42) shows that a mode hop will occur when the difference between the shift of phasematch maximum, $\Delta v_{s,pm}$, and the change in the signal frequency, Δv_s , is greater than half a signal FSR. This assumes that the maximum of the phasematch bandwidth initially coincides with the resonant signal frequency. It can be seen that if both $\Delta v_{s,pm}$ and Δv_s change in the same direction, the range of mode-hop-free tuning achieved by varying the pump frequency will be greater than that of an SRO with non-resonant pump and fixed cavity length. Conversely, if $\Delta v_{s,pm}$ and Δv_s have the opposite sign, the tuning range will be reduced compared to the simple SRO case.

Having dealt with the tuning behaviour of an SRO in its various guises, it is now time to consider the DRO. In addition to the phasematching and energy conservation requirements, the DRO cavity must also simultaneously resonate the signal and idler waves. Therefore, the signal and idler frequencies must both be resonant cavity modes as well as summing to the pump frequency. As a result of these constraints, the tuning behaviour of the DRO is significantly more complex than that of the SRO. The systematic tuning behaviour of the SRO, which can be modelled by equations (1.37) to (1.42), no longer occurs. In addition to hops between adjacent cavity modes, large frequency shifts known as cluster hops are often observed. Associated with these frequency shifts are significant fluctuations in output power, sometimes leading to the OPO switching off completely.

DRO tuning behaviour has been studied both theoretically and experimentally by a number of authors [28-30]. The reasons behind the complex tuning behaviour of the DRO and the subsequent consequences in terms of spectral quality and control have proved to be important issues in the context of this project. Rather than give a general explanation here, these issues are explored in chapters 5 – 7, with particular attention paid to the DRO used in the OPO-FCG project.

1.7) Chapter Summary

This chapter began by introducing the research project to be discussed by this thesis. The aim of the project was to combine the technologies of frequency comb generation and optical parametric oscillation, to develop a compact, low power device capable of generating wide spanning frequency combs centred at 1600nm.

1. Introduction & OPO Background

After a summary of the subsequent chapters, the rest of this introductory chapter was devoted to the discussion of the optical parametric oscillator. Beginning with the polarisation term in Maxwell's equation, the field of nonlinear optics was established. One particular aspect of nonlinear optics is difference frequency generation, upon which optical parametric generation is based. In OPG, a strong pump field mixes with two weaker signal and idler fields (whose frequencies sum to the pump frequency) in a nonlinear crystal such that the signal and idler fields experience gain, whilst the pump field is depleted. One of the most important factors in this process is the relative phase between the three fields within the crystal. To ensure maximum gain for the signal and idler, it is necessary for the wavevector mismatch between the three waves to equal zero. This can be achieved in one of two ways. Birefringent phasematching utilises the anisotropic properties of many of the nonlinear crystals used for OPG. In such crystals, the refractive index experienced by a wave is dependent on its polarisation and propagation direction. Hence, by choosing the correct polarisation for each of the three waves, a propagation direction will exist that ensures they experience the same refractive index – setting the wavevector mismatch to zero.

The second method of phasematching, quasi-phasematching, works by inducing a periodic π phase shift between the pump, signal and idler. This resets the phase difference between the three waves to zero, ensuring that power is continually transferred from the pump to the signal and idler. QPM is most commonly achieved by inverting ferro-electric domains within the nonlinear crystal, a process known as periodic poling.

The coupled-wave equations describe how the electric fields for the pump, signal and idler waves change as they propagate through the nonlinear crystal. From these equations, the Manley-Rowe relations can be derived. These describe the transfer of energy between the three waves and, in particular, show that the destruction of a single pump photon creates exactly one signal and one idler photon. As a result, the Manley-Rowe relations also give the fundamental efficiency of the particular OPG process.

When dealing with continuous waves rather than pulses, it is necessary to resonate at least one of the signal or idler if significant downconverted power is to be generated. This is known as optical parametric oscillation and in the simplest case, a pair of mirrors about the nonlinear crystal is used to resonate the signal or idler. Whilst this

1. Introduction & OPO Background

singly resonant oscillator is relatively simple to set up and offers systematic tuning, the threshold power required for the generation of signal and idler is typically quite large. As a result, a large research effort has led to the development of several types of OPO cavity with significantly reduced thresholds. One of the most straightforward is simply a modification to the SRO cavity, whereby the pump and/or non-resonant downconverted wave are reflected back through the nonlinear crystal for a second pass. Each wave that is double-passed can reduce the threshold by up to a factor of two. An OPO with both signal and idler resonant is known as a doubly resonant oscillator and typically offers threshold reduction factors of ~ 100 compared to the singly resonant case. The pump wave can also be double-passed in a DRO, offering a further reduction. A large pump field can be built up around the nonlinear crystal by resonating the pump wave. This is known as pump enhancement and reduces the double-pass pump threshold in either an SRO or DRO by the pump enhancement factor. This factor is related to both the finesse of the OPO cavity at the pump wavelength and the transmission of the input mirror. The final type of OPO under consideration was the intra-cavity OPO. In this case, the nonlinear crystal is placed inside the pump laser cavity, with a beamsplitter used to separate the downconverted waves from the laser crystal. This takes advantage of the large circulating pump field that exists within the laser cavity. Hence, the output power of the pump laser required to reach threshold is significantly reduced compared to the case where the OPO and pump laser are in separate cavities. However, there are issues relating to the interaction of the laser field with the nonlinear crystal that must be addressed.

The final section of this chapter looked at the tuning behaviour of the SRO and DRO. In an OPO, the signal and idler frequencies are determined in the first instance by the phasematching condition. It is normal to specify a bandwidth over which acceptable phasematching occurs and this is analogous to the gain bandwidth in a laser. However, in an OPO the centre of the phasematch bandwidth can be shifted over a considerable frequency range by varying parameters such as the pump frequency and crystal temperature. This results in coarse tuning of the downconverted frequencies.

Within a fixed phasematch bandwidth, signal and idler frequency selection is determined by energy conservation and resonance within the cavity. The SRO, with only one resonant wave, exhibits systematic tuning via variation of the pump frequency or cavity length. Tuning of the resonant wave will occur over a predictable range before a jump to an adjacent cavity mode, known as a mode hop. If pump

1. Introduction & OPO Background

enhancement is incorporated into the SRO and a stabilisation scheme is employed to keep the pump wave on resonance, then high frequency stability of the downconverted waves can be achieved. Also, the combination of pump tuning and resulting cavity length change due to the stabilisation system can result in an increased mode-hop-free tuning range.

The DRO, on the other hand, is an entirely different matter. Due to the constraints of energy conservation and the dual resonance of the signal and idler, complex tuning behaviour is often observed. As well as mode hops, this can include large frequency shifts that are difficult to predict. This results in significant fluctuations in output power. During the course of this project, the tuning behaviour of a DRO was found to be an important factor and is explored in detail in later chapters.

References

1. Giordmaine, J.A. and Miller, R.C., *Tunable Coherent Parametric Oscillation in LiNbO₃ at Optical Frequencies*. Phys. Rev. Lett., 1965. **14**(24): p. 973-976.
2. Diddams, S.A., et al., *Broadband Optical Frequency Comb Generation with a Phase-Modulated Parametric Oscillator*. Optics Letters, 1999. **24**(23): p. 1747-1749.
3. Yariv, A. and Louisell, W.H., *Theory of the Optical Parametric Oscillator*. IEEE J. Quantum Electron., 1966. **QE-2**(9): p. 418-424.
4. Colville, F.G., *An Analysis of the Performance Characteristics of Continuous-Wave Optical Parametric Oscillators*, in *Physics & Astronomy*. 1994, University of St Andrews.
5. Lindsay, I.D., *High Spatial and Spectral Quality Diode-Laser-Based Pump Sources for Solid-State Lasers and Optical Parametric Oscillators*, in *Physics & Astronomy*. 1999, University of St Andrews.
6. Byer, R.L., *Optical Parametric Oscillators*, in *Quantum Electronics: A Treatise*, H. Rabin and C.L. Tang, Editors. 1975, Academic Press: New York.
7. Boyd, G.D. and Ashkin, A., *Theory of Parametric Oscillator Threshold with Single-Mode Optical Masers and Observation of Amplification in LiNbO₃*. Physical Review, 1966. **146**(1): p. 187-198.

1. Introduction & OPO Background

8. Zernicke, F. and Midwinter, J.E., *Applied Nonlinear Optics*. 1973, New York: Wiley.
9. Yariv, A., *Quantum Electronics*. 3rd ed. 1989, New York: Wiley.
10. Boyd, G.D. and Patel, N.K., *Enhancement of Optical Second-Harmonic Generation (SHG) by Reflection Phase Matching in ZnS and GaAs*. Appl. Phys. Lett., 1966. **8**(12): p. 313 - 315.
11. Yamada, M., et al., *First-Order Quasi-Phase-matched LiNbO₃ Waveguide Periodically Poled by Applying an External Field for Efficient Blue Second-Harmonic Generation*. Appl. Phys. Lett., 1993. **62**(5): p. 435.
12. Fejer, M.M., et al., *Quasi-Phase-matched Second Harmonic Generation: Tuning and Tolerances*. IEEE J. Quantum. Electron., 1992. **QE-28**(11): p. 2631.
13. Leonhardt, U., *Measuring The Quantum State Of Light*. 1997: Cambridge University Press.
14. van Herpen, M., et al., *Combined Wide Pump Tuning and High Power of a Continuous-Wave, Singly Resonant Optical Parametric Oscillator*. Applied Physics B - Lasers and Optics, 2004. **78**(3-4): p. 281-286.
15. Gross, P., et al., *Fiber-Laser-Pumped Continuous-Wave Singly Resonant Optical Parametric Oscillator*. Optics Letters, 2002. **27**(6): p. 418-420.
16. Abitan, H. and Buchhave, P., *Continuous-Wave Singly Resonant Optical Parametric Oscillator placed inside a Ring Laser*. Applied Optics, 2003. **42**(33): p. 6630-6635.
17. Chen, D.W., *Continuous-Wave Tunable Midwave Infrared Generation near 4.5 μm with an Intracavity Optical Parametric Oscillator and Difference Frequency Generation*. Journal of the Optical Society of America B - Optical Physics, 2003. **20**(7): p. 1527-1531.
18. Carleton, A., et al., *Compact, Continuous-Wave, Singly Resonant Optical Parametric Oscillator based on Periodically Poled RbTiOAsO₄ in a Nd:YVO₄ Laser*. Optics Letters, 2003. **28**(7): p. 555-557.
19. Breitenbach, G., et al., *81-Percent Conversion Efficiency in Frequency-Stable Continuous-Wave Parametric Oscillation*. Journal of the Optical Society of America B - Optical Physics, 1995. **12**(11): p. 2095-2101.

1. Introduction & OPO Background

20. Lindsay, I.D., et al., *Doubly Resonant Continuous-Wave Optical Parametric Oscillator Pumped by a Single-Mode Diode Laser*. Optics Letters, 1998. **23**(24): p. 1889-1891.
21. Scheidt, M., et al., *Diode-Laser-Pumped Continuous-Wave KTP Optical Parametric Oscillator*. Journal of the Optical Society of America B - Optical Physics, 1995. **12**(11): p. 2087-2094.
22. Turnbull, G.A., et al., *Transient Dynamics of CW Intracavity Singly Resonant Optical Parametric Oscillators*. IEEE J. Quantum Electron, 1999. **35**(11): p. 1666-1672.
23. Ebrahimzadeh, M., et al., *Intracavity Continuous-Wave Singly Resonant Optical Parametric Oscillators*. Journal of the Optical Society of America B - Optical Physics, 1999. **16**(9): p. 1499-1511.
24. Lindsay, I.D., et al., *110GHz Rapid, Continuous Tuning from an Optical Parametric Oscillator Pumped by a Fiber-Amplified DBR Diode Laser*. Optics Express, 2005. **13**(4): p. 1234-1239.
25. Tsunekane, M., et al., *Broadband Tuning of a Continuous-Wave, Doubly Resonant, Lithium Triborate Optical Parametric Oscillator from 791 to 1620 nm*. Applied Optics, 1998. **37**(27): p. 6459-6462.
26. Kim, K., et al., *Tuning Characteristics of a Continuous-Wave KTP Optical Parametric Oscillator*. Journal of the Korean Physical Society, 1999. **34**(3): p. 227-230.
27. Powers, P.E., et al., *Continuous Tuning of a Continuous-Wave Periodically Poled Lithium Niobate Optical Parametric Oscillator by use of a Fan-Out Grating Design*. Optics Letters, 1998. **23**(3): p. 159-161.
28. Eckardt, R.C., et al., *Optical Parametric Oscillator Frequency Tuning and Control*. Journal of the Optical Society of America B - Optical Physics, 1991. **8**(3): p. 647-667.
29. Padgett, M.J., et al., *Mode Selection in Doubly-Resonant Optical Parametric Oscillators*. IEEE Journal of Quantum Electronics, 1994. **30**(12): p. 2979-2985.
30. Henderson, A.J., et al., *Doubly-Resonant Optical Parametric Oscillators: Tuning Behaviour and Stability Requirements*. Opt. Comm., 1995. **119**: p. 256.

Chapter 2

Frequency Comb Generation

In the past decade, a powerful technique has emerged in the field of optical metrology. Known as frequency comb generation, it allows the creation of a direct link between an unknown optical frequency and a precise microwave frequency [1]. A frequency comb consists of several thousand equally spaced optical frequencies (the teeth in the comb) spanning several THz (tens of nm in wavelength terms). The separation between individual frequencies is usually of the order of a few GHz. Hence, the spacing in the comb can be locked to a precision radio-frequency/microwave oscillator, whose output frequency is known to a high accuracy. By utilising this ‘optical bridge’, spanning some 5 orders of magnitude, an unknown optical frequency can be measured with a similar accuracy to that of the oscillator.

The technique of frequency comb generation has already found extensive use in the field of spectroscopy [2]. However, recent advances have led to a further exciting possibility – the application of frequency comb generation in the next generation of optical communication systems. Prior to a discussion of this subject, it is first necessary to summarise the main physical and optical processes involved in the generation of a frequency comb.

2.1) The Linear Electro-optic Effect

Perhaps the most fundamental process in the generation of a frequency comb is the linear electro-optic effect. It occurs when an electric field is applied to anisotropic crystals i.e. those where the velocity of propagation of an electromagnetic wave (and hence the refractive index) depends on the plane of polarisation of the wave. The linear electro-optic effect has been extensively discussed in several textbooks [3], [4]. What follows is a summary of the main points and equations.

Firstly, it is important to introduce the *index ellipsoid* or *optical indicatrix*. This is a three-dimensional representation of the refractive index in an anisotropic crystal, allowing the refractive index to be calculated for any given plane of polarisation.

2. Frequency Comb Generation

From Maxwell's theory of electromagnetism, the energy density, W , in a dielectric medium is given by

$$W = \frac{1}{2} D \cdot \xi \quad (2.1)$$

The electric displacement, D , and the electric field of the incident light, ξ , are related by

$$\begin{aligned} D_x &= \epsilon_{11} \xi_x \\ D_y &= \epsilon_{22} \xi_y \\ D_z &= \epsilon_{33} \xi_z \end{aligned} \quad (2.2)$$

Here, x , y and z represent the principal axes of the crystal and ϵ_{ij} are the relevant elements from the electric permittivity tensor. Combining equations (2.1) and (2.2) gives

$$W = \frac{1}{2} \left(\frac{D_x^2}{\epsilon_{11}} + \frac{D_y^2}{\epsilon_{22}} + \frac{D_z^2}{\epsilon_{33}} \right) \quad (2.3)$$

According to equation (2.3) a constant energy surface is represented by a three-dimensional ellipsoid. By dividing both sides of (2.3) by W and performing the substitution $x^2 \equiv \frac{D_x^2}{2\epsilon_0 W}$ (similarly for y and z) the final expression for the index ellipsoid can be obtained,

$$\frac{x^2}{n_x^2} + \frac{y^2}{n_y^2} + \frac{z^2}{n_z^2} = 1 \quad (2.4)$$

Note that n_x , n_y and n_z , which represent the semi-axes of the index ellipsoid, are given by $\sqrt{\frac{\epsilon_{11}}{\epsilon_0}}$, $\sqrt{\frac{\epsilon_{22}}{\epsilon_0}}$ and $\sqrt{\frac{\epsilon_{33}}{\epsilon_0}}$ respectively, as defined in Maxwell's equations.

Figure 2.1 shows an example of an index ellipsoid for a particular class of anisotropic crystals known as uniaxial. In such crystals, $n_x = n_y = n_o$, the ordinary refractive index, and $n_z = n_e$, the extraordinary refractive index. Since a wave propagating along the z -

2. Frequency Comb Generation

axis of a uniaxial crystal will always experience n_o , independent of the plane of polarisation, the z-axis is commonly termed the optical axis.

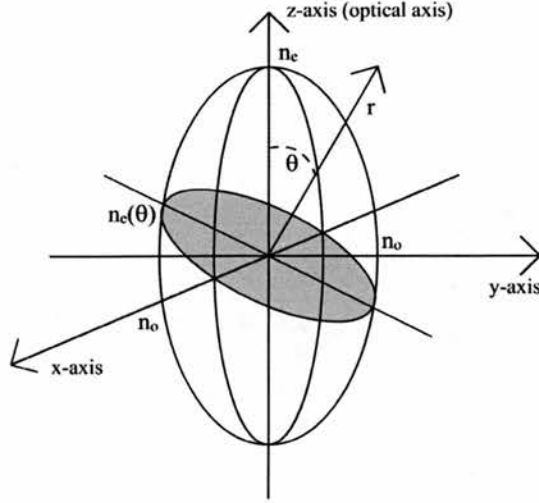


Figure 2.1 – Index ellipsoid for uniaxial crystal

If an external electric field is applied to an anisotropic crystal, a permutation in the lattice structure is created. This causes a change to the permittivity tensor and a deformation of the index ellipsoid. As a result, the axes of the ellipsoid no longer lie along the principal axes of the crystal. The index ellipsoid must now be represented by the general equation for an ellipsoid i.e.

$$\left(\frac{1}{n^2}\right)_1 x^2 + \left(\frac{1}{n^2}\right)_2 y^2 + \left(\frac{1}{n^2}\right)_3 z^2 + 2\left(\frac{1}{n^2}\right)_4 yz + 2\left(\frac{1}{n^2}\right)_5 xz + 2\left(\frac{1}{n^2}\right)_6 xy = 1 \quad (2.5)$$

The change in refractive index from the case of no applied field, described by equation (2.4), can be written as

$$\Delta\left(\frac{1}{n^2}\right)_i = \sum_{j=1}^3 r_{ij} \xi_j \quad (2.6)$$

with $i = 1, 2, \dots, 6$, $j = 1, 2, 3$, $\xi_{1, 2, 3} \equiv \xi_{x, y, z}$ and the 6×3 element matrix represented by r_{ij} is known as the electro-optic tensor. In most crystals, the symmetry of the lattice structure significantly reduces the number of non-zero elements in the electro-optic tensor. For instance, in KDP, a commonly used electro-optic crystal, the only non-zero elements are r_{41} , r_{52} ($= r_{41}$) and r_{63} .

2. Frequency Comb Generation

Continuing with the example of KDP, it is obvious from equation (2.6) that the first three terms of the general ellipsoid equation are identical to those of (2.4), since the relevant electro-optic coefficients and hence the change in refractive indices are 0. As a result, these terms are independent of the applied electric field. The other non-zero terms are cross-terms (shown in the latter half of (2.5)), induced by the applied electric field. Equation (2.7) gives the index ellipsoid for KDP when placed in an electric field of arbitrary direction.

$$\frac{x^2}{n_0^2} + \frac{y^2}{n_0^2} + \frac{z^2}{n_e^2} + 2r_{41}\xi_x yz + 2r_{41}\xi_y xz + 2r_{63}\xi_z xy = 1 \quad (2.7)$$

A comparison of equations (2.4) & (2.7) shows that the major axes of the ellipsoid are no longer parallel to the principal axes x , y and z . To determine the effect on an electromagnetic wave passing through the KDP crystal, it is necessary to find a new set of axes, x' , y' and z' , along which the major axes of the index ellipsoid now lie. Commonly, the electric field is applied along the z -axis of the KDP crystal (the original optic axis) such that $\xi_x = \xi_y = 0$. Equation (2.7) therefore simplifies to

$$\frac{x^2}{n_0^2} + \frac{y^2}{n_0^2} + \frac{z^2}{n_e^2} + 2r_{63}\xi_z xy = 1 \quad (2.8)$$

The desired x' , y' and z' are such that the resulting equation for the index ellipsoid contains no cross-terms and has the same form as (2.4) i.e.

$$\frac{x'^2}{n_{x'}^2} + \frac{y'^2}{n_{y'}^2} + \frac{z'^2}{n_{z'}^2} = 1 \quad (2.9)$$

Comparing equations (2.8) and (2.9) shows that $z' = z$ and therefore $n_{z'} = n_e$. Equation (2.8) is also symmetric in x and y , that is, replacing x with y and vice versa does not alter the equation. It can therefore be deduced that the new axes x' and y' are rotated through 45° from the original position of x and y (figure 2.2).

2. Frequency Comb Generation

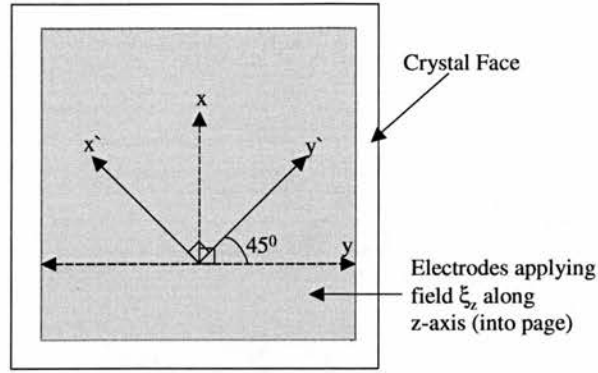


Figure 2.2 – Rotation of principal crystal axes

This gives the following relationships between the two sets of axes,

$$\begin{aligned} x &= x' \cos 45^\circ + y' \sin 45^\circ \\ y &= -x' \sin 45^\circ + y' \cos 45^\circ \end{aligned} \quad (2.10)$$

By substituting equations (2.10) into (2.8), the desired equation for the index ellipsoid, in the form of (2.9), is achieved.

$$x'^2 \left(\frac{1}{n_0^2} - r_{63} \xi_z \right) + y'^2 \left(\frac{1}{n_0^2} + r_{63} \xi_z \right) + \frac{z^2}{n_e^2} = 1 \quad (2.11)$$

Equations (2.9) and (2.11) show that the index ellipsoid has indeed been rotated such that its major axes now lie along the new principal axes x' , y' and z' . Also, the lengths of the major axes have been altered in the x' and y' directions such that

$$\begin{aligned} \frac{1}{n_{x'}^2} &= \frac{1}{n_0^2} - r_{63} \xi_z \\ \frac{1}{n_{y'}^2} &= \frac{1}{n_0^2} + r_{63} \xi_z \end{aligned} \quad (2.12)$$

From (2.12), the resultant change in the refractive index (assuming a small change so that $n_{x'} \approx n_{y'} \approx n_0$) is found to be

2. Frequency Comb Generation

$$\begin{aligned}\Delta n_{x'} &= n_{x'} - n_0 = \frac{n_0^3}{2} r_{63} \xi_z \\ \Delta n_{y'} &= n_{y'} - n_0 = -\frac{n_0^3}{2} r_{63} \xi_z\end{aligned}\tag{2.13}$$

Note that since $n_z = n_e$, as mentioned previously, there is no change in the refractive index along the z' ($= z$) axis.

Whilst the above analysis applies to KDP and other crystals in its class, similar equations can be derived for other crystal classes. Generally, the change in refractive index is of the same form as (2.13), but with a value of r specific to the class of crystal.

2.2) Phase Modulation

In the previous section it was shown that the application of an electric field to an anisotropic crystal such as KDP, results in a rotation of the principal axes by 45° and a change in refractive index along these axes proportional to the electric field strength (equations (2.13)). In this section, a specific application of the linear electro-optic effect will be discussed, namely phase modulation [5] – a key physical process in the generation of a frequency comb.

When an optical beam of wavelength λ passes through a medium of refractive index n and length L , the associated phase shift is given by

$$\phi = \frac{2\pi n}{\lambda} L\tag{2.14}$$

Now, consider linearly polarised light passing through an anisotropic crystal that is subject to an electric field, ξ , as described in the previous section (often described as an *electro-optic crystal*). If the crystal is orientated such that the plane of polarisation is aligned with one of the rotated principal axes, x' or y' , then the change in phase (compared to the case of $\xi = 0$) is directly proportional to the change in refractive index

$$\Delta\phi = -\frac{2\pi L}{\lambda} \Delta n = -\frac{\pi L}{\lambda} n_0^3 r \xi\tag{2.15}$$

2. Frequency Comb Generation

Here, n_0 is the refractive index of the crystal with no electric field present and r is the electro-optic coefficient of the crystal.

In the preceding analysis, a static electric field has been assumed. If instead, a sinusoidally varying electric field of frequency f_m is applied to the crystal i.e.

$$\xi = \xi_0 \sin(2\pi f_m t) \quad (2.16)$$

then, from equation (2.15), the change in phase will also have a sinusoidal variation i.e.

$$\Delta\phi = -\frac{\pi L n_0^3 r \xi_0}{\lambda} \sin(2\pi f_m t) \quad (2.17)$$

This situation, shown in figure 2.3, is usually described as phase modulation, with f_m known as the modulation frequency. As well as being an important part of many optical applications, phase modulation is also extensively used in long-range radio communications (e.g. satellite and deep space missions) due to its desirable noise properties and the fact that it can be produced by simple and robust electronic circuits.

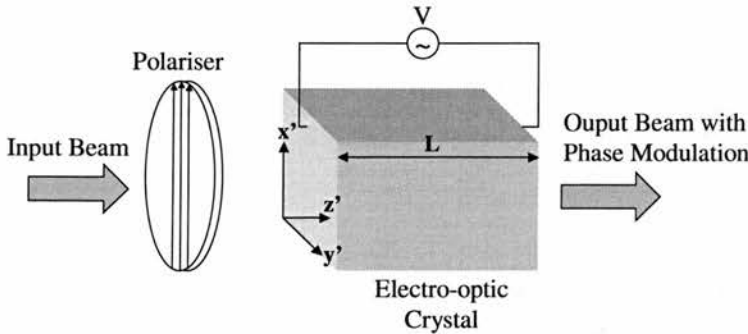


Figure 2.3 – Typical setup for electro-optic phase modulation

The question now arises as to the effect of phase modulation on the linearly polarised light passing through the electro-optic crystal. An optical field of the form

$$E_{in} = A \cos(2\pi f_0 t) \quad (2.18)$$

2. Frequency Comb Generation

incident on the input face of the crystal ($z = 0$) will emerge from the output face ($z = L$) as

$$E_{out} = A \cos(2\pi f_0 t + \phi_0 + \Delta\phi) \quad (2.19)$$

Here, the constant phase factor ($\phi_0 = \frac{2\pi n_0 L}{\lambda}$) can be ignored, since it does not affect

the final outcome. Combining equations (2.17), (2.19) and writing $\delta = \frac{\pi L n_0^3 r \xi_0}{\lambda}$ gives

$$E_{out} = A \cos(2\pi f_0 t - \delta \sin(2\pi f_m t)) \quad (2.20)$$

The factor δ is usually described as the *phase modulation index*. It is now possible to use the Bessel function identities,

$$\begin{aligned} \cos(\delta \sin(2\pi f_m t)) &= J_0(\delta) + 2J_2(\delta) \cos(4\pi f_m t) + 2J_4(\delta) \cos(8\pi f_m t) + \dots \\ \sin(\delta \sin(2\pi f_m t)) &= 2J_1(\delta) \sin(2\pi f_m t) + 2J_3(\delta) \sin(6\pi f_m t) + \dots \end{aligned} \quad (2.21)$$

to rewrite equation (2.20) as

$$E_{out} = A \left[\begin{aligned} &J_0(\delta) \cos(2\pi f_0 t) + J_1(\delta) \cos 2\pi(f_0 + f_m)t + J_1(\delta) \cos 2\pi(f_0 - f_m)t + \\ &J_2(\delta) \cos 2\pi(f_0 + 2f_m)t + J_2(\delta) \cos 2\pi(f_0 - 2f_m)t + J_3(\delta) \cos 2\pi(f_0 + 3f_m)t + \\ &J_3(\delta) \cos 2\pi(f_0 - 3f_m)t + \dots \end{aligned} \right] \quad (2.22)$$

From (2.22), it can be seen that the spectrum of the light emerging from the crystal will consist of a centre frequency, f_0 , surrounded by equally spaced sidebands that are separated from the centre frequency by multiples of the modulation frequency, f_m . Equation (2.22) also shows that the energy in the n th sideband is given by the value of the n th order Bessel function at the modulation index i.e. $J_n(\delta)$. Figure 2.4 shows how J_0 and J_1 (corresponding to the energy in the centre frequency and first order sidebands) vary with δ over the range -2π to $+2\pi$.

2. Frequency Comb Generation

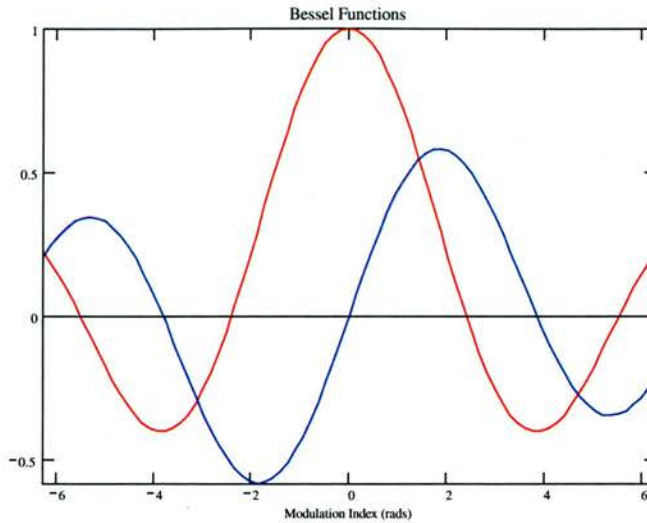


Figure 2.4 – 1st & 2nd order Bessel functions

In figure 2.5, a typical spectrum of a phase-modulated optical beam is shown. With the modulator switched off, the left hand image shows the single mode of the input laser beam. Switching the modulator on transfers a significant fraction of power from this central mode to the two first order sidebands, clearly visible in the right hand image.

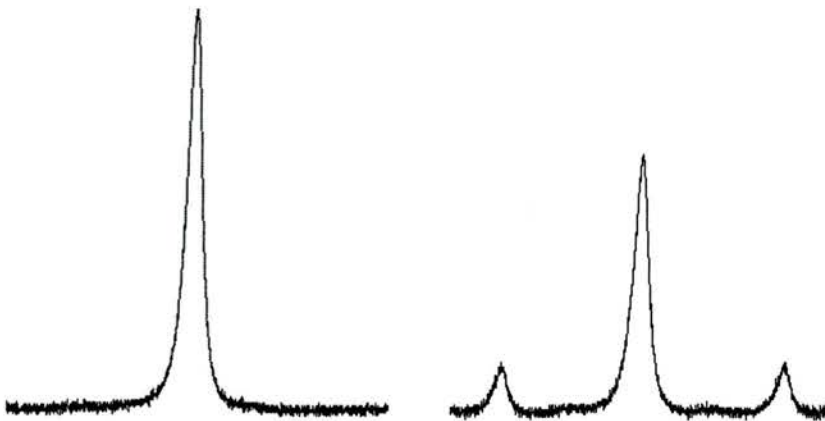


Figure 2.5 – Spectrum of phase-modulated laser beam with modulator off (left image) and modulator on (right image)

2. Frequency Comb Generation

2.3) Comb Generation in a Passive Cavity

Having discussed optical phase modulation and its effect on the frequency spectrum of a monochromatic light beam, the technique of frequency comb generation can now be described. Consider an electro-optic phase modulator (EOM) of length L_{mod} situated between two highly reflecting mirrors, separated by a distance L_{cav} and forming an optical cavity, as shown in figure 2.6. Light of frequency ν_0 is coupled into the cavity. Since there are no other active media between the mirrors, such a configuration is often called a passive or ‘cold’ cavity.

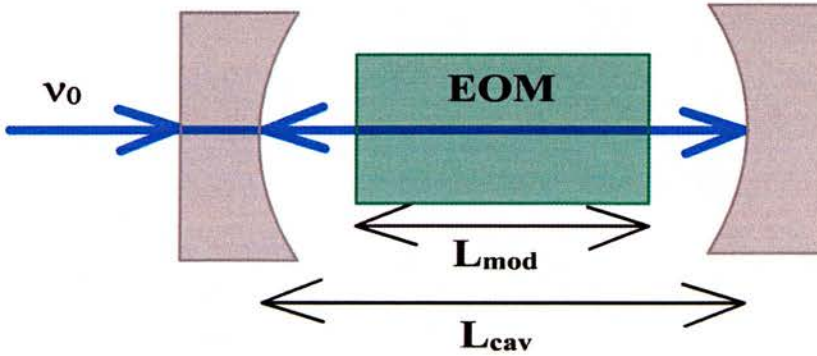


Figure 2.6 – EOM in an optical cavity

The resonant modes of this cavity are given by the standard equation

$$\nu_m = \frac{mc}{2(L_{cav} + (n-1)L_{mod})} \quad (2.23)$$

Here, n represents the refractive index of the EOM crystal and m is an integer. Hence the frequency separation between adjacent modes, also known as the free spectral range (FSR) of the cavity, is given by

$$\nu_{FSR} = \frac{c}{2(L_{cav} + (n-1)L_{mod})} \quad (2.24)$$

A frequency comb is generated by setting the modulation frequency of the EOM equal to the mode separation of the optical cavity i.e. $f_m = \nu_{f.s.r}$ [6]. To see how this works, first note that by setting $f_m = \nu_{f.s.r}$, the sidebands generated by the EOM will exactly

2. Frequency Comb Generation

overlay the cavity modes in frequency space. Hence, the sidebands will be resonant between the two mirrors and will pass back through the EOM, experiencing phase modulation. As a result, the initial sidebands will generate their own sidebands, which will also be resonant, and so on. The overall effect is a cascade process, producing a series of equally spaced frequencies, or modes, about ν_0 (the central frequency) over a wide bandwidth – a comb of frequencies, figure 2.7.

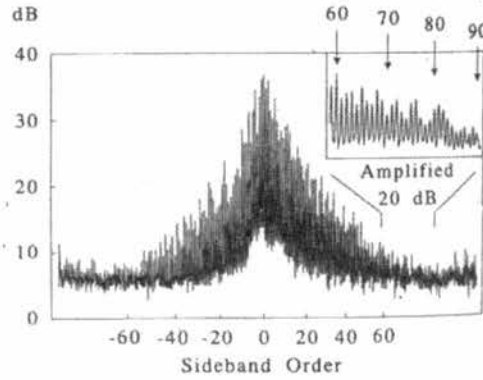


Figure 2.7 – Example of comb generated in a passive cavity [7]

Of course, since there is no source of optical gain, energy conservation dictates that the total power in the frequency comb must be equal to the optical power incident on the cavity (usually from a laser source). Herein lies the major problem with the passive cavity configuration. In terms of frequency comb generation the ideal case would be for the input optical power, P_i , to be equally distributed across all frequencies in the comb. However, it can be shown [8] that the fraction of power in the k -th sideband from the input ‘centre’ frequency is given by

$$\frac{P_k}{P_i} = \eta_{cav} \left(\frac{\pi}{2\delta.F} \right)^2 \exp\left(\frac{-|k|\pi}{\delta.F} \right) \quad (2.25)$$

δ is the phase modulation index as defined in section 2.2 and η_{cav} , F represent the input coupling and finesse of the optical cavity respectively. From equation (2.25) it can be seen that the power in each mode of the comb decreases exponentially with increasing mode number. It is also apparent that there will eventually be a mode with $P_k \sim 0$. At this point, the comb will be indistinguishable from the background noise.

2. Frequency Comb Generation

Therefore, (2.25) effectively defines the maximum extent of the comb. To increase the extent of the comb, it is necessary to increase η_{cav} , F and δ . An increase in the phase modulation index requires an increase in the electrical power supplied to the EOM. In practice, this can lead to undesirable heating of the modulator. Therefore, early efforts to increase the comb width concentrated on improving the quality of the optical cavity in the FCG set-up. For example, Kourogi et al [9] achieved a significant increase in cavity finesse and efficiency by applying a high reflection coating directly onto the ends of the modulator crystal, forming a monolithic comb generator. The resulting low round-trip loss was reflected in the maximum comb width of 6.1 THz, over 1.5 times larger than previously reported by the same group [8]. A different approach was taken by Bell et al [10], who incorporated an additional cavity before the EOM cavity in the comb generation set-up. The purpose of this ‘pre-cavity’ was to increase the coupling efficiency of laser light into the FCG cavity, thereby increasing the power transferred into the comb. This resulted in a comb containing 400 modes and spanning over 1 THz.

2.4) Comb Generation with an Active Medium

Whilst the methods described in the previous section can help to increase the width of the generated comb, the exponential decrease in mode power still exists. This is a fundamental problem with the passive cavity configuration, which can only be overcome by placing an active medium alongside the EOM in the cavity. The gain provided by the active medium counteracts the exponential power decrease, creating a flat comb with modes of approximately equal power.

In the context of frequency comb generation, there are two types of active medium. The first consists of conventional optical amplifiers, which operate on the same principles as a laser. For example, a frequency comb generation scheme proposed by Ho and Hahn [11] utilised an optical amplifier and modulator in a fibre loop. However, there are two major drawbacks to using an optical amplifier as the active medium. Firstly, the gain bandwidth of the amplifier will limit the span of the comb, since the power in any modes outside the bandwidth will rapidly decrease to negligible levels. The proposed set-up of Ko and Hahn was expected to generate a comb only spanning around 1 THz. This is significantly less than any of the comb

2. Frequency Comb Generation

widths generated by the passive cavity configurations. The second problem lies with the fact that an optical amplifier will add noise to the comb frequencies. As noted by Ko and Hahn, some of the noise peaks may have a greater power than the weaker comb frequencies. Obviously, this is highly undesirable in situations where a high signal to noise ratio is required, such as optical metrology and telecommunications.

The second type of active medium involves the use of parametric gain, through the second order nonlinear interaction. The unique nature of parametric gain gives several advantages over conventional optical gain. Since the parametric process does not depend on atomic or molecular transitions, it is inherently broadband and tuneable. As will be shown in chapter 5, the parametric gain bandwidth can extend to tens of THz. A second advantage is that, in most cases of parametric generation, the dominant noise source will be the pump laser, which can usually be stabilised to kHz precision. One further advantage of the parametric process is that the generated waves have a coherent phase link to the pump wave and between each other. Therefore, with parametric gain as the active medium in a frequency comb generator, a definite phase link can be created between all the modes in the comb.

Rather than introduce a source of parametric gain into a passive comb generator cavity, a more compact and elegant solution can be realised by incorporating the EOM into the cavity of an optical parametric oscillator. As discussed in chapter 1, an OPO generates coherent signal and idler waves whose frequencies sum to give the original pump frequency. By choosing the correct nonlinear crystal parameters such as temperature and grating period it is possible to set the signal and idler wavelengths equal to each other (i.e. $\lambda_s = \lambda_i = 2\lambda_p$), a condition known as degeneracy. If the signal/idler (for there is now no distinction between them) are then modulated at a frequency equal to their mutual FSR, a comb of frequencies will be produced about the degenerate wavelength. Such a device was demonstrated by Diddams et al [12], who introduced an EOM into the cavity of a degenerate OPO based on MgO-doped LiNbO₃ and pumped at 532nm. When operated at a pump power of 500mW (2.5 times threshold) and with the EOM driven by 400mW of RF power at around 350MHz, a flat comb spanning 5.6 THz (21nm) was generated about 1064nm.

The reader may have noted that whilst the frequency combs produced with an active medium are flat, they still have an abrupt cut-off. This is due to dispersion in the intra-cavity materials (e.g. modulator and nonlinear crystals). The concept of dispersion

2. Frequency Comb Generation

and its implications for frequency comb generation will be fully discussed in chapters 5 and 6. In summary, dispersion causes the mode spacing defined in equation (2.24) to be a roughly linear function of frequency. Therefore, the separation between resonant cavity modes will vary across the width of the comb. However, the separation between adjacent modes in the comb is defined by the modulation frequency and hence is a constant value. For a mode sufficiently far away from the central frequency, this results in a significant difference between the frequency of the generated sidebands and the nearest resonant cavity mode. This difference will increase with mode number (where the zero'th mode represents the central frequency in the comb) until the power transferred into the resonant mode is insufficient to overcome the round-trip loss in the cavity. Since no further modes can oscillate, the comb is cut-off at this point.

2.5) *FM Lasers*

In terms of experimental set-up, frequency comb generation with an active medium bears a number of similarities with a particular laser operational state known as *frequency modulated* (FM) oscillation. FM laser oscillation has been demonstrated in a number of different systems including standing wave [13] and ring [14] dye lasers, the solid-state Nd:YAG laser [15] and a broadband Ti:Sapphire oscillator [16]. In all cases, the basic laser cavity consisted of a gain medium and a mechanism for phase modulation surrounded by a standing or travelling wave resonator. As with frequency comb generation, the phase modulation occurred at a frequency equal or close to the longitudinal mode spacing of the resonator.

The parallels between FCG and FM lasers suggest that an examination of the latter process may well provide several insights into the former. A detailed analysis of FM laser oscillation was presented by Harris and McDuff in 1965 [17] and reinterpreted in a number of the references mentioned previously. One of the important parameters resulting from this analysis is the modulation index of the FM oscillation,

$$\Gamma = \frac{\delta \nu_{FSR}}{\pi \Delta \nu} \quad (2.26)$$

2. Frequency Comb Generation

Here, ν_{FSR} is the longitudinal mode spacing and $\Delta\nu$ is the detuning of the modulation frequency from the longitudinal mode spacing i.e.

$$\Delta\nu = f_m - \nu_{FSR} \quad (2.27)$$

The quantity δ refers to the round-trip phase retardation of the Fabry-Perot cavity with an intra-cavity phase modulator. It is related to the peak single-pass phase retardation of the modulator, δ_{PM} , by:

$$\delta = \frac{2L}{\pi x} \left(\sin \frac{\pi x}{2L} \right) \left(\cos \frac{z_0 \pi}{L} \right) \delta_{PM} \quad (2.28)$$

In equation (2.28), L is the cavity length and x the length of the modulator crystal. The distance from this crystal to the end mirror of the cavity is given by z_0 . This shows that for $x \ll L$, $\delta = \delta_{PM} \left(\cos \frac{z_0 \pi}{L} \right)$. Therefore, to access a large fraction of the peak phase retardation of the modulator, it is necessary to place the modulator as close to the end mirror as possible. Since this analysis applies to any Fabry-Perot cavity containing a phase modulator, the position of the modulator relative to the end mirror of the cavity must also be an important consideration for FCG.

From equation (2.26), it is clear that the modulation index will increase as the modulation frequency approaches the cavity mode spacing i.e. $\Delta\nu$ approaches 0. When $f_m = \nu_{FSR}$, the modulation index will be infinite. For a large modulation index, the full spectral width of the FM laser oscillation is given by:

$$\Delta\nu_{FSW} = 2\Gamma f_m \quad (2.29)$$

Given that, for high modulation indexes, $f_m \approx \nu_{FSR}$, equation (2.29) suggests that Γ is a good approximation to the total number of modes swept by the FM oscillation.

As $\Delta\nu$ is decreased and hence Γ increased, the operation of the FM laser is characterised by a number of stages. When $\Delta\nu$ is large, the laser will behave like a free-running laser. For an inhomogeneously broadened gain medium, this will mean oscillation on a number of independent cavity modes, with each accessing gain from effectively separate atomic populations (e.g. gas atoms with different associated

2. Frequency Comb Generation

Doppler frequencies). As $\Delta\nu$ is reduced, the phase modulator will cause the independent modes to each form frequency modulated spectra and become carriers of an FM signal. Gain competition occurs between the independent FM oscillations as before, but due to coupling effects caused by the overlap of sidebands with adjacent cavity modes, the broadening appears more like that in a homogeneous system. Therefore, the FM oscillations all interact with the same atomic populations to a good approximation. As a result, with decreasing $\Delta\nu$ there comes a point at which the strongest FM oscillation, usually closest to the centre of the gain profile, completely quenches the weaker oscillations and FM oscillation on a single longitudinal mode occurs.

With further reduction in $\Delta\nu$, the sidebands created by the phase modulation move away from line centre and laser energy is transferred to the edges of the gain profile. The resulting variations in gain experienced by separate sidebands allow multiple FM oscillations to occur once again and this region of operation is therefore known as *unquenched*.

The unquenched region marks the transition between the regions of FM oscillation and phase-locking (also known as mode-locking). Phase-locking occurs for very small values of $\Delta\nu$ and is a result of rephasing of the oscillating modes due to the large distortions experienced by the sidebands. In the phase-locked region, the output of the laser in the time domain consists of a series of periodic pulses whose repetition rate is equal to, or an integer multiple of, the modulation frequency. The duration of each pulse, τ_p , is related to the modulation frequency and index and is given by:

$$\tau_p = \frac{1}{2f_m\Gamma} \quad (2.30)$$

It should be noted that δ also plays an important role in the operation of the FM laser. In particular, if δ is too small then the regions of FM oscillation and phase-locking may never be reached, leaving just the initial unquenched operation. Also, a certain level of phase retardation is required for the unquenched region between FM oscillation and phase-locking to occur. This transition region is often characterised by a drop in laser power and, if δ is insufficient, the laser may switch off completely.

The question now arises as to the insight, with respect to frequency comb generation, that can be gained from studying the operation of the FM laser. In terms of cavity

2. Frequency Comb Generation

design the previously mentioned issue regarding modulator placement applies to frequency comb generation as well as the FM laser. On a more fundamental note, the different operating regimes of the FM laser may also apply when a frequency comb is generated. Therefore, the appearance of the output spectrum and beat frequencies between oscillating modes, as observed in the FM laser, could well provide important pointers as to the operation of the FCG. Of particular interest would be whether the spectral output of the FCG is an FM oscillation or phase-locked. Experimental observations of FM laser operation may well provide the answer to this question.

Of further interest are quantities associated with the FM laser, in particular the modulation index. As shown by equation (2.29), this can be used to calculate the full spectral width of the FM oscillation. If the same property is true of comb generation, then the modulation index would provide a quick and simple method of estimating the possible comb bandwidth.

It now seems prudent to look at some specific cases of FM laser operation, particularly those that compare favourably to OPO-FCG. In terms of the gain medium, an OPO is similar to a homogeneously broadened laser. Examples of such lasers are those based on liquid dye compounds and the solid-state Ti:Sapphire crystal. FM oscillation in a dye laser was achieved by Kane et al in both a standing wave [13] and ring [14] resonator configuration. For both cases, a phase modulator based on ADP was used to create frequency modulation. With the dye laser operating on a single frequency, an FM spectrum spanning up to 2.6 GHz was produced. By increasing the dye laser bandwidth to 40 GHz, through the use of intra-cavity elements, the width of the FM spectrum was increased to 175 GHz. For a detuning between modulation frequency and cavity FSR of <100 kHz, pulsed operation was observed with pulse widths around 2ns.

In the case of the Ti:S laser, FM oscillation was achieved by Curley and Ferguson [16] in a bow-tie resonator configuration and via MgO:LiNbO₃ phase modulator. A maximum FM bandwidth of 820 GHz was achieved in the basic system. The insertion of an intra-cavity birefringent tuning element reduced the maximum bandwidth to 150 GHz, but allowed larger detunings (20 kHz, compared to 3 kHz in the basic resonator). With the birefringent element, pulsed operation was observed for detunings <8 kHz, giving a shortest pulse length of 65ps.

Despite the similarity between OPO-FCG and the FM lasers described above in terms of gain broadening, there are some obvious differences. Initially, the OPO will only

2. Frequency Comb Generation

operate on one signal and idler mode pair at any one time and this pair will be coupled via the parametric interaction. This is in marked contrast to the initial free-running state of the FM laser, which can involve several independent longitudinal modes or one individual mode in the single frequency case. As discussed in chapter 1, section 1.5, the spectral behaviour of an OPO is governed by a number of constraints relating to phasematching, energy conservation and cavity resonance. The latter is the only constraint on spectral output of the FM laser. Despite these differences, the similarities between FM laser oscillation and frequency comb generation are still intriguing. It is hoped that further insight and answers to some of the questions above may be gained through the course of this thesis.

2.6) FCG & Optical Communications

The value of the frequency comb generation technique is well known in the fields of spectroscopy and metrology [18, 19]. However, frequency comb generation may also prove to be a very important tool for optical communications. Current telecommunications systems rely on a technique known as wavelength division multiplexing (WDM) to simultaneously send several optical channels down an optical fibre. A set of equally spaced optical frequencies is defined in a certain range. Each channel is then assigned a different carrier frequency from within this set. Data is encoded onto the carrier frequencies by the usual means and the channels are then combined into an optical fibre. At the receiver end, frequency selective optics are used to separate the channels and the data can then be extracted. Figure 2.8 shows a schematic of the WDM process.

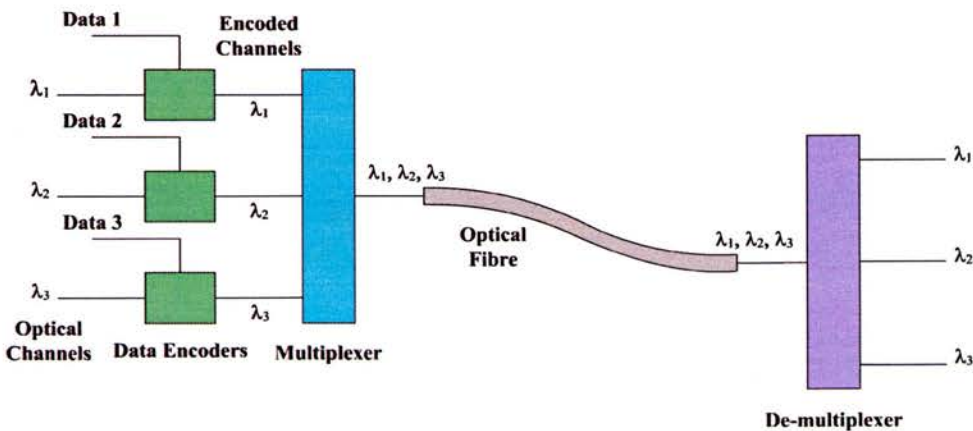


Figure 2.8 – Wavelength division multiplexing

2. Frequency Comb Generation

To be suitable for the channels in a WDM system, the set of optical frequencies must have a number of properties. Firstly, the number of frequencies must ideally be greater than the number of channels, to allow for the switching of channel frequencies and the expansion of the system. Current WDM systems typically operate on a few hundred channels, with this number expected to rise to around one thousand for next generation WDM (Dense Wavelength Division Multiplexing – DWDM) [20, 21]. Therefore, a set of several thousand optical frequencies would be desirable.

The frequencies themselves must be equally separated by a difference large enough to prevent crosstalk between channels (the leakage of signal from one channel into another). For example, the ITU-T (International Telecommunications Union – Telecommunication) specifies a frequency grid with 25 GHz spacing from 186200 THz to 196575 THz [22]. A narrow linewidth is also required of each frequency, again to prevent crosstalk. Typically, an acceptable linewidth would be around $\frac{1}{1000}$ th of the frequency spacing. So, a set of optical frequencies with a separation of several GHz and a linewidth of a few MHz would be required.

Obviously, the value of each channel frequency must remain constant to a very precise level to allow the channels to be separated during de-multiplexing. This leads to the final property of the set of optical frequencies – phase-locking. There must exist a definite phase relationship between all the frequencies in the set. As a result, the stabilisation of a single ‘control’ frequency will ensure the stabilisation of all frequencies in the set and prevent any undesirable drift in value or power.

Looking back to section 2.4, it is apparent that the properties of a set of optical frequencies required for WDM can be fulfilled by a comb generator based upon an optical parametric oscillator (OPO-FCG). However, such a device would have to be extremely compact, to allow for easy integration with the rest of the optical network. This places severe limits on the pump source for the OPO. Realistically, only a single-mode laser diode would be suitable. In a previous demonstration of an OPO-FCG, the pump threshold was 200mW with an operating power of 500mW [12]. This is far too high for the laser diode pump source mentioned above, whose typical maximum output power is around 150mW. Therefore, the task is to reduce the threshold and operating power to values such that pumping by a laser diode is feasible, which will be covered in the rest of this thesis.

2. Frequency Comb Generation

Before ending this chapter on frequency comb generation, it is pertinent to take a brief look at other techniques for frequency comb generation and assess their applicability to optical communications. In a proposal by Wong [23], a method of generating a 10 THz frequency comb at around $1.5\mu\text{m}$ was outlined. It involved the use of a stable laser source to simultaneously pump a set of ten phase-locked OPOs. The OPOs would be configured such that the signal and idler outputs were equally separated by ~ 500 GHz across the entire system. The OPO outputs would then be modulated at a frequency of 20 GHz, producing sidebands that would fill in the frequency space between each signal and idler wave. The overall result is a frequency comb spanning 10 THz, with a mode spacing of 20 GHz. Whilst the generated comb in this proposal satisfies all the criteria required for WDM, the system is far too large and cumbersome to be integrated with current telecommunications systems. Additionally, the power requirements and general complexity of the set-up are likely to be prohibitive when compared to the simplicity of other methods.

Throughout the discussions in this chapter, the method of modulation for generating a frequency comb has been electro-optic. However, there also exists another technique for in-situ modulation, namely acousto-optic. In this case, a sound wave is used to create a region of alternating high and low pressure in a transparent medium. This produces a change in the refractive index and the associated phase shift that leads to optical modulation, as summarised in section 2.2. Frequency comb generation via acousto-optic modulation has been demonstrated by Jessen & Kristensen [24]. Their set-up consisted of a dye laser and two acousto-optic modulators in a ring configuration, producing a frequency comb spanning a few hundred MHz with a mode spacing of around 6 MHz. In terms of optical communications, these values are significantly smaller than the minimum that would be acceptable. This highlights a fundamental limitation with using acousto-optic modulation for any form of frequency comb generation. The maximum modulation frequency of an acousto-optic modulator is inversely proportional to the time taken for the sound wave to pass through the medium. Given that in most materials the speed of sound is a few km/s, this means that the maximum modulation frequency is of the order of tens of MHz, even for the thinnest of media. Hence, it would never be possible to reach the modulation frequencies required for WDM with a comb generator based on an acousto-optic modulator.

2. Frequency Comb Generation

The final alternative method of frequency comb generation relies on a technique that is well known in the area of ultrafast optics i.e. mode-locking. Like the frequency comb generator, the spectrum of a mode-locked laser source consists of a series of equidistant frequencies whose separation is equal to the pulse repetition rate. This is due to the fact that the circulating pulse can be described as a superposition of the discrete longitudinal modes within the laser cavity. The use of the spectrum associated with a mode-locked source for bridging large frequency gaps has long been recognised in the area of metrology. Due to the inverse relationship between pulse length and spectrum width, it is only with the recent development of femtosecond sources based on Kerr-Lens mode-locking that frequency combs spanning tens of THz have become accessible [25-27]. A standard set-up would consist of a mode-locked femtosecond laser source whose repetition rate is locked to a stable microwave/RF source. This ensures a stable comb, since the mode separation has been shown to be equal to the repetition rate to a very high degree across the extent of the spectrum [28].

Further broadening of the frequency comb to several hundred THz can be achieved by passing the femtosecond output through a microstructured optical fibre. This has led to the demonstration of a direct link between microwave and optical frequencies [29] with a frequency comb spanning 300 THz. In the context of a telecommunications system, the very large bandwidth provided by such wide spanning combs would prove extremely attractive. However, there are several issues with mode-locked femtosecond systems that would need to be addressed. For metrological applications, the femtosecond lasers tend to be large and have significant power requirements, neither of which is favourable for telecoms. However, recent research into the development of compact, low power femtosecond lasers for telecoms applications may well solve this problem in the near future. A second issue with femtosecond frequency combs lies with the repetition rate of the mode-locked laser. Typical rates are of the order of hundreds of MHz, which is too small a separation between the modes in the comb (recall that channel spacings of several GHz are required for WDM). Again though, recent research into Ti:Sapphire based femtosecond oscillators with GHz repetition rates [30, 31] suggests that this may not be a problem for much longer. The final issue with comb generation based on mode-locked sources is one of inflexibility. As with any laser source, the centre frequency of the comb is limited to a narrow range of values determined by the lasing transition. Here, frequency comb

2. Frequency Comb Generation

generation based on a parametric source, with its inherent tunability, seems to offer a great advantage. However, as a final caveat, it is worth noting the research of Jones et al [32] who demonstrated that a femtosecond comb could be centred on arbitrary frequency. This was achieved via cross-phase modulation between a femtosecond pulse train and a continuous-wave laser beam whilst both were propagating through an optical fibre. In this case, the comb was fairly narrow with a mode spacing of only 90MHz. Nevertheless, if this technique could be combined with a GHz femtosecond system, it could prove a powerful tool in the area of telecommunications.

With each of the femtosecond comb techniques listed above there is one fundamental problem. By its very nature, a femtosecond comb will comprise a series of short optical pulses in the time domain. Associated with such pulses is a high peak power, which can potentially cause serious damage to the components within a telecommunications system. Wider femtosecond combs require shorter pulses and larger peak powers, exacerbating the problem.

2.7) Chapter Summary

At the beginning of this chapter, the fundamental process behind frequency comb generation was introduced. The electro-optic effect occurs when an electric field is applied to anisotropic crystals and results in a change to the refractive index along the principle crystal axes that is proportional to the applied electric field.

A particular application of the electro-optic effect, and one crucial to comb generation, is known as phase modulation. This is achieved by passing polarised light through the anisotropic crystal such that the plane of polarisation is parallel to either the x or y principle crystal axis. If a modulated electric field is then applied along the z-axis of the crystal, the modulation will be passed on to the refractive index experienced by the light. The overall result is a modulation of the phase of the light at the frequency of the electric field. In spectral terms, this creates equidistant sidebands about the original frequency of the light, whose separation is equal to the modulation frequency and whose amplitude is determined by the value of a Bessel function at the modulation index. The modulation index is determined by the electric field, wavelength of the light and properties of the anisotropic crystal.

2. Frequency Comb Generation

Phase modulation is the key to the generation of a frequency comb. The electro-optic modulator (or phase modulator) is placed inside an optical cavity and the modulation frequency set equal to the cavity mode spacing. As a result, sidebands generated on laser light that is coupled into the cavity coincide with longitudinal modes and are resonant. The resonant sidebands pass through the modulator and generate their own sidebands, which are also resonant cavity modes. This process continues, resulting in a comb of several thousand equally spaced frequencies over a wide bandwidth.

In this passive configuration, energy conservation dictates that the power within the frequency comb must be equal to the laser power coupled into the cavity. To satisfy this, the power in individual modes is found to fall off exponentially as they move away from the centre of the comb, eventually leading to the comb being cut off. Whilst various methods have succeeded in increasing the comb width, comb generation in a passive cavity will always suffer from the exponential drop in power.

The solution is to include an active medium alongside the modulator within the optical cavity. This can provide gain for the modes in the comb, counteracting the decrease in power. Perhaps the most elegant way of doing this is to place an EOM within the cavity of a degenerate OPO. As a source of gain, the parametric interaction offers several advantages in terms of gain bandwidth, low noise and inherent phase coupling. When modulating at the cavity mode spacing, the comb of frequencies is generated around the degenerate signal and idler frequency.

Whilst the use of an active medium can solve the problem of power loss across the comb, the comb will still be eventually cut off due to dispersion within the intra-cavity media. Dispersion gradually causes the generated sidebands and cavity modes to move out of alignment. At some point, the power transferred into the cavity mode becomes too low to sustain it and the comb is cut off.

There are many interesting similarities between comb generation in an active medium and FM laser oscillation. Both involve modulation at the cavity mode spacing alongside a source of gain. The FM laser is characterised by a modulation index that can be used to determine the spectral width of the oscillation, and can operate in either the FM oscillation or phase-locked (pulsed) regimes. The transition between these regimes occurs as the difference between modulation frequency and cavity mode spacing is decreased. It is hoped that the observations of the behaviour of the FM laser can provide some insight into the operating characteristics of the frequency comb generator.

2. Frequency Comb Generation

The final section of this chapter discussed the possibility of applying frequency comb generation to optical communications. Wavelength division multiplexing requires a series of equally spaced, phase-locked frequencies to act as optical channels. Such properties are satisfied by a frequency comb, with the added advantage of containing several thousand frequencies. However, the apparatus for comb generation will need to be significantly reduced in size and the spacing between modes in the comb increased to the order of a few GHz. Other methods of producing a frequency comb such were also examined. Of these, femtosecond lasers and the wide comb of frequencies associated with their short pulses were found to be the most realistic rivals to frequency comb generation in terms of application in telecommunications.

References

1. Hall, J.L., et al., *Ultrasensitive Spectroscopy, The Ultrastable Lasers, The Ultrafast Lasers, and the Seriously Nonlinear Fiber: A New Alliance for Physics and Metrology*. IEEE Journal of Quantum Electronics, 2001. **37**(12): p. 1482-1492.
2. Zhang, Y., et al., *Accurate Frequency Atlas of Molecular Iodine near 532 nm Measured by an Optical Frequency Comb Generator*. Optics Communications, 2001. **200**(1-6): p. 209-215.
3. Yariv, A., *Optical Electronics*. 4th ed. 1991: Saunders College Publishing.
4. Smith, *Optoelectronics: An Introduction*.
5. Young, *Electronic Communication Techniques*. 1985, Columbus, Ohio: Charles E Merrill Publishing Co.
6. Kobayashi, T., et al., *High Repetition-Rate Optical Pulse Generator using a Fabry-Perot Electro-Optic Modulator*. Applied Physics Letters, 1972. **21**(8): p. 341 - 343.
7. Brothers, L.R., et al., *Terahertz Optical Frequency Comb Generation and Phase-Locking of an Optical Parametric Oscillator at 665 Ghz*. Optics Letters, 1994. **19**(4): p. 245-247.
8. Kourogi, M., et al., *Wide-Span Optical Frequency Comb Generator for Accurate Optical Frequency Difference Measurement*. IEEE Journal of Quantum Electronics, 1993. **29**(10): p. 2693-2701.

2. Frequency Comb Generation

9. Kourogi, M., et al., *A Monolithic Optical Frequency Comb Generator*. IEEE Photonics Technology Letters, 1994. **6**(2): p. 214-217.
10. Bell, A.S., et al., *Efficient Optical Frequency-Comb Generator*. Optics Letters, 1995. **20**(12): p. 1435-1437.
11. Ho, K.P. and Kahn, J.M., *Optical Frequency Comb Generator using Phase Modulation in Amplified Circulating Loop*. IEEE Photonics Technology Letters, 1993. **5**(6): p. 721-725.
12. Diddams, S.A., et al., *Broadband Optical Frequency Comb Generation with a Phase-Modulated Parametric Oscillator*. Optics Letters, 1999. **24**(23): p. 1747-1749.
13. Kane, D.M., et al., *FM Dye-Lasers*. Applied Physics B - Photophysics and Laser Chemistry, 1986. **39**(3): p. 171-178.
14. Kane, D.M., et al., *Comparison of FM Dye-Lasers in Standing-Wave and Ring Configuration*. Applied Physics B - Photophysics and Laser Chemistry, 1986. **40**(3): p. 147-151.
15. Kuizenga, D.J. and Siegman, A.E., *FM-Laser Operation of the Nd:YAG Laser*. IEEE Journal of Quantum Electronics, 1970. **QE-6**(11): p. 673.
16. Curley, P.F. and Ferguson, A.I., *Frequency-Modulated Operation of a Ti:Sapphire Laser*. Optics Communications, 1991. **83**(1-2): p. 85-91.
17. Harris, S.E. and McDuff, O.P., *Theory of FM Laser Oscillation*. IEEE Journal of Quantum Electronics, 1965. **QE-1**(6): p. 245.
18. Wong, N.C., *Optical Frequency Counting from the UV to the Near IR*. Optics Letters, 1992. **17**(16): p. 1155-1157.
19. Udem, T., et al., *Accuracy of Optical Frequency Comb Generators and Optical Frequency Interval Divider Chains*. Optics Letters, 1998. **23**(17): p. 1387 - 1389.
20. Shakouri, H., *Wavelength Lockers Make Fixed and Tunable Lasers Precise*, in *WDM Solutions*. January 2002. p. 23.
21. Keiser, G.E., *A Review of WDM Technology and Applications*. Optical Fiber Technology, 1999. **5**(1): p. 3-39.
22. <http://www.tunablemsa.com/>
23. Wong, N.C., *Proposal for a 10-Thz Precision Optical Frequency Comb Generator*. IEEE Photonics Technology Letters, 1992. **4**(10): p. 1166-1168.

2. Frequency Comb Generation

24. Jessen, P. and Kristensen, M., *Generation of a Frequency Comb with a Double Acousto-Optic Modulator Ring*. Applied Optics, 1992. **31**(24): p. 4911-4913.
25. Lubkin, G.B., *Femtosecond Comb Technique Vastly Simplifies Optical Frequency Measurements*, in *Physics Today*. June 2000. p. 19.
26. Reichert, J., et al., *Phase Coherent Vacuum-Ultraviolet to Radio Frequency Comparison with a Mode-Locked Laser*. Physical Review Letters, 2000. **84**(15): p. 3232-3235.
27. Udem, T., et al., *Absolute Optical Frequency Measurement of the Cesium D-1 Line with a Mode-Locked Laser*. Physical Review Letters, 1999. **82**(18): p. 3568-3571.
28. Udem, T., et al., *Accurate Measurement of Large Optical Frequency Differences with a Mode-Locked Laser*. Optics Letters, 1999. **24**(13): p. 881-883.
29. Diddams, S.A., et al., *Direct Link Between Microwave and Optical Frequencies with a 300 THz Femtosecond Laser Comb*. Physical Review Letters, 2000. **84**(22): p. 5102-5105.
30. Ramond, T.M., et al., *Phase-Coherent Link from Optical to Microwave Frequencies by means of the Broadband Continuum from a 1-GHz Ti:Sapphire Femtosecond Oscillator*. Optics Letters, 2002. **27**(20): p. 1842-1844.
31. Bartels, A. and Kurz, H., *Generation of a Broadband Continuum by a Ti:Sapphire Femtosecond Oscillator with a 1-GHz Repetition Rate*. Optics Letters, 2002. **27**(20): p. 1839-1841.
32. Jones, D.J., et al., *Frequency Comb Generation using Femtosecond Pulses and Cross-Phase Modulation in Optical Fiber at Arbitrary Center Frequencies*. Optics Letters, 2000. **25**(5): p. 308-310.

Chapter 3

Pump-Enhanced OPOs

In the summary of optical parametric oscillators in the first chapter, the different ways of reflecting and resonating the down-converted waves were discussed. For these singly or doubly resonant oscillators, the pump light is generally assumed to pass through the nonlinear crystal once (or twice if it is double-passed) before exiting the cavity. Such cavity configurations all suffer from the same problem; a high pump threshold. This is particularly true in the case of the newer nonlinear crystals such as RTA and KTP, where thresholds can be in excess of a Watt [1, 2]. This necessitates a high power laser or diode array as a pump source, leading to problems if a compact and efficient device is required. As a result, much OPO research has concentrated on developing new cavity geometries and configurations in an effort to produce low threshold systems. One such technique, which has shown considerable success, is known as pump-enhancement (PE).

3.1) The Pump-Enhanced Cavity

The implementation of a pump-enhancement cavity in an OPO was demonstrated by Robertson et al in 1994 [3] and has been used with a variety of nonlinear crystals, notably LiNbO₃ [4] and RTA [5]. It has also been subject to several theoretical discussions e.g. [6] and found use in applications such as gas sensing [7] and smooth frequency tuning [8]. The technique involves coating the OPO mirrors to be reflective at the pump wavelength, in addition to one or both of the down-converted waves. This creates a resonant cavity for the pump wave about the nonlinear crystal, rather than simply providing a single or double pass. Typically, one of the mirrors will be specified as an input coupler, with a transmission designed to couple the optimum level of pump light into the cavity (see section 3.4). The other mirror will be a high reflector at all resonant wavelengths. Figure 3.1 shows a schematic of a standard pump-enhanced SRO, with the pump (blue) and signal (green) resonant in the cavity

3. Pump-Enhanced OPOs

created by the input coupler, nonlinear crystal and high reflector. The non-resonant idler (red) exits after a single pass.

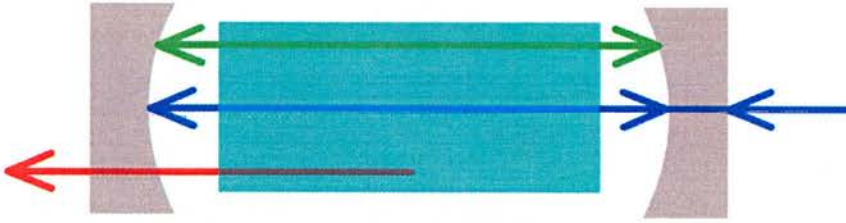


Figure 3.1 – Pump-enhanced SRO

By creating a resonant cavity for the pump wave, a high circulating pump field is created around the nonlinear crystal; much greater than the field incident on the input coupler. In this respect, the concept of pump-enhancement has many similarities with the intra-cavity OPO configuration, where the OPO crystal is situated directly inside the cavity of the pump laser [9-12]. Whilst the circulating pump field associated with an intra-cavity OPO is generally much higher than can be obtained with pump-enhancement, the latter does have a significant advantage over the former. The intra-cavity geometry can only be implemented for a narrow range of pump lasers (typically diode-pumped solid-state lasers or Ti:S ring oscillators). This precludes the use of many commercial laser sources and most significantly, stand-alone laser diodes. The pump-enhancement technique suffers from no such restrictions and is ideally suited for use with laser diode pump sources, which is very important in the context of the work described in this thesis.

The quality of the pump-enhancement cavity can be described by a single figure of merit, known as the *enhancement factor* (EF). This was defined in chapter 1 in terms of the enhancement cavity finesse. However, it also gives the ratio of the circulating pump power to the external pump power incident on the input mirror. As shown by the threshold expressions in chapter 1, the EF is the reduction in threshold that can be achieved by applying pump-enhancement to an OPO with a double-pass pump. This can be further understood by noting that an input coupler with 100% transmission in figure 3.1 will provide a double-passing of the pump and is also equivalent to an EF of 1.

The EF is dependent on only two factors, the parasitic losses in the cavity (including any transmission leakage at the high reflector) and the transmission of the input

3. Pump-Enhanced OPOs

coupler. To achieve a maximum EF and hence minimum pump threshold, it is first necessary to reduce the parasitic losses as much as possible. In practice, this means obtaining high quality optical coatings for the intra-cavity components and high reflector. In the case of the input coupler, the situation becomes significantly more complicated due to the conflicting requirements it represents. Decreasing the transmission of said component will reduce the overall loss in the cavity. However, to increase the power coupled into the cavity it is necessary to increase the transmission. As a result, there exists an optimum input transmission and an optimum input power, which will provide the maximum EF (see section 3.4 for further discussion). With the use of high quality optical components and optimum input coupling, enhancement factors of 10 or more can be achieved with relative ease, leading to an order of magnitude decrease in pump power requirements.

Whilst the advantage of the pump-enhancement technique in terms of pump threshold reduction is clear, some drawbacks do exist. Firstly, the optical coatings for mirrors and the OPO crystal become significantly more complex. A pump-enhanced SRO will require dual-band coatings at both the pump and signal (or idler) wavelengths. In the case of a DRO, the coatings must be triple-band. To produce such coatings, it is usually necessary to compromise on some of the reflectivity requirements, leading to a lower quality optical cavity.

Initially, it might seem that there is a further issue with keeping the cavity on resonance for both the pump and resonant signal/idler in a PE-SRO. However, it is only necessary to ensure that the pump is on resonance. The signal/idler will then operate on a resonant cavity mode that is closest to the centre of the phasematching bandwidth. The issue of resonating multiple waves is, of course, still a problem in a PE-DRO.

A major drawback lies with the fact that the pump and resonant down-converted wave(s) share the same cavity. It is therefore impossible to use intra-cavity components to modify or control the signal or idler without also disturbing the circulating pump field in a detrimental manner.

With these restrictions in mind, it is now time to introduce a cavity configuration that is regularly used in conjunction with the pump-enhancement technique – the split cavity.

3. Pump-Enhanced OPOs

3.2) *Split Cavity Configuration*

As the name suggest, the split cavity configuration involves the use of two separate optical cavities for each of the resonant waves. A typical split cavity is shown in figure 3.2.

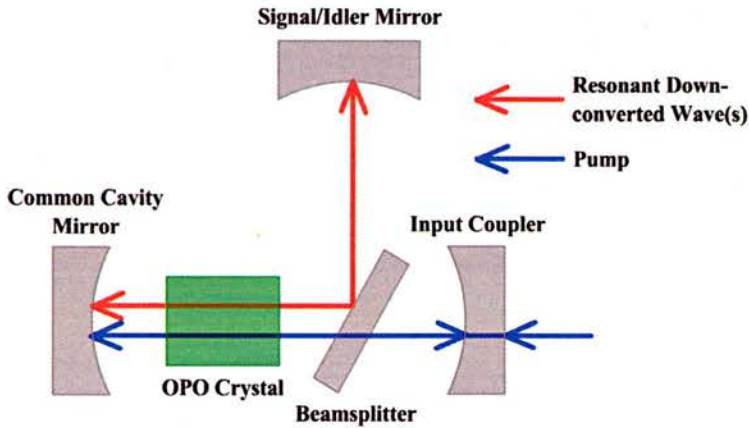


Figure 3.2 – Split Cavity OPO

In the split cavity OPO shown above the pump wave is resonant in one cavity, the *enhancement* cavity, and the down-converted wave(s) are resonant in a different cavity. The key component is the beamsplitter, which is coated to be highly reflecting at the down-converted wavelengths and highly transmitting at the pump wavelength. This separates the resonant waves into their respective cavities. Both cavities have a common section to the left of the beamsplitter, which contains the OPO crystal.

The split cavity configuration is particularly important when applied to a pump-enhanced OPO because it overcomes many of the inherent disadvantages of the pump-enhancement technique. In particular, it allows independent control of each cavity. This has implications for the tuning of the PE-SRO (as described in chapter 1, section 1.6). With a split cavity, any action to keep the pump cavity on resonance will not cause a change to the frequency of the signal or idler, allowing them to be tuned as in a standard SRO. Furthermore, the split cavity allows the utilisation of intra-cavity components in the signal/idler cavity with no adverse affect to the resonant pump. Although the section common to both cavities still requires complex optical coatings, the specifications for critical components such as the input coupler and signal/idler mirror are significantly relaxed.

3. Pump-Enhanced OPOs

The advantage relating to intra-cavity components is particularly important in the context of comb generation, since modulation of the resonant pump is neither required nor desirable. As well as the potential application in frequency comb generation, the split cavity configuration has been utilised in a variety of pump-enhanced OPO applications. It was first employed by Scheidt et al [13] in a signal and pump resonant OPO based on KTP and utilising type II non-critical phasematching. With pump enhancement, the resulting low threshold allowed a single mode laser diode to be used as the pump source. Separation of the resonant cavities was achieved by dispersion, physically realised by two Brewster prisms situated in the OPO resonator. This allowed large signal and idler tuning ranges of 1.1 – 1.6 μm and 2.5 – 3.3 μm respectively. Turnbull et al [14] also utilised the split cavity configuration to demonstrate a broadly tuneable, pump-enhanced OPO. Here, the nonlinear crystal was periodically-poled LiNbO₃ and a dichroic beamsplitter was used to separate the pump and signal cavities. A minimum threshold of 35mW was observed and the idler was coarsely tuned across two ranges: 2.71 – 3.26 μm and 4.07 – 5.26 μm . By placing an etalon into the separate arm of the signal cavity, smooth, mode-hop-free tuning of the idler over a range of 10.8 GHz was achieved. This is ~30 times larger than the tuning range possible in a similar common-cavity device.

Both of the above examples illustrate the advantages of the split cavity configuration with regard to tuning of the downconverted waves. The latter example also shows how separating the resonant cavities gives the additional benefit of allowing intra-cavity elements to be placed in the signal cavity.

3.3) Measuring the Enhancement Factor

As noted in section 3.1, the enhancement factor gives a measure of the quality of the pump-enhancement cavity as well as the reduction in OPO threshold. Therefore, when trying to optimise a pump-enhanced OPO, knowing the value of this factor is very important. A simple method of obtaining the EF involves measuring the pump power leakage through the common cavity mirror (high reflector) and dividing by the transmission of this mirror to obtain the circulating pump power. The EF is then given by the ratio of the circulating pump power to the input pump power. At this point it should be noted that there are two regimes where the EF can be measured – below and

3. Pump-Enhanced OPOs

above threshold. The difference is due to the presence of downconversion in the latter, which adds a further source of loss to the circulating pump field. It is therefore important to distinguish between the two regimes when discussing the EF in an experimental context.

There are many situations where the method mentioned previously is either impractical or impossible. Since the common cavity mirror is usually specified to be as close to 100% reflecting as possible at the pump wavelength, the actual transmission value may not be known. Also, the leakage from this mirror may be used for some other form of analysis, preventing the transmitted power from being measured.

Therefore, an in-situ method of measuring the EF is highly desirable. In the following the pump-enhancement cavity is analysed quantitatively to derive such a method.

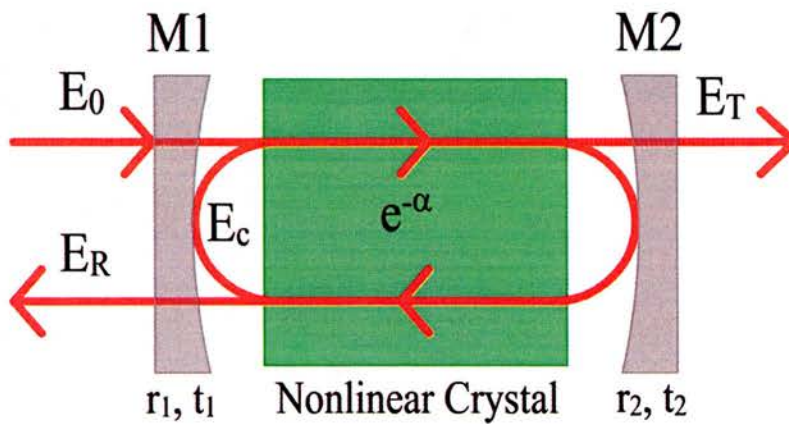


Figure 3.3 – Schematic of Pump-Enhancement Cavity

Figure 3.3 shows a schematic representation of a pump-enhancement cavity, consisting of a nonlinear crystal surrounded by two mirrors, M1 and M2. Mirror M1, which acts as an input coupler, has an amplitude reflectivity and transmission of r_1 and t_1 respectively. For the high reflector, M2, the amplitude reflectivity and transmission are given by r_2 and t_2 (generally unknown). The coefficient, α , represents all parasitic loss in the cavity. This includes absorption in the nonlinear crystal and mirror surfaces and scattering.

There are several amplitudes associated with the above cavity. Firstly, E_0 represents the light incident on M1, a fraction of which is coupled into the cavity. E_c is the large field circulating within the cavity. Light reflected from the cavity, E_R , consists of the

3. Pump-Enhanced OPOs

fraction of E_0 directly reflected by M1 and the fraction of E_C transmitted by M1. Finally, the light transmitted through M2 is given by E_T .

To find E_T it is necessary to sum all the transmissions due to single and multiple passes through the cavity. The table below gives the individual amplitude transmissions for a selection of passes.

No. Of Passes	Individual Amplitude Transmission
1	$E_{T1} = E_0 t_1 e^{-\alpha} e^{i\phi} t_2$
3	$E_{T3} = E_0 t_1 e^{-\alpha} e^{i\phi} \left[r_2 e^{-\alpha} e^{i\phi} r_1 e^{-\alpha} e^{i\phi} t_2 \right]$
5	$E_{T5} = E_0 t_1 e^{-\alpha} e^{i\phi} \left[r_2^2 e^{-2\alpha} e^{2i\phi} r_1^2 e^{-2\alpha} e^{2i\phi} t_2 \right]$

Table 3.1 – Amplitude Transmission for Various Cavity Passes

In all of the above transmissions, ϕ is the single pass phase shift associated with the cavity. The total amplitude transmission is given by

$$\begin{aligned}
 E_T &= E_{T1} + E_{T3} + E_{T5} + \dots \\
 &= E_0 t_1 e^{-\alpha} e^{i\phi} t_2 \left[1 + r_2 e^{-2\alpha} e^{2i\phi} r_1 + r_2^2 e^{-4\alpha} e^{4i\phi} r_1^2 + \dots \right]
 \end{aligned} \tag{3.1}$$

Since the number of possible cavity passes is effectively infinite, the above equation represents an infinite geometric series. It is well known that the sum of such a series is given by $\frac{1}{1-X}$, where X is the factor whose powers make up the series. In this case,

$$X = r_1 r_2 e^{-2\alpha} e^{2i\phi} \text{ and hence,}$$

$$E_T = \frac{E_0 t_1 t_2 e^{-\alpha} e^{i\phi}}{1 - r_1 r_2 e^{-2\alpha} e^{2i\phi}} \tag{3.2}$$

A similar procedure is utilised to obtain E_R . Noting that there is a π phase shift only for the case of direct reflection from M1 (E_{R0}), the individual amplitude reflections are given in table 3.2.

3. Pump-Enhanced OPOs

No. Of Passes	Individual Amplitude Reflection
0	$E_{R0} = -r_1 E_0$
2	$E_{R2} = E_0 t_1 e^{-\alpha} e^{i\phi} r_2 e^{-\alpha} e^{i\phi} t_1$
4	$E_{R4} = E_0 t_1 e^{-\alpha} e^{i\phi} r_2 e^{-\alpha} e^{i\phi} [r_1 e^{-\alpha} e^{i\phi} r_2 e^{-\alpha} e^{i\phi} t_1]$

Table 3.2 – Amplitude Reflection for Various Cavity Passes

The total reflection transmission is

$$\begin{aligned}
 E_R &= E_{R0} + E_{R2} + E_{R4} + \dots \\
 &= -r_1 E_0 + E_0 t_1^2 r_2 e^{-2\alpha} e^{2i\phi} [1 + r_1 r_2 e^{-2\alpha} e^{2i\phi} + \dots]
 \end{aligned} \tag{3.3}$$

As with the amplitude transmission, equation (3.3) is an infinite geometric series whose sum is given by

$$E_R = \frac{-r_1 E_0 + E_0 r_2 e^{-2\alpha} e^{2i\phi} (r_1^2 + t_1^2)}{1 - r_1 r_2 e^{-2\alpha} e^{2i\phi}} \tag{3.4}$$

This can be further simplified if it is assumed that absorption and scattering losses at M1 are negligible and, as a result, $r_1^2 + t_1^2 = 1$. Therefore, the total amplitude reflection becomes

$$E_R = \frac{-r_1 E_0 + E_0 r_2 e^{-2\alpha} e^{2i\phi}}{1 - r_1 r_2 e^{-2\alpha} e^{2i\phi}} \tag{3.5}$$

Since all experimentally measured quantities will be in terms of intensity rather than amplitude, it is necessary to convert equations (3.2) and (3.5) into an intensity transmission and reflection.

$$\frac{I_R}{I_0} = \frac{E_R E_R^*}{E_0 E_0^*} = \frac{(t_1 t_2 e^{-\alpha} e^{i\phi})(t_1 t_2 e^{-\alpha} e^{-i\phi})}{(1 - r_1 r_2 e^{-2\alpha} e^{2i\phi})(1 - r_1 r_2 e^{-2\alpha} e^{-2i\phi})} \tag{3.6}$$

3. Pump-Enhanced OPOs

For mirrors M1 and M2, the associated intensity transmission and reflection can be written respectively as $T_1 = t_1^2$, $T_2 = t_2^2$, $R_1 = r_1^2$, $R_2 = r_2^2$. This gives the total intensity transmission for the cavity as

$$\frac{I_T}{I_0} = \frac{T_1 T_2 e^{-2\alpha}}{1 + R_1 R_2 e^{-4\alpha} - 2\sqrt{R_1} \sqrt{R_2} e^{-2\alpha} \cos 2\phi} \quad (3.7)$$

Similarly, the total intensity reflection is

$$\frac{I_R}{I_0} = \frac{R_1 + R_2 e^{-4\alpha} - 2\sqrt{R_1} \sqrt{R_2} e^{-2\alpha} \cos 2\phi}{1 + R_1 R_2 e^{-4\alpha} - 2\sqrt{R_1} \sqrt{R_2} e^{-2\alpha} \cos 2\phi} \quad (3.8)$$

In the context of measuring the pump-enhancement factor, the key factor is the intensity reflection. However, there is a problem with this quantity in the form expressed by equation (3.8). Both R_2 and α are generally unknown (indeed, this was part of the motivation to derive an in-situ method of measuring the enhancement factor) and a measurement of the reflected intensity from the cavity cannot be used to determine both. Fortunately, it is not necessary to know the values of R_2 and α separately. Instead, a new quantity is defined

$$R_e = R_2 e^{-4\alpha} \quad (3.9)$$

The above equation represents a reflection inside the cavity, which takes into account both the (unknown) reflection from M2 and the double pass through the nonlinear crystal. In effect, R_e can replace the nonlinear crystal and M2 in figure 3.3. Equation (3.8) can now be rewritten as

$$\frac{I_R}{I_0} = \frac{R_1 + R_e - 2\sqrt{R_1} \sqrt{R_e} \cos 2\phi}{1 + R_1 R_e - 2\sqrt{R_1} \sqrt{R_e} \cos 2\phi} \quad (3.10)$$

As the single pass phase shift, ϕ , is varied, the total intensity reflection takes the form shown in figure 3.4 ($R_1 = 0.8$ & $R_e = 0.95$).

3. Pump-Enhanced OPOs

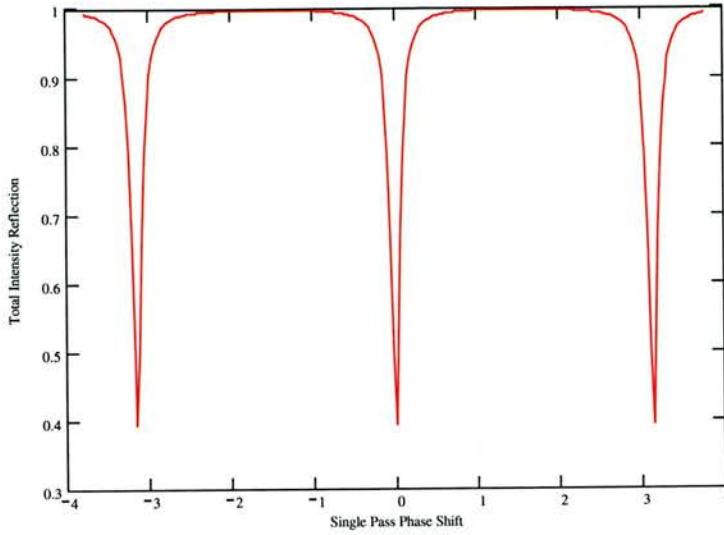


Figure 3.4 – Total Intensity Reflection vs. Single Pass Phase Shift

There are two points of interest in the above plot. Firstly, the peak reflection of close to 1, which means that $I_R \approx I_0$ i.e. the entire power incident on M1 is reflected back. The second point of interest is the minimum, which occurs whenever ϕ is a multiple of π . This is equivalent to a 2π phase shift between each reflected component (E_{R0} , E_{R2} etc) and is the requirement for resonance between M1 and M2. Therefore, each minimum in the total intensity reflection corresponds to the condition of resonance in the cavity. An expression for the minimum reflection can be found by setting $\phi = \pi$ in equation (3.10)

$$\frac{I_R(\text{min})}{I_0} = \frac{R_1 + R_e - 2\sqrt{R_1}\sqrt{R_e}}{1 + R_1R_e - 2\sqrt{R_1}\sqrt{R_e}} \quad (3.11)$$

The above quantity can be easily obtained by scanning the cavity to vary ϕ . A common method of achieving this is to mount M1 on a piezo-electric transducer (PZT), to which a ramp voltage is then applied. If the intensity reflected from M1 is focussed onto a photodetector, $\frac{I_R(\text{min})}{I_0}$ is simply the ratio of minimum and maximum voltages from the photodetector.

A simple rearrangement of equation (3.11) gives a quadratic equation in $\sqrt{R_e}$,

3. Pump-Enhanced OPOs

$$\left[\frac{I_R(\min)}{I_0} R_1 - 1 \right] R_e + \left[2\sqrt{R_1} - 2\frac{I_R(\min)}{I_0} \sqrt{R_1} \right] \sqrt{R_e} + \left[\frac{I_R(\min)}{I_0} - R_1 \right] = 0 \quad (3.12)$$

This can be easily solved using the standard quadratic method to give R_e .

The final step in obtaining the pump-enhancement factor involves deriving an expression for the circulating intensity inside the cavity, I_C . From figure 3.3, it can be seen that the transmitted intensity, I_T , is equal to the intra-cavity intensity after a single pass through the nonlinear crystal and transmission through M2. Therefore,

$$I_C = \frac{I_T}{T_2 e^{-2\alpha}} \quad (3.13)$$

and the pump-enhancement factor is given by the ratio of circulating to input intensity i.e.

$$EF = \frac{I_C}{I_0} = \frac{T_1}{1 + R_1 R_e - 2\sqrt{R_1} \sqrt{R_e} \cos 2\phi} \quad (3.14)$$

As would be expected, equation (3.14) confirms that the maximum enhancement factor occurs on resonance.

This is not quite the end of the story however. When determining R_e from the minimum intensity reflection, the quadratic method will yield two solutions. Physically, these solutions represent two possible situations. The solution with the positive quadratic discriminant will give R_e for the case of under-coupling. Here, $R_l > R_e$ and the losses internal to the cavity are greater than the input coupling. For the solution with the negative discriminant, R_e is obtained for the case of over-coupling. This time, $R_l < R_e$ and the input coupling is greater than the internal losses. For many pump-enhancement cavities, the two values of R_e will be quite different and the correct coupling situation obvious. However, if this is not the case then a method must be found to distinguish between the two values. The key to solving this problem lies with the finesse of the pump-enhancement cavity. The finesse is defined as follows

$$\mathfrak{F} = \frac{\text{Free Spectral Range}}{\text{FWHM}} \quad (3.15)$$

3. Pump-Enhanced OPOs

Here, FWHM refers to the full width at half maximum of the intra-cavity intensity. This is twice the phase shift, $\phi_{1/2}$, at which the circulating intensity has fallen to half its maximum value i.e.

$$\frac{T_1}{1 + R_1 R_e - 2\sqrt{R_1}\sqrt{R_e} \cos 2\phi_{1/2}} = \frac{1}{2} \left[\frac{T_1}{1 + R_1 R_e - 2\sqrt{R_1}\sqrt{R_e}} \right] \quad (3.16)$$

A straightforward rearrangement of the above equation produces an expression for $\phi_{1/2}$,

$$\phi_{1/2} = \cos^{-1} \left(2 - \frac{1 + R_1 R_e}{2\sqrt{R_1}\sqrt{R_e}} \right) \quad (3.17)$$

Remembering that in terms of phase, a FSR is equivalent to 2π , the finesse can now be written as

$$\mathfrak{F} = \frac{\pi}{\phi_{1/2}} \quad (3.18)$$

By using equations (3.17) and (3.18) to calculate the finesse for each value of R_e and then comparing with the finesse measured from the reflected intensity, the correct coupling situation can be determined. Hence, an accurate value can be obtained for the enhancement factor.

This finalises the in-situ method for determining the pump-enhancement factor, which is summarised in the following steps.

- 1) Use the back-reflected intensity from the input mirror (M1) to measure $\frac{I_R(\text{min})}{I_0}$.
- 2) Obtain the values of R_e for both types of coupling from equation (3.12).
- 3) Calculate the corresponding enhancement factors with equation (3.14)
- 4) Calculate the corresponding finesse with equations (3.17) and (3.18)

3. Pump-Enhanced OPOs

- 5) Measure the actual finesse from the back-reflected intensity and compare with the calculated values to determine the correct values of R_e and EF.

It should be noted that this method only requires a few simple measurements of the back-reflection from the input mirror. It is also common to monitor the back-reflection anyway, since it is often utilised to stabilise the pump cavity and keep it on resonance (see section 3.5 for more details). The technique described in this section was used to determine pump enhancement factors during the optimisation experiments, which are described in chapter 4, section 4.6.

3.4) *Optimum Pumping Level*

The in-situ method described in the previous section gives a quick and easy measurement of the pump-enhancement factor. A natural progression is to now look for an optimum pump power that will maximise various parameters of the PE-OPO such as the EF, down-conversion efficiency and output power.

First, consider the pump power incident on the input coupler (M1 in fig. 3.3). It is desirable to couple as much of this power as possible into the enhancement cavity to produce the largest achievable circulating field. In section 3.3 the intensity reflected from the cavity on resonance was given by equation (3.11). Effectively, this represents waste pump power that is rejected by the cavity. By reducing the reflected intensity, the power coupled into the enhancement cavity will be increased. Coupling of all the pump power will occur when the reflected intensity is zero. This situation is known as *impedance matching*. From equation (3.11), the condition for zero reflection with no downconversion present (below threshold) is simply

$$R_1 = R_e \quad (3.19)$$

Therefore, the maximum coupling of pump power into the enhancement cavity can be achieved by making the reflectivity of the input coupler as close as possible to the effective reflectivity of the cavity (which can be determined via the method described in section 3.3). Whilst this initial step does not directly lead to an optimum pumping

3. Pump-Enhanced OPOs

level, it does ensure that the maximum pump-enhancement factor will be obtained for a given pump power.

The next step is to consider the parameters that define the operating point of the PE-OPO, namely the EF, down-converted power and efficiency. Expressions for these quantities are derived by Dunn and Ebrahimzadeh [15] for the singly resonant case. This method employs the crucial assumption that, at all points above threshold, the intra-cavity pump field is clamped to its value at the OPO threshold and therefore remains constant whilst the OPO is operating. The root of this assumption lies with the fact that, above threshold, the saturated parametric gain must equal cavity loss for the resonant signal or idler wave. For a singly resonant oscillator (SRO), the fractional round-trip gain of the resonant down-converted wave is proportional to the pump field in the nonlinear medium. Hence, in this case a constant parametric gain does imply a constant intra-cavity pump field. The question now arises as to whether an approach to derive the operating point of a PE-OPO that relies on the assumption of a constant circulating pump field above threshold can be applied to a doubly resonant oscillator (DRO). This is, of course, directly relevant to the device discussed in this thesis.

To answer this question, it is first necessary to return to the PE-SRO. In the previously mentioned analysis, it is also assumed that the single pass loss due to down-conversion is sufficiently small for the pump field to be effectively constant throughout the nonlinear medium. This is a reasonable assumption because a typical input mirror will usually be around 10% transmitting. Since the input mirror is normally chosen to achieve impedance matching, equation (3.19) shows that the intra-cavity losses must also be around 10% per round trip. It is important to remember that in the situation being considered, the OPO is operating above threshold. Therefore, the effective reflectivity of the pump-enhancement cavity, as defined in the previous section, must now incorporate the loss due to down-conversion in the nonlinear medium. This can be achieved by defining a new effective reflectivity, R_m , which replaces R_e in all the relevant equations,

$$R_m = T_{opo} R_e \quad (3.20)$$

Here, T_{opo} is effective (power) transmission of the nonlinear crystal after down-conversion loss (nonlinear loss). Note that if the OPO is below threshold, $T_{opo} = 1$ and

3. Pump-Enhanced OPOs

R_m is indistinguishable from R_e . Given that the linear intra-cavity loss (T_2 and α) is normally quite small, most of the intra-cavity loss will be due to down-conversion. This means that the circulating pump field does not change by more than 10% for a single transit of the cavity. Such low pump-depletion suggests that the OPO is operating close to threshold. As far as the internal pump field is concerned, this is true and one might expect corresponding low conversion efficiency. However, this is not the case. Since the pump is resonant, it undergoes numerous passes through the nonlinear medium, with significant depletion occurring overall. Indeed, if impedance matching is achieved and no pump light is rejected via back-reflection, then close to 100% down-conversion can be realised.

Bearing this in mind, it is now time to consider the intra-cavity pump field in the case of a PE-DRO. A simplistic argument can be used to show that the pump field is clamped to the threshold value. This utilises the fact that the ratio of signal and idler fields is fixed, since one pump photon is converted into one signal and one idler photon (see Manley-Rowe relations, equation (1.20)). The round-trip gain experienced by the signal field, for example, must be equal to the cavity losses at the signal wavelength, α_s , and is given by

$$\delta E_s \sim j \frac{d_{\text{eff}} \omega_s}{c n_s} E_p E_i^* l = \alpha_s E_s \quad (3.21)$$

Here, l is the length of the nonlinear crystal and κ_s is a constant related to the signal frequency and various crystal parameters (see chapter 1). As a consequence of the Manley-Rowe relations, the ratio $\frac{\alpha_s E_s}{\alpha_i E_i}$ is fixed. Therefore, the gain experienced by

the idler field is directly proportional to the signal field and the complex conjugate of the idler field, E_i^* , can be replaced by the signal field

$$\delta E_s \sim j \frac{d_{\text{eff}} \omega_s}{c n_s} E_p [\text{const.} E_s] l = \alpha_s E_s \quad (3.22)$$

Hence, E_p must be held constant at the threshold value.

3. Pump-Enhanced OPOs

A more comprehensive argument can be employed by considering the relations for pump-depletion and down-conversion efficiency in the case of an SRO and DRO where no pump-enhancement is incorporated. The two relevant equations [15] are given below.

$$I_{DC} = (I_{in} - I_{out}) = 4\sqrt{I_{th}} (\sqrt{I_{in}} - \sqrt{I_{th}}) \quad (DRO) \quad (3.23)$$

$$I_{out} = I_{in} \cos^2 \left\{ \sqrt{\left(\frac{I_{in} - I_{out}}{I_{th}} \right)} \right\} \quad (SRO) \quad (3.24)$$

In both equations, I_{in} and I_{out} represent the input and output pump intensities at the nonlinear crystal respectively, I_{th} represents the pump intensity required to reach threshold and I_{DC} represents the amount of pump intensity that is down-converted. The next step is to find the number of times above threshold that the SRO and DRO must be pumped to achieve down-conversion efficiencies comparable to those obtained in a pump-enhanced OPO (as discussed previously, these efficiencies are of the order of 10%). Writing the number of times above threshold as $f = \frac{I_{in}}{I_{th}}$, the

fraction of the pump that is down-converted $\left(\eta = \frac{I_{DC}}{I_{in}} = \frac{I_{DC}}{f I_{th}} \right)$ is given by

$$\eta = \left(\frac{4}{f} \right) \{ \sqrt{f} - 1 \} \quad (DRO) \quad (3.25)$$

$$\eta = \left\{ 1 - \cos^2 \left(\sqrt{\eta f} \right) \right\} \quad (SRO) \quad (3.26)$$

Note that equation (3.26) can only be solved analytically by calculating f for a given value of η . Table 3.3 below shows the number of times above threshold required to give various values of η for both the SRO and DRO.

3. Pump-Enhanced OPOs

No. of times above threshold (f)	Fractional down-conversion of pump (η)	
	SRO	DRO
1.0033	0.01	0.006
1.017	0.05	0.033
1.033	0.10	0.063
1.054	0.15	0.101
1.075	0.20	0.137
1.097	0.25	0.17
1.12	0.30	0.21

Table 3.3 – Fractional down-conversion of pump for SRO & DRO

From table 3.3 it is apparent that the fractional down-conversion of the pump increases rapidly whilst the OPO is close to threshold and, perhaps surprisingly, this increase is faster for the SRO. It can be seen that for the DRO to achieve a down-conversion efficiency of around 10% (comparable to pump-enhanced OPO), the input pump intensity must be 5% above the threshold intensity.

Whilst this suggests that the intra-cavity pump field is very close to the threshold value for the typical operating level of a PE-DRO, it does not provide a definitive conclusion on the issue of a clamped pump field. However, such a conclusion can be gained by considering I_{out} and hence the average pump field in the nonlinear crystal. By rearranging the initial definition of η , the following expression for I_{out} can be obtained

$$I_{out} = I_{in}(1-\eta) \quad (3.27)$$

For an input pump level of $1.05I_{th}$ and 10% down-conversion, equation (3.27) gives an output pump level of $0.95I_{th}$. It is straightforward to show that the pump changes linearly with position through the nonlinear crystal [15] and on the basis of the previous values for I_{in} and I_{out} , this leads to the following diagram.

3. Pump-Enhanced OPOs

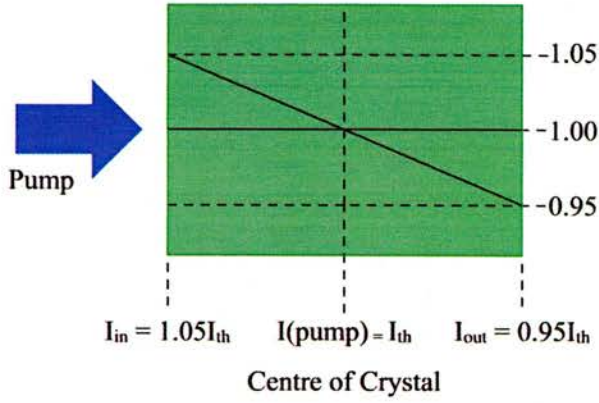


Figure 3.5 – Pump depletion in nonlinear crystal

As shown by figure 3.5, at the centre of the nonlinear crystal the intra-cavity pump intensity is equal to the value at threshold. To show that this is also the case at other down-conversion efficiencies in a DRO, table 3.4 gives the input and output pump intensities for a range of values of η .

Fractional down-conversion of pump in DRO (η)	Input pump intensity to nonlinear crystal (I_{in})	Output pump intensity from nonlinear crystal (I_{out})	Average pump intensity across crystal
0.033	$1.017I_{th}$	$0.983I_{th}$	I_{th}
0.063	$1.033I_{th}$	$0.968I_{th}$	I_{th}
0.101	$1.054I_{th}$	$0.947I_{th}$	I_{th}
0.137	$1.075I_{th}$	$0.927I_{th}$	$1.001I_{th}$
0.17	$1.097I_{th}$	$0.911I_{th}$	$1.004I_{th}$
0.21	$1.12I_{th}$	$0.88I_{th}$	I_{th}

Table 3.4 – Input & output pump intensities

Ignoring slight discrepancies due to rounding errors, table 3.4 shows that the average pump intensity in the nonlinear crystal is equal to the threshold value for each down-conversion efficiency. Therefore, the assumption of an intra-cavity pump field clamped to its value at threshold seems to hold for a PE-DRO.

As a result of the previous analysis, the optimisation equations derived for a PE-SRO can now be applied to a PE-DRO as well. A comprehensive study of these equations

3. Pump-Enhanced OPOs

can be found in *Handbook Of Optics IV* [15] and their derivation is given in appendix II. The following text summarises the essential points.

- (i) The pump field circulating in the cavity is given by

$$P_C = \frac{T_1 P_0}{\left[1 - \sqrt{(R_1 R_m)}\right]^2} \quad (3.28)$$

Here, P_0 is the pump power incident on the input mirror and the other quantities are as previously defined. In equation (3.28) the pump cavity is assumed to be on resonance (note the similarity to equation (3.14)). Also, from equation (3.20) it is worth remembering that R_m includes T_{opo} , the pump transmission through the OPO crystal after nonlinear loss. This allows the down-converted power to be written as

$$P_{DC} = (1 - T_{opo}) P_C \quad (3.29)$$

- (ii) The intra-cavity pump field is clamped at the threshold value, i.e. $P_C = P_{th}$
- (iii) Hence, P_{th} can be substituted for P_C . Combining this with equations (3.20), (3.28) and (3.29) allows the following equation for down-converted power to be derived

$$\frac{P_{DC}}{P_{th}} = 1 - \frac{1}{R_1 R_e} \left[1 - \sqrt{\frac{T_1 P_0}{P_{th}}}\right]^2 \quad (3.30)$$

An examination of equation (3.9) shows that if the reflectivity of the second mirror in the pump enhancement cavity is close to 100% and linear (parasitic) losses within the cavity are negligible then $R_e \sim 1$. This suggests that 100% down-conversion efficiency (i.e. $P_{DC} = P_o$) might be attainable in such a situation (see appendix II). However, the pump enhancement cavity must also be taken into account. To obtain 100% efficiency, no pump light must be wasted. Hence, there can be no back-reflection and the pump cavity must be

3. Pump-Enhanced OPOs

impedance matched. In practice it is usually impossible to achieve exact impedance matching and therefore 100% down-conversion efficiency cannot be reached. However, the preceding discussion does suggest that to obtain optimum efficiency, the pump cavity must be as close to impedance matched as possible.

- (iv) The pump power reflected back from the OPO is given by a modified version of equation (3.11), which includes T_{opo}

$$\mathfrak{R} = \frac{P_R}{P_0} = \left[\frac{\sqrt{R_l} - \sqrt{R_e T_{opo}}}{1 - \sqrt{R_l R_e T_{opo}}} \right]^2 \quad (3.31)$$

In the above equation, impedance matching occurs when $\mathfrak{R} = 0$, which implies that $R_l = R_e T_{opo}$. Of course, this is the same conclusion as is reached with equations (3.19) and (3.20).

It should be noted that in the four points stated above and all the previous analysis, P_{th} is the intra-cavity circulating pump power required to bring the OPO to threshold i.e. the threshold power in the absence of any pump enhancement. The value of P_{th} will depend on the various parameters of the OPO and whether it is singly or doubly resonant.

To find the optimum operating point for an OPO with specific values for R_l and R_e , equations (3.29), (3.30) and (3.31) can be evaluated as a function of input power (or number of times above threshold). If the OPO is output-coupled, then a knowledge of P_{DC} will give the output power and hence the overall efficiency of the device.

The four equations given above, having been shown to apply to a PE-DRO, are utilised in chapter 4, section 4.6 to provide a theoretical comparison to the results described therein.

3. Pump-Enhanced OPOs

3.5) *Stabilisation of Pump Cavity*

When modelling the operation of a pump-enhanced OPO, as detailed in the previous section, it is generally assumed that the pump cavity is on resonance, thereby ensuring that the intra-cavity pump field is at a maximum. Unfortunately, the pump cavity will not remain on resonance passively. Thermal fluctuations, air currents and vibrations can all contribute to moving either mirror by the few tens of nanometres required to drift off resonance. Hence, some form of active stabilisation must be incorporated into the pump cavity to ‘lock’ it on resonance. This final section to the pump enhancement chapter will give a brief overview of two of the most common stabilisation schemes, side-of-fringe locking and Pound-Drever-Hall locking.

The side-of-fringe technique is commonly used to stabilise an external cavity diode laser to an absorption feature in an atomic vapour [16, 17]. Recent improvements to this method have utilised Zeeman splitting and the hyperfine transition in Cs and Rb [18, 19]. By its very nature, the application of side-of-fringe locking to pump-enhancement means that the pump laser is ‘slaved’ to the optical cavity. In other words, the laser frequency is adjusted in response to changes to the cavity such that the resonance condition remains. As the name suggests, a key component is the cavity transmission fringe, an example of which is shown in figure 3.6 below.

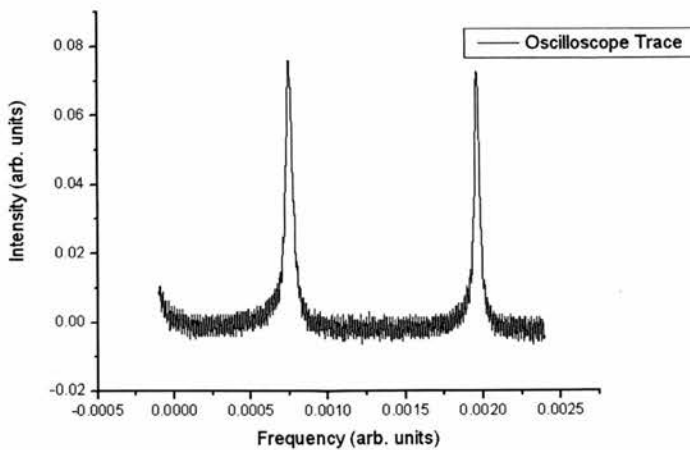


Figure 3.6 – Optical cavity transmission fringe

By focussing the transmitted laser light onto a photodetector and the use of appropriate biasing, a point on one side of the fringe, just off-resonance, can be

3. Pump-Enhanced OPOs

monitored. From figure 3.6, it can be seen that at this side point a change in laser frequency will cause a change in the transmitted intensity. Depending on the side used, the change in intensity will either be in phase or anti-phase with the change in frequency. To generate an error signal, the signal from the photodetector is processed via P.I.D feedback electronics. The error signal is then used to control the pump laser frequency.

Whilst the side-of-fringe technique is fairly easy to implement, it does suffer from several drawbacks. Firstly, it cannot distinguish between frequency and intensity variations of the pump laser. This can be overcome by using a second photodetector to monitor some fraction of the laser beam before it enters the optical cavity. Any intensity variations will then appear on both detectors and can be eliminated. However, this in itself leads to the difficulty of ensuring that both photodetectors are exactly matched and, as a result, limits the long-term stability of the system.

A second drawback of the side-of-fringe technique, particularly relevant to the pump enhancement case, is the fact that the pump laser cannot be locked to the peak of the cavity transmission, where intra-cavity power is at a maximum. This is because all frequency variations will cause a decrease in intensity at the peak and hence there is no way of knowing in which direction the frequency has shifted.

Although more complex, the Pound-Drever-Hall technique [20, 21] has none of the flaws associated with side-of-fringe locking. With Pound-Drever-Hall locking, the length of the optical cavity is adjusted to ensure resonance rather than the pump laser. This means that it can be used with a wide variety of laser systems.

The implementation of Pound-Drever-Hall locking begins with frequency or phase modulation of the pump laser beam. As already discussed in chapter 2, this generates sidebands on either side of the carrier (laser) frequency at a distance equal to the modulation frequency. In this case, the modulation frequency is specifically chosen so that the sidebands are out-with the passband of the cavity. In a further difference to the side-of-fringe technique, Pound-Drever-Hall locking utilises the laser light reflected from the optical cavity. This reflection consists of light directly reflected from the input mirror of the cavity, which includes the rejected sidebands, and light leaking through the input mirror from the intra-cavity field. By observing the reflected laser light with a fast photodiode, the beat signal between the sidebands and carrier frequency can be detected. This beat signal is the key to generating an error signal. There exists a well-defined phase relationship between the sidebands and the carrier

3. Pump-Enhanced OPOs

frequency. However, the phase of the carrier frequency is determined by the interference between the directly reflected component and the intra-cavity leakage. Therefore, the phases of the carrier frequency and the beat frequency depend on the frequency of the laser beam relative to the cavity resonance peak. Since the beat frequency is an RF signal, its phase can be measured and used to generate the error signal. This usually occurs via demodulation with the original modulation frequency before the signal is passed to P.I.D feedback electronics.

As well as allowing the laser frequency to be locked to the peak of the cavity resonance and being immune to intensity fluctuations in the laser beam, the Pound-Drever-Hall technique has the added advantage that it can correct for very fast frequency fluctuations. Typically, such fluctuations will occur on timescales much shorter than the cavity decay time. Hence, the intra-cavity field will not be able to follow the fluctuations. This means that the leakage beam will instead consist of an 'average' of the phase and frequency of the pump laser over the cavity decay time. On the other hand, the directly reflected beam will provide an instantaneous measure of the pump laser, including any fluctuations. Since a sudden fluctuation will cause a frequency/phase difference between the averaged leakage beam and the instantaneous direct reflection, an error signal will be generated by the feedback electronics and the cavity length adjusted accordingly. The side-of-fringe technique, working with the cavity transmission, cannot compensate for such fluctuations.

From the above discussion, the Pound-Drever-Hall technique is the obvious choice for locking a pump-enhancement cavity on resonance. Difficulties may arise due to the greater complexity of the required electronics and the need to include frequency/phase modulation. However, these can usually be overcome with the right expertise and as such, are not fundamental problems.

3.6) Chapter Summary

This chapter has introduced the concept of a pump-enhanced OPO. In such an OPO, the pump light is resonated, along with one or both of the down-converted waves. This allows a high pump field to build up around the nonlinear crystal, which is typically 10 – 20 times greater than the field produced by the pump source. Hence, the input pump power required for the OPO to reach threshold is significantly

3. Pump-Enhanced OPOs

reduced. The enhancement cavity itself is normally given a figure of merit, known as the enhancement factor. The EF is the ratio of the circulating pump field to the pump field coupled into the enhancement cavity and also gives the reduction in threshold when compared to a similar OPO without pump enhancement.

Whilst offering the advantage of an order-of-magnitude threshold reduction, pump-enhancement does suffer from drawbacks due to the increased complexity of mirror coatings and cavity length control. However, these drawbacks can be largely overcome by implementing a split cavity configuration. Here, a beamsplitter is used to create separate optical cavities for the pump and down-converted waves. Both cavities have a common section, in which the nonlinear crystal is situated. The rest is divided, allowing the cavity length for each resonant wave to be controlled independently. Also, intra-cavity components for the down-converted waves can be inserted without affecting the resonant pump.

In the next section of this chapter, a method for the in-situ measurement of the EF was described. This involves measuring the pump power reflected from the input mirror of the enhancement cavity and performing a few simple calculations. Crucially, the reflectivity of the common cavity mirror is not required and also, the leakage through this mirror is freed up for use by other analytical equipment.

With a method to measure the EF, the next step was to look at the optimisation of it and other important quantities such as the down-converted power and efficiency. Firstly, it was found that the pump power coupled into the enhancement cavity can be maximised by setting the input mirror transmission equal to the internal parasitic losses. This is known as impedance matching. Expressions for the EF, down-converted power and efficiency have been previously derived for the case of a pump-enhanced singly resonant oscillator. In these derivations, it was assumed that pump field throughout the nonlinear crystal is clamped at its threshold value. Since the resulting expressions would be employed for a doubly resonant oscillator in the case described by this thesis, it was necessary to show that the assumption of a clamped pump field still holds for a pump-enhanced DRO. This can be done in a simplistic way by invoking the Manley-Rowe relations. For a more compelling argument, the equations for pump-depletion and down-conversion efficiency in an SRO and DRO with no pump-enhancement are utilised. By considering the fractional down-conversion of the pump for various points above threshold, it can be shown that the average pump power across the nonlinear crystal is indeed equal to the threshold

3. Pump-Enhanced OPOs

value. Hence the initial assumption holds and the equations for a pump-enhanced SRO also apply to a pump-enhanced DRO. These expressions can be modelled as a function of pump power or number of times above threshold, to find the point at which down-converted power and efficiency are maximised.

The final section of this chapter compared two techniques for holding the pump cavity on resonance. In side-of-fringe locking, the transmitted power from the pump cavity is monitored at a point on the side of the transmission fringe. A change of frequency will correspond to a change in transmitted intensity, which generates an error signal. The error signal is then used to control the frequency of the pump laser. The main problem with the side-of-fringe method in the context of pump-enhancement is that it cannot lock to the peak of a transmission fringe, where the EF is maximised.

The other technique, Pound-Drever-Hall locking, does not suffer from this problem. In this case, the pump beam is frequency or phase modulated to generate sidebands on either side of the main centre frequency. The power reflected from the pump cavity is monitored and the phase of the beat signal between centre frequency and sidebands is used to generate an error signal. Here, the error signal controls the length of the pump cavity rather than the pump laser. As well as locking to the peak of reflection/transmission, the Pound-Drever-Hall technique can also compensate for very fast frequency fluctuations. Therefore, it is the method of choice for stabilisation of the pump cavity in a pump-enhanced OPO.

References

1. Slyusarev, S., et al., *Continuous-wave RbTiOAsO₄ optical parametric oscillator in optical frequency interval divider scheme*. Japanese Journal of Applied Physics Part 1-Regular Papers Short Notes & Review Papers, 2001. **40**(1): p. 134-136.
2. Yang, S.T., et al., *Continuous-Wave Singly Resonant Optical Parametric Oscillator Pumped by a Single-Frequency Resonantly Doubled Nd-Yag Laser*. Optics Letters, 1993. **18**(12): p. 971-973.
3. Robertson, G., et al., *Continuous-Wave Singly Resonant Pump-Enhanced Type-II LiNbO₃ Optical Parametric Oscillator*. Optics Letters, 1994. **19**(21): p. 1735-1737.

3. Pump-Enhanced OPOs

4. Schneider, K., et al., *Toward an optical synthesizer: a single-frequency parametric oscillator using periodically-poled LiNbO₃*. Opt. Lett., 1997. **22**: p. 1293.
5. Lindsay, I.D., et al., *Continuous-wave, pump-enhanced optical parametric oscillator based on periodically-poled RbTiOAsO₄*. Optics Express, 2003. **11**(2): p. 134-140.
6. Schiller, S., et al., *Theory of an optical parametric oscillator with resonant pump and signal*. Journal of the Optical Society of America B-Optical Physics, 1999. **16**(9): p. 1512-1524.
7. Stothard, D.J.M., et al., *Hyperspectral imaging of gases with a continuous-wave pump-enhanced optical parametric oscillator*. Optics Express, 2004. **12**(5): p. 947-955.
8. Stothard, D.J.M., et al., *Continuous-wave pump-enhanced optical parametric oscillator with ring resonator for wide and continuous tuning of single-frequency radiation*. Optics Express, 2004. **12**(3): p. 502-511.
9. Carleton, A., et al., *Compact, Continuous-Wave, Singly Resonant Optical Parametric Oscillator based on Periodically Poled RbTiOAsO₄ in a Nd : YVO₄ Laser*. Optics Letters, 2003. **28**(7): p. 555-557.
10. Colville, F.G., et al., *Continuous-Wave, Singly Resonant, Intracavity Parametric Oscillator*. Optics Letters, 1997. **22**(2): p. 75-77.
11. Turnbull, G.A., et al., *Continuous-wave singly-resonant intracavity optical parametric oscillator based on periodically-poled LiNbO₃*. Electronics Letters, 1997. **33**(21): p. 1817-1818.
12. Dabu, R., et al., *Eye-Safe Singly Resonant KTP Parametric Oscillator Pumped inside a Nd : YAG Laser Cavity*. Optical Engineering, 2001. **40**(3): p. 455-459.
13. Scheidt, M., et al., *Diode-Laser-Pumped Continuous-Wave KTP Optical Parametric Oscillator*. Journal of the Optical Society of America B-Optical Physics, 1995. **12**(11): p. 2087-2094.
14. Turnbull, G.A., et al., *Extended Mode-Hop-Free Tuning by use of a Dual-Cavity, Pump-Enhanced Optical Parametric Oscillator*. Optics Letters, 2000. **25**(5): p. 341-343.
15. Ebrahimzadeh, M. and Dunn, M.H., 22. *Optical Parametric Oscillators*, in *Handbook of Optics Vol. IV*, M. Bass, Editor. 2001, McGraw-Hill.

3. Pump-Enhanced OPOs

16. Wieman, C.E. and Hollberg, L., *Using Diode-Lasers for Atomic Physics*. Review of Scientific Instruments, 1991. **62**(1): p. 1-20.
17. Macadam, K.B., et al., *A Narrow-Band Tunable Diode-Laser System with Grating Feedback, and a Saturated Absorption Spectrometer for Cs and Rb*. American Journal of Physics, 1992. **60**(12): p. 1098-1111.
18. Clifford, M.A., et al., *Stabilization of an 852 nm extended cavity diode laser using the Zeeman effect*. Journal of Modern Optics, 2000. **47**(11): p. 1933-1940.
19. Corwin, K.L., et al., *Frequency-stabilized diode laser with the Zeeman shift in an atomic vapour*. Applied Optics, 1998. **37**(15): p. 3295-3298.
20. Drever, R.W.P., et al., *Laser Phase and Frequency Stabilisation Using an Optical Resonator*. Applied Physics B-Lasers and Optics, 1983. **31**: p. 97-105.
21. Black, E.D., *An Introduction to Pound-Drever-Hall Laser Frequency Stabilisation*. Am. J. Phys., 2000. **69**(1): p. 79.

Chapter 4

System Design & Optimisation

The first and perhaps most crucial task within the comb generation project was to design and model a suitable optical resonator. Given the potential telecommunication applications, the system had to be compact but with the flexibility to incorporate any additional components over the course of the project. Additionally, the necessity of a low pump threshold and operating point placed stringent requirements on the various cavity parameters.

Since the OPO was to be pump-enhanced, the split-cavity configuration described in chapter 3 was the obvious choice for the overall design of the comb generator. As well as the advantages offered with tuning and stabilisation of the OPO, a split-cavity would allow the EOM to be completely separated from the pump cavity. Consequently, the EOM could be operated with no adverse effect on the pump enhancement.

In the chapter that follows, the various stages of the design, construction and optimisation of the comb generator are described in chronological order.

4.1) Nonlinear Crystal

Before any cavity design could begin, it was first necessary to choose a nonlinear crystal to provide parametric generation. Emerging crystals based on phosphate and arsenate compounds (e.g. KTP, RTA) were immediately ruled out. Even with pump-enhancement or in the intra-cavity configuration, OPOs based on such crystals have shown thresholds of several hundred mW [1-4], well above the limits placed on threshold for this project. This left two candidates for the nonlinear crystal, lithium niobate (LiNbO_3) and the same compound doped with magnesium oxide ($\text{MgO}:\text{LiNbO}_3$).

LiNbO_3 is a well-known crystal that has been utilised in a variety of nonlinear optical applications. It can be poled for quasi-phasematching, although this is limited to crystals of 0.5mm thickness. This allows propagation along the crystal axis with the

4. System Design & Optimisation

largest nonlinear coefficient (approximately 18 pm/V with QPM). Hence, OPOs based on LiNbO₃ are usually characterised by very low pump thresholds. LiNbO₃ can also be acquired in a variety of lengths and with a variety of poling periods, without being prohibitively expensive. Whilst offering many significant advantages, LiNbO₃ does suffer from one main drawback. To prevent photo-refractive damage (the excitation of electrons to meta-stable states by visible and near-IR wavelengths, creating localised areas of refractive index change), the crystal must be kept at an elevated temperature of at least 150°C. This necessitates an oven to contain the crystal and some form of temperature control.

MgO:LiNbO₃ is commonly used in electro-optic applications, but is less well known as an OPO crystal. It does not suffer from photo-refractive damage and hence can be used at room temperature. Until recently, OPO systems based on MgO:LiNbO₃ were phasematched through birefringence and hence experienced a much lower nonlinear coefficient than standard LiNbO₃ [5-7]. However, in the past few years there have been several successful attempts at poling MgO:LiNbO₃ and using it in quasi-phasematched OPOs [8, 9]. This has allowed nonlinear coefficients similar to those in periodically-poled LiNbO₃ to be accessed. The main reason for considering MgO:LiNbO₃ was the fact that it was used as the nonlinear crystal in the previous OPO-FCG system developed by Diddams [10]. In this case, a 7.5mm long piece of MgO:LiNbO₃ with type I birefringent phasematching gave a threshold of around 200mW.

One of the aims of this project was to generate as wide a frequency comb as possible. The ultimate limiting factor for the comb width is the frequency range over which the OPO can provide gain. Outside this range, modes in the comb will rapidly diminish due to losses in the cavity. This range of gain is determined by the phasematching properties of the OPO. For a nonlinear crystal of length L and with poling period Λ , the equation for perfect phasematching is

$$\Delta k = 2\pi \left[\frac{n_p}{\lambda_p} - \frac{n_s}{\lambda_s} - \frac{n_i}{\lambda_i} - \frac{1}{\Lambda} \right] = 0 \quad (4.1)$$

Here, the subscripts p, s and i denote parameters for the pump, signal and idler waves respectively. If the centre wavelength is set as the signal (or idler) wavelength that

4. System Design & Optimisation

gives perfect phasematching then moving away from the centre wavelength will cause Δk to become non-zero and increase. As shown in chapter 1, the parametric gain is proportional to $\text{sinc}^2\left(\frac{\Delta k L}{2}\right)$, which is a maximum when $\Delta k = 0$ and decreases as Δk increases. By convention, the phasematch bandwidth is defined as the wavelength (or frequency) range over which $\Delta k \leq \frac{\pi}{L}$ i.e. the gain is reduced to around half its peak value.

Given the desire for a wide comb of frequencies, the phasematch bandwidth for each crystal was modelled for a range of signal wavelengths to see which would give the largest bandwidth at the operating wavelength of 1600nm. A common method for calculating the phasematch bandwidth is to expand the wavevector mismatch, Δk , as a Taylor series in terms of $\Delta\lambda$, the half-width of the phasematching curve [11]. However, this cannot give an exact analytical expression because the Taylor expansion is an infinite series. Therefore, a numerical approach was taken instead. Using MathCAD, an iterative program was developed that could calculate the phasematch bandwidth to a specified accuracy (see appendix III). Modelling was undertaken for 20mm long crystals of LiNbO_3 and $\text{MgO}:\text{LiNbO}_3$. A quasi-phasematched scheme was assumed, with all three waves propagating along the x-axis of the crystal and polarised parallel to the z-axis. For a fixed pump wavelength of 800nm and a crystal temperature of 190°C, the program first calculated the grating period required for perfect phasematching at the chosen signal wavelength. The signal wavelength was then varied from this central value and the wavevector mismatch calculated. Once the mismatch was within a specified tolerance of π/L , the phasematch bandwidth was obtained from the range over which the signal wavelength had been varied. The program then moved on to the next signal wavelength. Published Sellmeier data [12, 13] was used to obtain the refractive indices at each wavelength. Figures 4.1 and 4.2 show the results of this modelling – the variation of the phasematch bandwidth with signal wavelength for each crystal.

4. System Design & Optimisation

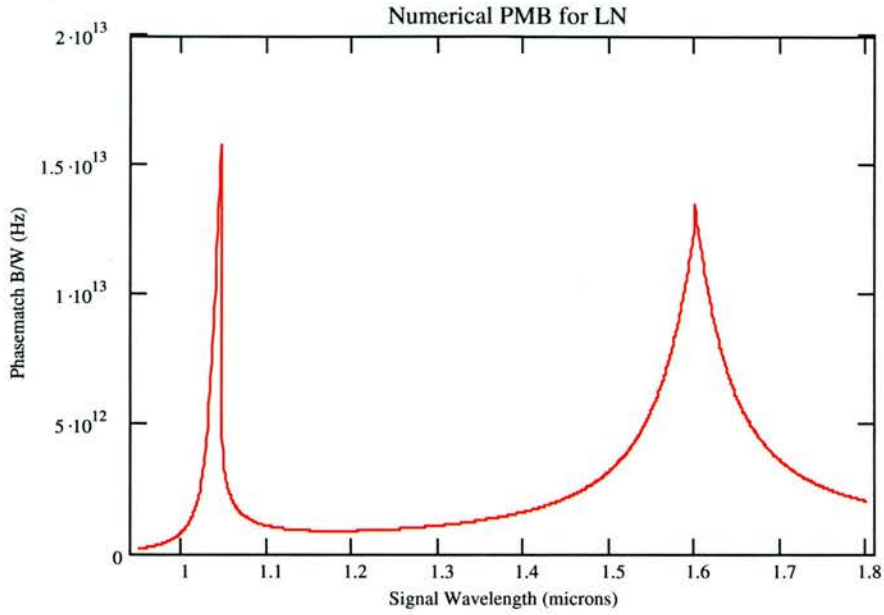


Figure 4.1 – Phasematch bandwidth for LiNbO_3

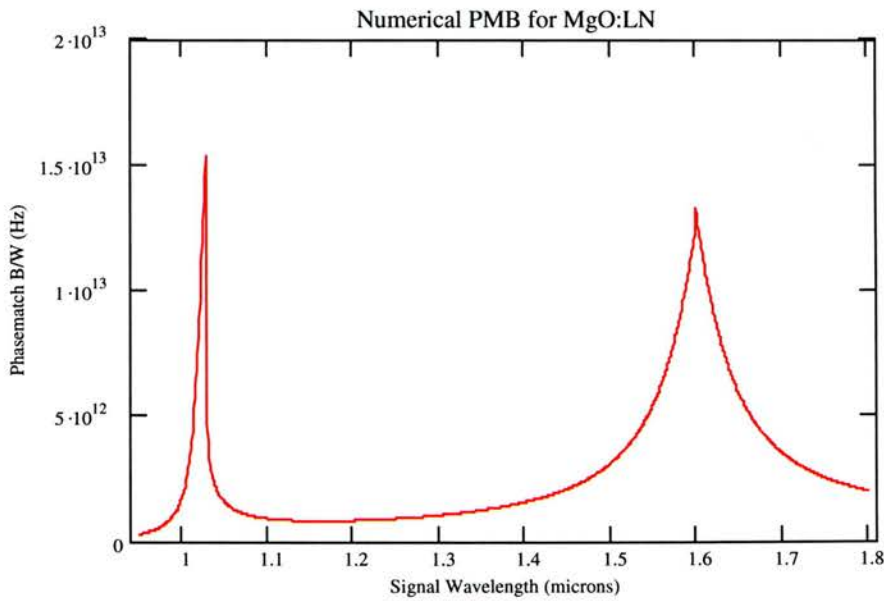


Figure 4.2 – Phasematch bandwidth for MgO:LiNbO_3

As might be expected from the similarity in chemical composition, both crystals show a variation in phasematch bandwidth that is almost identical with peaks of roughly the same height and position. The origin of these peaks can be found by looking at how the poling period required for perfect phasematching varies with signal/idler wavelength (figures 4.3 and 4.4).

4. System Design & Optimisation

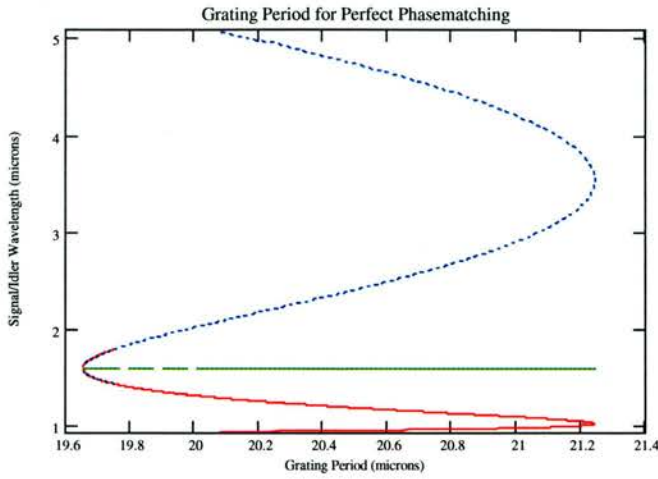


Figure 4.3 – Poling period for perfect phasematching in LiNbO_3

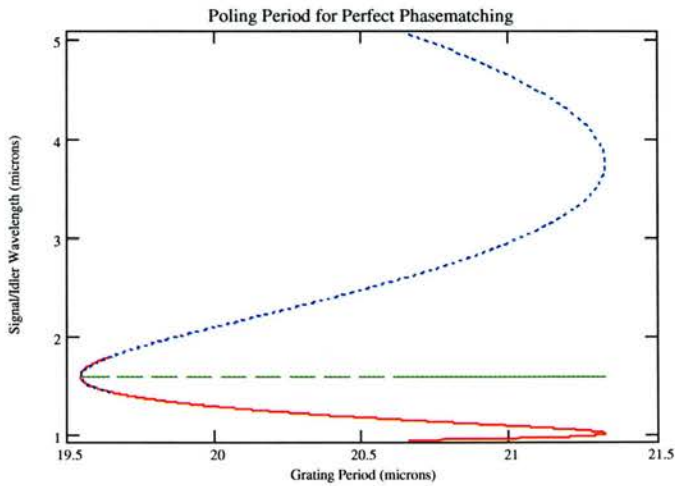


Figure 4.4 – Poling period for perfect phasematching in $\text{MgO}:\text{LiNbO}_3$

Each of the above curves has two particular grating periods at which there is a turning point, which correspond to the peaks in the phasematching bandwidths. Since the curve is effectively vertical at these turning points, a single grating period will provide phasematching for a much wider range of wavelengths. Hence, the phasematch bandwidth will significantly increase.

From figures 4.1 and 4.2 the phasematch bandwidth was found to be 13.5 THz and 13.3 THz at 1600nm for LiNbO_3 and $\text{MgO}:\text{LiNbO}_3$ respectively. Given that this difference is fairly insignificant and that the nonlinear coefficients for both crystals are approximately the same, there was little to choose between them. In the end,

4. System Design & Optimisation

LiNbO_3 was chosen as the nonlinear crystal for this project because it could be acquired quickly and cheaply.

The final step in obtaining the nonlinear crystal was to identify the poling period(s) required to give phasematching for a pump wavelength of 800nm and degenerate signal/idler wavelengths of 1600nm. Again, equation (4.1) was employed in MathCAD and a range of different crystal temperatures was also used. Since the crystal was to be kept at an elevated temperature, it was necessary to take into account the thermal expansion of the crystal and subsequent change in the poling period. Thermo-optic changes in LiNbO_3 (i.e. $n(T)$) were incorporated via the Sellmeier relation [12]. Figure 4.5 shows the poling periods at *room temperature*, which expand to phasematch the given signal/idler wavelengths at each specified crystal temperature.

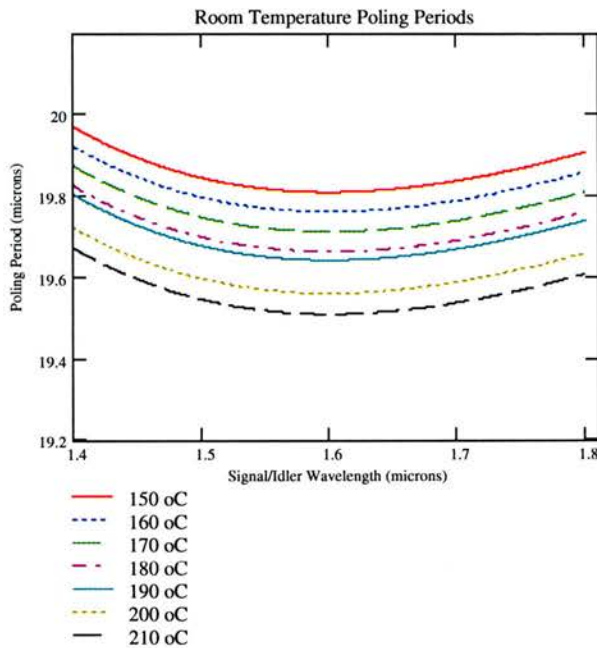


Figure 4.5 – Room temperature poling periods

Generally, it is only possible to obtain poling periods in steps of $0.2\mu\text{m}$. So, in the plot above only curves that are close to 19.6, 19.8 etc. at 1600nm provide a realistic choice. Given this restriction, there were two possibilities for the poling period: $19.8\mu\text{m}$ at 150°C and $19.6\mu\text{m}$ at 190°C . Since the temperature of the former is close to the limit for preventing photorefractive damage, the latter was the preferred choice. As it turned out, a LiNbO_3 crystal with 10 separate poling periods ranging from

4. System Design & Optimisation

18.6 μm to 20.4 μm became available, allowing either of the possible gratings to be used. The dimensions of the crystal were 20mm by 11mm by 0.5mm; a standard set compatible with readily available ovens and temperature controllers.

4.2) Requirements for Optical Resonator

With a suitable nonlinear crystal acquired, the design and modelling of an optical resonator for the frequency comb generator could begin. This task was complicated by the inclusion of the intra-cavity EOM and the need to match its modulation frequency to the cavity FSR, which placed a number of extra constraints on the physical parameters of the system.

The requirements of the comb generator cavity, in terms of the resulting spatial and temporal profiles of the resonated waves, can be split into two types. Those of the first type are general requirements, which can be applied to any OPO. The second type consists of the extra conditions that are necessary for the successful generation of a frequency comb.

The first set of requirements deal with the physical size and shape of the beam within the cavity. Firstly and most importantly the resonator must be stable, such that the intra-cavity field has a self-replicating Gaussian intensity distribution. As a result, the field at any point within the cavity can be described by two parameters [14, 15]: the radius of curvature of the wavefront (R) and the beam radius perpendicular to the resonator axis (w). The minimum radius is known as the beam waist (w_0) and at this point, R is infinite (plane wavefront) and the beam is collimated. The beam waist is important because it is the point where the beam irradiance (power per unit area) is highest and, due to the collimation, does not change significantly over a considerable distance. Consequently, to obtain a sufficiently low threshold it is a general requirement of all continuous-wave OPOs that the beam waists of all resonant waves be situated at the centre of the nonlinear crystal.

With the optimum position of the beam waist known, the same was also necessary of the size of the beam waist to ensure that the cavity would give as low a threshold as possible. In chapter 1, it was stated that the minimum OPO threshold occurs for confocal focussing of the pump beam. This is illustrated in figure 4.6 below.

4. System Design & Optimisation

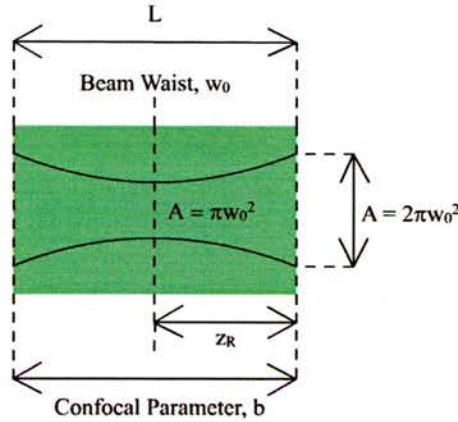


Figure 4.6 – Confocal focussing

At the waist, the beam cross-sectional area (A) is πw_0^2 . After a certain distance from the waist, known as the Rayleigh range (z_R), this area will have doubled to $2\pi w_0^2$. The confocal parameter (b) is defined as twice the Rayleigh range and is given by the following equation:

$$b = \frac{2\pi n w_0^2}{\lambda} \quad (4.2)$$

Here, λ is the wavelength of the beam and n is the refractive index of the medium through which the beam propagates. The confocal parameter can be thought of as the distance over which the size of the beam remains roughly constant. With confocal focussing (also known as the near field approximation), the confocal parameter is set equal to the length of the nonlinear crystal. If the waist is situated at the centre of the crystal, then this ensures the minimum pump volume throughout the nonlinear interaction. To calculate the beam waist in this case, equation (4.2) is rearranged and b set equal to L , giving

$$w_{0,\min}(\text{conf.}) = \sqrt{\frac{\lambda L}{2\pi n}} \quad (4.3)$$

Equation (4.3) gives the beam waist that will result in confocal focussing and is a useful estimate of the conditions required for a minimum pump threshold.

In the previous analysis, the assumption that the beam dimensions remain constant over the length of the nonlinear crystal is a rule-of-thumb approximation that leads to a general optimisation condition. A more detailed treatment on the minimisation of

4. System Design & Optimisation

the pump threshold when dealing with focussed Gaussian beams was published in a classic paper by Boyd and Kleinman [16]. This dealt with the DRO and assumed that the confocal parameters of the pump, signal and idler were all equal. Subsequently, Guha et al [17, 18] expanded the analysis of Boyd and Kleinmann to include the SRO and made no a priori assumptions regarding beam size. Given the resonant nature of all three waves in the OPO required for this project, Gaussian beams and similar confocal parameters are expected. Therefore, the Boyd and Kleinmann analysis is adequate for the purposes of this thesis. The result is a modification to the expression for minimum pump threshold by the addition of an extra multiplying factor, $h_m(B, \xi)^{-1}$. The function $h_m(B, \xi)$ is defined by two beam parameters relating to walkoff (B) and focussing (ξ). As mentioned in chapter 1, the use of quasi-phasematched materials can prevent beam walkoff and hence, $B = 0$. In this case, $h_m(B, \xi)$ is found to have a maximum of 1.2 (giving a minimum pump threshold) when $\xi = 2.84$. The focussing parameter is defined as the ratio of crystal length to confocal parameter,

$$\xi = \frac{L}{b} \quad (4.4)$$

Note that in the case of confocal focussing, $\xi = 1$. The minimum beam waist can be found by setting $\xi = 2.84$ and combining equations (4.2) and (4.4),

$$w_{0,\min}(foc.) = \sqrt{\frac{\lambda L}{5.68\pi n}} \quad (4.5)$$

Equation (4.5) gives the beam waist that will result in a minimum pump threshold when working with focussed Gaussian beams. Table 4.1 shows the pump and signal/idler beam waists for a 20mm piece of LiNbO₃, calculated for the cases of confocal focussing and focussed Gaussian beams.

4. System Design & Optimisation

Beam	Beam Waist (μm)	
	Confocal ($\xi = 1$)	Focussed ($\xi = 2.84$)
Pump ($\lambda = 0.8 \mu\text{m}$)	33	21
Signal/Idler ($\lambda = 1.6 \mu\text{m}$)	47	29

Table 4.1 - Beam waists required to give minimum threshold

The above values can be thought of as ideal beam waists that the cavity modelling described in section 4.4 was working towards. As a result, the beam waists actually employed in the final cavity design will be given at the end of section 4.4.

Whilst the beam waists given in table 4.1 are specific to the nonlinear crystal used in this project, the general requirements for cavity stability and beam waist position and size can be applied to any OPO. Hence, they belong to the first type of requirements mentioned previously. The second set of requirements relate to the successful generation of a frequency comb within the OPO. The most important of these, which was introduced in chapter 2, is the matching of the signal cavity FSR to the modulation frequency of the EOM (f_m) i.e.

$$\frac{c}{2L_{cav}} = f_m \quad (4.6)$$

Here, L_{cav} is the total *optical* length of the cavity, incorporating both the physical distance between optical elements and the refractive index of intra-cavity materials. When purchasing an EOM, it is usually necessary to specify the required modulation frequency, with upper and lower limits of $\sim 10\text{GHz}$ and DC respectively. This gives a wide range of possible signal cavity lengths. However, at frequencies above 4.6GHz , only modulators with specific resonant frequencies at 6.8GHz and 9.2GHz can be obtained. This is due to the method of modulation that must be utilised at high frequencies. To create the electric field required for the linear electro-optic effect (see chapter 2), the modulator crystal must be placed in a resonant microwave cavity. The cavity size decreases with increasing modulation frequency and this, coupled with design constraints, limits the possible modulation frequencies at the high end of the

4. System Design & Optimisation

range. Fortunately this proved to be no problem, since modulation frequencies above 4.6GHz correspond to signal cavities too small to contain the EOM casing.

Further requirements of the signal cavity are created by the inclusion of the EOM as an intra-cavity element. As with the first set of requirements, these relate to the physical properties of the beam passing through the EOM crystal. To obtain optimum modulation, the beam should keep roughly the same size and shape throughout the crystal. This necessitates collimation of the beam over a distance at least equal to the crystal length, a situation analogous to the confocal focussing arrangement previously described for the nonlinear crystal. Hence, there must be a secondary beam waist at the centre of the EOM crystal with a confocal parameter equal to the crystal length or greater. Since the modulator and nonlinear crystals are of the same material and the same length, the minimum signal waist for confocal focussing from table 4.1 also applies here ($\sim 50\mu\text{m}$). In practice, as large a secondary beam waist as possible is desirable to reduce the risk of optical damage to the modulator crystal.

4.3) Resonator Configurations

As explained at the start of this chapter, the split-cavity was the logical choice for the overall design of the comb generator cavity. As shown in chapter 3, figure 3.2 the standard split-cavity consists of a pump cavity containing the nonlinear crystal and a beamsplitter. A third mirror, in line with the beamsplitter and perpendicular to the pump cavity, completes the signal cavity. Unfortunately, such a set-up cannot create the secondary beam waist in the signal cavity that is required for the EOM. Therefore, before the dimensions of the comb generator cavity could be worked out, it was necessary to modify the standard split-cavity configuration. To create the secondary beam waist, a focussing element must be situated in the signal section of the split-cavity. Focussing elements can be split into two basic types – lenses and convex mirrors. This led to two feasible configurations for the comb generator resonator, which are described below:

- 1) **Folded Design** – The signal cavity mirror is rotated to give a non-normal angle of incidence. A further mirror is then used to create an extra arm of the cavity, in which the secondary beam waist lies.

4. System Design & Optimisation

- 2) **Right-Angled Design** – An intra-cavity lens is placed after the beamsplitter to focus the circulating field into a waist inside the EOM.

Schematics of each configuration are shown in figures 4.7 and 4.8.

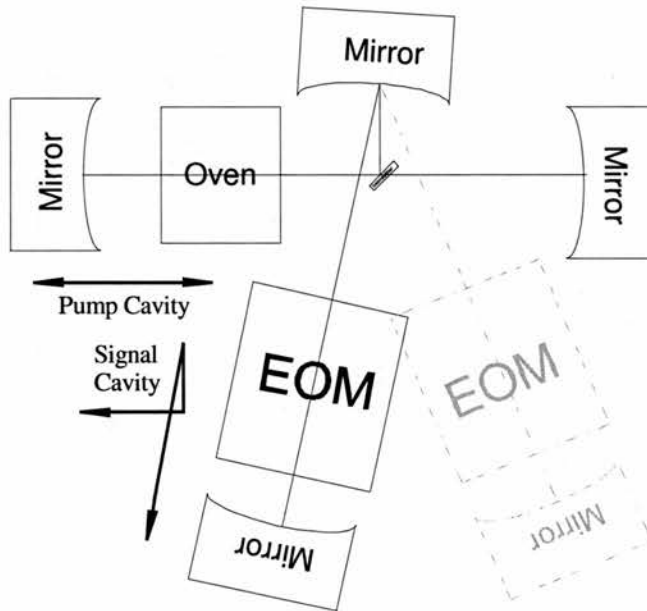


Figure 4.7 – Folded cavity design

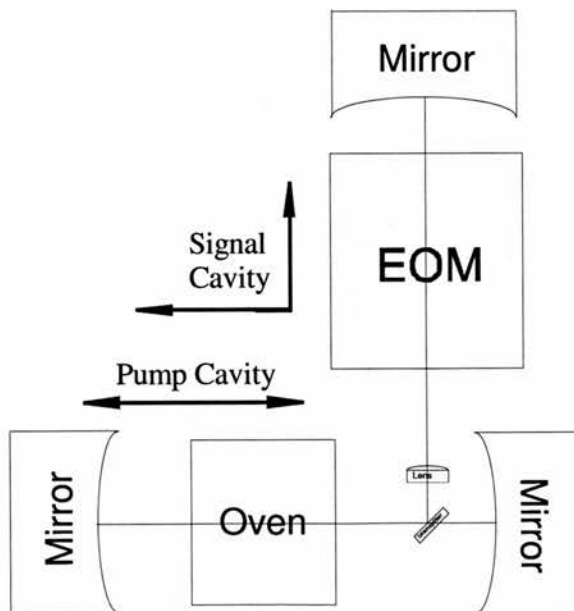


Figure 4.8 – Right-angled cavity design

4. System Design & Optimisation

The diagram of the folded cavity shows that there are two possible orientations for the extra arm, with the dotted arrangement giving greater freedom in the position of the EOM at the expense of increasing the angle of incidence at the tilted mirror. It is the tilted mirror that leads to the main drawback of the folded cavity design. This gives rise to a reflection from a curved surface that does not take place at normal incidence. Consequently, astigmatism will be introduced into the beam. This means that the beam waist in the vertical plane will, in general, differ in size and position to that of the beam waist in the horizontal plane. As might be expected, the effect on the OPO threshold is detrimental since the signal/idler irradiance through the nonlinear crystal can no longer be maximised. Decreasing the angle of incidence relative to the normal can reduce astigmatism. However, from figure 4.7 it is clear that a minimum tilt angle must exist, below which the intra-cavity field will clip the beamsplitter. As a result, astigmatism will always be present with the folded cavity design.

In the right-angled cavity shown by figure 4.8, all reflections occur at normal incidence and hence, there is no problem with astigmatism. Here, a lens takes the place of the tilted mirror and, whilst being the key to the creation of a secondary beam waist, also provides the main downside of this configuration. The lens will introduce extra loss to the cavity, via absorption and reflection of the intra-cavity field. This reduces the cavity finesse and leads to an increase in the OPO threshold. Although the loss attributed to the lens can be reduced by the application of an anti-reflection coating, it cannot be removed completely.

Having established the inherent problems with each cavity configuration, the choice of final design depended on whether the astigmatism induced in the folded cavity could be reduced to a negligible level. If this were the case then the folded cavity, with its lower round trip loss, would be the best design. On the other hand, should the astigmatism prove to be a significant problem, it would be necessary to utilise the right-angled cavity design and reduce the loss due to the intra-cavity lens as much as possible. To make the decision, the size and position of the beam waists in each cavity were needed, requiring a mathematical analysis of each configuration.

4.4) Cavity Modelling & The Final Resonator Design

The mathematical modelling of the FCG resonator was to serve two purposes. Firstly, as discussed in the previous section, it would show the effect of astigmatism in the folded configuration and whether it could be ignored. This would determine the configuration to be used. Secondly, by analysing the beam in the chosen configuration the optimum position of each component, to give the desired beam waists calculated in section 4.2, could be found.

The utilisation of the split-cavity meant that the pump and signal/idler cavities could be modelled separately. In each case, the procedure for modelling was as follows:

- 1) Find curvatures/focal length of mirrors/lens and their approximate positions using a simple geometric method.
- 2) Create a scale model of the required cavity with a CAD package (TurboCAD 8).
- 3) Perform an ABCD matrix analysis of the cavity to obtain the size and position of each beam waist.
- 4) Adjust cavity dimensions/positions of components as allowed by the scale model.
- 5) Repeat steps 3 and 4 until desired beam waists are produced.

In the first step, the geometric method refers to a technique developed by Spurr and Dunn [19]. This is part of a series, all of which allow the calculation of parameters of a Gaussian beam in various situations through a geometric approach. In the context of a stable optical resonator, the size and position of the beam waist can be obtained by drawing a circle at each mirror. Each circle should be positioned so that it just touches the associated mirror at the intersection between the mirror surface and the optic axis. The diameter of a circle is set equal to the radius of curvature of its mirror. As shown in figure 4.9, the point at which the two circles intersect is the position of the beam waist. The perpendicular distance from the optic axis to the intersection point is equal to $\frac{b}{2}$, where b is the confocal parameter and is related to the waist by equation (4.2).

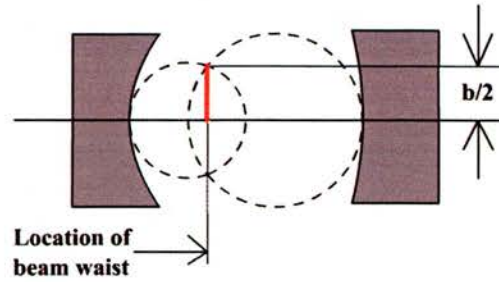


Figure 4.9 – Geometric method for obtaining beam waist

Conversely, if the size and position of the required beam waist are known, as was the case for the FCG resonator, then this method allows the position and radius of curvature of the mirrors to be estimated.

The main reason for creating the scale model in step 2 was to ensure that the cavity dimensions were physically possible. This was necessitated by the fact that the nonlinear crystal (in an oven) and the EOM crystal (in a resonant microwave cavity and casing) were both contained within dimensions significantly greater than the crystals. Also, for the purposes of reducing astigmatism in the folded configuration, the scale model allowed the minimum angle of incidence at the tilted mirror to be found precisely.

Steps 3 and 4 were perhaps the most crucial, producing a detailed description of the behaviour of the beam waist as various cavity dimensions were altered. The ABCD matrix method is a well-established technique for determining the size and position of beam waists in an optical resonator. Its theory and application has been described in detail by several authors, e.g. [20, 21], and will only be summarised here. The resonator is split into components e.g. mirror, free space, crystal and each component is represented by a 2×2 matrix. The elements of a particular matrix are determined by the properties of the component it describes. Table 4.2 below shows the ABCD matrices for some common cavity components.

4. System Design & Optimisation

Resonator Component	ABCD Matrix	Parameters
Free Space	$\begin{pmatrix} 1 & d \\ 0 & 1 \end{pmatrix}$	d = distance through free space
Crystal	$\begin{pmatrix} 1 & \frac{L}{n} \\ 0 & 1 \end{pmatrix}$	L = crystal length n = refractive index
Spherical Mirror (Normal Incidence)	$\begin{pmatrix} 1 & 0 \\ \frac{-2}{R} & 1 \end{pmatrix}$	R = mirror radius of curvature
Lens	$\begin{pmatrix} 1 & 0 \\ \frac{-1}{f} & 1 \end{pmatrix}$	f = lens focal length

Table 4.2 – Common ABCD matrices

A system matrix for the entire resonator is obtained by multiplying the ABCD matrices for all cavity components over a single round trip. The beam radius (w) and wavefront radius of curvature (R) at a chosen reference point in the cavity (the starting point of the round trip when calculating the system matrix) are determined by first imposing the stability condition. This states that the complex beam parameter, q , defined by equation (4.7) must be self-reproducing over a single round trip.

$$q = \left(\frac{1}{R} - i \frac{\lambda}{\pi w^2} \right)^{-1} \quad (4.7)$$

For a system matrix, $\begin{pmatrix} A & B \\ C & D \end{pmatrix}$, the stability condition results in the ABCD law,

$$q = \frac{Aq + B}{Cq + D} \quad (4.8)$$

Once the system matrix for a resonator is known, q , R and w can be calculated using equations (4.7) and (4.8). Equations (4.9) and (4.10) below will then give the size of the beam waist and its distance from the reference point (z).

4. System Design & Optimisation

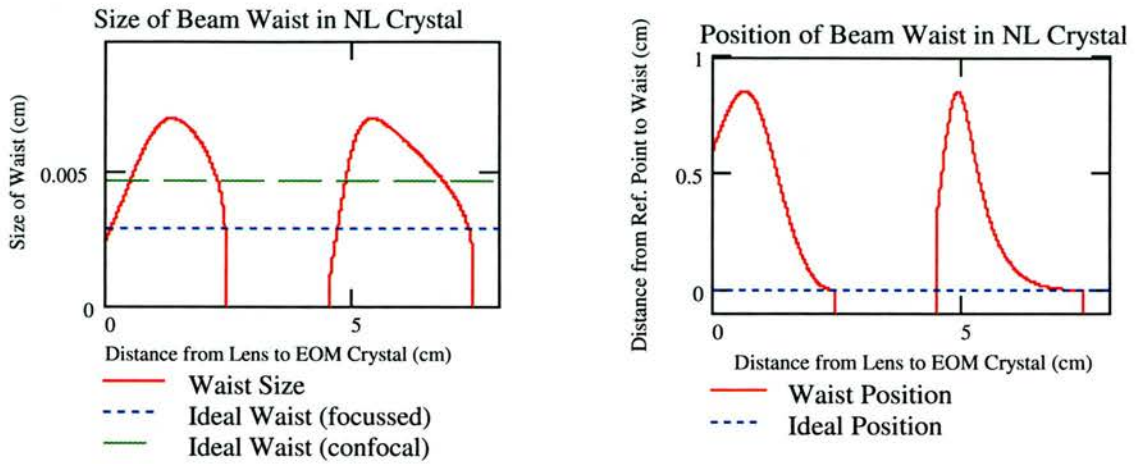
$$w_0^2 = \frac{w^2}{1 + \left(\frac{\pi w^2}{\lambda R}\right)^2} \quad (4.9)$$

$$z = \frac{R}{1 + \left(\frac{\lambda R}{\pi w^2}\right)^2} \quad (4.10)$$

Since the main aim of the ABCD analysis was to investigate the beam waists within the nonlinear and modulator crystals, it was convenient to choose a reference plane at the centre of each crystal. To determine the extent of astigmatism within the folded cavity configuration, it was necessary to perform the ABCD analysis for the signal/idler beam in both the horizontal and vertical planes. This quickly showed that astigmatism would prove to be a major problem. Even for the minimum incidence angle of 3° at the tilted mirror, the difference in the beam waist size between horizontal and vertical planes was found to be around $10\mu\text{m}$. Clearly, such a difference would cause a significant increase to the minimum attainable pump threshold. As a result, the emphasis on cavity design was changed to the right-angled configuration, with the folded option as a back-up.

Initially, the ABCD matrix analysis of the right-angled design established a stable cavity for an intra-cavity lens of focal length 20mm or 25mm. However, a cavity based on the 20mm lens would prove to be very compact with little flexibility in the position of resonator components. Therefore, it was decided to work with the 25mm lens. The next step was to vary the distance between cavity components (performing the ABCD analysis after each change in distance) in turn and plot the effect on the size and position of both beam waists in the signal/idler section and the single waist for the pump section. If necessary, mirror curvatures were also altered. Figures 4.10 and 4.11 show an example of the results obtained for the signal beam waist in the nonlinear crystal when varying the position of the intra-cavity lens with respect to the fixed modulator crystal. All other cavity components were also in a fixed position.

4. System Design & Optimisation



Figures 4.10 & 4.11 – Effect on beam waist parameters when changing cavity dimension

The left-hand plot shows the variation in the size of the beam waist. The green and blue dotted lines represent the ideal size for confocal and focussed Gaussian beams respectively, taken from table 4.1. The right-hand plot shows the effect on the position of the beam waist with respect to the reference plane (at the centre of the nonlinear crystal). The reference plane is the ideal position for the beam waist and is represented on the plot by the blue dotted line at zero. A comparison of the graphs shows two regions where the distance between lens and EOM crystal is such that the resulting beam waist has a size somewhere between the ideal values discussed earlier and lies close to the centre of the nonlinear crystal. Each region occurs just before the cavity becomes unstable (signified by the sudden sharp drop in beam waist size). Care must therefore be taken to choose a distance significantly far from the beginning of instability (so that any drift in this distance will not cause the resonator to become unstable), whilst still meeting the beam waist requirements. The first region lies between 2.25cm and 2.4cm and, on consulting the scale model, was found to be too small to fit the EOM into the cavity. Hence, the chosen distance for this section cavity of the cavity was taken from the second region (6.9cm to 7.3cm).

A similar procedure was repeated for all parts of the signal and pump cavities, first performing the ABCD matrix analysis and then checking the physical limitations with the scale model. In the case of the signal/idler cavity, this was also done for the beam

4. System Design & Optimisation

waist in the EOM crystal. After several iterations, during which the ABCD analysis was performed numerous times the final design for the right-angled cavity, shown in figure 4.12, was realised.

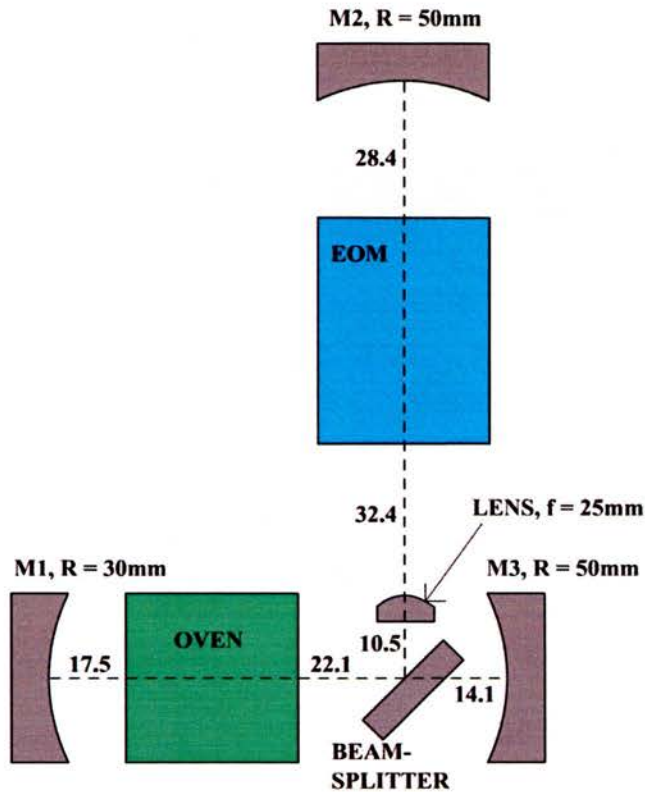


Figure 4.12 – Final design for right-angled FCG cavity

The above cavity (all distances in mm) is specifically designed to produce a tightly focussed beam waist ($w_0(p) \sim 30\mu\text{m}$ and $w_0(s,i) \sim 40\mu\text{m}$) at the centre of the nonlinear crystal (in the middle of the oven) and a second, larger beam waist ($w_0(s,i) > 50\mu\text{m}$) at the centre of the EOM crystal. Of course, the distances given in figure 4.12 are not set in stone. In particular, the mirrors are mounted on translation stages to allow fine adjustment to their position along the cavity axis. Once the OPO had been built, further refinement to the final design was achieved by using this adjustment to produce as low a pump threshold as possible.

4. System Design & Optimisation

4.5) EOM Set-up

This final section on the design of the FCG system will give a brief overview of the EOM and the equipment used to drive it. The EOM is a New Focus model 4423, consisting of a 20mm long piece of lithium niobate contained in a resonant microwave cavity. It is driven by a precision Hewlett-Packard microwave oscillator and RF amplifier, with in-line isolators to prevent damage to the driving components by power reflected from the EOM. For precision alignment, the modulator sits in a multi-stage cradle, allowing both vertical and horizontal translation and rotation in all three dimensions.

Choosing a resonant frequency for the modulator was made easier by the fact that it is equipped with a tuning slug. This allows the resonant frequency to be increased or decreased by around 10% of the centre frequency. Therefore, only an approximate value was required for the cavity FSR (= modulation frequency). From the initial cavity designs, this was found to be ~550MHz.

Before placing the EOM into the signal/idler cavity, some calibration experiments were performed to determine the resonance bandwidth of the device and establish the variation of modulation depth with input power. This was achieved by passing a He:Ne beam through the modulator and viewing the output with a Fabry-Perot interferometer. A typical trace is shown in figure 4.13.

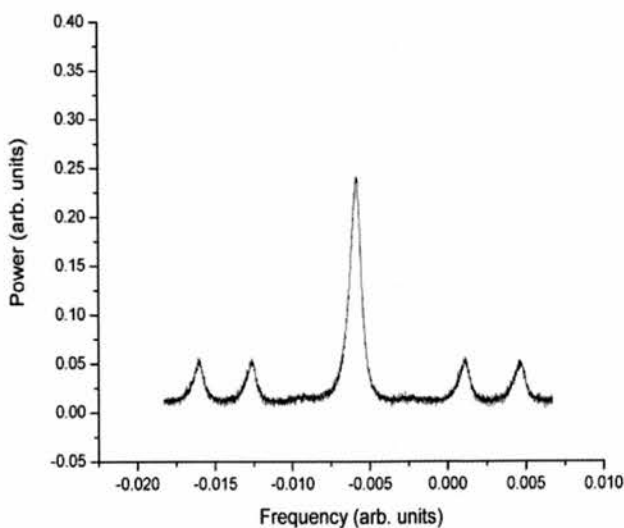


Figure 4.13 – Modulation of He:Ne beam

4. System Design & Optimisation

Figure 4.14a shows the change in sideband height (as viewed on an oscilloscope) as the modulation frequency was increased through the resonant frequency of 597.5MHz.

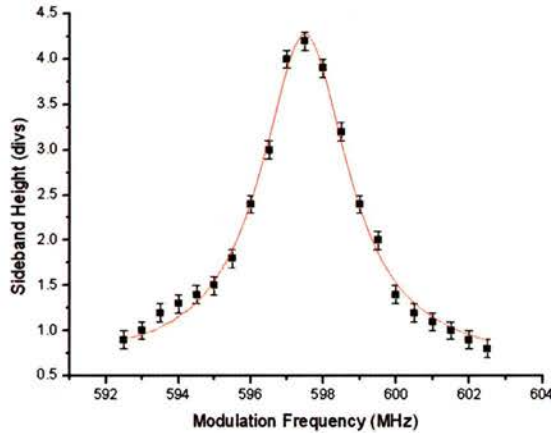


Figure 4.14a – Resonance bandwidth of EOM

A Lorentzian function is fitted to the data in figure 4.14a, which gives a resonance bandwidth of 2.9 MHz about the centre frequency. This is the range over which the modulation frequency can be changed without a significant decrease in the power coupled into the EOM. Out-with this range, the tuning slug must be used to change the resonant frequency.

For a particular input power and on RF resonance, the modulation depth was obtained by observing the power transferred into the generated sidebands and converting this into a phase shift via the Bessel function identities (see chapter 2, section 2). Figure 4.14b shows the results of this calculation for a range of input powers. Here, the x-axis denotes the output power of the signal generator before amplification.

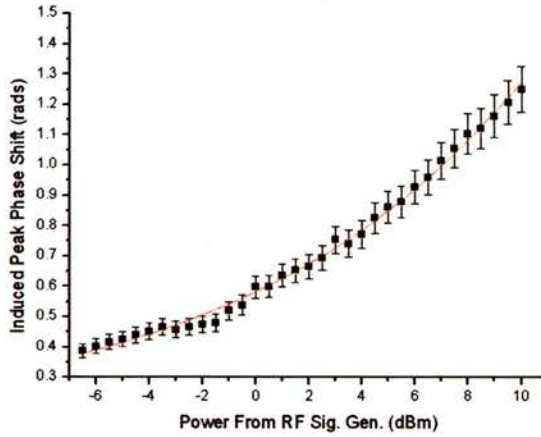


Figure 4.14b – Modulation depth of EOM

A function of the form $y = A + B \times 10^{\left(\frac{Cx}{2}\right)}$ is fitted to the above data, where A,B and C are constants. This comes from the equation [22] relating the peak phase shift ($\Delta\phi$) to the input RF power at the EOM (P),

$$\Delta\phi = \frac{2\pi}{\lambda} \left(\frac{n_e^3 r_{33}}{2} \right) \sqrt{\frac{2PQL}{\epsilon\omega bd}} \quad (4.11)$$

In equation (4.11) P is the RF power coupled into the modulator in Watts, L, b and d are the dimensions of the crystal (20mm x 2mm x 2mm) and Q is the quality of the resonant microwave cavity (186). Since the measured power was in dBm, 10^x must be used in the fitting function to convert between the two. The factor of $\frac{1}{2}$ in the power of 10 is due to the square root and the constants a, b and c account for the various constants and conversion factors in equation (4.11). It is important to remember that the data in figure 4.14 was measured at the He:Ne wavelength of 633nm. Since the induced phase shift is inversely proportional to wavelength, as shown by equation (4.11), it is necessary to multiply the data points by $\frac{633}{1600} \approx 0.4$ when utilising the

EOM at the degenerate signal and idler wavelength.

By measuring the RF power at the modulator input, the overall gain of the isolator-amplifier-isolator chain was found to be 23.5dB. Therefore, 10dBm from the signal generator, corresponding to around 0.5 rads of modulation depth at 1600nm, will give an input power of roughly 2W to the EOM. This agrees fairly well with equation

4. System Design & Optimisation

(4.11) above (it gives a value of ~ 0.7 for $\Delta\phi$ at an input power of 2W), although there is a significant uncertainty in the value of ϵ in LiNbO₃ at RF frequencies.

4.6) Optimisation – Pumping Level & Input/Output Coupling

The optimisation of pumping level and input/output coupling in the frequency comb generator is now considered. This had two aims. Firstly, for a given pumping level, to identify the input/output conditions that optimised the downconversion efficiency and relate them to the associated pump enhancement factor. Secondly, to find the optimum pumping level at the ideal input and output coupling conditions previously identified. In the context of a practical device for telecommunications, the second aim is particularly important. To create a compact, low power device, the optimum pumping level must be achievable by a single mode laser diode whilst still providing an output power of several mW. It was desirable to achieve the two aims in the order given above. However, experimental practicalities necessitated that this order be reversed, leading to the procedure described next.

Throughout this project, a Ti:Sapphire oscillator was used as a pump source. This was pumped by a 10W Argon Ion laser and produced around 1W of single-frequency power at 800nm. It could also be stabilised to a high degree, providing a pump beam with excellent spatial and spectral quality.

Three input couplers (5%, 10%, 20%) and two output couplers (1%, 2%) were available, giving six possible input/output combinations. For each combination, the output signal/idler power and fraction of pump light back-reflected were measured as the pump power was increased from zero to the maximum available (~ 500 mW). Figures 4.15 to 4.20 shows the results for the six input/output coupler combinations.

4. System Design & Optimisation

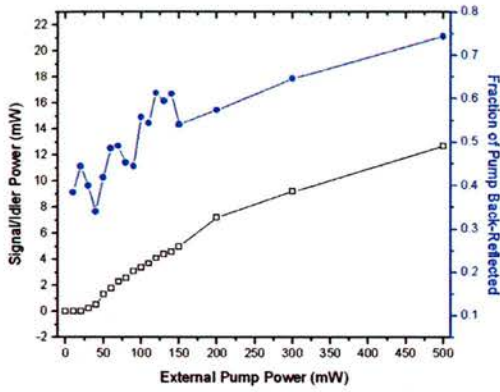


Figure 4.15 – 5% input & 1% output

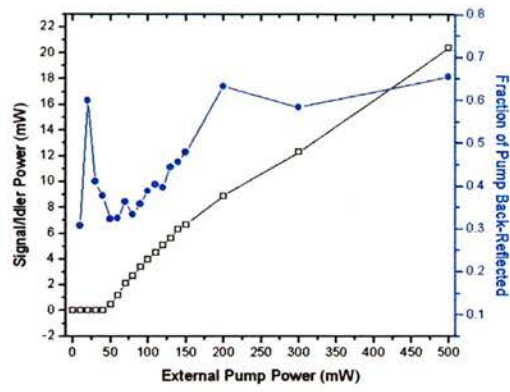


Figure 4.16 – 5% input & 2% output

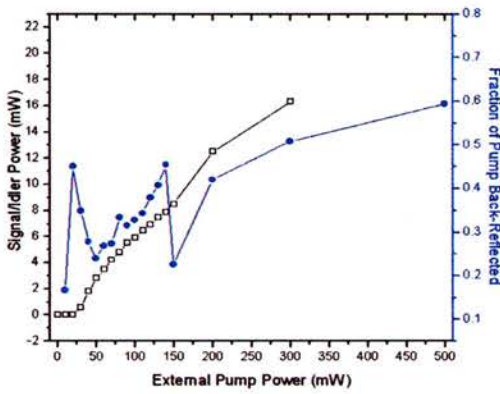


Figure 4.17 – 10% input & 1% output

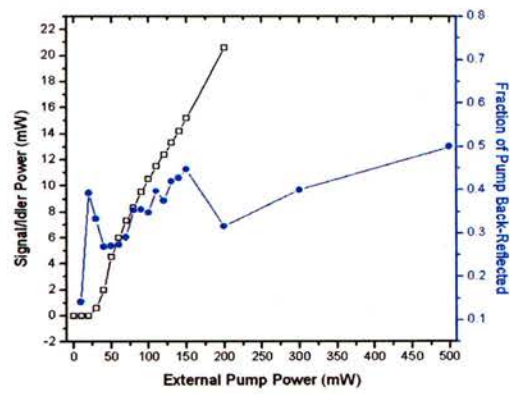


Figure 4.18 – 10% input & 2% output

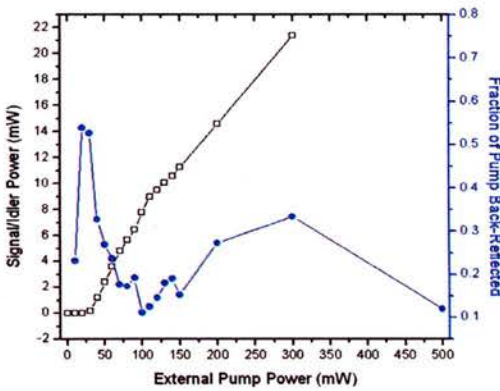


Figure 4.19 – 20% input & 1% output

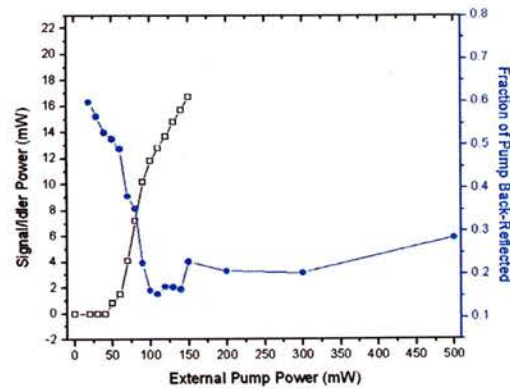


Figure 4.20 – 20% input & 2% output

In some of the above figures, data for the signal/idler power is missing at higher pump powers due to saturation of the detector above 22mW. An initial look at the output power plots shows a threshold of 30 to 50mW in each case. As expected, the higher thresholds occur for 2% output coupling. The input coupling seems to have little

4. System Design & Optimisation

effect on the threshold and this can be explained by observing the back-reflected pump. In each case the fraction of back-reflected pump is approximately the same, suggesting a similar enhancement factor. This makes sense, since losses in the pump cavity are wholly parasitic at threshold, with no component due to downconversion. For each input/output combination, the output power rises steeply at first, before beginning to tail off at higher pump powers. The highest output power is gained for the 20% input coupler and 2% output coupler.

Whilst showing some scatter due to power fluctuations during the operation of the OPO and uncertainties at very low pump powers, there is a general trend to each of the back-reflection plots. For both of the 5% input combinations, the fraction of pump back-reflected increases as the pump power is increased above threshold, with no obvious minimum. On the other hand, the data taken with 10% and 20% input couplers shows a definite minimum in every case. This can be explained by recalling section 3.4 on the optimum pumping level in chapter 3. Equations (3.19) and (3.20) show that a minimum back-reflection will be achieved when the input coupling is equal to the round-trip pump loss of the enhancement cavity. This is made up of the parasitic loss and, above threshold, the loss due to down-conversion, which depends on the pumping level. So, as the pump power is increased the round-trip loss will change. In the case of the 5% input coupler, no minimum in the back-reflection occurs because the initial parasitic loss is greater than or equal to 5% and so the input coupling is always less than the round trip loss i.e. the pump is always under-coupled. For the 10% and 20% input couplers this is not the case (pump is initially over-coupled) and as the pump power is increased, the round-trip loss approaches the input coupling, resulting in a back-reflection minimum.

To determine the best input/output coupler combination it is necessary to look at the variation in overall efficiency (output power compared to input power) with pump power, shown in figure 4.21.

4. System Design & Optimisation

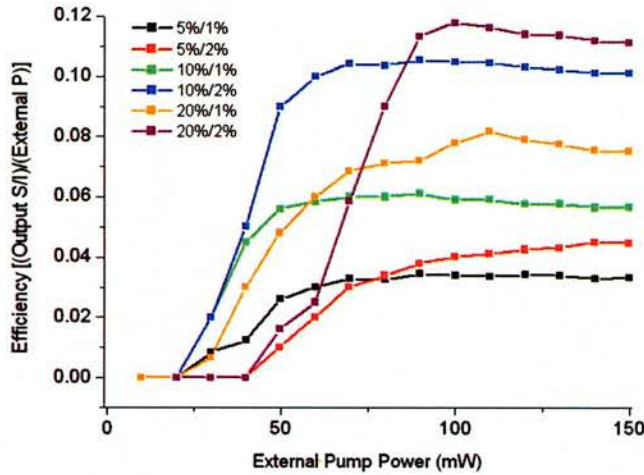


Figure 4.21 – Efficiencies for all input/output combinations

Note that the efficiency is only given up to an input power of 150mW, since the output power could not be measured for all input/output combinations above this pumping level. As expected from the output power plots, the efficiency for each input/output combination initially rises quickly with pump power before reaching a plateau. Beyond this point, the efficiency begins to slowly decrease. The greatest efficiency of around 12% is obtained with the 20% input coupler and 2% output coupler at a pump power of 100mW. Second best is the 10% input coupler and 2% output coupler, with an efficiency of around 10.5% at the same pump power.

Having obtained the optimum pumping level for efficiency, the same must be done for the pump-enhancement factor. Figures 4.15 – 4.20 show that the 20% input coupler gives the smallest fraction of back-reflected pump at 100-120mW. Taking the 20%/2% combination, which gave the highest efficiency, the back-reflection and efficiency data can be used to calculate a number of parameters relating to the operation of the PE-OPO. At threshold (30 – 50mW) the fraction of pump back-reflected is 0.515, decreasing to 0.172 at 120mW. The output power at the latter pumping level is 13.7mW. Utilising the method described in chapter 3, section 3.3 by way of a MathCAD program (see appendix III), the round-trip pump loss at threshold is found to be 3.6%, and the corresponding EF equal to 13.2. With negligible downconversion at the threshold level, this loss is entirely parasitic. At a pumping level of 120mW, the round-trip loss and EF are 9.2% and 9.0 respectively. From these values and figure 4.20, it is apparent that the total pump loss has increased due to the onset of downconversion and this has driven the pump-enhancement cavity towards

4. System Design & Optimisation

impedance matching. Assuming that the parasitic loss has not significantly changed, a simple subtraction gives the downconversion loss at 120mW as 5.6%. This corresponds to a downconverted power of 60.5mW (product of downconversion loss and circulating pump power), which is coupled out of the signal/idler cavity through M2 in a ratio determined by:

$$P_{output} = \frac{\alpha}{\alpha + \beta} P_{DC} \quad (4.12)$$

Here, α and β represent the output coupling (2%) and round-trip parasitic loss of the signal/idler cavity respectively. The parasitic loss is primarily due to absorption in the EOM crystal and scattering/transmission at the various surfaces in the cavity. Taking the observed and calculated figures for output power and downconverted power, equation (4.12) gives 6.8% as the round-trip parasitic loss in the signal/idler cavity and the total signal/idler loss ($\gamma = \alpha + \beta$) is therefore 8.8%.

To ensure energy conservation, the various losses at the pump should add up to the initial pumping level. The three loss mechanisms to consider are due to parasitic loss, downconversion and back-reflection. Respectively, these are 39mW, 60mW and 21mW, using the percentage losses calculated previously. The sum of these losses is exactly 120mW, showing that energy is indeed conserved.

The calculation of the total signal/idler loss above allows the threshold of the OPO-FCG in the absence of pump-enhancement to be obtained. A quick and simple method of achieving this involves taking the threshold of the Diddams device [10], which was a DRO with double-pass pump, and applying the appropriate scaling factor. From equation (1.30) in chapter 1, this scaling factor has four parts and is given below:

$$\begin{aligned} P_{th}^{OPO-FCG} &= \left(\frac{\lambda_p^{OPO-FCG}}{\lambda_p^{Diddams}} \right)^3 \left(\frac{L_{Diddams}}{L_{OPO-FCG}} \right) \left(\frac{\gamma_{OPO-FCG}}{\gamma_{Diddams}} \right)^2 \left(\frac{d_{eff}^{Diddams}}{d_{eff}^{OPO-FCG}} \right)^2 P_{th}^{Diddams} \\ &= \left(\frac{800}{532} \right)^3 \left(\frac{7.5}{20} \right) \left(\frac{8.8}{2} \right)^2 \left(\frac{5}{18} \right)^2 \times 200mW \end{aligned} \quad (4.13)$$

Putting the appropriate values into equation (4.13), as shown above, results in a scaling factor of 1.9 and hence a non-pump-enhanced threshold of ~400mW for the OPO-FCG. Given the scatter in the experimental data and the rough nature of the

4. System Design & Optimisation

calculations performed previously, this is consistent with the observed threshold of 30-50mW and EF of 13.

The experimental data shows that the 20% input coupler and 2% output coupler give the greatest device efficiency and largest pump enhancement factor. Most importantly, both occur at approximately the same pumping level. In fact, a closer inspection of figures 4.20 and 4.21 shows that neither the efficiency nor back-reflection change significantly between pump powers of 100mW and 140mW. This suggests that pumping anywhere within this range when utilising the 20% input coupler and 2% output coupler should give close to the optimum efficiency and enhancement factor.

The question now arises as to whether the conclusions gained from the experimental results correspond to a theoretical evaluation of the optimum pumping level as discussed in chapter 3, section 3.4. By using the equations given at the conclusion to section 3.4 (equations 3.29 – 3.31) and results gained from the experimental data (pump & signal/idler cavity losses and non-PE threshold), both the efficiency and back-reflection for any input/output combination can be modelled as a function of external pump power. It should be noted that the efficiency given by the modelling is the *down-conversion* efficiency (the ratio of signal and idler power at the crystal to the external pump power) rather than the overall efficiency. Therefore, it is necessary to calculate the experimental down-conversion efficiency to give a proper comparison. The experimental down-converted power can be calculated from the output power using equation (4.12) above.

Figure 4.22 shows a comparison of theoretical and experimental values for the down-conversion efficiency and fraction of pump back-reflected with the 20% input coupler and 2% output coupler. Figure 4.23 shows the same for the 20%/1% combination.

4. System Design & Optimisation

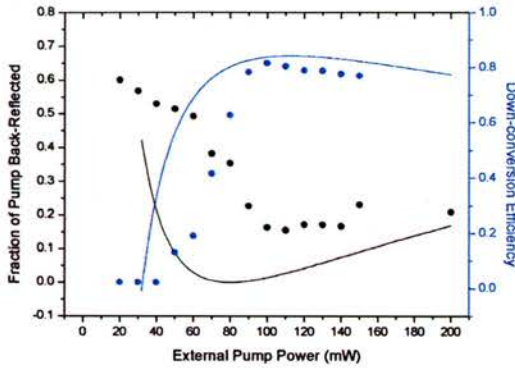


Figure 4.22 – Comparison of theory & experiment for 20%/2% combination

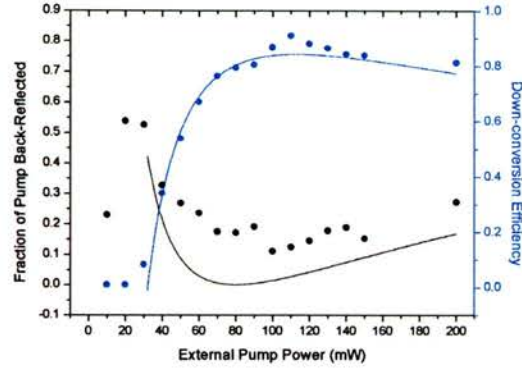


Figure 4.23 - Comparison of theory & experiment for 20%/1% combination

It is immediately apparent that the general shape of the experimental curves closely matches that of the theoretical curves in all cases. In particular, there is good agreement for the down-conversion efficiency at higher pump powers and the modelling predicts peak efficiency at the same pump powers as observed experimentally. The discrepancy between experimental and theoretical efficiency at lower pump powers for the 2% output coupler can be explained by the fact that the signal/idler parasitic loss must be estimated. This does not take into account changes in the loss as the results were taken, which could be caused by a variety of factors such as thermal effects and drift in the alignment of cavity components.

Unfortunately, there is a significantly greater mismatch between theory and experiment for the fraction of pump back-reflected, particularly at lower pump powers. Again, a possible explanation for this is the use of a constant value for R_c in equation (3.31), thereby ignoring any changes in loss that could occur with increasing pump power (due to downconversion in particular). Whilst the comparison of back-reflection results is disappointing, encouragement can be gained from the fact that the modelling still predicts a small fraction in the optimum pumping region, not that much greater than the minimum value.

The desired outcome of the optimisation of the frequency comb generator was an optimum pumping level compatible with the requirement for a compact, low power device. By using a 20% input coupler and 2% output coupler an optimum pumping level of ~120mW was achieved, producing an output power of nearly 14mW. Such an external pump power can easily be achieved by a single mode laser diode, giving compactness and compatibility with current telecommunications systems.

4.7) Chapter Summary

A crucial stage in the development of the frequency comb generator was the design and optimisation of an optical resonator, a procedure described in detail in this chapter. The first step was to select a suitable nonlinear crystal. Of the two candidates, LiNbO_3 was found to have a slightly higher phasematching bandwidth than $\text{MgO}:\text{LiNbO}_3$ at 1600nm. Although the crystals were evenly matched in terms of properties, LiNbO_3 was chosen to be the nonlinear crystal in the comb generator because it was readily available. A further analysis of the crystal showed that a poling period of $19.6\mu\text{m}$ was the best option for the phasematching of degenerate signal and idler wavelengths at 1600nm.

When creating a design for the optical resonator, it was first necessary to identify the requirements of the resonator in terms of the spatial and temporal properties of the circulating optical fields. To ensure as low a pump threshold as possible, both pump and signal/idler waves must have a minimum beam radius (known as the beam waist) at the centre of the nonlinear crystal. The optimum size for each beam waist is obtained by employing the focussed Gaussian beam analysis of Boyd and Kleinman, giving $21\mu\text{m}$ for the pump and $29\mu\text{m}$ for the signal/idler. Additional requirements are placed on the optical resonator by the inclusion of the EOM. The FSR of the signal/idler cavity must equal the modulation frequency of the EOM to generate a comb of frequencies. However, the wide range of modulators available meant that this was not a serious concern. Of greater importance is the need to create a large secondary beam waist in the signal/idler wave at the centre of the EOM crystal to give optimum conditions for modulation and reduce the risk of optical damage.

To produce the secondary beam waist, the standard split-cavity design must be modified by the inclusion of a focussing element. There are two ways of doing this, leading to two possible configurations for the resonator. In the first, known as the *folded cavity*, the signal mirror is tilted and a further mirror used to create an extra arm in the cavity. The *right-angled cavity* utilises an intra-cavity lens placed between the beamsplitter and EOM. The folded cavity suffers from the problem of astigmatism, where the beam waist in the nonlinear crystal is a different size in the horizontal and vertical planes. This could lead to an increase in pump threshold. The

4. System Design & Optimisation

right-angled cavity, whilst not experiencing astigmatism, has an additional loss-producing element in the shape of the lens.

To decide upon the configuration to use and also produce the final resonator design, a mathematical model was created. This utilised the well-known ABCD matrix method to obtain the size and position of each beam waist. The first results for the folded cavity showed that even the minimum possible astigmatism would still give a difference of $10\mu\text{m}$ in the size of the beam waist between the two planes. As a result, the right-angled cavity was chosen with the aim to reduce the loss due to the lens as much as possible. In the next stage of the modelling, the various sections of the right-angled cavity were varied in size to find dimensions that would give the optimum position and size for each beam waist. A scale model of the cavity was also created to ensure that the results of the ABCD matrix method were physically possible.

With the final design of the optical resonator attained, the last part of the design process was to obtain and characterise the EOM. The modulator was purchased from New Focus with a modulation frequency of $\sim 550\text{MHz}$. However, this is tunable by around $\pm 60\text{MHz}$. Further experimentation on the EOM outside of the signal/idler cavity demonstrated a bandwidth of 2.9MHz about any particular resonant frequency and established a relationship between the power from the driving oscillator and the induced phase shift.

Optimisation of the frequency comb generator was required for two reasons. Firstly, to find the input and output coupler combination that would give the largest efficiency and enhancement factor and secondly to find the optimum pumping level for the chosen input/output pair. Of the six combinations, the 20% input coupler and 2% output coupler gave the greatest overall efficiency and largest enhancement factor at a pump power of around 120mW , resulting in an output power of nearly 14mW . These results were then compared to the theory by utilising the equations given in chapter 3 at the end of section 3.4. The experimental efficiencies agree well with the theory, particularly at higher pump powers, and both give the greatest efficiency at the same pumping level. Unfortunately, there is not a similar level of agreement for the fraction of pump back-reflected, although both experiment and theory show a small fraction at the optimum pumping level.

Overall, the optimisation results show that a compact device pumped by a single mode laser diode is feasible, whilst still producing an output power of several mW .

4. System Design & Optimisation

This is important in the context of telecommunications, where systems must be small and have low power requirements.

References

1. Edwards, T.J., et al., *Continuous-Wave Singly-Resonant Optical Parametric Oscillator based on Periodically Poled RbTiOAsO₄*. Optics Letters, 1998. **23**(11): p. 837-839.
2. Edwards, T.J., et al., *Continuous-Wave, Singly-Resonant, Optical Parametric Oscillator based on Periodically Poled KTiOPO₄*. Optics Express, 2000. **6**(3): p. 58-63.
3. Lindsay, I.D., et al., *Continuous-Wave, Pump-Enhanced Optical Parametric Oscillator based on Periodically-Poled RbTiOAsO₄*. Optics Express, 2003. **11**(2): p. 134-140.
4. Weise, D.R., et al., *Continuous-Wave 532nm Pumped Singly Resonant Optical Parametric Oscillator with Periodically Poled KTiOPO₄*. Optics Communications, 2000. **184**(1-4): p. 329-333.
5. Schneider, K. and Schiller, S., *Narrow-Linewidth, Pump-Enhanced Singly-Resonant Parametric Oscillator Pumped at 532 nm*. Applied Physics B - Lasers and Optics, 1997. **65**(6): p. 775-777.
6. Tsunekane, M., et al., *Continuous-Wave, Broadband Tuning from 788 to 1640nm by a Doubly-Resonant, MgO:LiNbO₃ Optical Parametric Oscillator*. Applied Physics Letters, 1998. **72**(26): p. 3414-3416.
7. Kozlovsky, W.J., et al., *Efficient Monolithic MgO:LiNbO₃ Singly Resonant Optical Parametric Oscillator*. Optics Letters, 1988. **13**(12): p. 1102-1104.
8. Nakamura, M., et al., *Quasi-Phasematched Optical Parametric Oscillator using Periodically Poled MgO-doped LiNbO₃ Crystal*. Japanese Journal of Applied Physics Part 2 - Letters, 1999. **38**(11A): p. L1234-L1236.
9. Capmany, J., et al., *Continuous-Wave Self-Pumped Optical Parametric Oscillator based on Yb³⁺-doped Bulk Periodically Poled LiNbO₃ (MgO)*. Applied Physics Letters, 2001. **79**(3): p. 293-295.

4. System Design & Optimisation

10. Diddams, S.A., et al., *Broadband Optical Frequency Comb Generation with a Phase-Modulated Parametric Oscillator*. Optics Letters, 1999. **24**(23): p. 1747-1749.
11. Barnes, N.P. and Corcoran, V.J., *Parametric Generation Processes: Spectral Bandwidth and Acceptance Angles*. Applied Optics, 1976. **15**: p. 696-699.
12. Jundt, D.H., *Temperature-Dependent Sellmeier Equation for the Index of Refraction n_e in Congruent Lithium Niobate*. Opt. Lett., 1997. **22**: p. 1553.
13. Eckardt, R.C., et al., *Optical Parametric Oscillator Frequency Tuning and Control*. Journal of the Optical Society of America B - Optical Physics, 1991. **8**(3): p. 647-667.
14. Svelto, O., *Principles of Lasers*. 3rd ed. 1989: Plenum Press. 351.
15. Siegman, A.E., *Lasers*. 1986, Mill Valley: University Science Books.
16. Boyd, G.D. and Kleinman, D.A., *Parametric Interaction of Focused Gaussian Light Beams*. J. Appl. Phys., 1968. **39**(8): p. 3597.
17. Guha, S., et al., *The Effects of Focusing on Parametric Oscillation*. IEEE Journal of Quantum Electronics, 1982. **18**(5): p. 907-912.
18. Guha, S., *Focusing Dependence of the Efficiency of a Singly-Resonant Optical Parametric Oscillator*. Applied Physics B - Lasers and Optics, 1998. **66**(6): p. 663-675.
19. Spurr, M.B. and Dunn, M.H., *Euclidean Light*. Optics & Photonics News, 2002. **13**(8): p. 40.
20. Casperson, L.W., *Mode Stability of Lasers and Periodic Optical Systems*. IEEE Journal of Quantum Electronics, 1974. **QE-10**(9): p. 629-634.
21. Kogelnik, H. and Li, T., *Laser Beams and Resonators*. Proceedings of the IEEE, 1966. **54**(10): p. 1312-1329.
22. *New Focus Model Series 44xx & 485x User's Manual: High-Frequency Electro-optic Phase Modulators*. 2002.

Chapter 5

Comb Generation in a Dispersive Cavity

The first attempts at generating a comb of frequencies actually took place between the design and optimisation stages detailed in the previous chapter. After the FCG had been constructed and aligned such that the OPO was oscillating well, the decision was taken to perform proof-of-principle experiments and check that a frequency comb could be generated. Assuming these experiments were successful, the next step would be the optimisation of the system in terms of input/output coupling and the pumping level (see chapter 4, section 4.6). In this chapter, section 5.2 discusses the proof-of-principle experiments and presents the subsequent results. Section 5.3 reports on similar experiments that were performed with the optimum input and output coupling and at the optimum pumping level; after the optimisation stage.

In the title of this chapter and chapter 7, an important distinction is made. All the comb generation experiments discussed in this chapter took place under the condition of full dispersion in the intra-cavity media. Here, the nonlinear and EOM crystals make up the majority of the intra-cavity media, with the lens also having a contribution. During the course of the comb generation experiments, it was discovered that dispersion is an important factor. Section 5.4 and the following chapter examine this in detail. Chapter 7 then deals with the implementation of a dispersion compensation scheme in the FCG resonator and the resulting effects on comb generation. During the course of the dispersion compensation experiments, comb generation was further explored in the case of no compensation. These results provided several interesting insights into the comb generation process and are summarised in the final section of this chapter.

5.1) Modelling of Comb Bandwidths

As mentioned in chapter 2 and subsequently clarified in chapter 6, the main limiting factor on the comb width is dispersion in the intra-cavity media of the FCG resonator.

5. Comb Generation in a Dispersive Cavity

Prior to beginning the comb generation experiments, modelling of the dispersion-limited comb bandwidths was undertaken, to gain some indication as to the widths attainable experimentally. Previous study of dispersion-limited frequency combs has been carried out by Kouroggi et al [1], who derived a simple expression to calculate the comb bandwidth. This is given below in a slightly altered form.

$$\Delta f_{\max} = \left[\frac{4\beta}{L \frac{\partial^2 k}{\partial \omega^2} \pi^2} \right]^{\frac{1}{2}} \quad (5.1)$$

In equation (5.1), β is the depth (or index) of modulation applied by the EOM, L the length of the intra-cavity media (i.e. nonlinear and modulator crystals) and $\frac{\partial^2 k}{\partial \omega^2}$ should be evaluated at the centre frequency of the comb. The latter is the key factor in the comb bandwidth equation because it is determined by the refractive index, which relates directly to the dispersion relations and Sellmeier data [2, 3]. Utilising equation (5.1), figure 5.1 shows the variation of comb bandwidth with signal wavelength with 40mm of intra-cavity media (20mm for both nonlinear and EOM crystals).

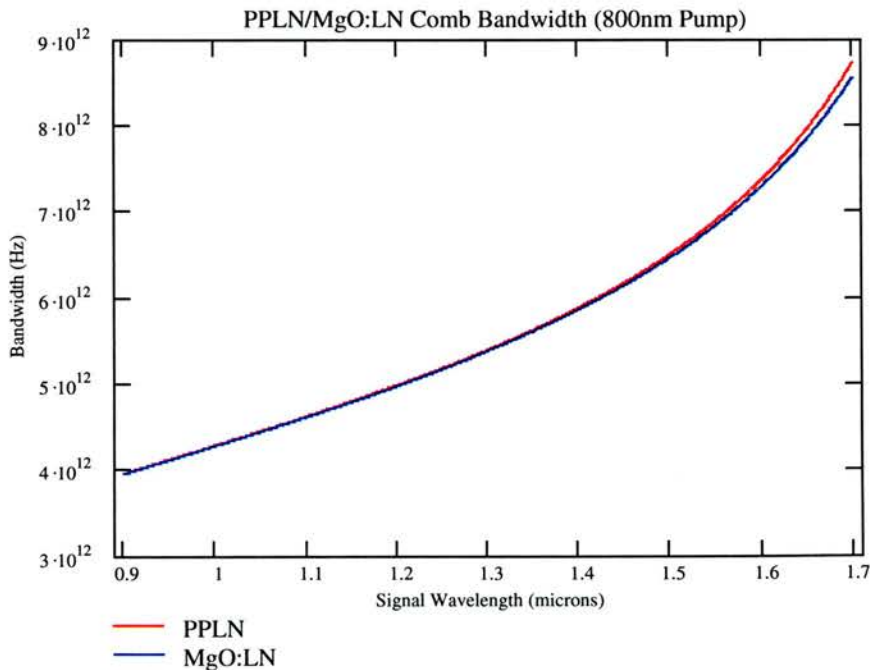


Figure 5.1 –Comb bandwidths for a range of signal wavelengths

5. Comb Generation in a Dispersive Cavity

In the above plot, comb bandwidths are shown for both LiNbO_3 (periodically poled) and $\text{MgO}:\text{LiNbO}_3$, which were the two options for the nonlinear crystal, discussed in chapter 4. As might be expected from previous work on the modelling of phasematching bandwidths (see chapter 4, section 4.1), there is a rapid rise in the comb bandwidth as the signal wavelength increases to degeneracy. The model also shows that LiNbO_3 gives a slightly higher bandwidth of 7.36 THz at the degenerate wavelength of 1600nm, giving further credence to the decision to use it as the nonlinear crystal. However, as mentioned in chapter 4, section 4.1, the main reason for choosing LiNbO_3 was its availability as a periodically poled crystal. The plots in figure 5.1 were calculated for a crystal temperature of 180°C. However, equation (5.1) can also be employed for a fixed signal wavelength over a range of crystal temperatures. This is shown in figure 5.2, again for LiNbO_3 and $\text{MgO}:\text{LiNbO}_3$.

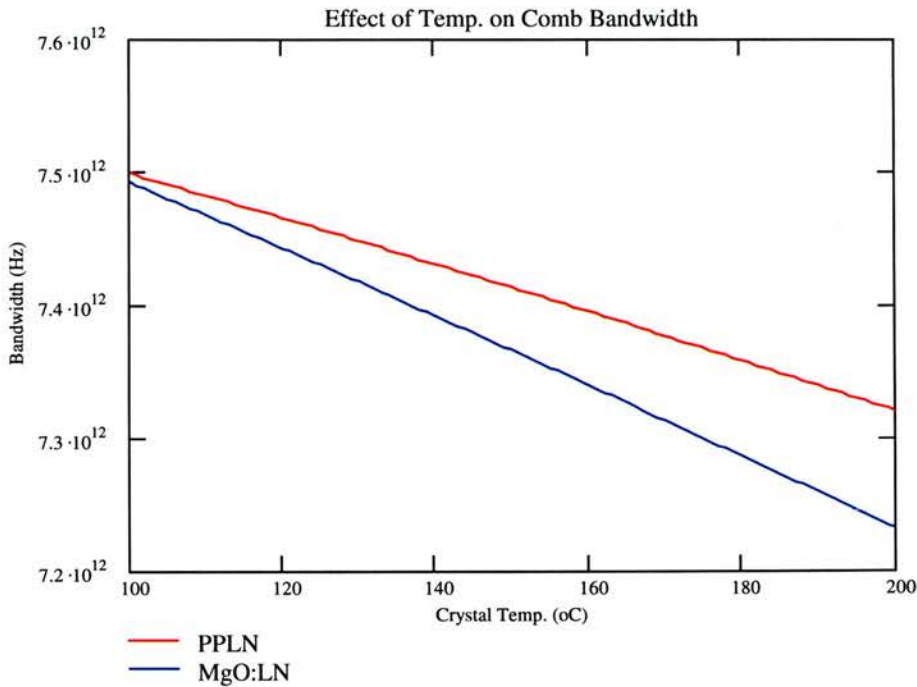


Figure 5.2 – Comb bandwidths for a range of crystal temperatures

The difference between LiNbO_3 and $\text{MgO}:\text{LiNbO}_3$ is more apparent in the above figure. In particular, $\text{MgO}:\text{LiNbO}_3$ shows a much sharper drop in comb bandwidth with increasing crystal temperature. As far as the frequency comb generator is concerned, figure 5.2 suggests that the crystal temperature should be set low as

5. Comb Generation in a Dispersive Cavity

possible (within the limits set by photorefractive damage and the desired signal/idler wavelength) to maximise the comb bandwidth.

Modelling of the dispersion-limited frequency comb has shown that it should be possible to generate comb widths in excess of 7 THz (60nm) with the system described in this thesis. This is significantly greater than the maximum width of 5.6 THz (21nm) produced by Diddams et al [4].

5.2) Experimental Comb Generation 1 (Proof of Principle)

As mentioned in the introduction to this chapter, the experiments described in this section took place before the optimisation of the FCG resonator. The main purpose was to check that the system would actually generate a comb of frequencies and if so, that comb widths comparable to those suggested by the theoretical modelling could be produced.

The output from the FCG was analysed in the optical and radio frequency (RF) regimes. For the former, a fraction of the FCG output was fibre-coupled into an HP 86140B optical spectrum analyser (OSA). Analysis in the RF regime was undertaken by focussing the FCG output onto a fast InGaAs PIN photodiode, which was connected to an RF spectrum analyser (RFSA). The purpose of the OSA was to show the full extent of the generated comb, allowing its width and power fluctuations to be measured. On the other hand, the fast photodiode and RFSA were used to look at beat frequencies between individual modes in the comb. The observation of beat frequencies at multiple harmonics of the modulation frequency provides evidence that a phase-locked frequency comb has been generated. To understand this, consider the case where the modes in the comb are not phase-locked and instead are oscillating independently. In this situation, there is nothing to link the phase of a beat frequency between a pair of modes to the beat frequency between any other mode pair. When added together, the random nature of the phase means that the total fundamental beat frequency (between adjacent modes in the comb) averages to zero. The same argument holds for the higher harmonics. In this case, any observed harmonics would be entirely due to beating between the initial carrier frequency and sidebands imposed upon it by the modulation. Hence, the power in the observed beat frequencies would be very low. In the case of a phase-locked frequency comb, the relative power in the

5. Comb Generation in a Dispersive Cavity

harmonics would be expected to increase, due to the accumulation of multiple beats between modes in the comb.

To begin the comb generation experiments, it was first necessary to obtain the correct modulation frequency to match the cavity FSR. Measurement of the signal/idler cavity length and allowing for the refractive and dispersive properties of the intra-cavity elements gave a mode spacing between 593 MHz and 603 MHz. With the OPO oscillating well above threshold (pump power ~ 550 mW) and EOM switched off, no beat frequencies could be seen on the RFSA. This was expected, since an OPO will only operate on a single signal and idler mode pair at any instant. On driving the EOM at 600 MHz with a modulation depth of ~ 0.6 rad, a strong beat frequency at the modulation frequency and several of its harmonics immediately appeared.

A thorough analysis of the beat frequencies over the tuning range of the modulator (450 – 700 MHz) showed the following results:

- The fundamental beat frequency was always present at a significant strength. This is not surprising, since the modulator will always generate first order sidebands.
- The 2nd harmonic began to appear at 450 MHz and, although low in strength, was still present at 700 MHz.
- The 3rd harmonic appeared at ~ 505 MHz and disappeared at ~ 670 MHz
- The 4th harmonic appeared at ~ 550 MHz and disappeared at ~ 640 MHz
- The 5th harmonic appeared at ~ 560 MHz, but the frequency at which it disappeared could not be determined because it was above the upper range of the RFSA.
- All harmonics increased in size to a peak at ~ 595 MHz and then decreased in size as the modulation frequency was increased beyond this.
- A further examination of the 4th and 5th harmonics at modulation frequencies around 595 MHz showed a peak at 593 MHz.

5. Comb Generation in a Dispersive Cavity

The peak in the higher harmonics at 593 MHz and the fairly symmetric emergence and disappearance of said harmonics around this point suggested that this modulation frequency was the closest match to the cavity FSR.

After investigating the beat frequencies, the output from the FCG was observed on the OSA. At this point, the output coupler was mounted on a PZT to allow changes to be made to the signal/idler cavity length on the nm scale. Increasing the voltage applied to the PZT caused it to expand, thereby decreasing the length of the signal/idler cavity by 10nm per Volt. With the EOM switched off, a single signal and idler mode pair could be seen on the OSA, approximately 30 – 40nm either side of 1600nm (the degenerate wavelength). At first, both modes were quite jittery, hopping several times in a short space of time. However, by turning off as many sources of vibration in the laboratory as possible and placing a box around the FCG to remove air currents, the stability of the FCG output was drastically improved. It was then possible to move the mode pair closer to degeneracy by lengthening the signal/idler cavity via the PZT. Unfortunately, it was not possible to reach degeneracy before both signal and idler would jump back to their starting wavelengths of ~1560nm and ~1640nm respectively. To solve this problem, the temperature of the nonlinear crystal was decreased to 170.5°C, tuning the signal and idler modes closer to 1600nm. Now, degeneracy could be reached by adjusting the PZT. With the EOM on, a quick check of the beat frequencies showed that the temperature and PZT adjustments had reduced the optimum modulation frequency to 591 MHz.

When driving the EOM to generate a comb of frequencies, it was decided that modulation depths of ~1 rad be used (around twice the depths used in previous work [4]). Figure 5.3 shows a series of traces taken from the OSA at various stages in the comb generation process. With the EOM initially switched off, a single near-degenerate signal and idler mode pair were observed on the OSA (trace **a**). On driving the EOM at the optimum modulation frequency, spectral broadening of the signal and idler was immediately apparent (trace **b**) due to the transfer of fundamental power into sidebands. The next step was to move the signal and idler modes towards 1600nm by increasing the cavity length with the PZT. After a 50nm increase, the signal and idler modes had each moved by ~15nm and broadened further (trace **c**). Another increase of 50nm saw the signal and idler branches begin to merge (trace **d**) characterised by intensity fluctuations at the degenerate wavelength of 1600nm. A final small increase of the cavity length caused the two branches to lock together in a comb spanning

5. Comb Generation in a Dispersive Cavity

approximately 25nm, equivalent to 3 THz (trace e). If the EOM was subsequently switched off whilst a comb was formed, then the output of the FCG reverted back to a near-degenerate signal and idler mode pair (trace f), similar to that observed in trace a.

a.

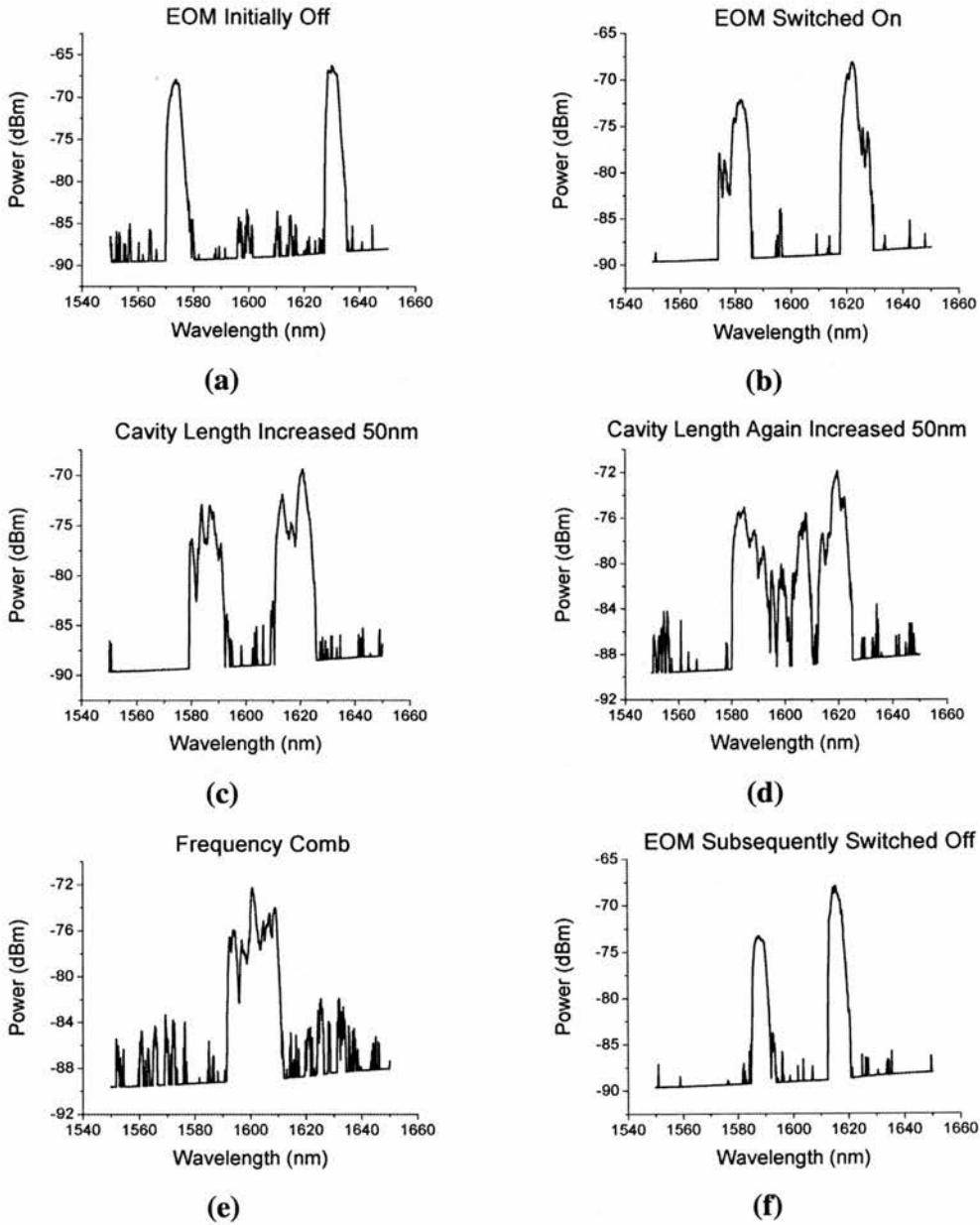


Figure 5.3 – OSA traces of comb generation process

Whilst the spectral extent of the FCG output was being recorded on the OSA, the beat frequencies between modes in the comb were simultaneously detected by the fast

5. Comb Generation in a Dispersive Cavity

photodiode and observed on the RFSA. Figure 5.4 shows images of the RFSA screen taken at the same time as the OSA traces in figure 5.3 were recorded.

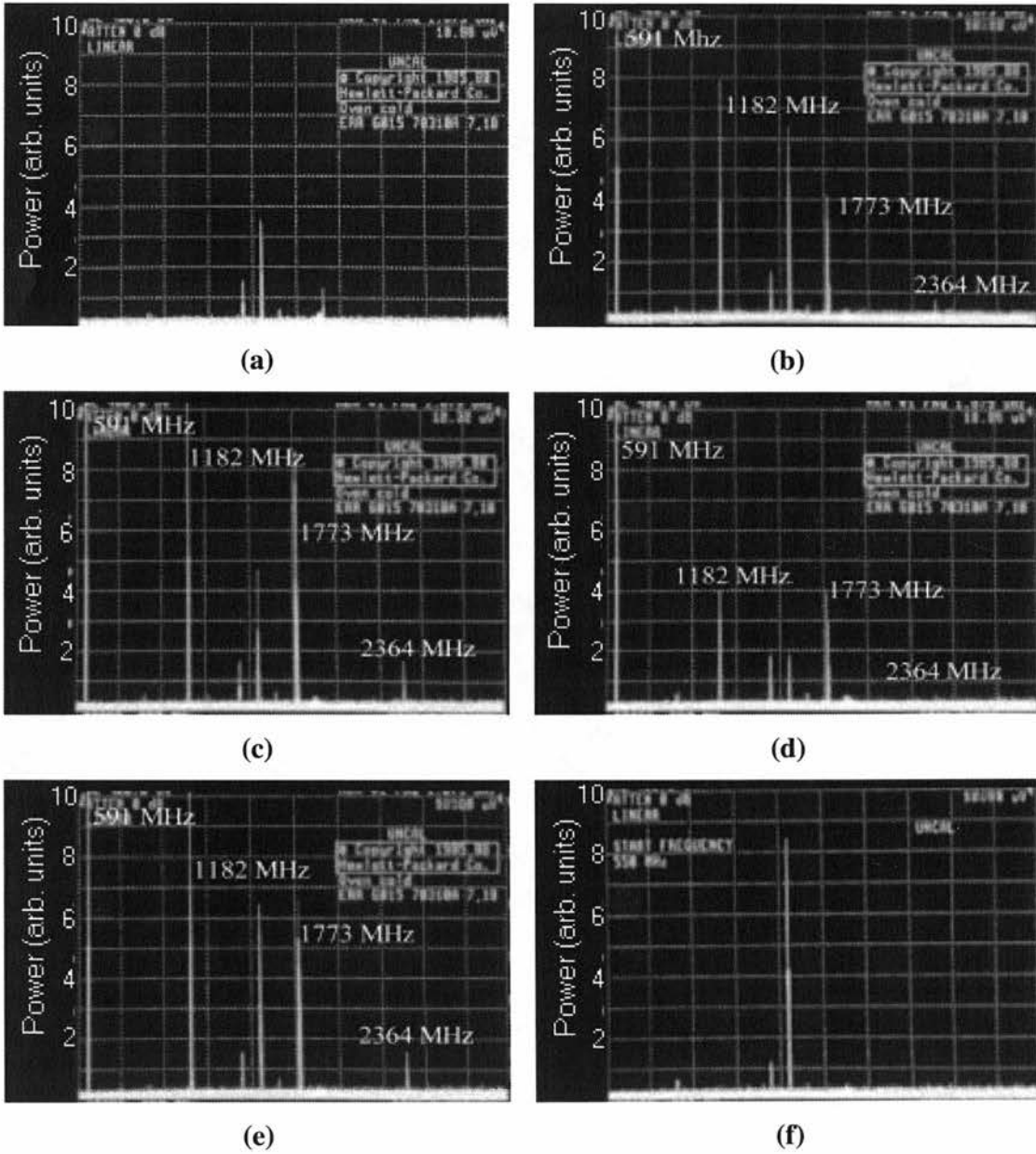


Figure 5.4 – RFSA images of comb generation process

In the first image, taken when the EOM was initially off, no beat frequencies are present, as was expected. Incidentally, the frequencies displayed in this image, which also appear in every subsequent image, correspond to an unknown source of external

5. Comb Generation in a Dispersive Cavity

interference. In images **b-e**, where the EOM was being driven, beat frequencies up to the 4th harmonic were observed and are indicated. Higher harmonics were unfortunately above the upper range of the RFSA. Fluctuations in the strength of the four harmonics can be seen across the images. However, the beat frequencies are strongest in image **e**. This corresponds to the locking of the signal and idler modes into a frequency comb, as shown by figure 5.3, trace **e**. Image **f** confirms that no beat frequencies were present and the OPO was operating on a single mode pair when the EOM was switched off during comb generation.

The frequency comb in figure 5.3 shows some undesirable intensity fluctuations. Unfortunately, this was a symptom of a general lack of stability. As well as fluctuating in intensity, the comb width was observed to change over repeated attempts. Combs spanning up to 60nm (7 THz) were generated on at least one occasion. The problem with stability also reduced the lifetime of the comb to minutes at most. After this time, it would invariably split into signal and idler branches similar to that shown in figure 5.3, traces **b & c**.

An examination of the trouble with stability and the overall issue of dispersion in the FCG cavity will take place in section 5.4 and subsequent chapters. On a more positive note, the maximum observed comb width of 60nm is in very good agreement with the theoretical prediction at 1600nm (see section 5.1). This is significantly larger than previous examples of comb generation with an active medium (chapter 2, section 2.4) and comparable to many of combs generated in a passive cavity (also see chapter 2, section 2.3). However, passive cavity combs suffer from an exponential decay in power across their width. In contrast, the comb in figure 5.3e shows no exponential decay and a maximum power difference of 10dBm, with a sudden cut-off attributed to intra-cavity dispersion. The detection of strong beat frequencies at several harmonics of the modulation frequency suggests that the comb contains 5000 to 10,000 phase-locked modes, depending on the exact width.

5.3) Experimental Comb Generation 2 (Optimum Pumping Level)

The proof-of-principle comb generation experiments described in the previous section were performed before any optimisation of the OPO had taken place. Consequently,

5. Comb Generation in a Dispersive Cavity

the results were obtained for the maximum available pump power of $\sim 500\text{mW}$. Such a pumping level is far too high, given that the aim of this project was to develop an efficient, low power device suitable for pumping by a laser diode. At the conclusion of the optimisation experiments described in chapter 4, section 4.6, the optimum pumping level was found to be 120mW – around three times above threshold. With the aims of the project in mind, the next logical step was to attempt comb generation at the optimum pump power.

Due to various minor adjustments to the FCG cavity, the required modulation frequency had changed to 593 MHz . At this point the EOM had also been fully calibrated, allowing a modulation depth of $\sim 0.5\text{ rad}$ to be used. With these settings, a similar procedure to that used for the proof-of-principle experiments (section 5.2) was undertaken. Unfortunately, the OSA traces observed in the previous experiments could not be replicated. In particular, great difficulty was experienced in tuning the signal and idler modes to 1600nm using the PZT. This was characterised by a sudden drop in output power and fairly wild fluctuations visible on the OSA, after which the OPO would hop to a position away from degeneracy.

As in the first set of experiments, the beat frequencies were simultaneously observed using the fast photodiode and RFSA. Figure 5.5 shows two plots taken from the RFSA. In plot **a** the EOM is switched off, and in plot **b** the OPO is tuned close to degeneracy and the EOM driven at 593 MHz .

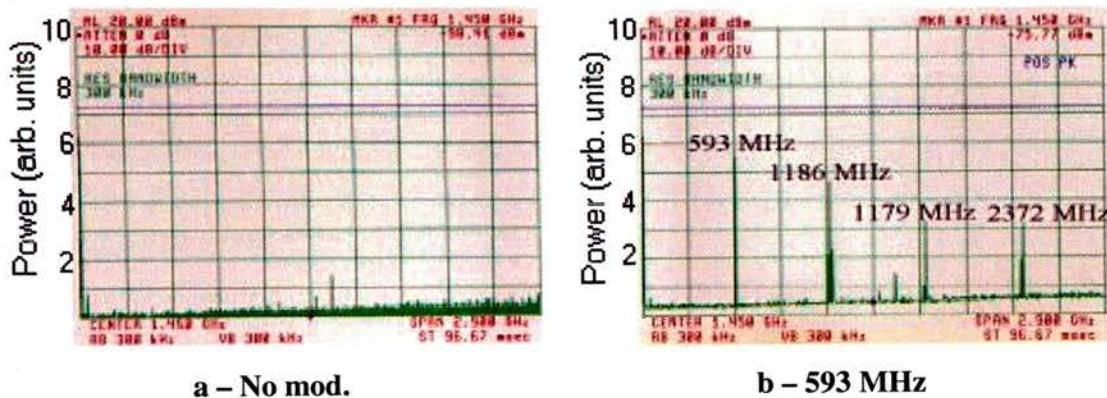


Figure 5.5 – Plots from RFSA

With the EOM off, there were no beat frequencies and the frequencies appearing on the plot are again due to external interference. With the EOM being driven, however,

5. Comb Generation in a Dispersive Cavity

strong beat frequencies up to the 4th harmonic were observed, as indicated on the second plot. This picture is very similar to the RFSA images of figure 5.4, taken from the proof-of-principle experiments (where a frequency comb was generated).

In the hope of resolving the conflict between the OSA and RFSA results, the beat frequencies were examined further. The modulation frequency was increased to 623 MHz and the EOM driven at the same modulation depth. The resulting RFSA plot is shown in figure 5.6.

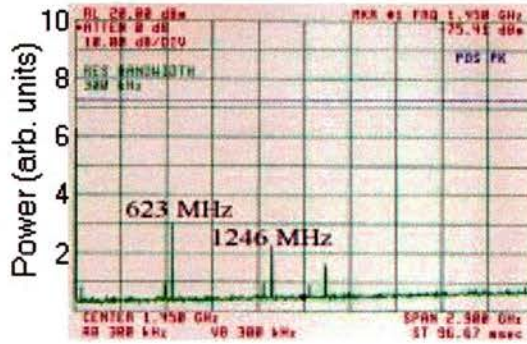


Figure 5.6 – RFSA plot at 623 MHz

A comparison of figures 5.5 and 5.6 shows that, at a modulation frequency of 623 MHz, only the first and second harmonic were observed, with significantly reduced amplitudes. This was further reinforced by narrowing the RFSA frequency span to only look at the first harmonic in each case, as in figure 5.7.

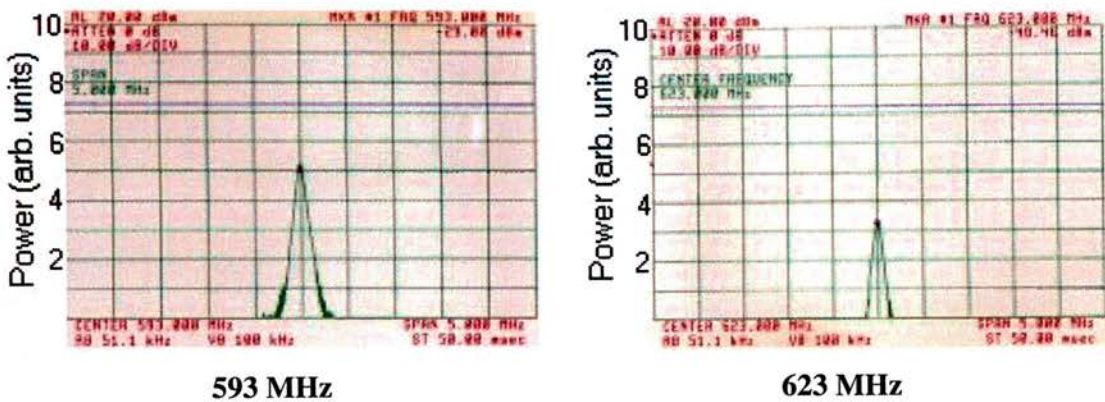


Figure 5.7 – Fundamental beat frequency at 593 MHz and 623 MHz

5. Comb Generation in a Dispersive Cavity

Figures 5.6 and 5.7 clearly show that increasing the modulation frequency to 623 MHz reduced both the strength and number of the harmonics of the beat frequency. In the context of frequency comb generation this makes sense. Moving the modulation frequency away from the cavity FSR will lessen the overlap between generated sidebands and cavity modes. This will cause a corresponding reduction in the power transferred into adjacent cavity modes. The overall effect will be a decrease in the number of phase-locked modes and hence, the strength of the beat frequencies.

Unfortunately, the examination of the beat frequencies has not proved very successful in resolving the conflicting OSA and RFSA results. At the very least, the beat frequencies seem to show that spectral broadening was occurring at the signal and idler modes. However, the resulting branches could not be merged at 1600nm to form a comb of frequencies. An explanation is therefore required, that can account for these observations and the proof-of-principle results. The key to this explanation lies with dispersion in the intra-cavity media.

5.4) Problems with a Dispersive Cavity

The issue of dispersion in relation to the limits placed on frequency comb widths has already been touched on in chapter 2, section 2.4 and section 5.1 of this chapter. Dispersion is also a major factor in determining the tuning behaviour of doubly-resonant oscillators, the class of OPOs to which the device described in this thesis belongs. A large body of theoretical and experimental work has been produced on the subject, for cases where the OPO is both near and non-degenerate [2, 5-8].

To describe the tuning behaviour of any OPO, it is necessary to find the signal and idler mode pair on which the OPO operates for a given set of parameters. The effect on this operating point due to a change in one of these parameters e.g. pump frequency, crystal temperature, cavity length will then show how the OPO tunes. The allowed signal and idler frequencies are always governed by the conservation of energy. In the absence of any other constraints, phasematching (conservation of momentum) will determine the signal and idler mode pair with the lowest threshold. However, in the case of a DRO two further restrictions are placed on the signal and idler frequencies. To resonate in the cavity, both signal and idler modes must correspond to longitudinal modes. These four constraints and the relevant equations

5. Comb Generation in a Dispersive Cavity

for the signal/idler frequencies are summarised in table 5.1. Subscripts refer to quantities relating specifically to the pump (p), signal (s) and idler (i) i.e. frequency (ν), refractive index (n), mode number (m) and optical length of cavity (L).

Constraint	Related Equation
Energy Conservation	$\nu_p = \nu_s + \nu_i$
Phasematching	$\Delta k = \frac{2\pi}{c} [n_s \nu_s + n_i \nu_i - n_p \nu_p] = 0$
Signal Resonance	$\nu_s = \frac{m_s c}{2L_s}$
Idler Resonance	$\nu_i = \frac{m_i c}{2L_i}$

Table 5.1 – Constraints on signal & idler frequencies for DRO

Normally, it is impossible to satisfy all four of the DRO constraints simultaneously. Since energy conservation cannot be violated, the oscillating signal and idler mode pair will generally be detuned from the cavity mode frequencies and, in addition, may experience non-perfect phasematching ($\Delta k \neq 0$). This is best illustrated by a ‘vernier scale’ diagram, first used by Giordmaine and Miller [9].

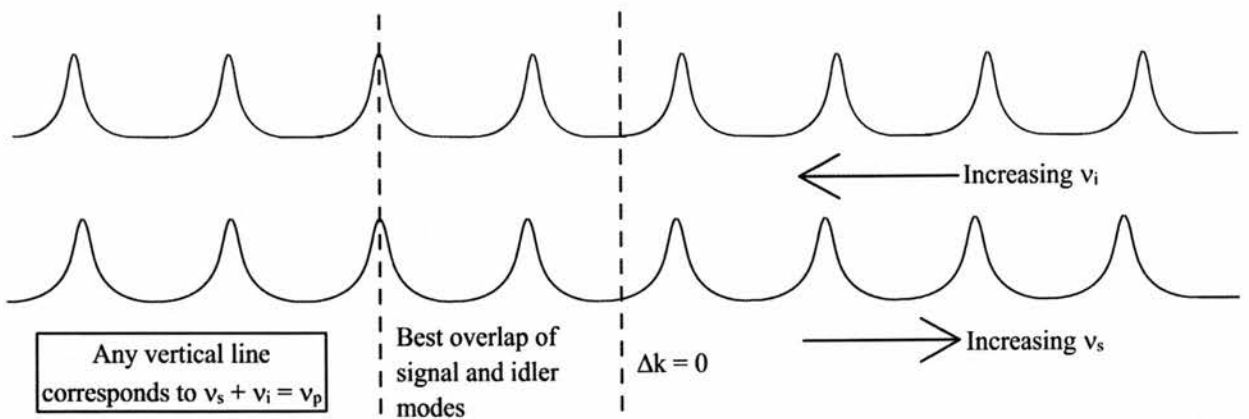


Figure 5.8 – ‘Vernier scale’ diagram of signal and idler cavity modes

In figure 5.8, the resonant signal (bottom) and idler (top) modes are shown. The frequency scales increase in opposite directions, such that any vertical line gives the

5. Comb Generation in a Dispersive Cavity

signal and idler frequencies that satisfy energy conservation. Due to dispersion in the intra-cavity media, the intermode spacing is different for the signal and idler modes. To satisfy the energy conservation and resonance constraints, a signal mode must overlap with an idler mode in the vernier scale diagram. As shown by figure 5.8, this is not the case for the majority of the modes. Of the cavity modes that do overlap, the corresponding oscillation frequencies will be those that satisfy energy conservation (denoted by vertical line through the centre of the overlap region on the diagram). Hence, ν_s and ν_i will be detuned from the cavity mode frequencies. The mode pair with the closest alignment will experience the least detuning and hence the lowest threshold. This will be the signal and idler frequencies at which the DRO operates. Note that the mode pair with the best overlap does not necessarily lie at $\Delta k = 0$ (corresponding to degeneracy for the system under discussion), resulting in a detuning from the perfect phasematching condition.

The vernier scale diagram shows the mode pair that the DRO will operate on in the steady-state. A perturbation to the DRO will affect the diagram in one of two ways. A change in either the temperature of the intra-cavity media or the cavity length will alter the position and spacing of the modes relative to the frequency scale, which remains fixed. If, on the other hand, the pump frequency is changed then one frequency scale (signal or idler) will shift relative to the other, whilst the position and spacing of the modes on the scale are unaffected. In either case, the perturbation will result in a different pair of modes having the best overlap, shifting the oscillating signal and idler frequencies. A closer inspection of figure 5.8 shows that the modes around the pair with the best overlap have an overlap that is only slightly worse. Such mode pairs are grouped into a cluster. If, after the perturbation, the new oscillating modes are in the same cluster as the previous pair, then the DRO is said to have undergone a *mode hop*. A *cluster hop* is characterised by a shift to a pair of modes in a different cluster, usually accompanied by a large change in oscillation frequencies. For more on mode hopping and cluster hopping in a DRO, see Lindsay et al [10] and the PhD thesis by the same author [11].

It should be noted that mode and cluster hopping occur because of the difference in intermode spacing between the signal and idler modes, which is a direct result of dispersion in the intra-cavity media. The previous discussion on the tuning behaviour of a DRO leads to a possible explanation of the difficulties with the optimum

5. Comb Generation in a Dispersive Cavity

pumping experiments and the apparent success of the proof-of-principle experiments. It seems likely that perturbations to the comb generator in the form of cavity length fluctuations and, to a lesser extent, temperature variations caused the output to shift away from degeneracy in the form of a cluster hop. It is also likely that another factor, such as one of the optical coatings on the mirrors or intra-cavity elements, acted to discriminate against oscillation at degeneracy. When combined, these factors made it impossible for the signal and idler branches to be merged at 1600nm in the optimum pumping experiments. Credence is led to this theory by the fact that the removal of air currents and as many sources of vibration as possible greatly improved the stability of the system in the proof-of-principle experiments. However, in these experiments the signal and idler branches were successfully merged at 1600nm to form a comb, which must also be explained by this theory.

Looking back to the proof-of-principle experiments, the main difference to the optimum pumping experiments (apart from the pump power) was the modulation depth used – over 1 rad compared to a maximum of 0.5 rad for the latter. This resulted in a significantly larger transfer of power into the sidebands, large enough to override the push for a cluster hop. Hence, it was possible to merge the signal and idler branches. Even so, the instability of the subsequent comb and reversion to separate signal and idler branches shows that this override was only temporary. Of course, the larger modulation depth also caused a greater loss to the central signal and idler modes. However, in the proof-of-principle experiments the OPO was being operated at over ten times threshold, providing enough gain to overcome the loss.

There is also the matter of the beat frequencies observed during the optimum pumping experiments. They suggest that the signal and idler branches similar to those in traces **b** and **c** of figure 5.3 were being created and the problem lay in trying to merge these branches at degeneracy. This fits with the dispersion-related explanation given above. With the problems due to dispersion in the FCG cavity now apparent, both in terms of the limit to the generated comb width and the spectral instability of the OPO, it was decided that the dispersion issue should be explored further. The next chapter will look at the origin and magnitude of dispersion in the current comb generation system and potential methods to compensate for it.

5. Comb Generation in a Dispersive Cavity

5.5) Experimental Comb Generation 3 (Uncompensated)

Originally, the previous section was to be the last in this chapter. However, results that were obtained during the dispersion compensation experiments (see chapters 6 and 7) have necessitated the inclusion of this final section. These results were taken with the cavity design for the implementation of dispersion compensation (chapter 7, section 7.1) but without any actual compensation in place. As before, a modulation depth of around 0.5 rad was used and, due to an increase in the cavity length with the new design, the required modulation frequency was found to be around 522.05 MHz. As in figure 5.3 previously, figure 5.8 overleaf shows the various stages of the comb generation process.

5. Comb Generation in a Dispersive Cavity

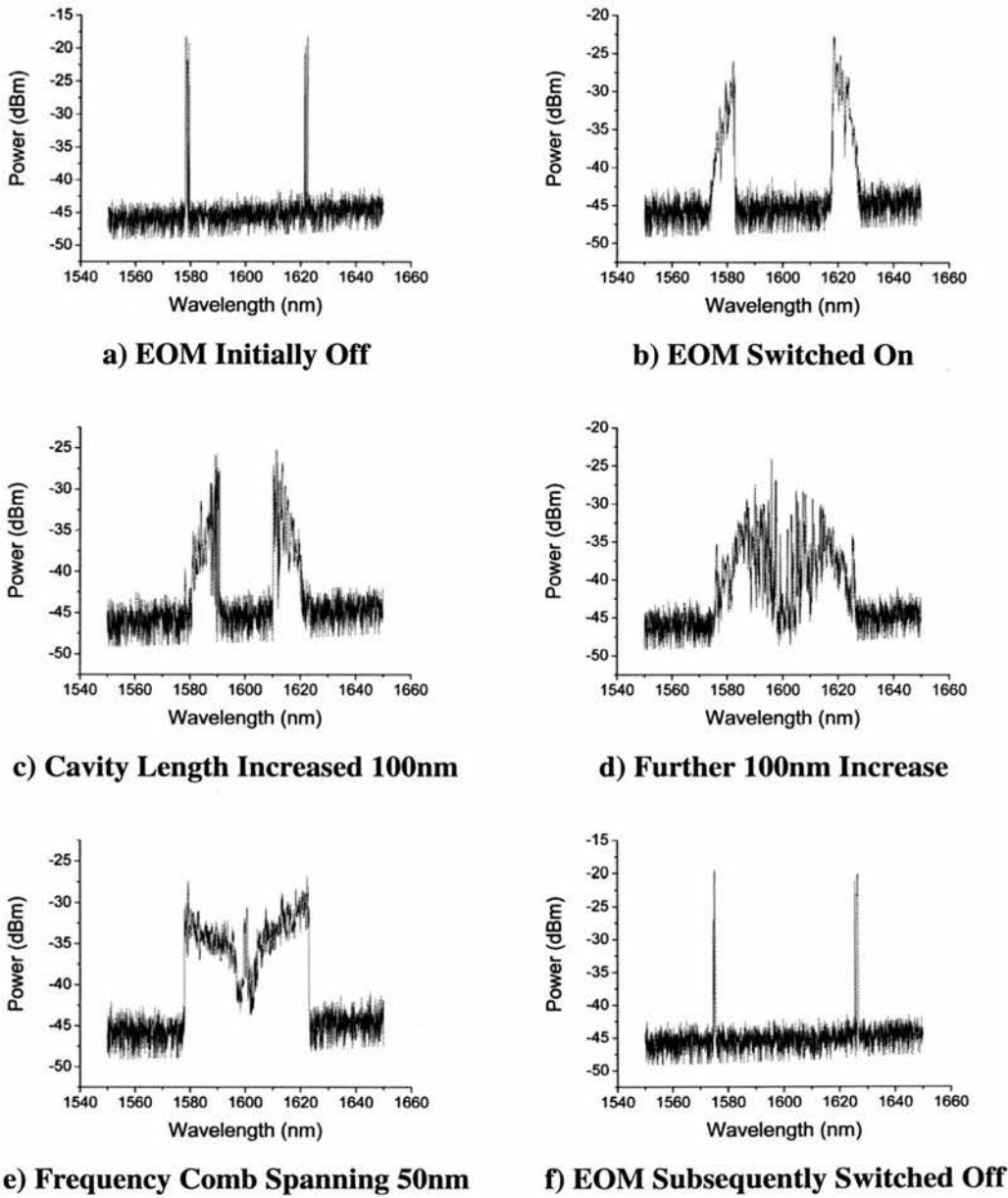


Figure 5.8 – OSA traces of comb generation process

The six traces above were all taken from the OSA with a resolution bandwidth of 0.5nm (significantly smaller than in figure 5.3) to show as much fine detail as possible. The similarities with previous results are clear to see. When the EOM was switched off before and after the comb was generated, the OPO operated on a single near-degenerate signal and idler mode pair (traces **a** and **f**). As soon as the EOM was driven at the required modulation frequency, significant spectral broadening was observed at the signal and idler (trace **b**). Traces **c** and **d** show an increase in

5. Comb Generation in a Dispersive Cavity

broadening and a merging of the signal and idler branches at degeneracy following two consecutive increases in the cavity length by 100nm. A final small increase in the cavity length resulted in trace e, a frequency comb spanning approximately 50nm. Across the comb, the overall decrease in power is less than 15dBm, although a significant drop does occur close to degeneracy. The exact cause of this drop is not known, but one possible explanation is a decrease in the reflectivity or transmission of an optical coating (mirror or intra-cavity surface) at the points where the drop occurs. An examination of the FCG output in the RF region was also undertaken. In this case however, particular attention was paid to the fundamental beat frequency and, specifically, its behaviour as the modulation frequency was altered. These results are summarised in figure 5.9.

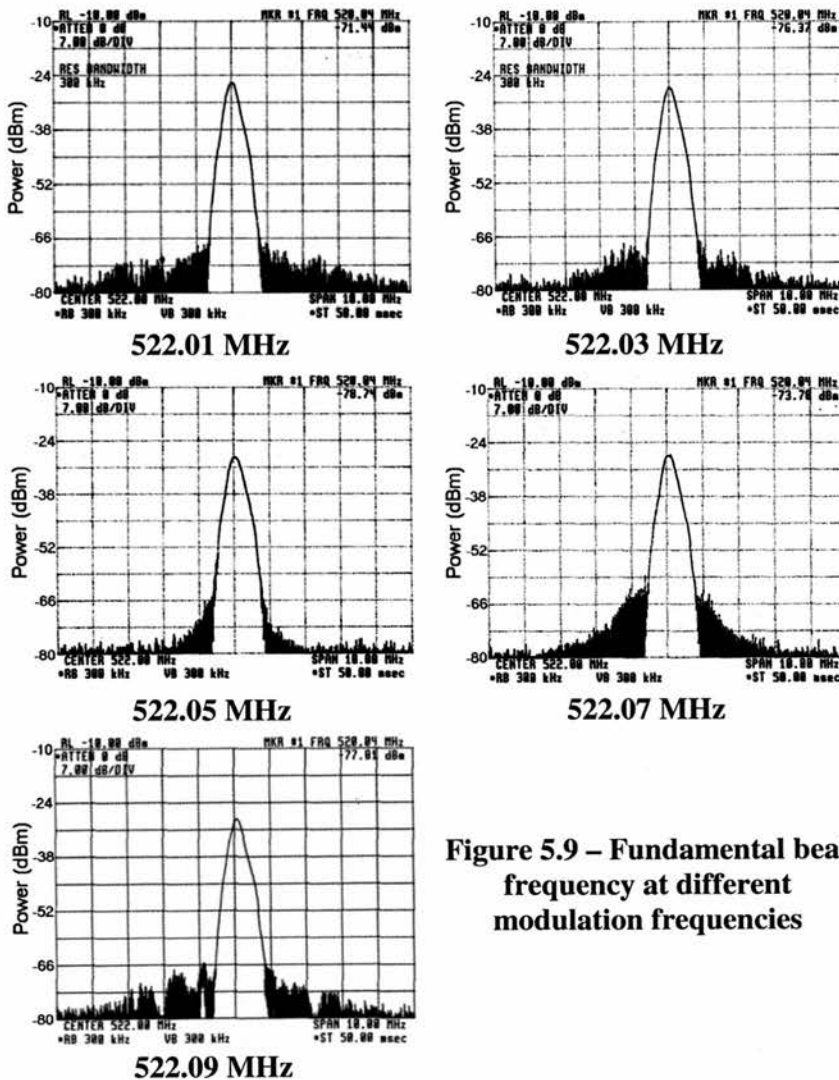


Figure 5.9 – Fundamental beat frequency at different modulation frequencies

5. Comb Generation in a Dispersive Cavity

The pictures above were taken with a resolution bandwidth of 300 kHz and a 10 MHz span. As the modulation frequency was increased in steps of 20 kHz the line profile of the beat frequency remained unchanged. However, as figure 5.9 shows, the noise at the wings of the beat frequency became progressively quieter as the modulation frequency approached the cavity FSR (522.05 MHz). With further increase of the modulation frequency beyond this point, the noise is shown to increase again. The results for a significantly larger change in modulation frequency (1 MHz) are shown in figure 5.10.

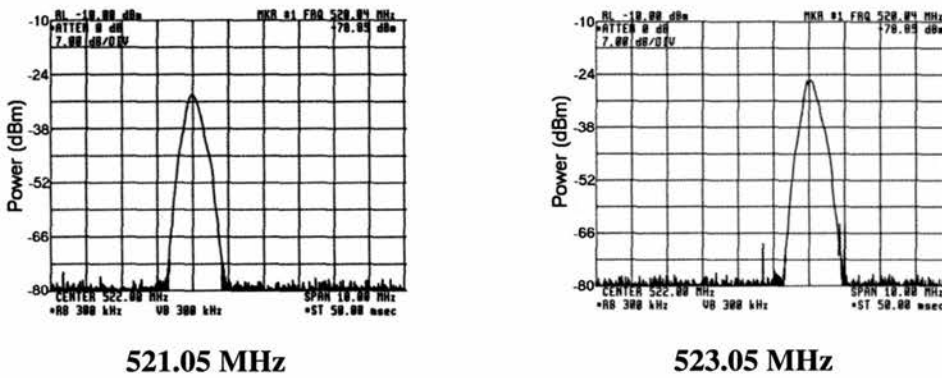


Figure 5.10 – Fundamental beat frequency at modulation frequency ± 1 MHz

In the above beat frequency traces, the noise level appears to have dropped significantly, right down to the noise floor of the RFSA. Given the traces of figure 5.9, this seems paradoxical at first. However, an explanation can be found by considering the transfer of power between sidebands and cavity modes during the comb generation process. If there is a small mismatch between the modulation frequency and cavity FSR, then most of the sideband power will still be transferred into a cavity mode. In the RF region, this manifests as the fundamental beat frequency. However, due to the mismatch a fraction of the sideband power will not be transferred into a cavity mode. This power will beat with adjacent cavity modes, creating the noise observed at the wings of the beat frequency. As the mismatch is increased, less and less sideband power is transferred into a cavity mode, increasing the noise level. However, if the mismatch is above a certain value there will not be enough overlap between sideband and cavity mode to transfer any power. In this case the fundamental beat frequency is purely due to the mixing between the central

5. Comb Generation in a Dispersive Cavity

signal/idler frequency and the first sidebands. Hence, no noise is observed at the wings of the beat frequency. In the results above, this explanation was confirmed by the OSA trace, which showed no broadening of the signal and idler when the modulation frequency was changed by 1 MHz.

By simultaneously observing the beat frequency noise and the signal and idler on the OSA, it was possible to estimate the range of modulation frequencies over which comb generation would occur. This was found to be approximately 200 kHz, centred on the optimum modulation frequency of 522.05 MHz. Beyond this point, broadening of the signal and idler was significantly reduced and consisted of individual modes rather than the branches shown in figure 5.8, trace **b**.

A comparison of figures 5.3 and 5.8 shows that the comb generation in the latter looks significantly better. This cannot be entirely due the decrease in the resolution bandwidth of the OSA. When obtaining the results in this section, it was discovered that the spatial profile of the signal and idler beam within the FCG cavity played a crucial role. Quite simply, a good approximation to TEM₀₀ was required to achieve comb generation. With operation on a higher order spatial mode, the effects shown in figures 5.8 – 5.10 could not be repeated. This is illustrated by figure 5.11 below.

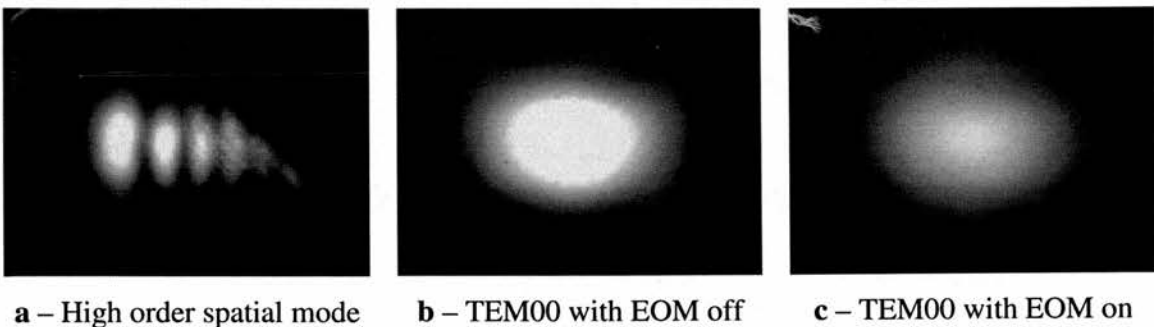


Figure 5.11 – Signal/Idler beam profile of OPO-FCG

Picture **a** shows a typical high order spatial profile, where no comb generation could be achieved. Also noticeable with this profile was a decrease in the output power of the OPO-FCG, possibly due to clipping of the spatially extended transverse mode within the EOM. Pictures **b** and **c** show the good approximation to TEM₀₀ required to generate a frequency comb. Also emphasised is the immunity of the spatial profile to modulation of the signal/idler field. As shown by figure 5.11, switching on the EOM caused a reduction the signal/idler power, but did not alter the spatial profile.

5. Comb Generation in a Dispersive Cavity

To achieve the TEM₀₀ modes shown above, careful alignment between the two intra-cavity lenses was required. This necessitated adjustment of the second lens (just before the EOM – see figure 7.4) on a micron scale in all 3 dimensions, followed by adjustment to the EOM position and the plane output coupler (M2).

An explanation for the effect of the transverse beam profile lies with the fact that the required modulation frequency could not be accurately predicted for a higher order spatial mode, particularly since the structure of this mode was liable to change. There is also the question of how well the EOM could work for a beam that was not TEM₀₀, given the small input aperture and requirement for a well-collimated beam through the modulator crystal.

Unfortunately, the spatial profile of the signal and idler was overlooked when performing the original comb generation experiments. In light of the results in this section, there is now a strong suspicion that the beam profile had a part to play in causing the problems that were encountered in the original experiments. It should be noted here that some of these problems were encountered in the latest comb generation experiments too, such as the varying comb width and power fluctuations. In particular, the frequency comb only tended to last for about a minute before returning to the signal and idler branches away from degeneracy. In the last section, this behaviour was explained by cluster hopping, which is a consequence of dispersion within the cavity of a DRO. Therefore, it is clear that dispersion is still a major issue, even if the problem with beam profile is negated.

All previous results in this section were taken with a pump power of around 600mW, many times the recorded threshold of ~35mW. To complete this set of experiments, comb generation was attempted at the optimum pumping level of ~150mW (see chapter 4, section 4.6). The same modulation depth as in previous experiments was used and care was taken to ensure a TEM₀₀ spatial mode. Figure 5.12 shows the spectral output that was observed on the OSA.

5. Comb Generation in a Dispersive Cavity

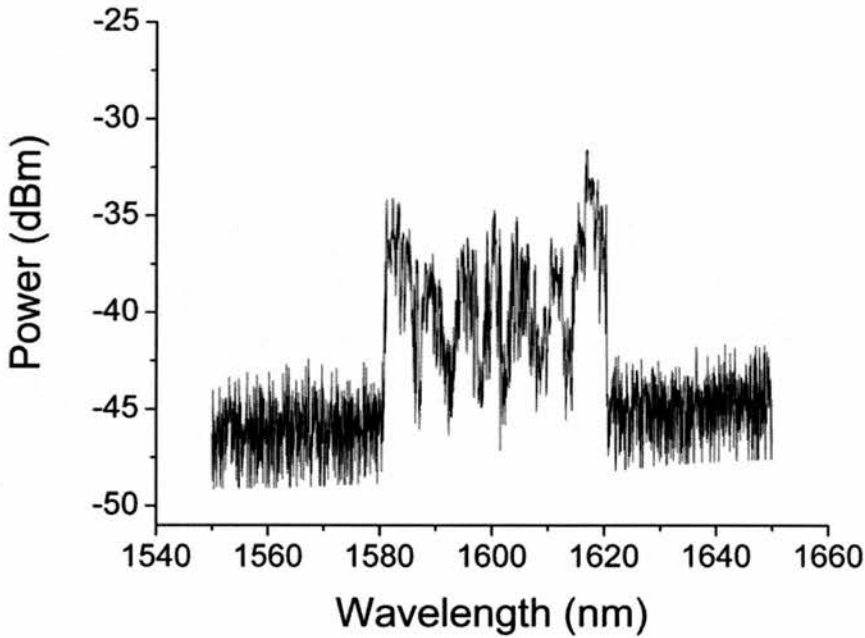


Figure 5.12 – Comb generation at optimum pumping level

The comb generated at the optimum pumping level was observed to span around 40nm, which is comparable to previous experiments. Whilst the overall power in the comb was reduced, fluctuations in power across the comb bandwidth covered less than 15dBm. The problems with comb lifetime and varying width were also encountered here. It should be noted that it was quite difficult to achieve a stable comb at the optimum pumping level, with fine control of the signal/idler cavity length required. To improve the comb shown in figure 5.12, with regard to increasing the power level and fluctuations, the problems with stability and beam profile must be addressed. The most obvious solution is to redesign the OPO-FCG resonator and this is discussed in the section on *future work* in chapter 8.

The results in this final section have shown that frequency combs spanning 50nm or more were consistently achieved in the uncompensated FCG. These comb widths are in good agreement with the theoretical predictions discussed in section 5.1. Whilst the issue of the spatial profile of the signal/idler was raised by these results, the problems with stability and power fluctuation suggest that dispersion was still an important factor.

5.6) Chapter Summary

This chapter describes three sets of comb generation experiments. The first set took place before the OPO was optimised and aimed to show that comb generation was possible with the current system. The second set were performed at the optimum pumping level determined by the optimisation experiments and aimed to show that comb generation was feasible at this level (and therefore feasible in a diode-pumped system). The final set were obtained from the uncompensated FCG before dispersion compensation was implemented.

Prior to the experimental work, modelling of the dispersion-limited comb width was undertaken. Two types of intra-cavity media were considered, periodically poled LiNbO_3 and $\text{MgO}:\text{LiNbO}_3$ (the two candidates for the nonlinear crystal, discussed in chapter 4). The model suggested that for a fixed temperature of 180°C , LiNbO_3 would give a comb width of around 7 THz (60nm) - slightly higher than $\text{MgO}:\text{LiNbO}_3$. Further modelling showed that by reducing the crystal temperature, the maximum comb width could be increased.

In the first set of comb generation experiments, the output from the FCG was observed on an OSA and an RFSA. This allowed both the full spectrum of the comb and beat frequencies between individual modes to be measured. A detailed analysis of the beat frequencies over a range of modulation frequencies gave the modulation frequency that was the closest match to the cavity FSR. With this known, comb generation could begin.

After switching on the EOM, harmonics of the beat frequency were observed over the full range of the RFSA and spectral broadening of the signal and idler was apparent on the OSA. By increasing the cavity length with a PZT attached to the output coupler, the signal and idler branches were brought together at 1600nm and merged to form a comb of frequencies. Throughout this procedure, the harmonics of the beat frequency were always present. Unfortunately, the comb was not very stable and only lasted for a few minutes before reverting to separate signal and idler branches. The comb width was also seen to vary, with bandwidths of up to 60nm observed on more than one occasion.

For comb generation at the optimum pumping level, the aim was to repeat the results of the first experiments. Unfortunately, this could not be achieved on the OSA.

5. Comb Generation in a Dispersive Cavity

However, strong harmonics of the beat frequency were observed on the RFSA. A further analysis of these harmonics showed a significant reduction in both strength and number as the modulation frequency was tuned away from the cavity FSR. These results suggested that branches were being formed around the signal and idler modes as before, but the branches could not be merged at degeneracy.

To explain the results of both sets of experiments, it was necessary to look at the effect of dispersion on the spectral output of the OPO. In the current system, which is effectively a DRO, the requirement that both signal and idler be resonant places extra constraints on the device. This can be represented by overlapping the signal and idler cavity modes on a 'vernier scale' diagram, such that a vertical line corresponds to energy conservation. Modes that overlap will then satisfy both the resonance and energy conservation conditions. Dispersion causes the intermode spacing to vary across the spectrum of signal and idler modes. As a result, only a few mode pairs will show a significant overlap on the vernier scale diagram. The pair with the closest alignment and hence lowest threshold will oscillate in the cavity. A perturbation to the DRO, in the form of a change in the pump frequency or a change to the signal/idler cavity, will cause the mode positions to change on the vernier scale. As a result, a different mode pair will come into alignment and the DRO will oscillate on this pair instead. Depending on the relative positions of the original and new mode pairs, this is known as either a mode hop or a cluster hop. The latter is characterised by a large shift in the signal and idler frequency.

It seems likely that cluster hopping was behind the difficulty in creating a comb of frequencies at the optimum pumping level. On reaching 1600nm, a perturbation to the signal/idler cavity (vibration or temperature change) caused the OPO to cluster hop away from degeneracy. The fact that this did not happen in the first proof-of-principle experiments was down to the use of a much larger modulation depth than in the optimum pumping experiments. This transferred enough power into adjacent cavity modes to prevent a cluster hop from occurring whilst the comb was forming.

After the comb generation experiments had taken place, it became clear that dispersion was a key factor in limiting both the width of the generated comb and the spectral stability of the OPO. Therefore, the next stage of the project was to closely examine dispersion in the signal/idler cavity and determine a method to compensate for it.

5. Comb Generation in a Dispersive Cavity

The final section of this chapter is effectively an addendum, since it details results that were taken a significant time after the first two sets. These experiments attempted to generate a comb of frequencies in the modified cavity described in chapter 7, before dispersion compensation was implemented. A comb spanning 50nm was generated at 1600nm, but only after ensuring that the spatial mode of the signal/idler was close to TEM₀₀. Thus, the spatial profile of the downconverted waves was found to be an important factor that had not been considered in previous experiments. An examination of the comb in the RF regime showed that the noise in the wings of the fundamental beat frequency decreased as the modulation frequency approached the cavity FSR. However, beyond a certain frequency mismatch no noise was visible. This could be explained by considering the overlap of sideband and cavity mode as the modulation frequency was altered.

To finish these experiments, comb generation was attempted at the optimum pump power of ~150mW. This produced a comb spanning 40nm with power fluctuations under 15dBm across its width. However, as with earlier experiments, the lifetime of the comb was short, with a tendency to drift into separate signal and idler branches. This suggested that dispersion was still an issue to be contended with.

References

1. Kourogi, M., et al., *Limit of Optical-Frequency Comb Generation Due to Material Dispersion*. IEEE Journal of Quantum Electronics, 1995. **31**(12): p. 2120-2126.
2. Eckardt, R.C., et al., *Optical Parametric Oscillator Frequency Tuning and Control*. Journal of the optical Society of America B - Optical Physics, 1991. **8**(3): p. 647-667.
3. Jundt, D.H., *Temperature-Dependent Sellmeier Equation for the Index of Refraction n_e in Congruent Lithium Niobate*. Optics Letters, 1997. **22**: p. 1553.
4. Diddams, S.A., et al., *Broadband Optical Frequency Comb Generation with a Phase-Modulated Parametric Oscillator*. Optics Letters, 1999. **24**(23): p. 1747-1749.

5. Comb Generation in a Dispersive Cavity

5. Colville, F.G., et al., *Smooth Frequency Tuning from Optical Parametric Oscillators*. OSA Proceedings on Advanced Solid-State Lasers, ed. T.Y. Fan and B.H.T. Chai. Vol. 20. 1994.
6. Henderson, A.J., et al., *Continuous Frequency Tuning of a CW Optical Parametric Oscillator through Tuning of its Pump Source*. Optics Letters, 1995. **20**(9): p. 1029 - 1031.
7. Henderson, A.J., et al., *Doubly-Resonant Optical Parametric Oscillators: Tuning Behaviour and Stability Requirements*. Opt. Comm., 1995. **119**: p. 256.
8. Padgett, M.J., et al., *Mode Selection in Doubly-Resonant Optical Parametric Oscillators*. IEEE Journal of Quantum Electronics, 1994. **30**(12): p. 2979-2985.
9. Giordmaine, J.A. and Miller, R.C., eds. *Optical Parametric Oscillation in LiNbO₃*. Physics of Quantum Electronics, ed. P.L. Kelley, B. Lax, and P.E. Tannenwald. 1966, McGraw-Hill: New York.
10. Lindsay, I.D., et al. *Cluster Selection in Doubly Resonant OPOs based on Quasi-Phase-Matched Materials*. in *Conference on Lasers and Electro-optics*. 2000. Washington.
11. Lindsay, I.D., *High Spatial and Spectral Quality Diode-Laser-Based Pump Sources for Solid-State Lasers and Optical Parametric Oscillators*, in *Physics & Astronomy*. 1999, University of St Andrews.

Chapter 6

Dispersion Compensation

In the previous chapter, the effects of dispersion on both the width of the generated frequency comb and the spectral stability of the OPO were introduced. In this chapter, dispersion in the current comb generation set-up will be examined in a greater detail, concluding with a discussion of possible compensation schemes. Dispersion is a material property and is defined as the dependence of the refractive index on the frequency of incident light i.e. $n(\nu) / n(\omega)$. Its root cause lies in the electric polarisation induced in a material when light is incident upon it. To see how this arises, consider the classical picture of an atom in figure 6.1, consisting of a heavy nucleus connected to a light electron by a spring.

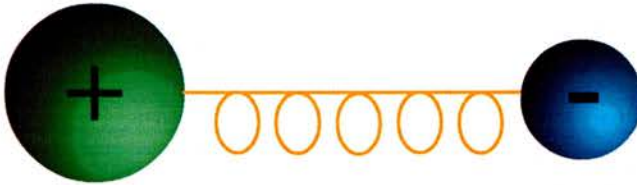


Figure 6.1 – Classical ‘atom on a spring’

Assuming that, for a small displacement x , the restoring force is proportional to the displacement ($F = -kx$) and that the incident light wave has a harmonic form with frequency ω , the equation of motion for the atom under illumination is:

$$eE_0 \cos \omega t - m_e \omega_0^2 x = m_e \frac{d^2 x}{dt^2} \quad (6.1)$$

Here, e is the electronic charge, m_e the mass of an electron and ω_0 is the resonant frequency of the electron-nucleus system. Equation (6.1) represents a driven harmonic oscillator, with the second term on the left representing the restoring force. It is assumed that the frequency of the incident field is far away from absorption bands

6. Dispersion Compensation

within the material and hence damping terms can be neglected. From experience, solutions to this type of equation are of the form

$$x(t) = x_0 \cos \omega t \quad (6.2)$$

By substituting equation (6.2) into equation (6.1) and utilising the fact that the induced polarisation is related to the displacement by $P = exN$ (N is the number of electrons per unit volume), an expression for the induced polarisation can be derived.

$$P = \frac{e^2 NE}{m_e (\omega_0^2 - \omega^2)} \quad (6.3)$$

E represents the electric field of the incident light, $E_0 \cos \omega t$. The polarisation is related to refractive index via the permittivity of the material as shown in the two equations below.

$$\epsilon = \epsilon_0 + \frac{P(t)}{E(t)} \quad (6.4)$$

$$n^2 = \frac{\epsilon}{\epsilon_0} \quad (6.5)$$

Combining equations (6.3), (6.4) and (6.5) gives the dispersion relation i.e. n as a function of ω .

$$n^2(\omega) = 1 + \frac{Ne^2}{\epsilon_0 m_e} \left(\frac{1}{\omega_0^2 - \omega^2} \right) \quad (6.6)$$

Equation (6.6) is surprisingly similar to the result that arises from a quantum mechanical treatment of the induced polarisation [1, 2], with the relevant equation given below.

$$n^2(\omega) = 1 + \frac{Ne^2}{\epsilon_0 m_e} \sum_j \left(\frac{f_j}{\omega_{0j}^2 - \omega^2} \right) \quad (6.7)$$

In the quantum mechanical treatment, the system consists of j discrete oscillators within the N molecules per unit volume. Each has a distinct ω_{0j} and f_j . Rather than representing a resonant frequency, the ω_{0j} correspond to frequencies at which the

6. Dispersion Compensation

atom will move between energy levels, absorbing or emitting energy in the process. Hence, each f_j (which sum to 1 in total) is the probability that the associated atomic transition will occur.

From equation (6.7), n will increase as ω increases towards a particular ω_{0j} . This is known as *normal dispersion* and occurs between regions of absorption (at which $\omega \sim \omega_{0j}$), where the material will appear transparent. Within the regions of absorption, close to ω_{0j} , n is found to decrease as ω increases. This is called *anomalous dispersion* and is of particular importance when compensating for dispersion in optical systems (see section 6.3).

For a particular material, the exact form of the dispersion relation is usually found experimentally in the form of a Sellmeier equation. This involves adapting a previous equation or proposing an entirely new one and then fitting measured data to the equation over a designated frequency or wavelength range. The measured data is often obtained by use of an optical parametric oscillator or some other nonlinear optical process [3-5]. As might be expected, the resulting equation tends to be quite complex. As an example, equation (6.8) gives the Sellmeier equation for the extraordinary refractive index of congruent lithium niobate (the type used for periodic poling and hence in the system described in this thesis) [6]:

$$n_e^2 = a_1 + b_1 f + \frac{a_2 + b_2 f}{\lambda^2 - (a_3 + b_3 f)^2} + \frac{a_4 + b_4 f}{\lambda^2 - a_5^2} - a_6 \lambda^2 \quad (6.8)$$

Here, f is a temperature parameter given by $f = (T - 24.5^\circ\text{C})(T + 570.82)$ and the constants represented by a_i and b_i are parameters determined by the fitting of experimental data.

Dispersion and its effects have long been an important consideration in the design of ultra-short pulse systems, where pulse durations are typically between ten and several hundred fs [7-9]. Dispersion becomes an issue due to the large spectral bandwidths associated with such pulses. On passing through the intra-cavity media, the variation in refractive index causes different spectral regions of the pulse to travel with different group velocities. This leads to a significant velocity difference between the highest and lowest frequency components and, in the case of normal dispersion, results in a temporal broadening of the pulse.

6. Dispersion Compensation

With the desire to generate shorter and shorter pulses, much theoretical and experimental work has gone into the development of various dispersion compensation schemes. Given the similarities, in spectral terms, between ultra-short pulse generation and frequency comb generation, it seems a good idea to look to the former when discussing dispersion and its compensation in the present FCG system.

6.1) Dispersion in the FCG System

Before examining the various schemes for dispersion compensation, it is necessary to determine the magnitude of dispersion in the FCG cavity. The source of dispersion is the intra-cavity media, consisting of two 20mm crystals of lithium niobate and a small contribution from the fused silica focussing lens. Utilising the Sellmeier equations for these two materials [6, 10], the procedure for calculating dispersion can now be developed.

Looking to the theory behind the effect of dispersion in ultra-short pulse generation [11, 12], the starting point is the group velocity and the phase shift on passing through a medium of length L . These quantities are defined respectively by equations (6.9) and (6.10) below:

$$v_g = \left(\frac{d\omega}{d\beta} \right)_{\beta=\beta_c} \quad (6.9)$$

$$\phi(\omega - \omega_c) = \beta(\omega - \omega_c) L \quad (6.10)$$

Group velocity, v_g , is defined for a pulse of centre frequency, ω_c , and width, $\Delta\omega_c$. The propagation constant, β , is calculated at ω_c . Note also that the phase shift is referenced to the centre frequency of the pulse. The delay between two spectral components of the pulse, ω_1 and ω_2 , after traversing the medium can be derived from equations (6.9) and (6.10) as,

$$\Delta\tau = \phi'(\omega_2) - \phi'(\omega_1) = \phi''(\omega_1) \Delta\omega \quad (6.11)$$

Here, $\Delta\omega = \omega_2 - \omega_1$ and the dashes represent first and second derivatives with respect to ω . To gain some further insight, ϕ can be expanded as a polynomial series about the centre frequency of the pulse:

6. Dispersion Compensation

$$\phi(\omega) = \phi_c + \left(\frac{d\phi}{d\omega} \right)_{\omega_c} (\omega - \omega_c) + \frac{1}{2} \left(\frac{d^2\phi}{d\omega^2} \right)_{\omega_c} (\omega - \omega_c)^2 + \dots \quad (6.12)$$

The first term in the series, ϕ_c , is a measure of the absolute phase accumulated at the centre frequency after passing through the medium. The coefficient of the linear term, $\phi'(\omega_c)$ is known as the group delay. As suggested by equation (6.11), this is the time taken for a spectral component at the centre frequency to propagate through the medium at the associated local group velocity. Whilst neither of these quantities is considered important when designing short pulse systems, the coefficient of the quadratic term, $\phi''(\omega_c)$, proves to be very useful. It is known as the *group delay dispersion (GDD)* and from the definition of ϕ in equation (6.10),

$$\phi''(\omega_1) = L \left(\frac{d^2\beta}{d\omega^2} \right)_{\omega_1} \quad (6.13)$$

The magnitude of the GDD gives the broadening per unit bandwidth of the pulse at ω_1 . A second quantity, the *group velocity dispersion (GVD)*, can also be defined:

$$\begin{aligned} GVD &= \left(\frac{d^2\beta}{d\omega^2} \right)_{\omega_1} = \left(\frac{d \frac{1}{v_g}}{d\omega} \right)_{\omega_1} \\ &= \frac{\phi''(\omega_1)}{L} \end{aligned} \quad (6.14)$$

The magnitude of the GVD gives the broadening per unit length per unit bandwidth and is only applicable in the case of a homogeneous medium. For an inhomogeneous medium or multiple intra-cavity components, the GDD must be used and each component or layer treated separately.

From the above analysis, it seems that the magnitude of dispersion in an optical system is effectively given by the GDD and GVD. This ties in with much of the literature on dispersion compensation schemes, where the magnitude of compensation is given in terms of GDD or GVD (see section 6.3). Figures 6.2 and 6.3, respectively, show the variation of propagation constant and GVD (measured in fs^2/m) with wavelength for lithium niobate.

6. Dispersion Compensation

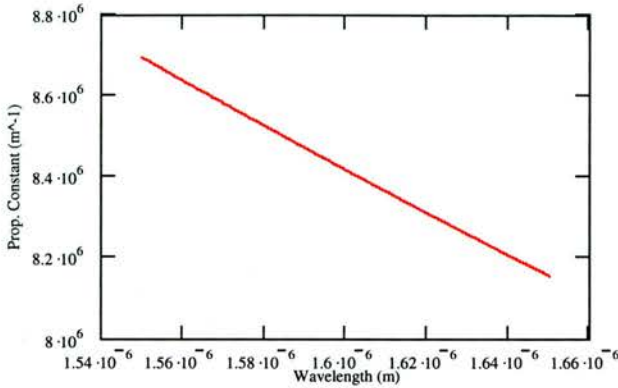


Figure 6.2 – Variation of β with wavelength for LiNbO₃

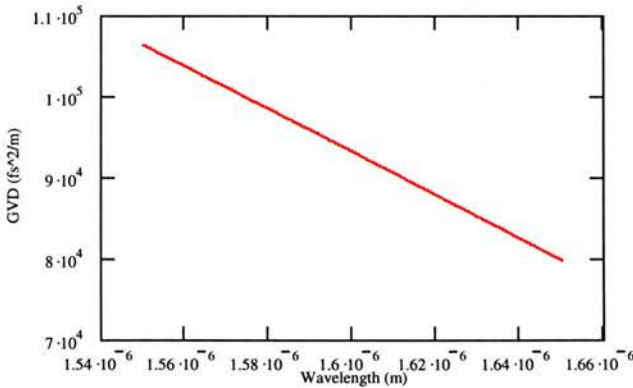


Figure 6.3 – Variation of GVD with wavelength for LiNbO₃

The two figures above show a decrease of both β and GVD with increasing wavelength (the wavelength range covers the region over which frequency combs have been generated – see chapter 5, section 5.2). Since this corresponds to a decrease in frequency, the above results represent normal dispersion. At the degenerate wavelength of 1600nm, figure 6.3 gives a GVD of $9.3 \times 10^4 \text{ fs}^2/\text{m}$ for lithium niobate. This is comparable to other nonlinear crystals. For instance, KTP has a GVD of around $7.8 \times 10^4 \text{ fs}^2/\text{m}$ at the slightly shorter wavelength of 1300nm [13]. On the other hand, BBO has a negative GVD of approximately $-5 \times 10^4 \text{ fs}^2/\text{m}$ at 1600nm [14]. As well as lithium niobate, the FCG cavity also contains a small amount of fused silica in the form of the focussing lens. Figures 6.4 and 6.5 give the variation of β and GVD over the same wavelength range for this material.

6. Dispersion Compensation

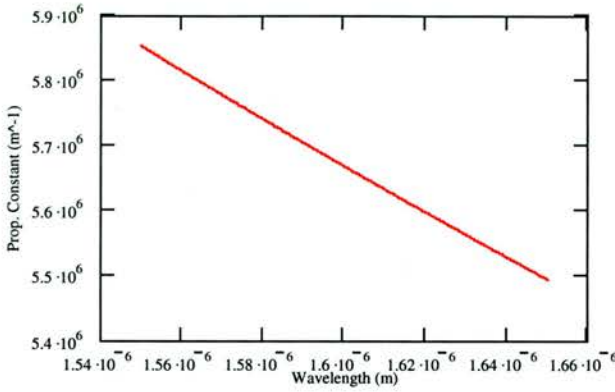


Figure 6.4 – Variation of β with wavelength for fused silica

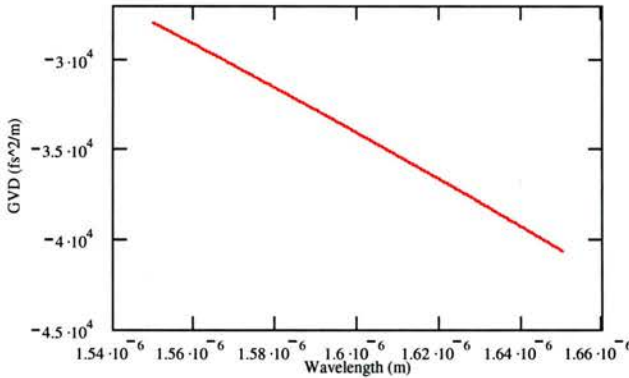


Figure 6.5 – Variation of GVD with wavelength for fused silica

As with lithium niobate, fused silica shows a decrease in both β and GVD as wavelength increases, a characteristic of normal dispersion. However, the GVD is negative throughout the wavelength range, with a value of $-3.4 \times 10^4 \text{ fs}^2/\text{m}$ at 1600nm. This is an important feature of fused silica in the context of dispersion and its implications for dispersion compensation will be explored in section 6.3. It is interesting to note that the GVD for fused silica is positive at a wavelength of 800nm. Hence, fused silica is often the main contribution to intra-cavity dispersion in femtosecond Ti:Sapphire systems. This shows that the effect of dispersion can vary significantly between the visible and infrared regions of the EM spectrum.

Whilst the GVD gives the dispersion per unit length, the absolute magnitude of dispersion in the FCG cavity is obtained from the GDD. This is calculated for each intra-cavity component separately (nonlinear crystal, EOM crystal and lens) then summed to give a total GDD at the specified wavelength. Figure 6.6 shows the *single-*

6. Dispersion Compensation

pass GDD for the FCG cavity across the same wavelength range as in figures 6.2 – 6.5.

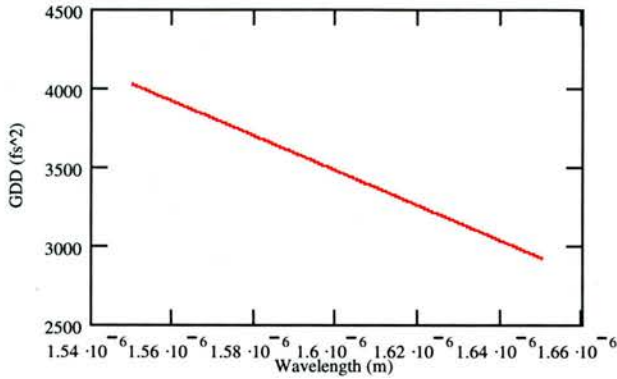


Figure 6.6 – Variation of total GDD with wavelength for FCG cavity

At 1600nm, figure 6.6 gives the total GDD as 3474.7 fs^2 . Remembering that this is for a single pass of the signal/idler cavity in the comb generator, the total GDD for a round trip is nearly 7000 fs^2 . This is over 20 times larger than the typical GDD in current modelocked femtosecond systems [15] and is mainly due to the significantly greater amount of intra-cavity material in the comb generator. The consequences of this difference, in terms of the application of dispersion compensation schemes, will be discussed in section 6.3.

As well as the specific value at 1600nm, the overall trend of the GDD plot is also of interest. Figure 6.6 shows a linear variation over the wavelength range with a gradient of $-11 \text{ fs}^2/\text{nm}$. This must be taken into account when designing a system for dispersion compensation.

6.2) Consequences of Dispersion for FCG & OPO

Having calculated the magnitude of dispersion in the FCG system, it is now time to examine in detail the resulting consequences to the operation of the comb generator. There are two processes to be considered here; the operation of the OPO, particularly in terms of its spectral output, and the generation of the frequency comb.

Taking the latter process first, the effect of dispersion on the generated frequency comb has already been touched upon in chapters 2 and 5. In the comb generation process, some form of frequency or phase modulation is used to transfer power from a

6. Dispersion Compensation

central frequency into two sidebands. The sideband separation is determined by the modulation frequency, which is set to the mode spacing at the central frequency. Hence, power is transferred into longitudinal modes, which are resonant in the cavity and can generate their own sidebands. The problem lies with the fact that the modulation frequency must be set to a fixed value. As stated, this is usually the mode spacing at the central frequency. For modes close to the central frequency the overlap between generated sidebands and adjacent modes will be almost perfect, since the modulation frequency and mode spacing will closely match. However, as power is transferred to modes further and further out from the central frequency, the fixed modulation frequency and varying mode spacing will differ by an increasing amount. Eventually, the overlap between sideband and longitudinal mode will have reduced to the extent that the power transferred is insufficient to overcome losses in the cavity. At this point, no further modes can oscillate in the cavity and the comb is abruptly cut off.

This is the origin of the dispersion limited comb width expressed mathematically in equation (5.1) and modelled for the system described in this thesis. The effect can be reduced (and hence the comb width increased) in a number of ways. More power can be transferred from each mode to its neighbour by increasing the modulation depth. However, this requires an increase in the power used to drive the modulator and consequently, undesirable heating of the device due to dissipative effects. Decreasing the amount of dispersive material in the cavity (nonlinear and modulator crystals) can actively reduce the magnitude of dispersion. Hence, the variation in mode spacing across the spectrum will be diminished. Unfortunately, this method is impractical in most cases. Reducing the length of the nonlinear crystal will have a detrimental effect on the pump threshold of the system and in commercial modulators the crystal length is fixed. This leaves the second method for reducing the magnitude of dispersion - the introduction of a system for dispersion compensation.

The effect of dispersion on the spectral operation of an OPO (more specifically, a DRO) has also been discussed previously in chapter 5. In particular, it was shown that the OPO will oscillate on a signal and idler pair with the closest overlap on a vernier scale diagram (where a vertical line represents conservation of energy). Due to the variations in mode spacing caused by dispersion, a perturbation to the OPO cavity will cause a new signal/idler pair to overlap more closely and oscillate. This new pair

6. Dispersion Compensation

could potentially be separated from the previous pair by a large frequency shift, thus causing a significant ‘jump’ in the spectral output of the OPO.

The variation in mode spacing or FSR can be examined mathematically by considering the simple cavity shown in figure 6.7 below.

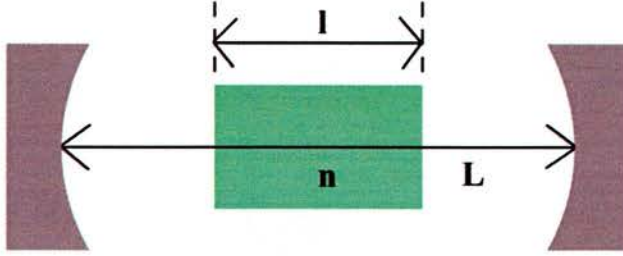


Figure 6.7 – Simple optical cavity

In terms of phase, the condition for the mode designated by the number p is

$$\begin{aligned}\phi_p &= (L-l)k_0 + k_0nl \\ &= p\pi\end{aligned}\tag{6.15}$$

In equation (6.15), the first term represents the phase change in the empty section of the cavity and the second term represents the phase change in the medium. The wavevector in free space is given by k_0 . Note that k is equivalent to β used earlier, with both representing the propagation constant.

The change in phase between adjacent modes is given by $\frac{\delta\phi_p}{\delta p}$, with $\delta p = 1$:

$$\delta\phi_p = \delta k_0(L-l) + \delta k_0nl + k_0l\delta n = \pi\tag{6.16}$$

Utilising the fact that $k_0 = \frac{\omega}{c}$, where ω is the free space angular frequency and rewriting δn as $\frac{\delta n}{\delta k_0} \frac{\delta\omega}{c}$ allows equation (6.16) to be rearranged in terms of $\delta\omega$.

$$\delta\omega = \frac{c\pi}{\left[L + (n-1)l + k_0l \frac{\delta n}{\delta k_0} \right]}\tag{6.17}$$

6. Dispersion Compensation

The next step is to convert $\frac{\delta n}{\delta k_0}$ into a more manageable form. By definition, n is the ratio of the wavevector in the medium to the wavevector in free space i.e. $n = \frac{k_m}{k_0}$.

Therefore,

$$\frac{\delta n}{\delta k_0} = \frac{1}{k_0} \frac{\delta k_m}{\delta k_0} - \frac{k_m}{k_0^2} \quad (6.18)$$

Multiplying equation (6.18) by $k_0 l$ and substituting into equation (6.17) gives the final equation for $\delta\omega$. Since this represents the change in frequency between adjacent modes; $\delta\omega$ is the FSR.

$$(\delta\omega)_{FSR} = \frac{c\pi}{\left[(L-l) + cl \frac{\delta k_m}{\delta\omega} \right]} \quad (6.19)$$

To obtain the change in FSR due to dispersion, it is necessary to obtain the derivative of equation (6.19) with respect to angular frequency.

$$\frac{d}{d\omega} [(\delta\omega)_{FSR}] = \frac{-c\pi}{\left[(L-l) + cl \frac{\delta k_m}{\delta\omega} \right]^2} \times cl \frac{\delta^2 k_m}{\delta\omega^2} \quad (6.20)$$

Noting that the first multiplying factor is equal to $-\frac{(\delta\omega)_{FSR}^2}{c\pi}$ allows equation (6.20) to be rewritten as

$$\frac{d}{d\omega} [(\delta\omega)_{FSR}] = -\frac{l}{\pi} \frac{\delta^2 k_m}{\delta\omega^2} (\delta\omega)_{FSR}^2 \quad (6.21)$$

The dimensions of $\frac{\delta^2 k_m}{\delta\omega^2}$ are $[s^2 m^{-1}]$. This is the same as $\phi''(\omega)$, the group velocity dispersion defined in equation (6.14). Hence, the change in mode spacing can be directly linked to the dispersion whose magnitude was calculated in the previous section, and subsequent dispersion compensation schemes based on this calculation.

Finally, it is convenient to also give equation (6.21) in terms of standard frequency, ν .

6. Dispersion Compensation

$$\frac{d}{d\nu}[(\delta\nu)_{FSR}] = -4\pi l \frac{\delta^2 k_m}{\delta\omega^2} (\delta\nu)_{FSR}^2 \quad (6.22)$$

Both equation (6.21) and equation (6.22) give the overall change in FSR per unit bandwidth, assuming that the change in FSR is small compared to the mode spacing. For the system described in this thesis, a rough calculation (ignoring changes in $(\delta\nu)_{FSR}$ and $\frac{\delta^2 k_m}{\delta\omega^2}$) utilises the following values: $l \sim 0.04\text{m}$, $(\delta\nu)_{FSR} \approx 600 \times 10^6 \text{ Hz}$ and $\frac{\delta^2 k_m}{\delta\omega^2} \approx 9 \times 10^4 \text{ fs}^2 \text{ m}^{-1}$ at $\lambda = 1600\text{nm}$ from figure 6.3, giving a change in mode spacing of 9.6 Hz for a single FSR. The effect across the entire comb bandwidth observed in the previous chapter is around 100 kHz, which agrees well with the range of modulation frequencies over which comb generation was observed. The 9.6 Hz shift will occur for every mode within the bandwidth and hence, the cumulative effect on the mode spacing (i.e. frequency shift of N^{th} mode relative to the case of no dispersion where the FSR is constant across the entire bandwidth) will be several orders of magnitude larger. Therefore, to obtain the cumulative change in mode spacing, it is necessary to sum the contributions to the change in mode spacing from every FSR. Assuming that the change in mode spacing varies linearly with mode number (this seems valid, since the total GDD of the cavity, which is responsible for the change in mode spacing, is shown to vary linearly with wavelength in figure 6.6), the cumulative change at any mode, N , is given by $N\Delta\nu$, where $\Delta\nu$ is the change in mode spacing for a FSR. The cumulative effect or total offset can then be found using

$$\text{Total Offset} = \sum_0^{N_f} N\Delta\nu \quad (6.23)$$

Here, N_f represents the final mode number within the specified bandwidth. For the maximum comb bandwidth of 7 THz (also the extent over which cluster hopping occurred), N_f is approximately 12000. As an approximation, the sum in equation (6.23) can be converted to an integral with respect to dN i.e.

$$\text{Total Offset} = \int_0^{N_f} N\Delta\nu dN = \frac{N_f^2 \Delta\nu}{2} \quad (6.24)$$

Putting the values for N_f and $\Delta\nu$ into the above equation gives the cumulative change in mode spacing across the entire comb bandwidth as roughly 650 MHz. Note that this

6. Dispersion Compensation

is very close to a FSR of the signal/idler cavity. Since a change in mode spacing of a FSR will move a whole group of modes back into alignment, this explains the cluster hopping that was observed between degeneracy and 1570/1630nm.

Having looked at the changes in FSR and mode frequency that occur due to a change in cavity length and as a result of the effects of dispersion, further insight can be gained by modelling the spectral behaviour of the OPO directly. This is achieved with a MathCAD program (see appendix III), which is based on the vernier scale diagram discussed in the previous chapter. The program is structured into four parts, which are described below:

- 1) Calculate the position of all cavity modes from a specified centre frequency and within a specified bandwidth, taking into account the change in FSR due to dispersion.
- 2) Overlap signal and idler modes to satisfy energy conservation.
- 3) Look for the modes with the closest overlap to determine the pair on which the OPO oscillates.
- 4) Introduce a perturbation in the form of a cavity length change and calculate the changes to the mode structure to find the new oscillating mode pair.

In the first part, the mode spacing is calculated at each consecutive mode to obtain the best possible accuracy. The frequency and number of all the modes within the specified bandwidth are then put into an array. For the second and third parts, the frequencies of signal and idler modes are summed and compared to the pump frequency. To find the closest match and hence the oscillating mode pair, a signal mode is compared to the 20 idler modes with the nearest mode number. To introduce a perturbation, a frequency shift, $\Delta\nu$, due to a change in cavity length, ΔL , is added to the mode frequencies before they are entered into the array. Once the calculation has been completed, the program outputs the frequency and number of the oscillating signal and idler modes.

6. Dispersion Compensation

Applying this model to the current FCG set-up with a centre wavelength of 1600nm and a bandwidth of 7 THz resulted in the following plot of oscillating signal and idler wavelengths against cavity length detuning.

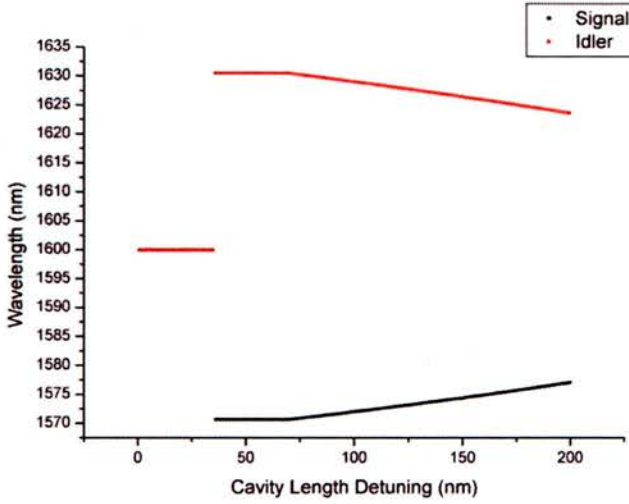


Figure 6.8 – Oscillating signal and idler modes 1

Immediately apparent from figure 6.8 is a cluster hop that occurs at a detuning of around 35nm. This causes the signal and idler wavelengths to jump from degeneracy to 1572nm and 1629nm respectively. From the proof-of-principle results in chapter 5, it can be seen that these wavelengths correspond almost exactly to the operating point of the FCG with the EOM initially off. Prior to and immediately after the cluster hop, the signal and idler frequencies remain constant. After the cavity length has been changed by 70nm, the OPO begins to hop at a rate of approximately 9 modes per nm towards degeneracy. The mode-hopping rate seems to remain constant up to a cavity length change of 200nm. Figure 6.9 shows the general trend for the signal and idler wavelengths beyond 200nm.

6. Dispersion Compensation

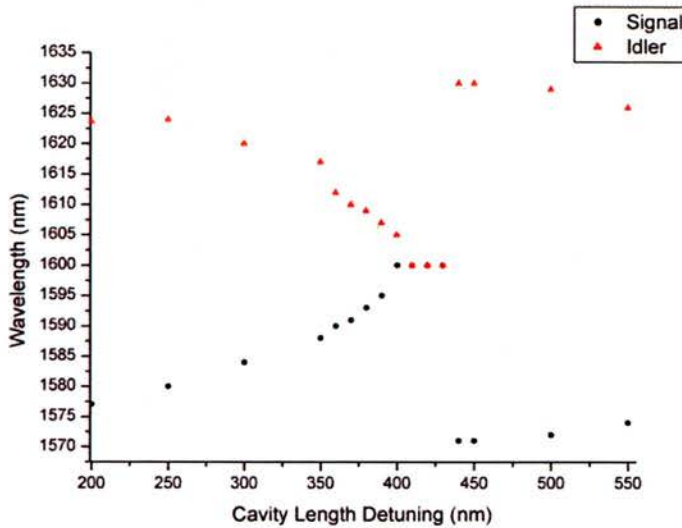


Figure 6.9 – Oscillating signal and idler modes 2

In figure 6.9, there is marked increase in signal and idler wavelength shift as the change in cavity length is increased. From approximately 350nm onwards, the mode-hopping rate is around 23 modes per nm until degeneracy is reached at 400nm. A cluster hop, very similar to that shown in figure 6.8, then occurs at 440nm and the pattern first seen in figure 6.8 seems to repeat.

The behaviour shown in figure 6.9 closely matches the experimental observations that were presented in chapter 5. In particular, from the point when the EOM was switched on, a 100nm increase in the cavity length was required to shift the signal and idler branches to degeneracy. Looking at the results of the modelling and working backwards, it can be seen that from degeneracy at 400nm, the signal and idler wavelengths at 300nm are 1584nm and 1617nm respectively. These are the approximate positions of the observed signal and idler branches in the proof-of-principle experiments before the cavity length was increased. Similarly, there is also a close match between the model and experimental observations after a 50nm increase in the cavity length (corresponding to a cavity length detuning of 350nm on figure 6.9). Finally, the cluster hop that occurs on the model after a short change in the cavity length at degeneracy was regularly observed during the comb generation experiments. It was this cluster hopping that seemed to be preventing the frequency comb from forming during the optimum pumping level experiments. The model suggests that a 40nm change in cavity length is required for the cluster hop to occur. It

6. Dispersion Compensation

is quite conceivable that such a change could be caused by vibration and/or a change in temperature.

There are some discrepancies between the model and experimental results. The close match in tuning behaviour only occurs after an initial cavity length change of 300nm on the model. This is due to the accuracy of the measured signal and idler cavity length, which leads to an error in the setting of the 'zero' position in the model. Since the accuracy of the cavity length is of the order of 10^{-4} m, an error of a few hundred nm in the 'zero' position does not seem unreasonable. The model also does not take into account phasematching or any external factors that might influence the oscillation of certain modes. Examples of such factors include damage to or dust on the intra-cavity surfaces and variations in the reflectivity of coatings applied to these surfaces. The overall effect of these features would be to increase the threshold of a particular mode pair, such that it is more favourable for another pair to oscillate, even though the former has the greater overlap on the vernier scale diagram. In such a case, the oscillating mode pair given by the model would not agree with experimental observations.

6.3) Dispersion Compensation Methodologies

In the previous section, the mode structure and spectral behaviour of the OPO within the FCG was analysed both mathematically and with the aid of a computer model. The results were in good agreement with observations and data taken during the proof-of-principle and optimum pumping experiments. In particular, the cluster hopping that seemed to be preventing the generation of a frequency comb in the latter experiment was predicted by the computer model. Both the model and mathematical analysis are based on the effect of dispersion on the position and separation of the longitudinal modes in the signal/idler cavity. Furthermore, dispersion is well documented as the main limiting factor to the maximum frequency comb width.

Taking all this into account, it was decided to investigate the possibility of introducing dispersion compensation into the FCG. If successful, this would be expected to negate the effects described in the previous section, increasing the maximum comb width and improving the spectral stability of the FCG.

6. Dispersion Compensation

The theory behind dispersion compensation begins with the group delay dispersion, ϕ'' . In figure 6.6, the total GDD for a single pass of the FCG cavity is shown to be positive and decreasing with wavelength. As already mentioned, this is known as normal dispersion. Since the total GDD is given by summing the individual ϕ'' for every component in the cavity, dispersion compensation can be achieved by introducing an element (or elements) with $\phi'' < 0$ over the wavelength range of interest. To see how this can be realised physically, it is necessary to return to the delay between two spectral components, $\Delta\tau$, given by equation (6.11). Rearranging this equation in terms of ϕ'' gives

$$\phi''(\omega_1) = \frac{\Delta\tau}{\Delta\omega} = \frac{\phi'(\omega_2) - \phi'(\omega_1)}{\omega_2 - \omega_1} \quad (6.25)$$

From the definition of ϕ in equation (6.10) and the group velocity in equation (6.9),

$$\phi' = L \left(\frac{d\beta}{d\omega} \right)_{\omega_c} = \frac{L}{v_g} \quad (6.26)$$

The term on the far right of equation (6.26) can be written as τ_g , the delay experienced by a pulse of centre frequency, ω_c , on traversing a medium of length, L . This allows equation (6.25) to be rewritten as

$$\phi''(\omega_1) = \frac{\tau_2 - \tau_1}{\omega_2 - \omega_1} \quad (6.27)$$

Therefore, $\phi'' < 0$ requires $\tau_2 < \tau_1$ for $\omega_2 > \omega_1$. In other words, the delay for the higher frequency spectral component must be less than the delay for the lower frequency component.

Methods for achieving this can be grouped into two main categories. The first utilises materials, whose properties are such that $\phi'' < 0$ over the wavelength range of interest. This is commonly known as negative material dispersion. As an example, figure 6.5 shows that this is exhibited by fused silica at wavelengths close to 1600nm. To

6. Dispersion Compensation

compensate for the total positive GDD within the optical system, it is simply a matter of choosing the correct path length through the negative dispersion medium to give the appropriate negative GDD. This can be achieved by direct transmission through the material or, if space is at a premium, with a total internal reflection (TIR) arrangement, where the optical beam bounces between the inner surfaces of the material a set number of times (see figure 6.10).

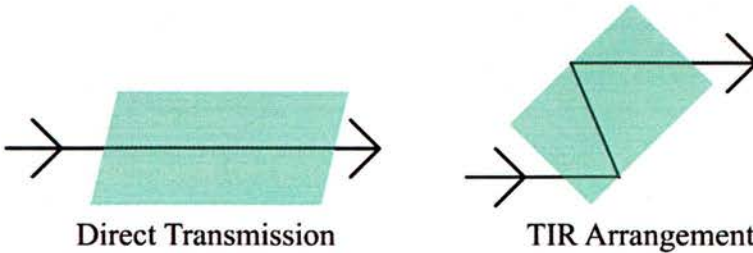


Figure 6.10 – Dispersion compensation via negative material dispersion

Using negative dispersion materials has the advantage of being easy to implement, with the anti-reflection coated or Brewster cut crystal simply placed at the chosen point in the optical system. In the case of a standing-wave optical cavity, the crystal need only compensate for single-pass GDD, since the circulating field will pass through it twice on any round-trip.

One of the main drawbacks with negative dispersion materials is a lack of coverage across the visible and near to mid IR part of the EM spectrum. As previously mentioned, fused silica exhibits a positive GDD at wavelengths around 800nm and therefore cannot be used to compensate for dispersion at such wavelengths. Particularly in the case of OPO applications, where a wide number of wavelengths are accessed, there may be situations where it is impossible to find a suitable negative dispersion material to act as a compensator. Another problem with utilising negative dispersion lies with the fact that a significantly long crystal may be required to completely negate the positive GDD. Again, this applies particularly to OPOs where the nonlinear crystal and other intra-cavity media can amount to several cm in length. For example, to compensate for the total GDD of the FCG system given in figure 6.6, a 10.2cm piece of fused silica is required. Even allowing for a shorter crystal in the TIR arrangement, this is still a significant fraction of the total signal/idler cavity length. The inclusion of such a crystal will have implications for the minimum size of

6. Dispersion Compensation

the optical system in question and may well be impractical if a compact system is required. Another related issue is the decrease in mode spacing caused by the insertion of the negative dispersion material. For example, the 10.2cm piece of fused silica required to compensate for dispersion in the signal/idler cavity will cause the mode spacing to decrease by 105 MHz. In devices such as the frequency comb generator, where the allowable mode spacing is limited by the tuning range of the EOM, this may prevent the device from working. Despite these drawbacks, negative dispersion materials have found use as compensators in many ultra-short pulse systems. For example, in compact systems based on Cr:LISAF and operating at 1500nm, where the positive GDD is small, dispersion compensation has been accomplished with slabs of fused silica in the Littrow configuration [16].

The second method of achieving $\tau_2 < \tau_1$ for $\omega_2 > \omega_1$ involves the use of elements that separate the various spectral components into different paths. By ensuring that the path for ω_1 is longer than the path for ω_2 , the condition $\tau_2 < \tau_1$ will be satisfied. The elements for spectral separation can be split into the three types: diffractive, refractive and interferometric. The most common example of a diffractive element is a diffraction grating, which creates an angular separation between spectral components. The use of a pair of diffraction gratings for dispersion compensation is a well-known technique that has been established for over 30 years [17]. However, it introduces relatively large losses due to scattering into higher diffraction orders (an inherent part of the diffraction process). Another disadvantage with diffractive elements is a lack of flexibility. In particular, it is difficult to adjust the dispersion through zero and therefore compensate for an overall negative GDD in the optical system.

The problems with the use of diffractive elements, led Martinez et al [18] to propose the use of refractive elements as dispersion compensators. Refractive elements consist of slabs and, most commonly, prisms of transparent material e.g. fused silica. The important feature of such elements is that they can provide an overall negative GDD, despite their parent material exhibiting positive dispersion at the operating wavelength(s). Like a diffraction grating, a prism also creates angular separation between different spectral components. However, it does so without causing any significant loss. The use of prisms for negative dispersion was first demonstrated by Fork et al [19], who introduced the now classic four-prism sequence shown in figure 6.11.

6. Dispersion Compensation

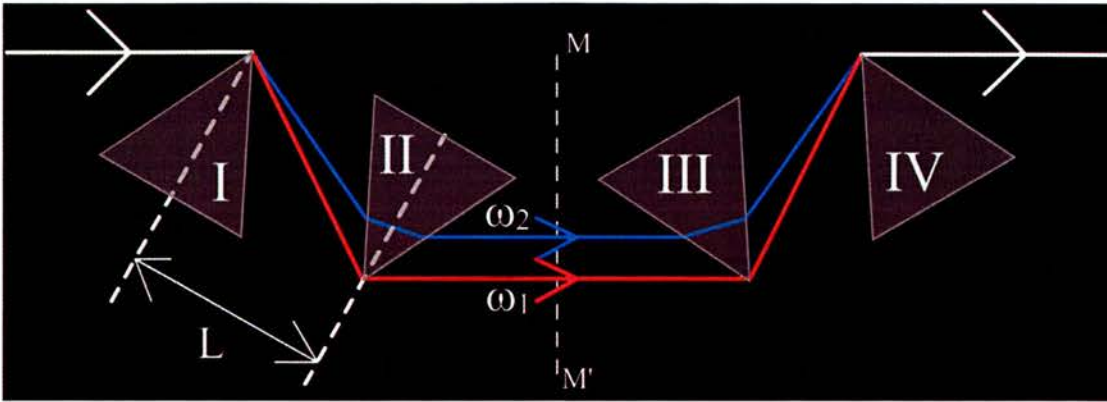


Figure 6.11 – Four-prism dispersion compensator

The dispersion compensation scheme in figure 6.11 consists of four prisms orientated at Brewster's angle for incidence, to negate reflection losses. The entrance face of prism II is parallel to the exit face of prism I and vice versa. This is also true of the III, IV prism pair and hence MM' , at the midpoint between prisms II and III, represents the plane of symmetry in the system. As the diagram shows, the angular separation induced by the first two prisms creates a path difference between ω_1 and ω_2 such that the path for ω_1 is longer. The second prism pair then reverses the angular separation, such that the transmitted beam is collinear to the input beam, with no transverse displacement between the spectral components. Notice that the overall dispersion of the four-prism sequence is the sum of two components: the negative dispersion due to the difference in path length and the positive material dispersion experienced on transmission through each prism (assume here that the prism material exhibits positive dispersion at the operating wavelength). The negative component can be altered by changing the distance, L , between prisms I and II (and also prisms III and IV if the angular separation is to be reversed). The positive component is altered by translating any one of the crystals along an axis perpendicular to its base (dotted lines on figure 6.11), thereby changing the length of material through which the spectral components must travel. These two adjustments allow a wide range of total dispersion values to be accessed by the four-prism scheme, including continuous tuning of the dispersion through zero.

The four-prism sequence does suffer from the drawback of a fairly large footprint. However, if compensation is required for a standing wave cavity, prisms III and IV

6. Dispersion Compensation

can be replaced by a reflector situated at the symmetry plane, MM' . The angular separation of the spectral components will then be reversed on the second pass through prisms I and II. Care must be taken when adjusting the positive component of dispersion in this case, since the effect will be doubled compared to the four-prism case. It is also common to use an aperture to force the spectral components to overlap after the second pass through the prisms. As shown by Gordon and Fork [20], it is even possible to use a single prism in a ring cavity, with an adjustable dispersion of either sign.

The final type of element for spectral separation, interferometric, consists of a special class of multilayer optical coatings. In most cases, the coating is laid down on a substrate, as shown in figure 6.12, to act as a reflector. It is common to refer to such reflectors as *chirped mirrors* [21].

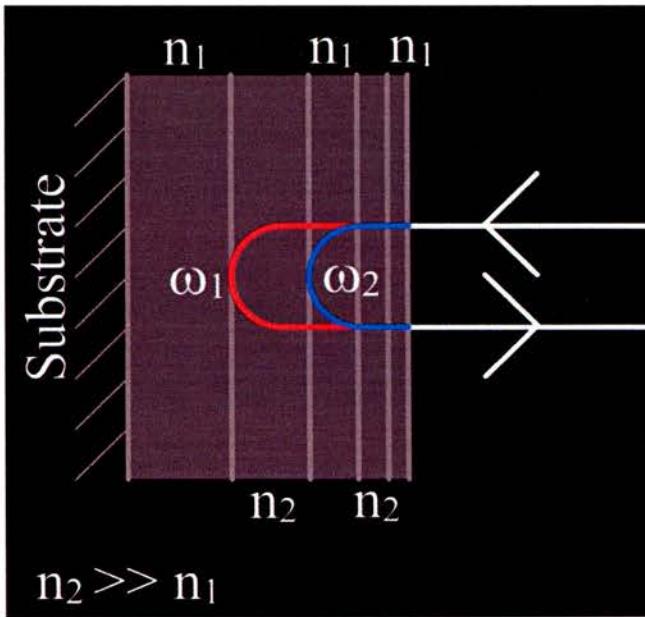


Figure 6.12 – Multilayer coating for dispersion compensation

Figure 6.12 shows a simplified schematic of a chirped mirror, which consists of a series of alternating high and low refractive index layers. A commonly used pair of materials for the layers is TiO_2 (high n) and SiO_2 (low n), since they have the highest refractive index ratio in the near-IR spectral region. Typically, around 40 layers will be deposited on the substrate, with the layer thickness increasing as the substrate is approached. The thickness of each layer is specifically chosen to ensure high

6. Dispersion Compensation

reflectivity (usually $> 99\%$) over the spectral bandwidth of interest, like any normal reflective coating. However, the layers are also designed so that ω_1 , the lower frequency spectral component, penetrates further into the layer structure than ω_2 . Hence, the path length for ω_1 is longer, satisfying the condition for negative dispersion. In this case, the separation of spectral components is achieved by interference between multiple reflections from the various layer interfaces.

As well as creating negative second order dispersion (GDD), careful design of the layer structure can also negate or cause cancellation between higher order dispersion ($\phi'''(\omega_c), \phi''''(\omega_c)$ in equation (6.12)). This is particularly important for ultra-short pulse systems, where the spectral bandwidths associated with pulses of a few fs are large enough for higher order dispersion to have significant detrimental effects. Today, chirped mirrors are designed for a prescribed reflectivity and negative dispersion by use of Fourier-transform techniques [22] and various optimisation algorithms [23], often with dedicated computer software packages. The mirrors are then created using standard beam deposition techniques, allowing several to be produced in a single coating run and reducing the associated costs.

The possibility of using chirped mirrors for broadband dispersion control in ultra-short pulse lasers was first suggested by Szipöcs et al [24], who realised a mirror design providing 99.9% reflectivity and a GDD of -45 fs^2 at 800nm. Subsequently, the application of chirped mirrors for dispersion compensation was experimentally realised in a femtosecond Ti:Sapphire laser [25] and other ultra-short pulse systems [26, 27]. Chirped mirrors have also been utilised for dispersion control in femtosecond OPOs. Hebling et al [13] described a ring KTP oscillator, pumped by a femtosecond Ti:Sapphire laser and incorporating multiple reflections between chirped mirrors with a reflectivity of 99.5% and a GDD of -85 fs^2 . The device produced near-transform limited pulses of around 100 fs, continuously tunable from 1.18 μm to 1.32 μm . In further studies by the same author [28], the use of -140 fs^2 chirped mirrors resulted in pulse widths as short as 50 fs.

As providers of negative dispersion, multilayer optical coatings have several advantages. They can be designed and produced to a wide range of specifications using well-established techniques. As a result, the associated cost is not prohibitively high, being comparable to standard optical coatings. In the form of highly reflective chirped mirrors, multilayer coatings can replace cavity mirrors with little or no effect

6. Dispersion Compensation

on the cavity length. This gives multilayer coatings a major advantage over negative dispersion materials and refractive elements in compact systems. Furthermore, there is no issue with transverse or angular separation of the spectral components. It should, however, be noted that multilayer coatings and other methods of dispersion compensation are not mutually exclusive. By their very nature, optical coatings offer the possibility of being combined with prisms or negative dispersion materials to form a hybrid compensation scheme. So, versatility is another advantage of the multilayer coating.

The only real drawback suffered by multilayer coatings is a limit to the extent of the negative dispersion they can provide. Typically, the achievable negative GDD will go up to a few hundred fs^2 . Usually, this is more than adequate for compact systems where the intra-cavity material is kept to a minimum. However, for systems where a large GDD is to be compensated for, multiple reflections between pairs of chirped mirrors may be required.

Having examined the magnitude and effects of dispersion in the current FCG system and discussed the various possibilities for dispersion compensation, the incorporation of a compensation scheme into the FCG cavity can now be addressed. The following chapter describes the choice and implementation of such a scheme and the resulting effects on the OPO and frequency comb generation.

6.4) Chapter Summary

In the preceding text, a detailed examination of dispersion, the dependence of the refractive index on optical frequency, in the current FCG system has been given. Starting with the material origin and using the theory of dispersion in ultra-short pulse generation, two quantities were defined as a measure of the magnitude of dispersion. The group delay dispersion (GDD) is a measure of the broadening per unit bandwidth of an optical pulse. The group velocity dispersion (GVD) is closely related to the GDD and is defined as the broadening per unit length of dispersive material per unit bandwidth. GVD for both LiNbO_3 and fused silica was calculated as a function of wavelength and found to be $9.3 \times 10^4 \text{ fs}^2/\text{m}$ and $-3.4 \times 10^4 \text{ fs}^2/\text{m}$ respectively at 1600nm. The absolute magnitude of dispersion for the entire FCG cavity was given by the GDD and found to be 3474.7 fs^2 at 1600nm, with a linear variation of $-11 \text{ fs}^2/\text{nm}$.

6. Dispersion Compensation

Next, the effects of this dispersion on the spectral operation of the OPO and the generation of a frequency comb were discussed. Taking the latter first, dispersion causes a gradual change in the longitudinal mode spacing, moving away from degeneracy. Since the modulation frequency and hence the sideband spacing is fixed, this means that the generated sidebands and longitudinal modes will gradually move out of coincidence. Eventually, the overlap will be so small that the power transferred into the longitudinal mode will be insufficient to overcome losses in the cavity. As a result, the frequency comb will be abruptly cut-off at this point.

The effect of the spectral operation of the OPO had previously been touched upon with the vernier scale diagram in section 5.4 of chapter 5. This was expanded here with a mathematical analysis of the variation in mode spacing. The resulting equation contained a term with the same dimensions as the GVD, showing the link between the variation in mode spacing and the magnitude of dispersion previously calculated. Using these results, a quick calculation gave a cumulative change in mode spacing of 650 MHz over a 7 THz bandwidth (the maximum comb width). This was in good agreement with experimental observations of cluster hopping.

A computer program was also used to model the spectral behaviour of the OPO directly, using the vernier scale scheme to determine the oscillating mode pair as the cavity length was altered. The results of this modelling showed cluster hopping and frequency tuning behaviour that closely matched experimental observations. In particular, the cavity length change required for a cluster hop to occur was found to be $\sim 40\text{nm}$. This could easily be achieved by thermal or mechanical vibrations in the system, lending credence to the theory this was the cause of previous trouble with comb generation.

Having established that the dispersion calculated at the start of this chapter was responsible for much of the spectral behaviour of the OPO and the associated problems, the possibility of compensating for this dispersion was examined. Generally, dispersion compensation requires an element or elements with negative GDD. This means that the delay on traversing the element(s) must be less for a higher frequency spectral component than a lower frequency component. Achieving the difference in delay either requires a material with a natural negative GDD over the wavelength range of interest or elements that can separate the spectral components into different paths.

6. Dispersion Compensation

Negative dispersion materials (such as fused silica at 1600nm) can be placed directly into the optical cavity and hence are simple to use. However, they are limited in availability over the visible and near to mid infrared wavelength ranges. They also increase the length of the cavity and the size of the optical system.

Elements that separate the spectral components consist of diffractive, refractive and interferometric types. Diffractive types, such as gratings, create an angular separation between the spectral components, which leads to a longer path for those with the lower frequencies. Unfortunately, gratings are associated with significant losses and their dispersion cannot be easily tuned through zero. Refractive types such as prisms are widely used today as dispersion compensators. They also create an angular separation between spectral components, but do not exhibit significant losses and offer continuous tuning of their dispersion through zero. A common set-up is the 4-prism scheme, but compensators with two and even one prism have also been demonstrated. Like negative dispersion materials, the main problem with refractive elements is the associated increase in cavity length and system size. Interferometric types consist of multilayer coatings, which are usually coated onto substrates to create chirped mirrors. The coatings are made up of alternating high and low refractive index layers of varying thickness. This ensures high reflectivity and the deeper penetration of lower frequency components, with the path separation of spectral components achieved by interference between multiple reflections from the interfaces of these layers. Chirped mirrors have the advantage of versatility and can be produced using well-established techniques. Since they can replace cavity mirrors, their effect on the cavity length is negligible. The only drawback with multilayer coatings is a limit on the negative dispersion that can be achieved, leading to the possibility of multiple reflections being required.

References

1. Yariv, A., *Quantum Electronics*. 3rd ed. 1989, New York: Wiley.
2. Hecht, E., *Optics*. 3rd ed. 1998: Addison Wesley Longman Inc.
3. Bruner, A., et al., *Temperature-dependent Sellmeier equation for the refractive index of stoichiometric lithium tantalate*. *Optics Letters*, 2003. **28**(3): p. 194-196.

6. Dispersion Compensation

4. Feve, J.P., et al., *Phase-matching measurements and Sellmeier equations over the complete transparency range of $KTiOAsO_4$, $RbTiOAsO_4$, and $CsTiOAsO_4$* . Journal of the Optical Society of America B-Optical Physics, 2000. **17**(5): p. 775-780.
5. Kato, K. and Takaoka, E., *Sellmeier and thermo-optic dispersion formulas for KTP*. Applied Optics, 2002. **41**(24): p. 5040-5044.
6. Jundt, D.H., *Temperature-dependent Sellmeier equation for the index of refraction ne in congruent lithium niobate*. Optics Letters, 1997. **22**: p. 1553.
7. Sibbett, W., et al., *Broadly tunable femtosecond solid-state laser sources*. Applied Physics B-Lasers and Optics, 1994. **58**(3): p. 171-181.
8. Sibbett, W., et al., *Versatile femtosecond laser sources for time-resolved studies: configurations and characterizations*. Philosophical Transactions of the Royal Society of London Series a-Mathematical Physical and Engineering Sciences, 1998. **356**(1736): p. 283-296.
9. Keller, U., *Recent developments in compact ultrafast lasers*. Nature, 2003. **424**(6950): p. 831-838.
10. Ghosh, G., et al., *Temperature-dependent Sellmeier coefficients and chromatic dispersions for some optical-fibre classes*. Journal of Lightwave Technology, 1994. **12**(8): p. 1338-1342.
11. Walmsley, I., et al., *The role of dispersion in ultrafast optics*. Review of Scientific Instruments, 2001. **72**(1): p. 1-29.
12. Svelto, O., *Principles of Lasers*. 4th ed. 1998: Plenum Press. 351.
13. Hebling, J., et al., *Chirped-mirror dispersion-compensated femtosecond optical parametric oscillator*. Optics Letters, 1995. **20**(8): p. 919-921.
14. Liu, H., et al., *2nd and 3rd harmonic-generation in BBO by femtosecond Ti:Sapphire laser pulses*. Optics Communications, 1994. **109**(1-2): p. 139-144.
15. Leburn, C.G., et al., *Femtosecond Cr⁴⁺: YAG laser with 4GHz pulse repetition rate*. Electronics Letters, 2004. **40**(13): p. 805-807.
16. Brown, C.T.A., et al., *Compact laser-diode-based femtosecond sources*. New Journal of Physics, 2004. **6**: p. art. no.-175.
17. Treacy, E.B., *Optical pulse compression with diffraction gratings*. IEEE Journal of Quantum Electronics, 1969. **QE-5**(9): p. 454-458.

6. Dispersion Compensation

18. Martinez, O.E., et al., *Negative group-velocity dispersion using refraction*. Journal of the Optical Society of America a-Optics Image Science and Vision, 1984. **1**(10): p. 1003-1006.
19. Fork, R.L., et al., *Negative dispersion using pairs of prisms*. Optics Letters, 1984. **9**(5): p. 150-152.
20. Gordon, J.P. and Fork, R.L., *Optical resonator with negative dispersion*. Optics Letters, 1984. **9**(5): p. 153-155.
21. Szipocs, R. and Kohazi-Kis, A., *Theory and design of chirped dielectric laser mirrors*. Applied Physics B-Lasers and Optics, 1997. **65**(2): p. 115-135.
22. Szipocs, R. and Kohazi-Kis, A., *Design of dielectric high-reflectors for dispersion control in femtosecond lasers*. Proceedings of the SPIE, 1994. **2253**: p. 140-149.
23. Dobrowolski, J.A. and Kemp, R.A., *Refinement of Optical Multilayer Systems with Different Optimization Procedures*. Applied Optics, 1990. **29**(19): p. 2876-2893.
24. Szipocs, R., et al., *Chirped Multilayer Coatings for Broadband Dispersion Control in Femtosecond Lasers*. Optics Letters, 1994. **19**(3): p. 201-203.
25. Stingl, A., et al., *Generation of 11-Fs Pulses from a Ti-Sapphire Laser without the Use of Prisms*. Optics Letters, 1994. **19**(3): p. 204-206.
26. Naumov, S., et al., *Directly diode-pumped Kerr-lens mode-locked Cr⁴⁺: YAG laser*. Optics Letters, 2004. **29**(11): p. 1276-1278.
27. Wagenblast, P.C., et al., *Generation of sub-10-fs pulses from a Kerr-lens mode-locked Cr³⁺: Li:CAF laser oscillator by use of third-order dispersion-compensating double-chirped mirrors*. Optics Letters, 2002. **27**(19): p. 1726-1728.
28. Hebling, J., et al., *Mirror-dispersion-compensated femtosecond optical parametric oscillator*. Optics Communications, 1997. **141**(3-4): p. 229-236.

Chapter 7

Comb Generation in a Dispersion Compensated Cavity

The implementation of dispersion compensation in the frequency comb generator was undertaken with two main aims: to increase the comb width and improve the spectral stability of the OPO. Compensating for the positive dispersion exhibited by the intra-cavity material would negate the change of refractive index with frequency, thereby equalizing the longitudinal mode spacing across the bandwidth of interest. With equal mode spacings, the sidebands generated by the EOM would always coincide with a longitudinal mode. As a result, the comb could potentially cover the entire frequency range over which the OPO can provide gain i.e. the phasematching bandwidth, calculated to be ~13 THz in chapter 4, section 4.1. In terms of the spectral properties of the OPO, with equal mode spacing, cluster and mode hopping would no longer occur. Instead, there would be a series of regular cavity lengths, determined by the mode spacing, at which all signal and idler mode pairs would simultaneously overlap. The peak of the phasematching curve would then determine the oscillating mode pair. At all other cavity lengths, no mode pairs would overlap and hence the OPO would be ‘switched off’. Careful control of the signal and idler cavity would be needed, to ensure that it remained at the length required for oscillation.

Before determining how best to incorporate dispersion compensation into the FCG cavity, it was first necessary to decide on which compensation scheme to use. As shown by figure 6.5, fused silica has a negative GVD over the wavelength range 1550 – 1650nm. Therefore, the possibility exists that a suitable length of fused silica could compensate for the positive dispersion of the LiNbO₃ crystals. The GVD and GDD calculations in chapter 6, section 6.1 suggest that a 10.2cm length of fused silica will give the appropriate negative dispersion at 1600nm. The consequential decrease in the cavity FSR can be calculated using equation (7.1) below:

7. Comb Generation in a Dispersion Compensated Cavity

$$\Delta \nu_{FSR} = -\frac{2\nu_{FSR}^2}{c} \Delta L \quad (7.1)$$

Here, ΔL is the change in the *optical* length of the cavity and hence is given by the length of the fused silica multiplied by its refractive index at 1600nm, to a first approximation. For an initial FSR of 600 MHz, the resulting change in FSR is 353 MHz. This means that the FSR will be reduced to less than half its initial value, well out with the tuning range of the EOM. Even if the large change in cavity FSR and the increase in the footprint of the device could be tolerated, there is a more fundamental issue with fused silica that makes it unsuitable as a dispersion compensator in this case. Any dispersion compensation scheme must negate the positive GDD across the entire comb bandwidth. From figure 6.6, it can be seen that the GDD varies linearly with wavelength. Over the 1550 – 1650nm range, the variation is $-11 \text{ fs}^2/\text{nm}$. To give full dispersion compensation, the chosen scheme must therefore have a gradient of $+11 \text{ fs}^2/\text{nm}$ over the wavelength range. However, in the case of fused silica, figure 6.5 shows that it exhibits a negative gradient in GVD between 1550nm and 1650nm. This means that it can only compensate for dispersion at a single chosen wavelength, rather than the entire comb bandwidth. Furthermore, the negative GVD gradient also prevents fused silica from being used in a prism-based compensation scheme and in combination with a multilayer coating.

The problems with fused silica do not rule out prisms completely. There exists the possibility of using another material for the prisms with the correct dispersive properties. However, the main problem with a prism-based scheme is the resulting increase in cavity length and change in FSR. Since the current FCG system is based on a standing wave cavity, at least two prisms would be required. To achieve any magnitude of negative dispersion, a path length of at least 140mm would be required between the two prisms [1]. Full compensation for the large positive GDD in the FCG cavity would need a considerably larger path length. This would cause a significant increase in the optical length of the FCG cavity and the size of the overall system.

Having discounted the possibility of using fused silica or a prism-based scheme for dispersion compensation, the only realistic option left was a multilayer coating in the form of chirped mirrors. In the next section, the implementation of a dispersion compensation scheme based on chirped mirrors is described.

7. Comb Generation in a Dispersion Compensated Cavity

7.1) Incorporating Dispersion Compensation into the OPO-FCG

After making some informal enquiries [2], it was discovered that highly reflecting chirped mirrors with a negative GDD up to -550 fs^2 were available at 1600nm. In the current FCG system, the total positive GDD is 3475 fs^2 at the central wavelength of 1600nm with a linear variation of -11 fs^2 per nm over the range 1550 – 1650nm. This corresponds to a gradient of $-0.32\%/nm$ (i.e. 0.32% of the centre value = $0.0032 \times 3475 \text{ fs}^2$). Therefore, alongside the specified GDD of approximately -550fs^2 at 1600nm, the chirped mirrors also needed to have a linear variation in the GDD with a gradient of $+0.32\%/nm$. As a result, a custom coating had to be manufactured and this was laid down on a standard 0.5-inch diameter substrate made from fused silica. To allow for a range of negative GDDs, two further coatings were ordered, with centre GDD of approximately -250 fs^2 and -100 fs^2 respectively and both with a gradient of $+0.32\%/nm$.

As expected, the maximum negative GDD of -550 fs^2 available from a single chirped mirror meant that multiple reflections from a pair of such mirrors would be needed to fully compensate for the positive intra-cavity GDD. In this case, a minimum of six reflections was required. This was achieved with the configuration shown in figure 7.1.

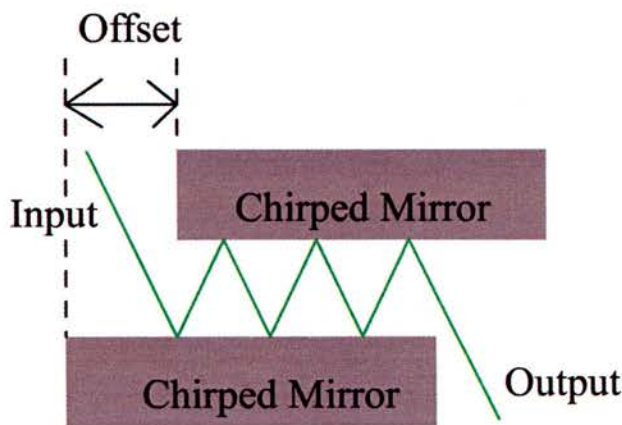


Figure 7.1 – 6-Bounce parallel chirped mirror configuration

7. Comb Generation in a Dispersion Compensated Cavity

The mirrors are placed parallel and facing each other, but with a horizontal offset. The input beam is incident on the first mirror at a prescribed angle and then strikes each mirror three times, giving six reflections, before exiting. Keeping the mirrors parallel ensures that the input and output beams are collinear, making alignment of the configuration in the FCG cavity significantly easier.

Before determining how exactly to mount the mirrors in the parallel configuration, it was first necessary to obtain the maximum decrease in cavity FSR and hence increase in cavity length that could be tolerated. This was set by the tuning range of the modulator and in particular, the fall off of RF power coupled into the modulator as it was tuned away from its central frequency. Starting with the non-compensated cavity FSR of 591 MHz and an input power of 200mW to the EOM, figure 7.2 shows the variation in fractional forward power (power coupled into EOM/input power) with modulation frequency. At each frequency, the tuning slug on the EOM was adjusted so that the reflected power was zero, ensuring that maximum input coupling was achieved.

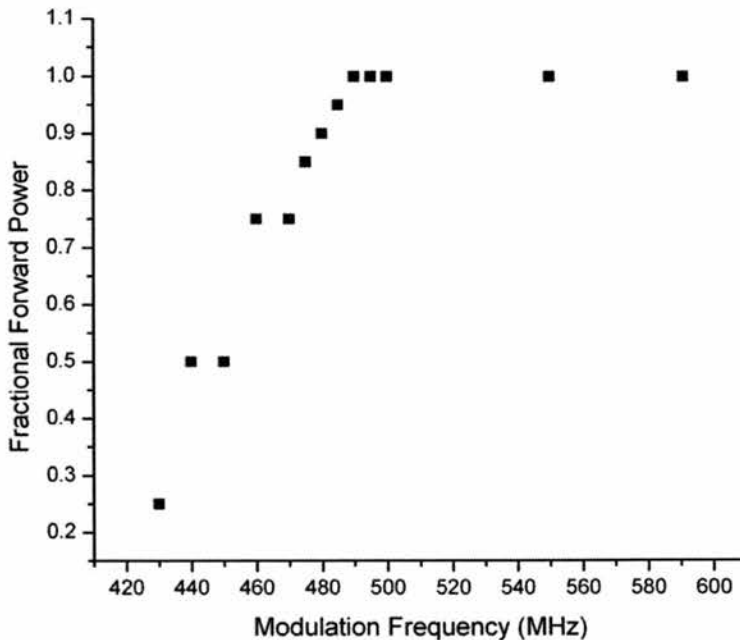


Figure 7.2 – RF power coupled into EOM

Figure 7.2 shows that for frequencies down to 490 MHz, all of the input RF power was coupled into the modulator. Below 490 MHz, the coupled power started to fall off

7. Comb Generation in a Dispersion Compensated Cavity

rapidly, dropping to 75% at 470 MHz. Taking 75% as the tolerance limit for power coupled into the modulator gives an allowable decrease in modulation frequency, and hence cavity FSR, of ~120 MHz. This equates to an increase in cavity length of ~52mm.

The next step was to decide upon how exactly to incorporate the EOM and dispersion compensation mount within the signal/idler cavity without going beyond the allowed increase in cavity length, given above. It was also necessary to keep the EOM as close to the output coupler as possible to ensure the maximum modulation depth could be accessed (as discussed in the section on FM lasers – chapter 2, section 2.5). To satisfy both these constraints, the simplest method was to insert a second lens into the signal/idler cavity and replace the curved output coupler with a plane mirror. This would create a collimated section between the lens and mirror, into which the EOM would be inserted. The dispersion-compensating mount could then be situated at the secondary beam waist between the two lenses

The required positions and focal length of the lens were found by modelling the signal/idler cavity using a piece of software known as PSST! [6].

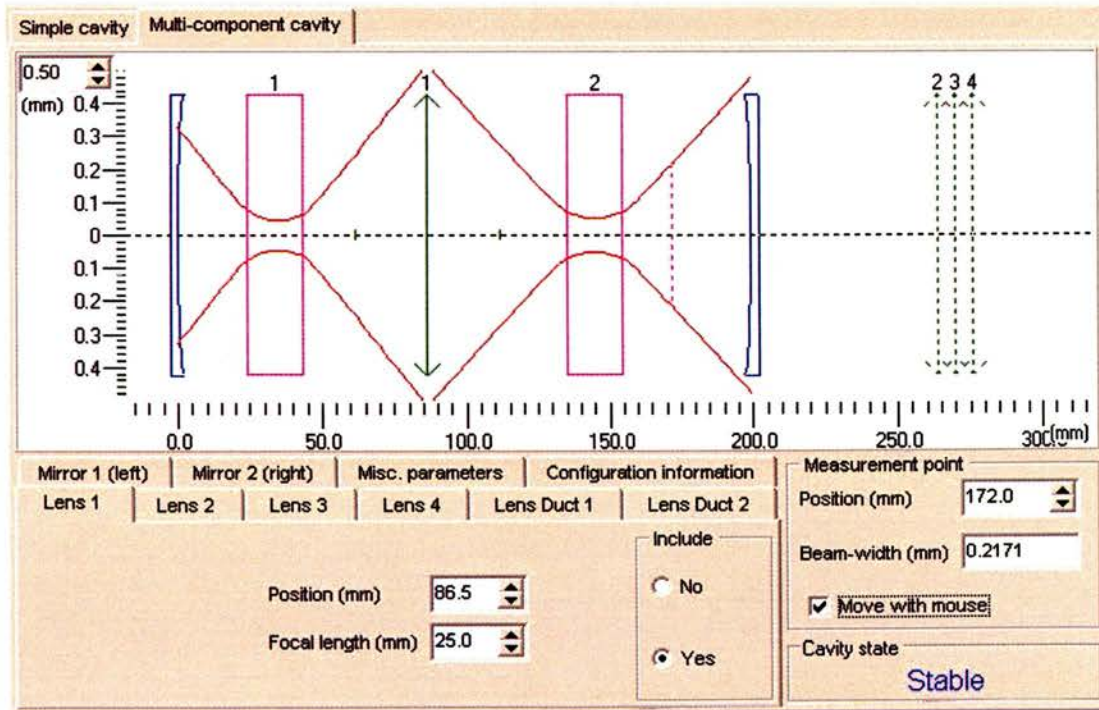


Figure 7.3 – Schematic of original signal/idler cavity

[1 – NL crystal, 2 – EOM crystal]

7. Comb Generation in a Dispersion Compensated Cavity

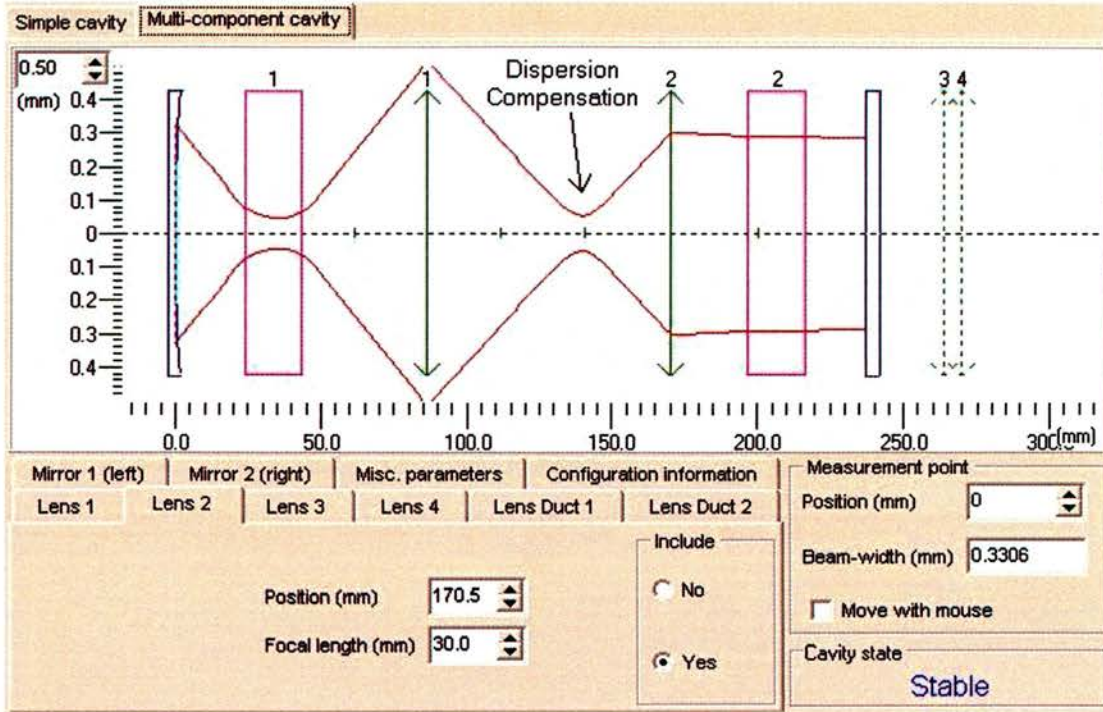


Figure 7.4 – Schematic of signal/idler cavity with collimated section
[1 – NL crystal, 2 – EOM crystal]

Figures 7.3 and 7.4 respectively show schematics of the signal/idler cavity before and after the collimated section was created. The transverse extent of the intra-cavity field (in red) is also overlaid on each schematic.

The first schematic, figure 7.3, shows the cavity whose design and development was discussed in chapter 4. Blocks 1 and 2 represent the nonlinear and EOM crystals respectively and lens 1 is the 25mm focal length lens situated before the EOM. The figure also shows that the intra-cavity field has a beam waist at the centre of each crystal, as was required when the cavity was designed. As shown by figure 7.4, the collimated arm was created by placing a 30mm focal length lens after the first lens and moving the (plane) output coupler back. The EOM was then situated in the collimated section as close to the plane mirror as possible, with the dispersion compensating mirrors at the second beam waist as indicated. The resulting increase in the optical length of the cavity was around 46mm, well below the upper limit of 52mm.

The first design for the compensating mirror mount was based on a modular system, consisting of separate mirror holders, a mounting block and interchangeable base

7. Comb Generation in a Dispersion Compensated Cavity

plates that would offset the two mirrors such that 2, 4 or 6 bounces could be achieved. Unfortunately, this system was unable to provide the required degree of parallelism between the two mirrors. As a result, a second design for the compensating mirror mount was developed. Shown in figure 7.5, the new design foregoes the modular system. Instead, the mount was milled out of a single piece of aluminium.

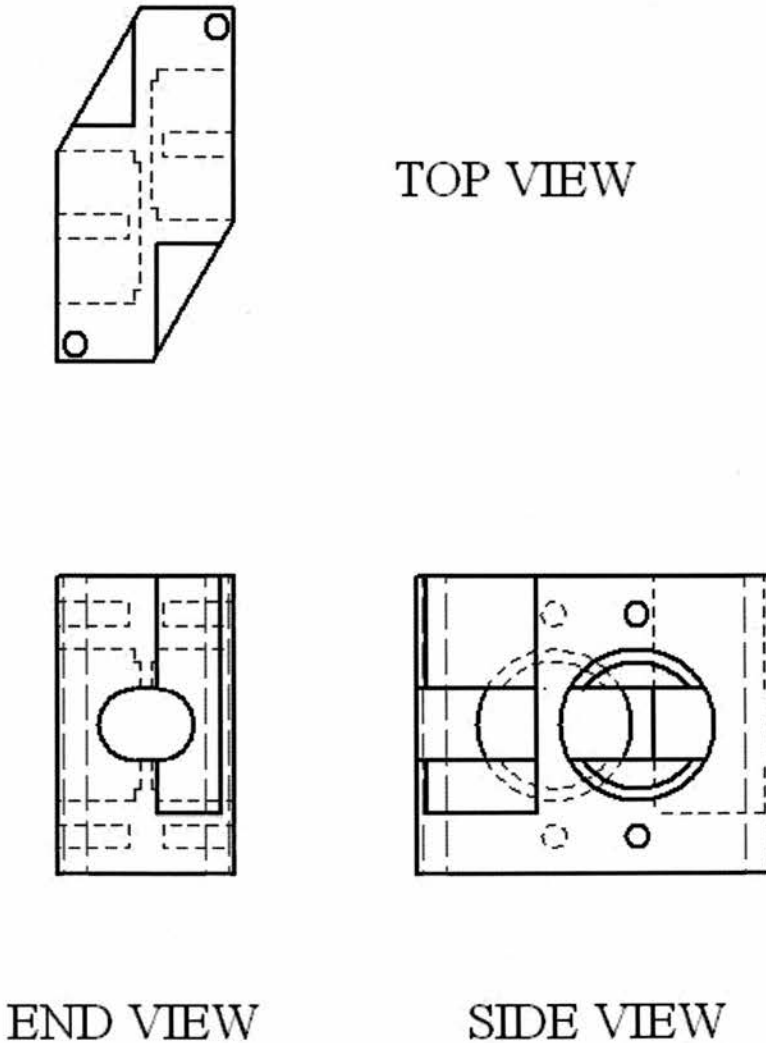


Figure 7.5 – Second design for compensating mirror mount

Holes corresponding to the diameter of the mirrors were drilled into each side of the piece, with a lip at the end of each hole for the mirrors to rest against. This ensured that the mirrors were kept parallel at a set distance apart. An elliptical bore was then created, perpendicular to the holes, to define a space for the beam to pass through.

7. Comb Generation in a Dispersion Compensated Cavity

The angular edges on each side of the mount (see top view) were designed such that a beam entering the mount on a perpendicular axis to the edge would be incident on the first mirror at an angle of 30 degrees. This was the specified incidence angle when the mirrors were ordered. A right-angled section was removed from the angular edges to give as large an input aperture as possible.

Three different mounts were designed, each with different mirror positions, to give 2, 4 and 6 bounces between the two mirrors. Each mount can be fitted onto a single block, designed to raise the whole assembly to the correct height. The block itself was mounted on a translation stage to allow fine adjustment of the compensating mirror mount within the intra-cavity field. Once the mounts had been constructed, tests outside of the FCG with the compensating mirrors inserted showed that the input and output beams were collinear. Hence, the mirrors were in the parallel configuration.

Before trying out the new mounts in the FCG, it was first necessary to calculate the increase in path length for a beam passing through each mount. This increase had to be taken into account to ensure that the cavity length did not increase above the allowable limit of 52mm. Figure 7.6 shows the parallel mirror configuration in the 6-bounce case, with the relevant distances and angles to calculate the path increase.

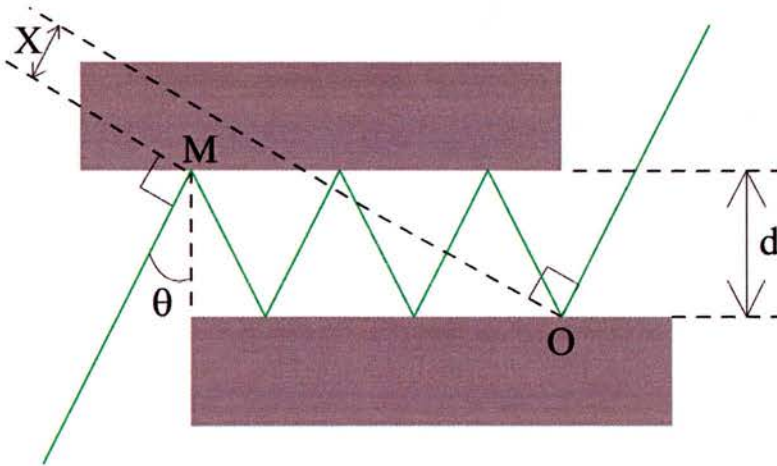


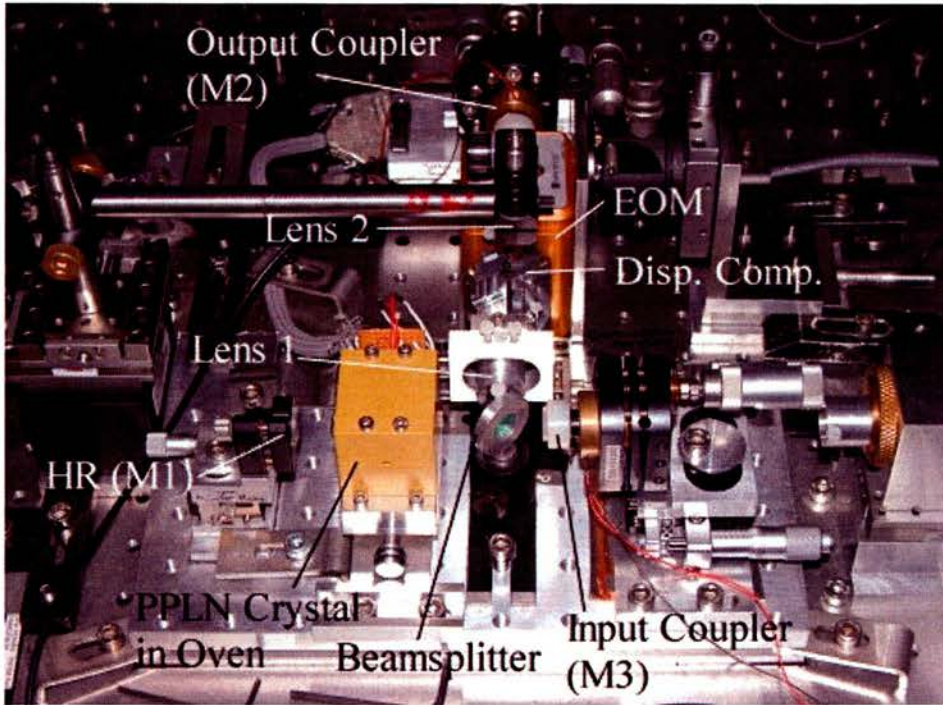
Figure 7.6 – Path increase on passing through dispersion compensation assembly

From figure 7.6, it is clear that the path increase is equal to the length of the path MO minus the distance X. Using simple trigonometry, the following equation for the path increase is obtained:

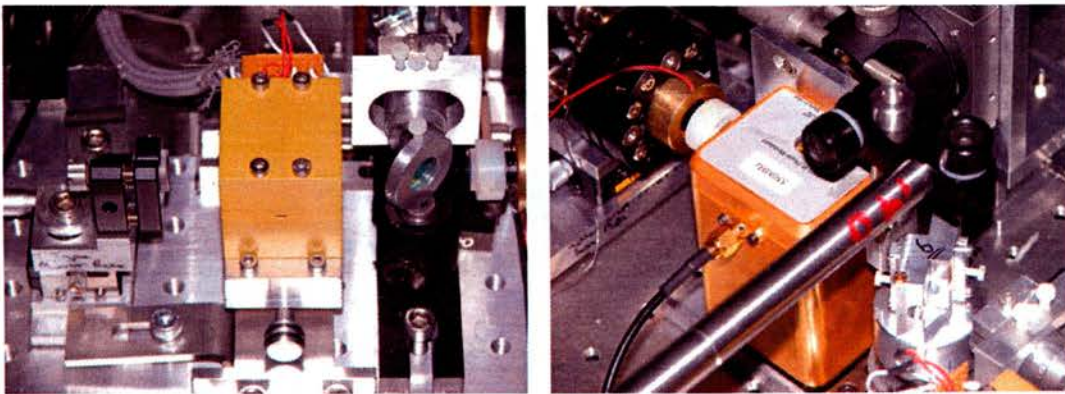
$$\text{Path Increase} = \frac{5d}{\cos \theta} - d\sqrt{1 + 25 \tan^2 \theta - 36 \sin^2 \theta} \quad (7.2)$$

7. Comb Generation in a Dispersion Compensated Cavity

In this case, $d = 2\text{mm}$ and $\theta = 30^\circ$, giving a path increase of 10.4mm. Similar calculations for the 4-bounce and 2-bounce cases give path increases of 6.9mm and 3.5mm respectively.



a



b

c

Figure 7.7 – Pictures of dispersion compensated OPO-FCG

The images in figure 7.7 above show various pictures of the dispersion compensated OPO-FCG. Image a gives an overall view of the experiment, with the main

7. Comb Generation in a Dispersion Compensated Cavity

components identified. Images **b** and **c** show a close-up of the oven containing the PPLN crystal and the EOM and dispersion compensating mount respectively.

7.2) Dispersion Compensated OPO

Given that the insertion of chirped mirrors into the cavity of a continuous wave OPO was a technique that had not been tried before, it seemed a good idea to obtain as much data as possible on the operation of such an OPO and the differences between the compensated and uncompensated cases. To this end, it was decided to place the dispersion compensation assembly into the original signal/idler cavity on its own, without the EOM present; to create a dispersion compensated OPO. This was achieved simply, by removing the EOM from its mount and replacing it with the dispersion compensation mount. It was then necessary to re-position and re-align the output coupler to give OPO oscillation. Since approximately half of the intra-cavity material, in the shape of the EOM, had been removed, half of the maximum negative dispersion was required for compensation. This corresponded roughly to the two – 250fs² mirrors in the 6-bounce mount.

The first noticeable change was in the output power characteristics of the compensated OPO. Figures 7.8 and 7.9 show the output power from the OPO in the uncompensated and compensated cases respectively. In each case, the pump cavity was locked on resonance and the signal/idler cavity scanned through a FSR.

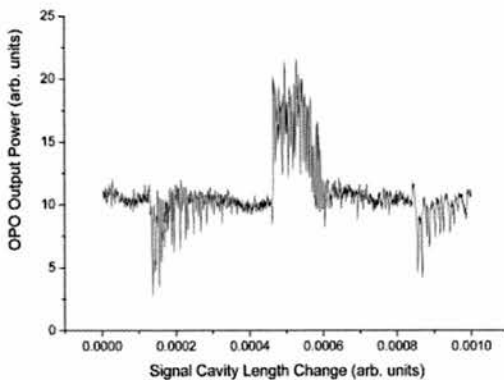


Figure 7.8 – Output power of uncompensated OPO

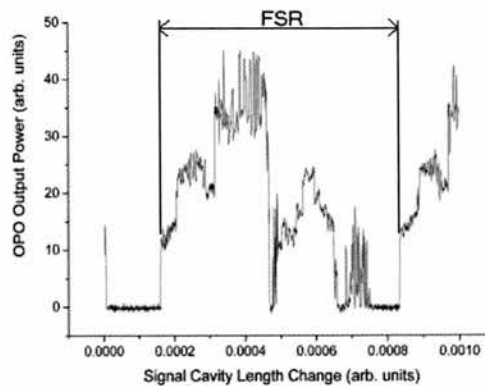


Figure 7.9 – Output power of compensated OPO

7. Comb Generation in a Dispersion Compensated Cavity

In the case of the OPO without dispersion compensation, there were significant fluctuations in the output power as the signal/idler cavity was scanned. However, the OPO remained on for the duration of the scan. The maximum output power occurred roughly at the centre of the scan, when the mirror was at the 'zero' position. This was expected, since the length of the signal/idler cavity had been optimised prior to this experiment.

With dispersion compensation, the OPO again showed significant fluctuations in output power. This time though, as shown by figure 7.9, there were also several points during the scan at which the OPO did not oscillate. This 'switching off' behaviour is exactly what would be expected with partial dispersion compensation. Recalling the vernier scale diagram from chapter 5, section 5.4, a change in cavity length causes the signal and idler modes to slide over each other. With full dispersion and a linear variation in mode spacing, there is always an overlapping signal and idler mode pair as the cavity length is altered. Therefore, the OPO always oscillates. With complete dispersion compensation, the spacing between modes is set equal. This means that there will be one particular cavity length, for each free spectral range, where all the signal and idler mode pairs overlap simultaneously and the OPO will oscillate. At all other cavity lengths, no modes will overlap and the OPO will remain off. If the dispersion compensation is only partial, as was the case in these experiments, then the operation of the OPO will be somewhere between the full dispersion and complete compensation cases. In other words, over the duration of the signal/idler cavity scan, the OPO will show periods of oscillation interspersed with points at which the OPO is off. The better the dispersion compensation, the shorter the on period for the OPO.

Also noticeable, was an improvement in the stability of the OPO. This can be put down to the lessening of mode/cluster hopping caused by the dispersion compensation. However, there is also a second factor, which comes about as an unexpected side effect of the insertion of the compensating mirrors. Previously, in the dispersive OPO, some pump light was observed to be leaking into the signal/idler cavity due to the small, but non-zero pump reflectivity of the beamsplitter. In turn, a fraction of this pump light was reflected back into the pump cavity (this reflection was used to align mirror M2 in the signal/idler cavity). Although the reflected pump light was very small, the possibility still existed that it could interfere with the downconversion process and reduce the overall stability of the OPO. Now, the

7. Comb Generation in a Dispersion Compensated Cavity

chirped mirrors were not designed to be highly reflective at the pump wavelength, although some inherent reflectivity may well exist. Therefore, the dispersion compensating assembly, with 6 bounces between the two mirrors, will filter out any residual pump light in the signal/idler cavity via transmission through the mirrors. As a result, with no reflected pump light to cause interferometric effects, the stability of the OPO would be expected to improve.

To observe the spectral properties of the dispersion compensated OPO, part of the output was fibre-coupled into an OSA, as with previous experiments. This showed that, with the current set-up, the OPO was operating away from degeneracy, between 1560nm and 1580nm for the signal and 1640nm and 1660nm for the idler. In an attempt to tune the OPO towards degeneracy and also to observe the effect on the dispersion compensation, it was decided to change the temperature of the nonlinear crystal from 169°C to 168°C in steps of 0.2°C. Figure 7.10, shows the output power of the OPO in each case as the signal cavity was scanned at 20 Hz.

7. Comb Generation in a Dispersion Compensated Cavity

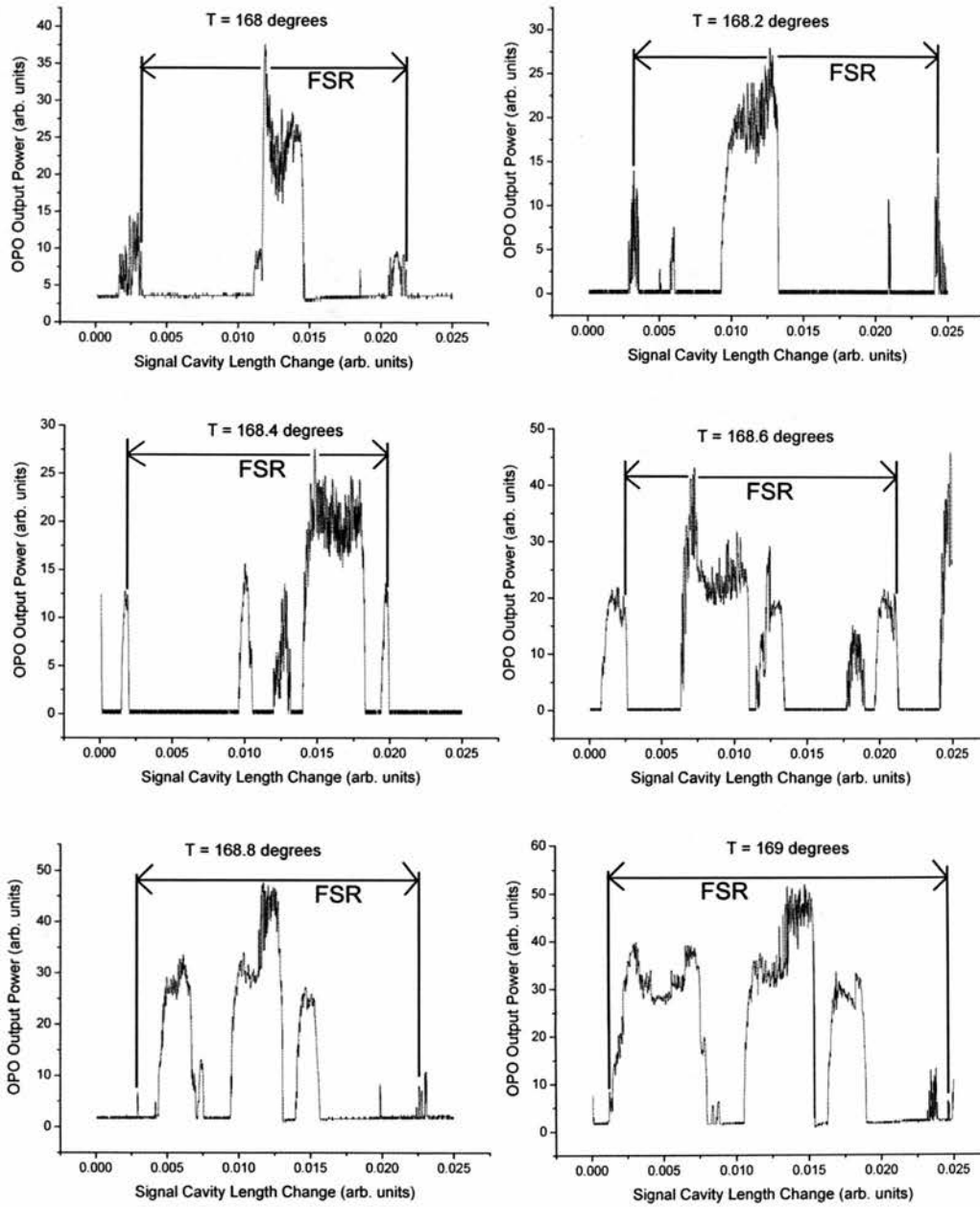


Figure 7.10 – Output power of OPO as crystal temperature decreased

It is immediately apparent from the output power traces that points at which the OPO was off during the signal cavity scan increased dramatically as the temperature of the nonlinear crystal was decreased. These results can be explained by the consideration of two factors. Firstly, the positive dispersion in the cavity is due to the variation of refractive index with frequency. Since the refractive index is also dependent on the temperature of the crystal, a change in temperature would be expected to alter the crystal dispersion. Here, the effect on the positive dispersion was to decrease it

7. Comb Generation in a Dispersion Compensated Cavity

towards the negative dispersion provided by the chirped mirrors, thereby improving the compensation. The variation of positive dispersion with crystal temperature can be modelled, as shown in figure 7.11, by utilising the analysis in chapter 6, section 6.1 and the Sellmeier data for LiNbO_3 [3]. This confirms that the positive intra-cavity dispersion does decrease as the temperature of the nonlinear crystal is decreased. As previously discussed, better compensation leads to a shorter on period on the output power trace.

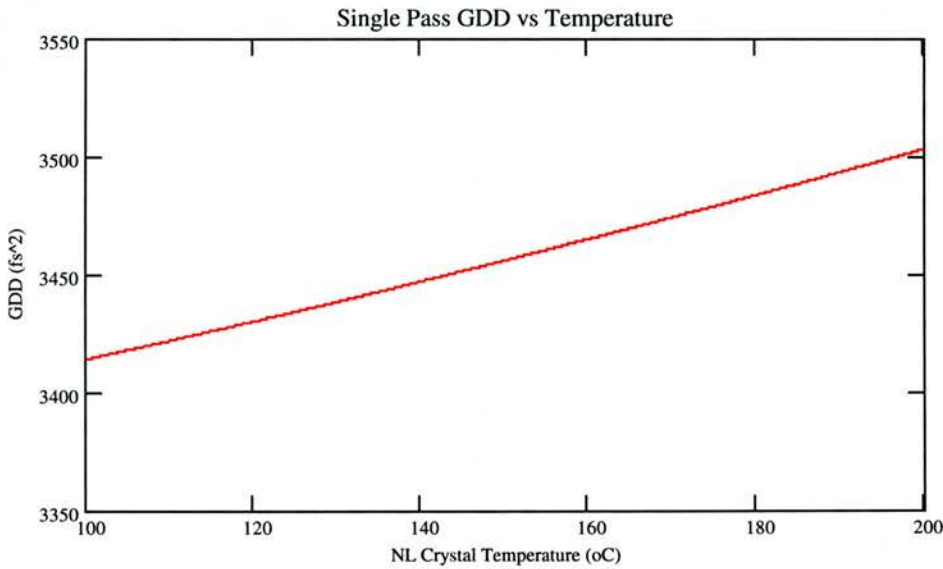


Figure 7.11 – Variation of positive dispersion with NL crystal temperature

The second factor is the location and extent of the phasematching bandwidth of the OPO. All other things being equal, this is also dependent on the crystal refractive index. Therefore, a temperature change will alter the extent of the phasematching bandwidth and its centre frequency. In this case, the output power traces indicate that the centre of the bandwidth was moved towards degeneracy. This is confirmed by the temperature tuning curve for PPLN in figure 7.12, which utilises equation (1.22) and the Sellmeier data for LiNbO_3 [3] to plot the signal and idler wavelengths that will give perfect phasematching for a fixed grating period. Figure 7.12 shows that the signal and idler wavelengths move towards degeneracy (at just below 170°C) with decreasing crystal temperature. As a result, overlapping mode pairs far away from degeneracy experienced a reduction in gain to the point that they could no longer oscillate, accounting for the observed increase in the off period during the signal cavity scan.

7. Comb Generation in a Dispersion Compensated Cavity

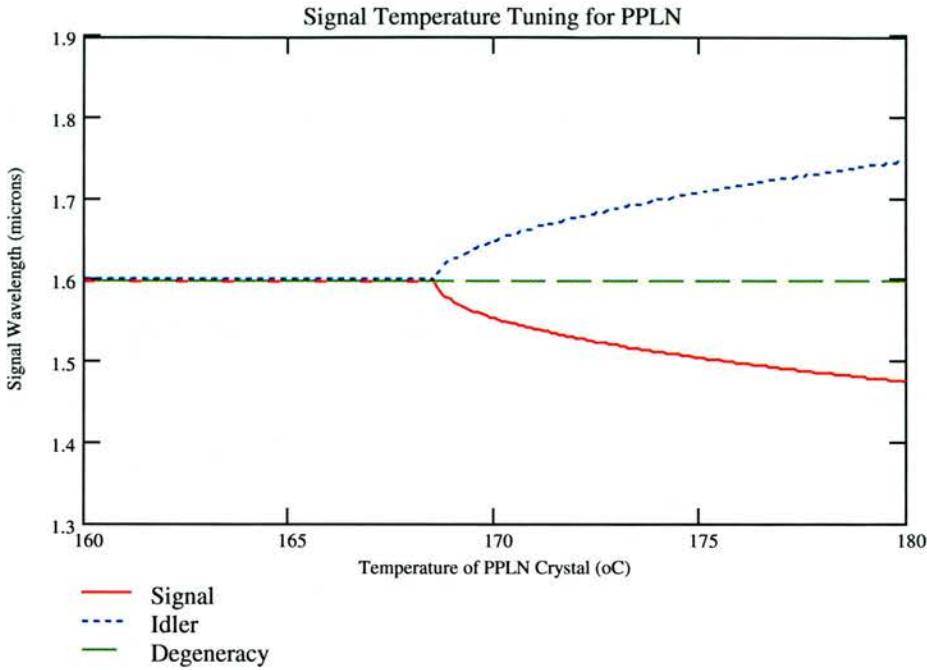


Figure 7.12 – Temperature tuning curve for PPLN

The spectral output of the OPO at the final temperature of 168°C is shown in figure 7.13 below.

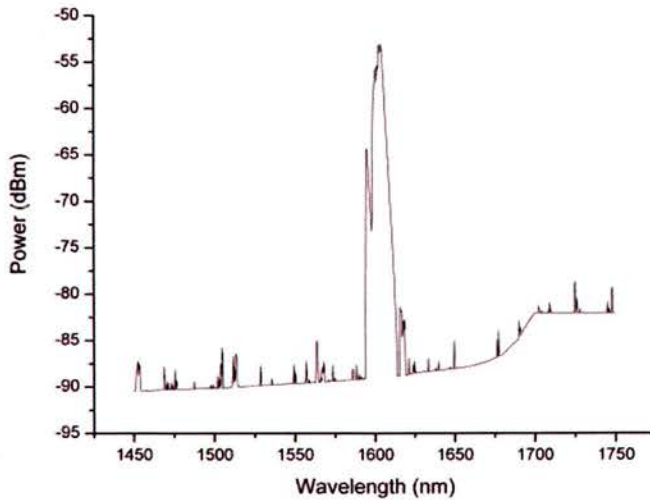


Figure 7.13 – Spectral output of OPO at T = 168°C

It can be seen from the OSA trace in figure 7.13 that, with a crystal temperature of 168°C, the OPO operated around degeneracy with signal/idler wavelengths confined to a narrow range between 1590nm and 1615nm. This strongly suggests that the

7. Comb Generation in a Dispersion Compensated Cavity

centre of the phasematching bandwidth was moved close to degeneracy by the temperature change.

In the final experiment performed with the dispersion compensated OPO, one of the -250fs^2 mirrors in the compensation assembly was replaced, firstly with a -100fs^2 mirror and then with a -550fs^2 mirror. The purpose of this experiment was to confirm that the pair of -250fs^2 mirrors were providing the best dispersion compensation. Whilst the previous results indicated that this was the case, it was felt necessary to obtain as much evidence as possible.

As a further advantage of the dispersion compensation assembly, the changing of the mirror was accomplished in-situ, with the OPO oscillating as soon as the replacement mirror was secured in place. At most, a slight adjustment of the output coupler was required to obtain the maximum output power.

The output power and spectral results with the -100fs^2 mirror at a crystal temperature of 168°C are given in figures 7.14 and 7.15 respectively.

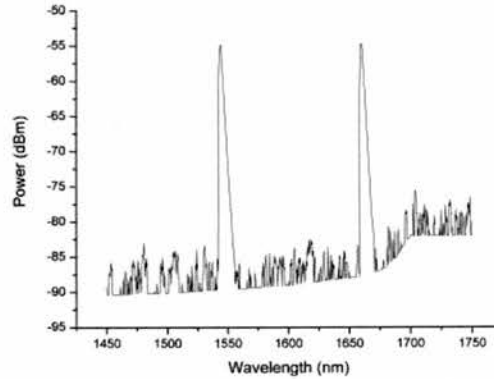
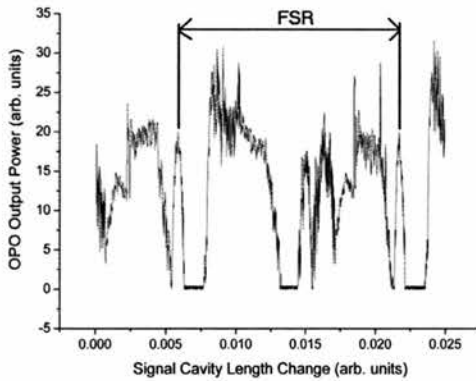


Figure 7.14 – Output power with -100fs^2 mirror

Figure 7.15 – Spectral output with -100fs^2 mirror

In comparison with the final trace of figure 7.10, it is obvious from figure 7.14 that the time over which the OPO was on during the signal cavity scan had significantly increased. The OSA trace in figure 7.15 shows the OPO operating away from degeneracy at around 1550nm and 1660nm. It was also observed to operate at degeneracy, suggesting that some cluster hopping was taking place between these regions.

Figures 7.16 and 7.17 show similar results for the -550fs^2 mirror.

7. Comb Generation in a Dispersion Compensated Cavity

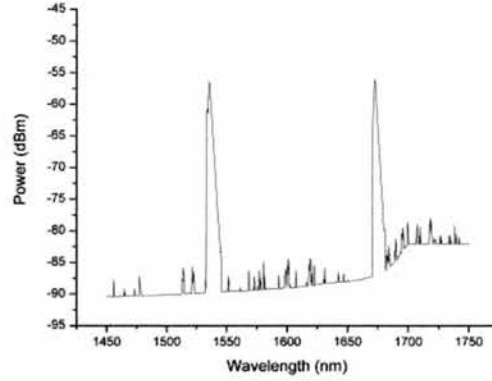
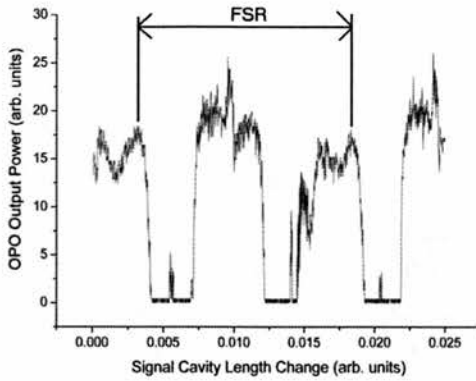


Figure 7.16 – Output power with -550fs^2 mirror **Figure 7.17 – Spectral output with -550fs^2 mirror**

As with the -100fs^2 mirror, figure 7.16 shows that the insertion of the -550fs^2 mirror caused a significant increase in the on period of the OPO. The similarity in the spectral outputs between the -100fs^2 and -550fs^2 mirrors is also clear to see from figure 7.17. Again, the OPO operated away from degeneracy around 1540nm and 1675nm and was also observed to operate at degeneracy, pointing towards the occurrence of a cluster hop.

In both cases, the increase in the time that the OPO was on and the shifting of spectral output away from degeneracy imply that the dispersion compensation was significantly worsened, compared to the pair of -250fs^2 mirrors.

Concluding that two -250fs^2 mirrors gave the optimum dispersion compensation in the case of the OPO with no EOM, when the EOM was returned to the signal/idler cavity alongside the dispersion compensation assembly (see figure 7.4) the two -550fs^2 mirrors were used to provide compensation. In the next two sections, experiments and subsequent results for frequency comb generation with dispersion compensation are discussed.

7. Comb Generation in a Dispersion Compensated Cavity

7.3) *Characterisation of Dispersion Compensated FCG*

After inserting the compensating mirrors and re-aligning the plane mirror (M2), a quick power measurement showed that the threshold had approximately doubled over the non-compensated case. There are a couple of factors likely to be responsible for the increase in threshold. Due to the 6 bounces between the chirped mirrors, even a very small transmission or absorption at the mirror surface will be amplified on passing through the entire assembly. Furthermore, the beam passes through the assembly twice on a single round trip, doubling the overall loss. The second factor is the change that was made to the design of the signal/idler cavity and its effect on the size of the beam waist in the nonlinear crystal. The PSST! simulations show that the position of the second intra-cavity lens is critical here, with a small translation of the lens along the cavity axis causing a large change in the beam waist. Since the radius of the beam waist is crucial in determining the threshold (see chapter 4, section 4.2), the increase in threshold could well be due to the lens being slightly out of the optimum position.

As stated in the introduction, to ensure that the OPO remained on it was necessary to carefully control the length of the signal/idler cavity. Normally, this requires some form of active stabilization with electronic feedback and in this case a simple side-of-fringe scheme (see chapter 3, section 3.5) was employed. The output from mirror M2 was focused onto a photodetector. A variable bias voltage was then subtracted from the proportional voltage produced by the photodetector to create an error signal, which was fed back to the PZT on M2 via high voltage amplifier. By altering the bias voltage, the output power level to which the OPO would lock could be varied.

Figure 7.18 shows the output power of the FCG with dispersion compensation as the signal/idler cavity was scanned at 20 Hz, with the temperature of the nonlinear crystal set to 168°C.

7. Comb Generation in a Dispersion Compensated Cavity

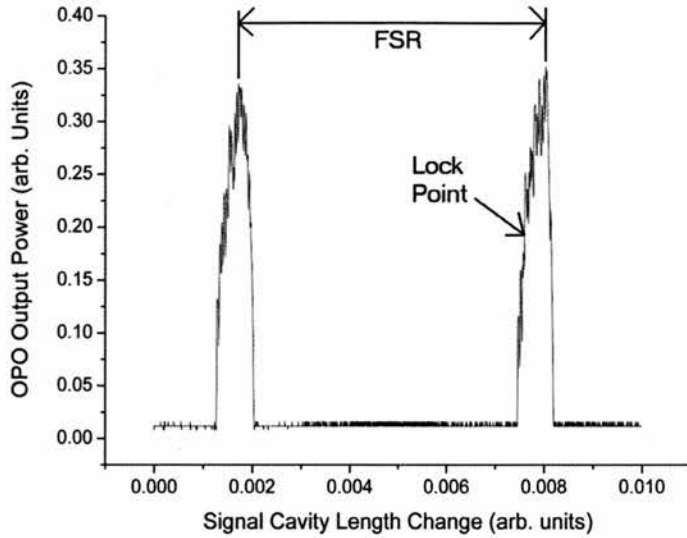


Figure 7.18 – Output power of dispersion compensated FCG

It is immediately apparent from the above figure that the OPO was off for the majority of the cavity scan, with the on period corresponding to roughly $1/10^{\text{th}}$ of the entire FSR. As explained in the previous section, this suggests that the dispersion compensation is very good, with a close match between the positive intra-cavity GDD and the negative GDD of the dispersion compensation assembly.

Spectral data for the dispersion compensated FCG, taken with the OSA, is shown in figures 7.19 and 7.20 below.

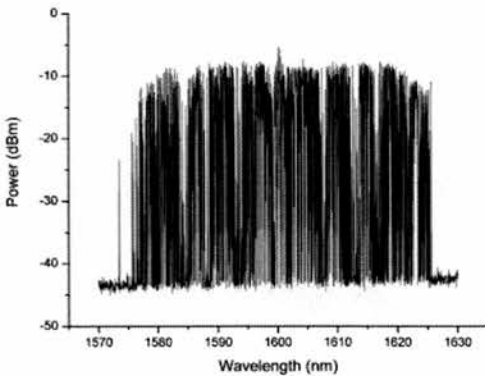


Figure 7.19 – Overall spectral structure

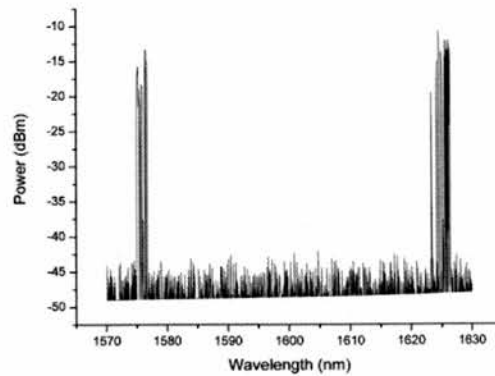


Figure 7.20 – Spectral output when signal/idler cavity stabilised

7. Comb Generation in a Dispersion Compensated Cavity

The figure on the left was taken with the signal/idler cavity scanned at the usual 20 Hz and with the OSA on a very slow scan – 0.05 Hz. This meant that the signal/idler cavity was scanned 400 times for a single scan of the OSA. As a result, figure 7.19 shows the entire range of wavelengths over which the OPO operated during the numerous cavity scans. The picture can also be interpreted as a representation of the gain bandwidth of the OPO, which covers approximately 50nm (1575nm to 1625nm), appears to peak at degeneracy and begins to fall off at the wings. This suggests that the gain bandwidth is centred at or close to degeneracy.

The right hand figure shows the spectral output of the OPO when the signal cavity was stabilised using the side-of-fringe scheme. In this case the bias voltage was set high, to lock the OPO at a low output power level. This corresponded to the outer edges of the gain bandwidth, as shown by figures 7.19 and 7.20. By changing the bias level and hence the output power level at which the OPO was locked, the OPO could be made to operate at various points within the gain bandwidth. It should be noted that, whilst locked, the OPO operated continuously at the signal and idler wavelengths shown in figure 7.20 with no sign of cluster hopping or significant drifting in frequency. The position of the lock point, in terms of the OPO output power level, is shown on figure 7.18. The fact that this point is on the left hand side of the power curve and the overall shape of the curve itself can be explained by a consideration of the location of the phasematching bandwidth, and will be discussed at the end of this section.

With the spectral and output power data from figures 7.18 and 7.19, it is possible to obtain an approximate value for the change in mode spacing per FSR with dispersion compensation. The procedure is very similar to that used in chapter 6, section 6.2, which gave a change in mode spacing of 9.6 Hz for a single FSR. Recalling equation (6.26),

$$Total\ Offset = \int_0^{N_f} N \Delta \nu dN = \frac{N_f^2 \Delta \nu}{2} \quad (7.3)$$

In this case, the OPO was on for 1/10th of the signal/idler cavity FSR, which represents the total offset in mode spacing across the gain bandwidth. The FSR of the signal/idler cavity with the dispersion compensation assembly was found to be around 520 MHz, giving a total offset of 52 MHz. Within the gain bandwidth of 50nm (5.85 THz), the total number of modes, N_f , is approximately 11200. After rearranging

7. Comb Generation in a Dispersion Compensated Cavity

equation (7.3), the change in mode spacing for a FSR, $\Delta\nu$, turns out to be around 1 Hz. Between adjacent mode pairs, the mode spacing increases progressively by 1 Hz and the change in mode spacing at the final mode pair (opposite side of bandwidth) is therefore equal to 11.2 kHz. This results in a cumulative change in mode spacing of 52 MHz, less than $1/10^{\text{th}}$ of the value in the non-compensated case.

Previous results have suggested that the gain bandwidth of the OPO was centred on degeneracy. Further indication can be gained by a close examination of the output power curve when the signal/idler cavity is scanned. To see how this arises, consider the following vernier scale diagram, which shows a series of signal and idler modes with heavily exaggerated changes in mode spacing.

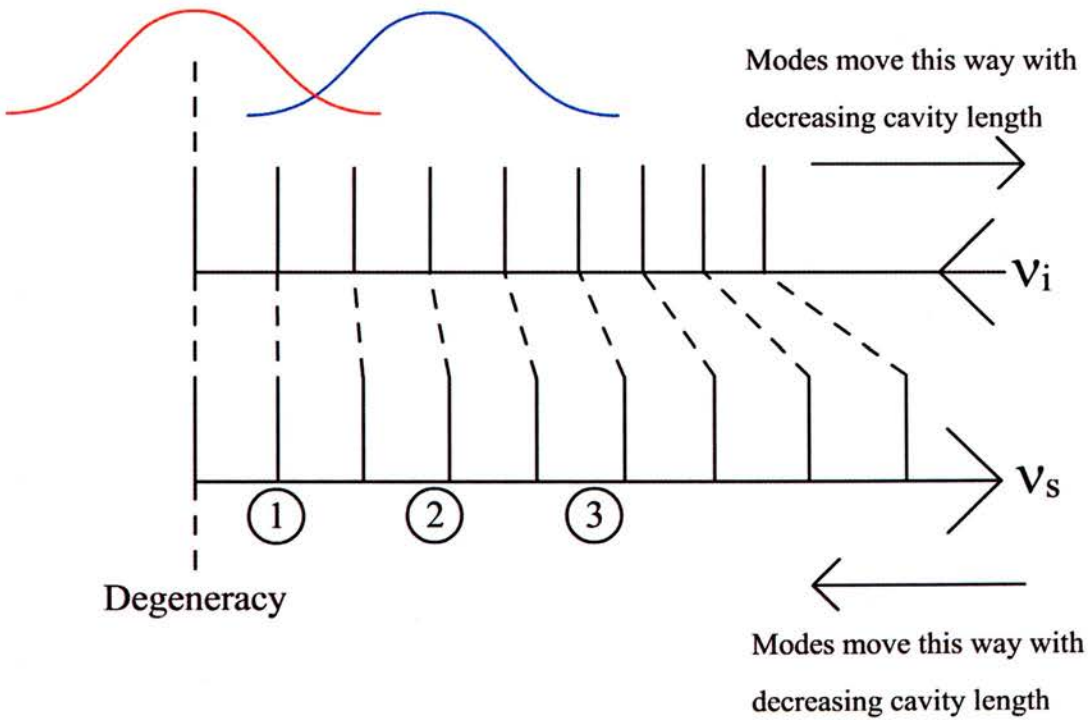


Figure 7.21 – Vernier scale diagram and gain bandwidth

In figure 7.21, the frequency of the idler modes increases from right to left and for the signal modes, from left to right. In this way, for any vertical line, the sum of the idler and signal frequencies can be arranged to sum to the pump frequency, thus fulfilling the energy conservation constraint. The vertical lines shown on the diagram represent cavity resonance frequencies and alignment of a signal resonance with an idler resonance corresponds to signal and idler resonance conditions being satisfied

7. Comb Generation in a Dispersion Compensated Cavity

simultaneously. This alignment must occur within the parametric gain bandwidth for oscillation to occur. Tuning the cavity by altering the cavity length causes one set of modes to slide to the right and the other set to the left as indicated.

Taking the blue gain bandwidth first, whose centre is shifted away from degeneracy, what would be the shape of the output power curve? Starting from a cavity length where no modes line up on the vernier scale and decreasing the cavity length, the modes at position 1 would line up first, followed by 2 and 3. Taking the gain at each of these positions, the output power curve would have a symmetric shape, with the peak corresponding to the centre of the gain bandwidth at position 2 (shown diagrammatically in figure 7.22).

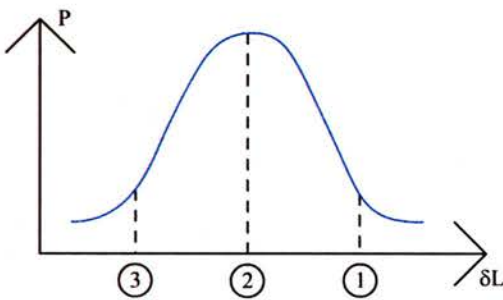


Figure 7.22 – Symmetric output power curve corresponding to blue gain bandwidth

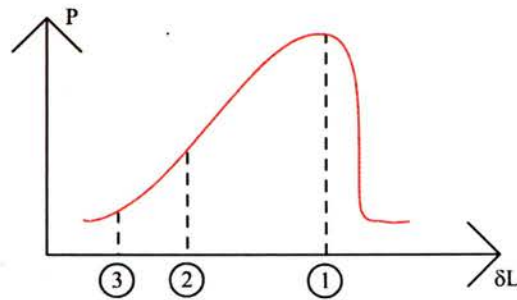


Figure 7.23 – Asymmetric output power curve corresponding to red gain bandwidth

If the gain bandwidth is more like the red case and centred at or near to degeneracy then, with the same conditions as before, the mode pairs will come into alignment in the same order. However, in this case, the peak of the bandwidth corresponds to position 1. In terms of the output power curve, this manifests as a sharp increase to a peak followed by a much shallower decrease as the modes at positions 2 and 3 come into alignment. The resulting shape of the curve will therefore be asymmetric, as shown in figure 7.23. It is apparent from figure 7.21 that, if the cavity length is increased beyond the point where the mode pair at degeneracy align (and hence come in to oscillation), no further alignments can occur. Therefore, the OPO will switch off very abruptly, explaining the rapid decrease in output power to the left of point 1 in figure 7.23.

7. Comb Generation in a Dispersion Compensated Cavity

From the previous analysis, it is clear that an examination of the shape of the output power curve can give a good indication as to the position of the gain bandwidth with respect to degeneracy. In the dispersion compensated FCG, it seemed likely that the gain bandwidth was centred on degeneracy. Therefore, an asymmetric output power curve would be expected. To see if this was the case, a magnified trace of the output power curve was taken from the oscilloscope with the timebase reduced by a factor of 10. Figure 7.24 shows this trace, alongside a trace taken at the previous timebase for comparison.

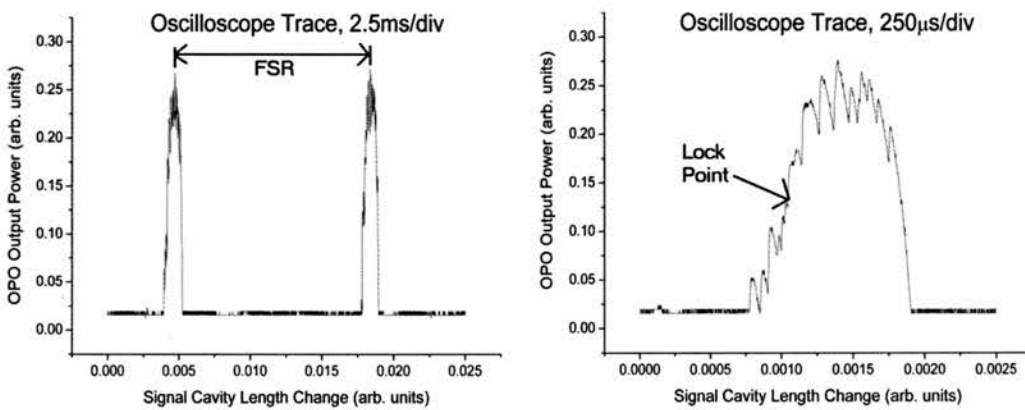


Figure 7.24 – Close-up of output power trace

Despite some fluctuations in power, the right hand trace clearly shows that the output power curve was asymmetric. This confirms, as expected, that the phasematching bandwidth for the dispersion compensated FCG was centred on, or very close to degeneracy. The OPO was locked at the point shown on the right hand trace. From the previous analysis, this corresponds to signal and idler frequencies away from degeneracy, which is confirmed by the experimental results in figure 7.20.

So far, all of the results in this section have dealt with the characterisation of the OPO and the dispersion compensation within the FCG. In conclusion, these results show a frequency stable OPO with a phasematching bandwidth centred on degeneracy and spanning at least 50nm. Compensation for the positive intra-cavity dispersion appears to be close to perfect, with the FSR only changing by around 1 HZ per mode pair. With characterisation of the OPO and dispersion compensation complete, it was time to begin the comb generation experiments.

7. Comb Generation in a Dispersion Compensated Cavity

7.4) *Experimental Comb Generation 4 (Dispersion Compensated)*

The previous results from the characterisation of the dispersion compensated FCG were all taken at the maximum available pumping level of $\sim 600\text{mW}$. Given the difficulty in achieving comb generation at the optimum pumping level in the uncompensated case, it was decided to continue working at the maximum level for the following experiments.

The first task was to find the correct modulation frequency to match the cavity FSR, also known as the *resonance* point. This was necessary because components in the signal/idler cavity had been moved during the insertion of the compensating mirrors. Whilst steps were taken to ensure that the cavity length changed as little as possible over the uncompensated case, some variation in the mode spacing was expected. Additionally, there was also the possibility that the compensating mirrors might introduce a first order phase shift to the intra-cavity field, resulting in a change to the mode spacing. To facilitate the search, mirrors with low negative dispersion (-100 fs^2) were used initially. This ensured that the OPO remained on over a wide range of cavity lengths whilst scanning for the correct modulation frequency.

Starting from the modulation frequency used for comb generation in the uncompensated case, 522.05 MHz (see chapter 5, section 5.5), and searching outwards, the new resonance point was found at 514.24 MHz . This corresponded to a relatively large change in cavity length of 4.5mm . Therefore, it seems likely that the shift in resonance was due to a combination of cavity length change and phase shift at the compensating mirrors.

Since the dispersion compensating mirrors could be exchanged in-situ, negligible change in cavity length was expected when inserting the mirrors for full compensation (-550 fs^2). However, with full compensation, a shift in the resonance point to 514.165 MHz was observed. This was put down to either a change in phase shift between the two sets of mirrors or a small drift in cavity length ($\sim 40\mu\text{m}$). When generating a frequency comb at this modulation frequency, a modulation depth of $\sim 0.5\text{ rad}$ was used (as in the uncompensated case). It was also necessary to have the OPO free running, as modulating at the resonance point interfered with the stabilisation of the

7. Comb Generation in a Dispersion Compensated Cavity

signal/idler cavity. Figure 7.25 and shows a number of OSA traces of the resulting frequency combs and a comb generated with low compensation for comparison.

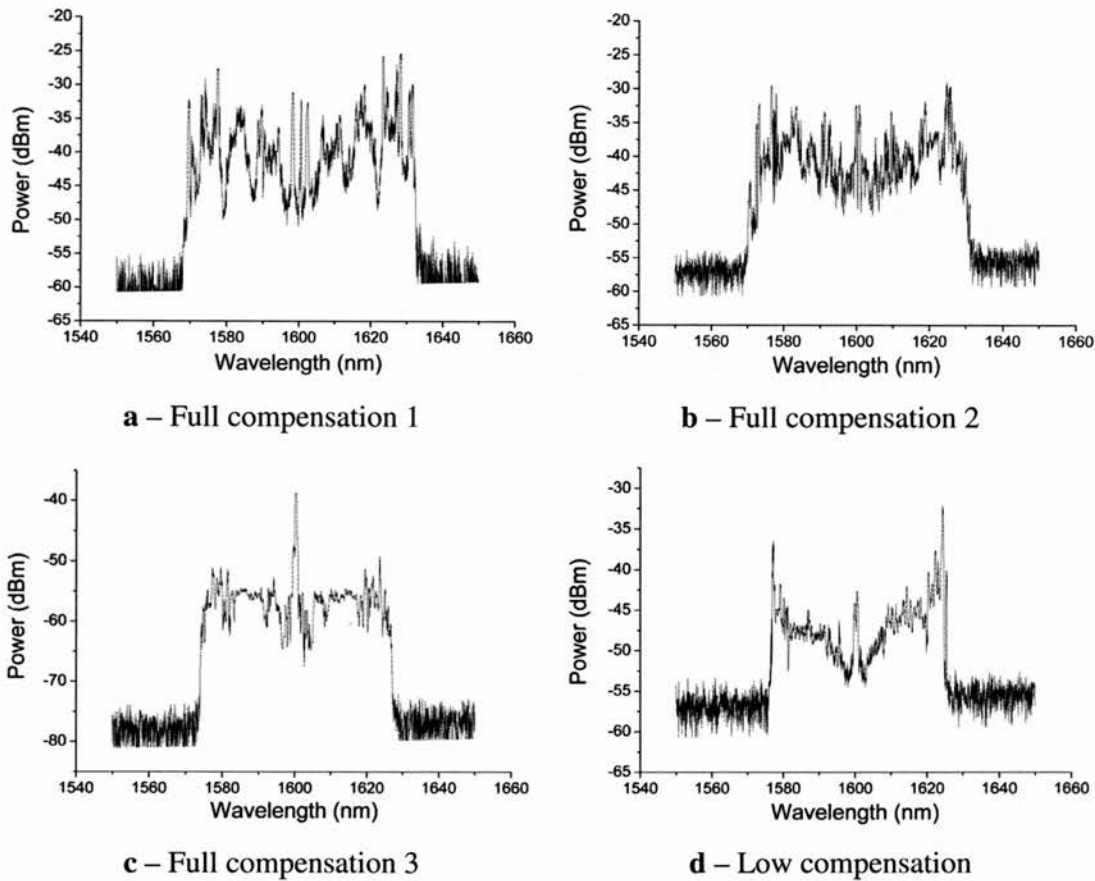


Figure 7.25 – Frequency comb generation with dispersion compensation

It should be first noted that the differences in power amongst the images in figure 7.25 were due to repositioning or realignment of the analysis equipment rather than an effect of the dispersion compensation. As might be expected, the frequency comb generated with low dispersion compensation, image **d**, has a similar width to the uncompensated case of around 50nm (see chapter 5, figure 5.8). In this case, the negative dispersion of the mirrors was only $1/6^{\text{th}}$ of the positive intra-cavity dispersion and therefore comparable to having no compensation at all.

With full compensation, figure 7.25a shows that a comb spanning $\sim 70\text{nm}$ (8.2 THz) and centred on 1600nm was generated. Given the modulation frequency of around 514 MHz, this suggests the simultaneous oscillation of nearly 16000 modes. However, this image also shows large power fluctuations of around 23dBm. Through careful control of the FCG cavity length, the combs shown in 7.25b and 7.25c were generated, with power fluctuations of 18dBm and 13dBm respectively. The width of

7. Comb Generation in a Dispersion Compensated Cavity

these combs was narrower than 7.25a at around 60nm. There is a large central feature in 7.25c, which can also be seen, to a lesser extent in the other images. It is most apparent in figure 7.25c because this trace was taken after the fibre input to the OSA had been moved behind M1, to collect the signal/idler leakage and allow the heterodyne experiment (see next section) to be set up. The fact that the feature was detected with the FCG cavity blocked indicated that it was due to parametric fluorescence rather than a product of the comb generation process.

Also observed was an increase in the lifetime of the comb. Despite minor fluctuations in width, it was observed to last for several minutes. The disappearance of the comb often coincided with the OPO switching off altogether, suggesting that it might have been due to a drifting of the cavity length.

The results in figure 7.25 show that the implementation of dispersion compensation increased the comb width by up to 20nm over the uncompensated case. Significant reduction in power fluctuations across the comb envelope was also achieved, but with a reduction in the maximum comb width of around 10nm. The increase in comb width in both cases does seem a little disappointing, given the effect of the dispersion compensation on the operation of the OPO seen in the previous sections. However, the observed spectral width in figure 7.19 indicates a phasematching bandwidth of around 50nm, which is comparable to the dispersion compensated comb widths. This implies that it is the phasematching bandwidth that limits the comb widths in figure 7.25a-c, which would be expected when there is no limitation due to dispersion. As a result, there exists the potential to further increase the comb width by optimising the phasematching bandwidth via the PPLN temperature, for example. Alternatively, the PPLN could be replaced by a nonlinear crystal with a larger phasematching bandwidth.

In terms of the resonance bandwidth i.e. the range of modulation frequencies over which comb generation took place, there was a significant difference between the compensated and uncompensated cases. With full compensation, a change in modulation frequency of 10 kHz was enough to have a detrimental effect on the frequency comb. This corresponds to $1/10^{\text{th}}$ of the bandwidth of the uncompensated FCG and is in good agreement with the predicted change in mode spacing across the comb width (see section 7.3).

Another notable difference was observed in the fundamental beat frequency. This is shown for a range of modulation frequencies about the resonance point in figure 7.26

7. Comb Generation in a Dispersion Compensated Cavity

and should be compared to figure 5.9 in chapter 5. The resolution bandwidth and sweep time were 300 kHz and 50 ms respectively.

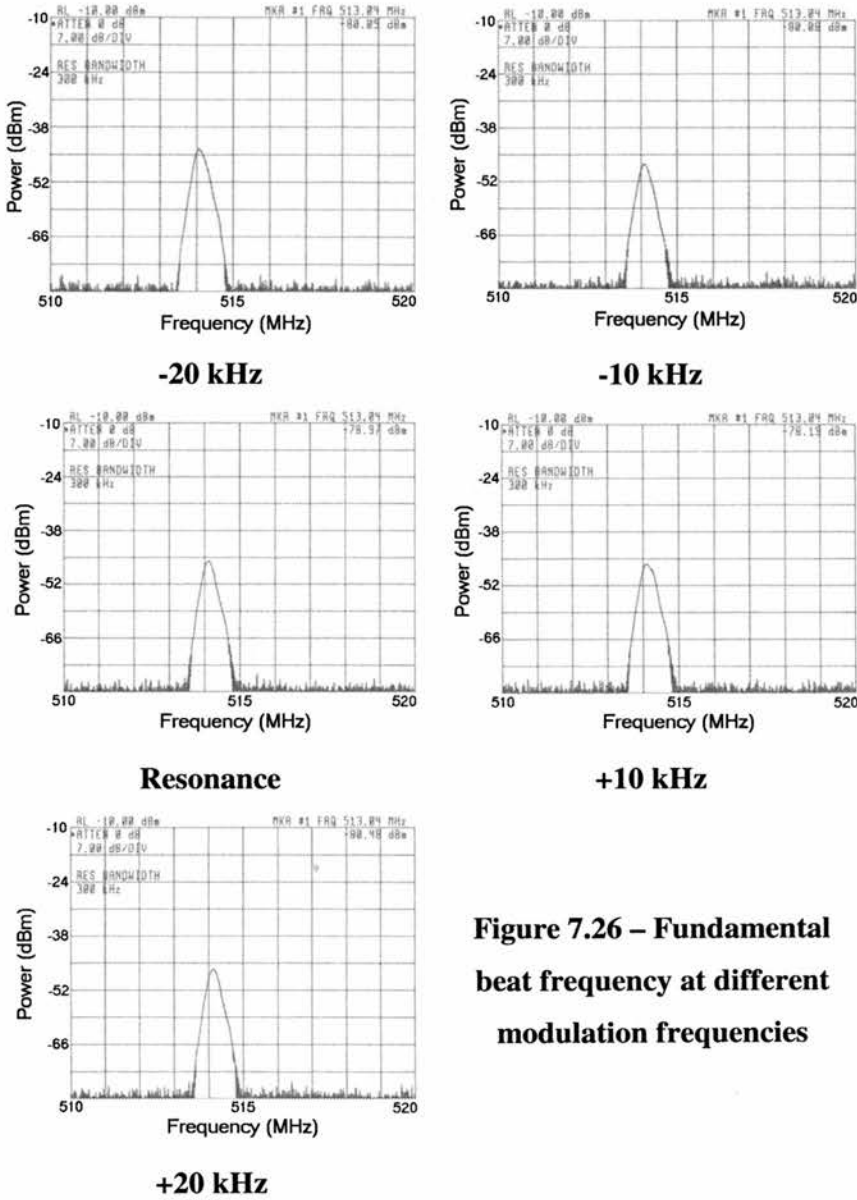


Figure 7.26 – Fundamental beat frequency at different modulation frequencies

The above traces show that the noise level in the wings of the fundamental beat frequency remains at the noise floor of the RFSA as the modulation frequency is varied through the resonance point. This is in marked contrast to the uncompensated case, which shows a decreasing noise level as resonance is approached. The results in figure 7.26 do however seem to fit with the large decrease in resonance bandwidth and the equalisation of longitudinal mode spacing across the width of the comb. With

7. Comb Generation in a Dispersion Compensated Cavity

equal mode spacings, even a small shift in modulation frequency away from the resonance point will result in every sideband being out of alignment. Therefore, the transfer of power into adjacent cavity modes will rapidly diminish and significant beating will only occur between sidebands and the central signal/idler frequency. Hence the observation of a noise-free beat frequency.

7.5) Heterodyne Experiments

To conclude the dispersion compensation experiments and the entire project described by this thesis, it was decided to obtain definitive confirmation that a comb of phase-locked frequencies existed beneath the envelopes shown in figure 7.25. This was achieved by heterodyning the comb output with a narrow linewidth, single-frequency source at an arbitrary wavelength within the comb, as previously undertaken by Diddams et al [4]. A suitable, inexpensive source was found to be a fibre-coupled DBR laser diode [5], with wavelengths available in the region of 1600nm and linewidths under 10 MHz. The output from this diode was mixed with the OPO-FCG output on the fast photodiode and the resulting RF signal viewed on the RFSA. Figures 7.27 shows two traces taken from the RFSA, with a frequency span from 0 – 600 MHz, a resolution bandwidth of 300 kHz and a sweep time of 1s.

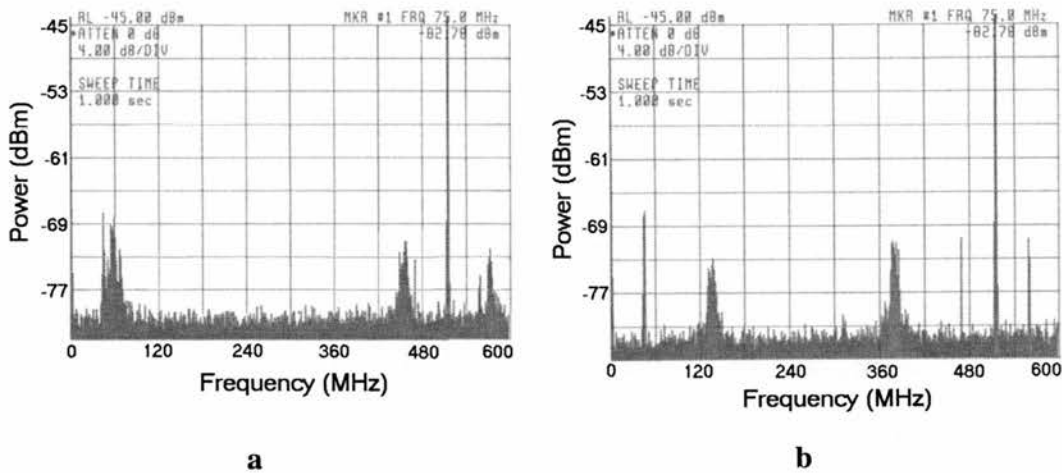


Figure 7.27 – Heterodyne signal between frequency comb and DBR laser

Trace **a** shows four peaks of interest. The large, narrow peak corresponds to the fundamental beat frequency between modes in the comb, at a frequency of just over

7. Comb Generation in a Dispersion Compensated Cavity

514 MHz. The high amplitude is due to the fact that it is made up of contributions from every mode within the comb. The other three peaks are at frequencies of ~55 MHz, ~457 MHz and ~570 MHz. These correspond to beat frequencies between the DBR laser output, at a wavelength of around 1609.5nm, and the modes in the frequency comb. The first two peaks, whose frequencies sum to the modulation frequency, represent heterodyning with the two nearest neighbour modes to the DBR frequency. The latter peak ($\approx 514 + 55 \text{ MHz}$) represents heterodyning with the second nearest neighbour mode. In trace **b**, the RF signal is shown after changing the temperature of the DBR laser. This corresponded to a shift in wavelength of 0.45nm and a shift in frequency of 52 GHz (i.e. across 100 modes within the frequency comb). As a result the peaks from trace **a** shifted to new positions at ~137 MHz and ~378 MHz, whilst the beat between modes in the comb remained at a constant frequency. In fact, during the temperature tuning of the DBR laser the peaks were clearly observed to move on the RFSA screen. The origin of the smaller, narrow peaks in trace **b** is unclear. However, they were found to be unrelated to the DBR laser, since they did not disappear when it was switched off.

The existence of beat frequencies between the comb and DBR laser at an arbitrary wavelength within the comb envelope provides definitive proof that a series of equally spaced, phase-locked modes exists. Further confirmation is provided by the shifting of the beat frequencies as the DBR output is tuned across these modes. Additionally, the spectral width of the beat frequencies can provide some information as to the linewidth of the modes in the comb. From the two traces in figure 7.24, the beat frequencies between DBR laser and frequency comb all span approximately 13.5 MHz. This is comparable to the linewidth of the DBR laser, which was quoted at around 10 MHz. This means that the linewidth of any mode in the frequency comb could not be significantly larger than that of the DBR laser and must have been of the order of a few MHz. Hence, as well as proving the existence of equally spaced, phase-locked modes within the comb envelope, the DBR laser has also shown that the frequencies are all sharp, with a narrow linewidth.

7. Comb Generation in a Dispersion Compensated Cavity

7.6) Chapter Summary

At the beginning of this chapter, the reasons for incorporating dispersion compensation, with regard to extending the comb width and improving stability were repeated. This was followed by a justification for choosing a multilayer coating as a compensation scheme. Alternate schemes based on fused silica blocks or prisms were rejected because of the large resulting increase in cavity length and the fact that the fused silica dispersion curve had the wrong gradient to provide compensation over a range of wavelengths.

A range of chirped mirrors were ordered, with central negative dispersions of -100fs^2 , -250fs^2 and -550fs^2 and the correct dispersion gradient to provide compensation over the range 1550 – 1650nm. To fully compensate for the positive dispersion within the FCG cavity, multiple bounces between a pair of chirped mirrors was required. This was achieved by a custom designed mount, which kept the two mirrors parallel. To incorporate this mount into the cavity, a collimated section was created by the addition of a second lens after the secondary beam waist. The EOM was then placed in this section between the lens and a plane output coupler to ensure that it was as close to the end of the cavity as possible. Finally, the dispersion compensation mount was situated at the secondary beam waist in place of the EOM. Testing of the EOM ensured that the cavity length did not increase beyond the point at which modulation could occur at the cavity FSR.

Initially, the chirped mirrors were tested in the original FCG cavity, without the EOM, to observe their effect on the OPO. The first change was noticed in the output power characteristics. During a scan of the FCG cavity, the dispersion compensated OPO showed periods at which it was off completely. These periods increased in size as the total negative dispersion approached the positive intra-cavity dispersion. This was in marked contrast to the uncompensated case, when the OPO remained on for the entire duration of the cavity scan. It was noted that this behaviour fit perfectly with ‘vernier-scale’ explanation of DRO frequency tuning given in previous chapters. Another noticeable difference was in the stability of the OPO, with no cluster hopping observed.

Temperature tuning of the nonlinear crystal within the dispersion compensated OPO was found to change the length of the off periods and therefore the level of

7. Comb Generation in a Dispersion Compensated Cavity

compensation. Spectrally, as the level of compensation was increased (producing longer off periods) the signal and idler wavelengths were found to move towards degeneracy at 1600nm. An optimum configuration consisting of two -250fs^2 mirrors and a crystal temperature of 168°C gave the longest off period and signal/idler wavelengths of 1600nm.

In the next set of experiments, the frequency comb generator with dispersion compensation was characterised. After inserting the dispersion-compensating mount, the OPO threshold was found to have approximately doubled over the uncompensated case. This was attributed to an accumulation of losses from each chirped mirror bounce and a slight misalignment of the second lens. An output power trace showed that the OPO was off for most of the FCG cavity scan, suggesting a high level of compensation. The FCG cavity could also be stabilised, using a simple side-of-fringe scheme. When operated, a stable spectral output could be produced with no drift or cluster hopping. Spectral data taken with a long OSA sweep time showed the range of wavelengths over which the OPO operated during the cavity scan. This gave a rough indication of the phasematching bandwidth, putting it at about 50nm and centred at degeneracy. The position of the PMB was further confirmed by a close examination of the output power curve (during the on period). This was asymmetric, which can only occur if the bandwidth centre coincides with degeneracy.

The spectral and output power data allowed the change in mode spacing per FSR to be calculated for the dispersion compensated FCG. The mode spacing was found to increase progressively by 1 Hz, giving a change of 11.2 kHz at the final mode pair and a cumulative change of 52 MHz. This was less than $1/10^{\text{th}}$ of the value in the uncompensated case.

To generate a comb of frequencies, a modulation depth of ~ 0.5 rad was used once again. The required modulation frequency was found to have changed to 514.165 MHz, a decrease that was attributed to slight changes in cavity length incurred during the insertion of the dispersion compensating mount and a phase change at the chirped mirrors. When modulating at this frequency, a frequency comb spanning up to 70nm and comprising ~ 16000 oscillating modes was generated. This corresponded to a 20nm increase over the uncompensated case. An increase in the lifetime of the comb to several minutes was also observed.

The range of modulation frequencies over which frequency comb generation occurred was found to have drastically decreased to ~ 20 kHz. This fit well with the previous

7. Comb Generation in a Dispersion Compensated Cavity

calculations of the change in mode spacing across the comb bandwidth. An examination of the fundamental beat frequency on the RFSA showed a virtually identical RF signal as the modulation frequency was changed, with negligible noise. Again, this was consistent with a series of cavity modes, all with nearly identical FSRs.

To finish the experiments performed with the dispersion compensated FCG, the frequency comb was mixed on a fast photodiode with the output from a narrow linewidth DBR laser operating at 1609.5nm. The resulting heterodyne signal was viewed on the RFSA and showed two beat frequencies. These frequencies summed to the modulation frequency and corresponded to mixing between the DBR output and the two closest modes in the frequency comb. After temperature tuning of the DBR wavelength across 100 modes within the comb, the beat frequencies were observed to shift to a new position.

The existence of beat frequencies between the comb and DBR output provided conclusive proof that a series of equally spaced, phase-locked modes existed within the envelope shown on the OSA. Additionally, the spectral width of the beats, at ~13.5 MHz and close to the DBR linewidth, showed that the comb frequencies were sharp, with a narrow width.

References

1. Fork, R.L., et al., *Negative Dispersion Using Pairs of Prisms*. Optics Letters, 1984. **9**(5): p. 150-152.
2. Layertec, *Quotation*. 2004: Germany.
3. Jundt, D.H., *Temperature-Dependent Sellmeier Equation for the Index of Refraction n_e in Congruent Lithium Niobate*. Optics Letters, 1997. **22**: p. 1553.
4. Diddams, S.A., et al., *Broadband Optical Frequency Comb Generation with a Phase-Modulated Parametric Oscillator*. Optics Letters, 1999. **24**(23): p. 1747-1749.
5. <http://www.avanex.com/Products/datasheets/Transmission/PwrSource.1905L MI.L.pdf>
6. <http://www.st-andrews.ac.uk/~psst/>

Chapter 8

Conclusions & Further Work

To provide a suitable finish to this thesis, the following short chapter will give a broad summary of the work that was presented and the conclusions that were gained. This will then lead into suggestions for future work that could be carried out and directions in which the project, as a whole, could be taken.

8.1) Overall Summary

The initial motivation for the research project described by this thesis was the development of a device that succinctly combined the previously separate technologies of optical parametric oscillation and frequency comb generation [1]. It was realised that the wide-bandwidth comb of frequencies generated by such system had potential applications in the previously unconnected field of optical communications. For such applications to be feasible, the combined OPO-FCG would need to be compact and have low power requirements. This led to the commencement of the work presented in this thesis, with the aim of developing a frequency comb generator based upon an optical parametric oscillator, operating at telecommunications wavelengths (1600nm) and capable of being pumped by a single laser diode.

The twin technologies of optical parametric oscillation and frequency comb generation were described in chapters 1 and 2 respectively. In particular, chapter 2 highlighted the potential application of frequency comb generation to optical communications, whereby a comb of frequencies could provide a stable reference for the channels in a DWDM system.

Chapter 3 introduced the concept of pump enhancement, a relatively recent modification to the standard OPO design. By resonating the pump field within an OPO cavity, alongside one or both of the downconverted waves, a high circulating field can be built up around the nonlinear crystal. This, in turn, reduces the required input pump power, opening the door for a laser diode pump source. Furthermore, by

8. Conclusions & Further Work

separating the resonant cavities for the pump and downconverted waves in a split cavity design, intra-cavity elements such as the electro-optic modulator required for FCG can be utilised without affecting the circulating pump field. Chapter 3 also described the development of an easy method to measure the level of the intra-cavity pump field, known as the enhancement factor, and the theoretical background for optimisation of the device.

The important matter of designing and optimising a suitable optical resonator for the OPO-FCG was discussed in chapter 4. Firstly, lithium niobate was determined to be the best option for the nonlinear crystal due to the large phasematching bandwidth that it exhibited at 1600nm. A right-angled cavity design was chosen and various modelling methods used to ensure that the resonant waves were focussed to the correct sizes in the nonlinear and modulator crystals. The final cavity design was then obtained by a process of iteration. Optimisation of the resonator was achieved by trying various combinations of input and output coupler and measuring the output power and back-reflected pump power as the input pump power was increased. From this, the downconversion efficiency and pump enhancement factor could be calculated as a function of pump power. It was discovered that the optimum configuration was a 20% input coupler and a 2% output coupler. This gave a maximum efficiency and enhancement factor at a pump power of 150mW (3.5 times threshold) and was in good agreement with theoretical calculations. Importantly, such a pumping level can be achieved by a single mode laser diode.

The first frequency comb generation experiments were presented in chapter 5. Utilising a modulation depth of 0.5 rad and a modulation frequency of around 520 MHz, frequency combs spanning 50nm were generated. This agreed well with predicted values based on theoretical calculations. The range of modulation frequency over which comb generation occurred was found to be +/-100 kHz. Within this range an examination of the fundamental beat frequency between modes in the comb showed that the noise level in the wings of the RF spectrum decreased as the optimum modulation frequency was approached.

It was discovered that the stability of the entire OPO-FCG set-up was an important factor when attempting to generate a frequency comb. For comb generation to occur at all, a TEM00 spatial mode was required for the downconverted waves. Also crucial was the reduction of thermal and vibrational noise. Even so, the generated frequency comb remained largely unstable, with a short lifetime and tendency to jump into

8. Conclusions & Further Work

separate signal and idler branches away from degeneracy. The root cause of this instability was determined to be dispersion - the dependency of refractive index on frequency.

In chapter 6, the issue of dispersion within the OPO-FCG cavity and methods for compensation were explored. Dispersion affects both the OPO and FCG in negative and separate ways. In the case of the OPO the combination of dispersion and the dual resonance of signal and idler cause erratic tuning behaviour. This is due to the change in longitudinal mode spacing that results from the frequency dependence of the refractive index. Consequently, a slight perturbation to the OPO cavity due to, for example, vibrations or thermal effects can cause it to hop between widely separated signal and idler mode pairs. Computer modelling of spectral behaviour of the OPO as the cavity length was changed showed a cluster hop occurring between degeneracy and wavelengths that closely matched the observed signal and idler positions after the frequency comb had reverted to separate branches. With further calculation the change in mode spacing across the entire comb bandwidth was found to be 100 kHz. This fitted with the previously observed range of modulation frequencies over which comb generation occurred. In the case of FCG, dispersion results in a gradual mismatch between cavity modes and the sidebands generated by the modulator. Eventually, the mismatch becomes so great that the power transferred into the cavity mode from the sideband is too small for it to oscillate above threshold. At this point the frequency comb is cut off.

Compensation for the positive dispersion within an optical cavity can be achieved by a number of methods. The most common involve the use of materials that exhibit a natural negative dispersion at the wavelengths of interest (fused silica blocks or prisms) or special multilayer optical coatings. For this project, the latter was chosen as only it could give the correct dispersion gradient across the comb bandwidth to provide adequate compensation.

The compensation of dispersion in the OPO-FCG resonator was expected to both improve the stability and increase the width of the generated frequency comb. Chapter 7 described the final set of experiments in which a dispersion compensation scheme was implemented. A special mount was designed to produce multiple bounces between a pair of chirped mirrors and the signal/idler cavity redesigned to incorporate both the mount and the modulator. Before attempting comb generation, an initial characterisation showed significant differences between the compensated and

8. Conclusions & Further Work

uncompensated OPO. In the compensated case, the OPO was observed to switch off completely for certain periods during the duration of a cavity scan. These 'off' periods increased in length as the level of negative dispersion was increased. This could only be explained by the fact that the spacing between cavity modes was equalising, suggesting that the compensation scheme was having the desired effect. Calculations showed that the change in mode spacing across the comb bandwidth had decreased to around 11 kHz. Spectrally, the OPO was observed to operate at near-degenerate signal and idler, close to 1600nm, with no sign of cluster hopping.

With two -550fs^2 chirped mirrors in a 6-bounce mount, providing close to perfect compensation, a modulation depth of 0.5 rad and modulation frequency around 515 MHz was used to generate a frequency comb spanning 70nm. This corresponded to the simultaneous oscillation of nearly 16000 modes and an increase of 20nm over the uncompensated case. The modulation bandwidth for comb generation was found to be only ± 10 kHz and negligible noise was observed on the RF spectrum of the fundamental beat frequency.

In the final set of experiments, the dispersion compensated frequency comb was heterodyned with the output from a narrow linewidth DBR laser operating at 1609.5nm. The resulting RF spectrum showed two beat frequencies, with spectral widths of 13.5 MHz, corresponding to a mixing between the DBR frequency and the two closest modes within the frequency comb. This proved conclusively that the observed frequency comb with dispersion compensation consisted of a series of phase-locked, narrow linewidth frequencies.

8.2) Further Work

The directions in which this project can next be taken all relate in some way to the potential applications for optical communications. Three such examples of further work are given here. The first two are certainly applications orientated, whilst the last offers some interesting theoretical insights that may well lead to further applications.

8. Conclusions & Further Work

a) Laser Diode Pumping

One of the original aims of this project was to develop a device capable of being pumped by a single-mode laser diode. With the optimisation experiments in chapter 4 showing that this is feasible and the results of chapter 5 showing that comb generation can be achieved at the optimum pumping level (albeit in the uncompensated case and not without difficulty), the next logical step is to switch to a laser diode pump source from the Argon Ion-Ti:S chain.

To ensure that the output from the laser diode is correctly coupled into the pump enhancement cavity to give the required beam waist in the nonlinear crystal, a number of beam-shaping and focussing optics will be required. Beam-shaping is needed to convert the elliptical diode beam into a circular TEM₀₀ mode. However, there are now a number of diodes on the market that have built in beam-shaping optics (see for example [2]). Such diodes can be purchased at the required pump powers, which therefore leaves the focussing optics. Determining the required optics should simply be a matter of obtaining the divergence of the circularised diode output and then using any one of a number of procedures [3-5] to match it into the beam waist in the nonlinear crystal.

One potential issue here lies with the dispersion compensation. All frequency comb generation experiments in this case were performed at the maximum pump power and it is therefore unknown whether the results of chapter 7 will be repeatable at lower pump powers. Additionally, no optimisation of the dispersion compensated FCG has been performed. The doubling of the threshold suggests that the optimum pumping level is likely to have changed from that obtained in chapter 4. It would therefore seem appropriate to repeat the optimisation experiments for the FCG cavity with dispersion compensation before diode pumping is attempted.

b) Redesign of Dispersion Compensated FCG

It is clear that the frequency comb generator, in its present form, cannot be integrated with current telecommunications system, even with a laser diode as a pump source. The biggest issues here are the size and stability of the current device. It is still a proof-of-principle experiment and is built from individual components that can be moved and adjusted independently. Whilst this is useful from an experimental point of

8. Conclusions & Further Work

view, it means that the device is particularly prone to thermal variations, air currents and mechanical vibrations, all of which can introduce instabilities.

As a result, the first step in redesigning the frequency comb generator towards an application-orientated system would be to move towards a monolithic design, where a single block is used to hold all of the cavity components and the pump source in the correct position. Such a device would be less susceptible to mechanical and thermal changes. Additionally, it could easily be sealed to remove problematic air currents. Any new design should also look to miniaturise the entire set-up. This would require tighter focussing by the intra-cavity mirrors and lenses, but should be achievable using the same methods as were employed in chapter 4.

In the current system, the largest single component is the EOM. Due to the fact that it utilises a resonant microwave cavity to create the electric field required for phase modulation, the size of the modulator is determined by the resonant modulation frequency. This in turn, is dependent on the length of the FCG cavity. Fortunately, the size of such modulators scales in the right way. As the modulation frequency increases, the size of the resonant cavity and the EOM itself decrease. An increase in modulation frequency corresponds to a decrease in cavity length. Therefore, as the FCG gets smaller, the size of the required EOM will also decrease.

From the aspect of telecommunications, a redesign of the FCG is important for a number of reasons. The reduction in size and improvement in stability will lead to a device that can be better integrated with current telecommunications technology. Additionally, the increase in modulation frequency resulting from the decrease in cavity length will produce a comb with a larger separation between modes. For a DWDM system this is essential, since the current mode spacing of ~ 520 MHz is far too small to provide a series of separate optical channels for communications. In fact, the currently specified channel spacing is almost two orders of magnitude greater at 25 GHz. This would require a cavity length approximately 50 times smaller, but does raise the possibility of modulating at multiples of the cavity FSR. For instance, a cavity with a FSR of 2.5 GHz (only around 5 times smaller than at present) could be modulated at 10 times the mode spacing to give the required 25 GHz. The question here is whether the FCG would generate a single comb of frequencies with mode spacing equal to 25 GHz or 10 independent combs, each with the 25 GHz spacing but combining to oscillate at all the cavity modes. This is another potential avenue of future work, which could be explored during the redesign of the FCG.

8. Conclusions & Further Work

c) Temporal Behaviour of Dispersion Compensated FCG

One particularly interesting issue that arises from the results of chapters 5 – 7 is the temporal behaviour of the output from the FCG. There are two possible regimes to consider here and both are analogous to the regions of operation of the FM laser before and after a phase transition (see chapter 2, section 2.5). The first possible mode of temporal operation is *frequency modulation*. In this case, the FCG output is a continuous wave that periodically sweeps across the entire range of frequencies within the comb bandwidth. The rate of this sweep is simply given by the modulation frequency and is therefore equal to the cavity FSR. The other possible temporal regime consists of a *phase-locked* operation. This situation is comparable to mode-locking in ultrafast laser systems, with the output from the FCG comprising a series of short optical pulses. The duration of an individual pulse is given by the inverse of the comb width, as with an FM laser, and the pulse repetition rate is equal to the cavity FSR.

In the context of telecommunications, the temporal operation of the FCG is an important factor when considering possible applications. For instance, a FCG providing a frequency modulated CW output offers a significant advantage in terms of optical damage. The continuing drive to transmit larger volumes of data requires sources with extremely large spectral widths. In the case of the pulsed systems that are currently used, this requires a very short pulse due to the inverse relationship between pulse duration and bandwidth. Associated with such short pulses is a large peak power, which can often approach the optical damage threshold of the various components within a communications network. On the other hand, a FCG operating in the frequency modulated regime can provide a spectrum of a similar width, but with CW powers that are orders of magnitude less than the peak power of a pulsed system. Hence, optical damage is no longer a problem.

Should the FCG operate in the phase-locked regime instead, the wide comb bandwidths that were observed in chapter 7 suggest the possibility of producing very short pulses. Taking the dispersion-compensated comb width of 8.2 THz and inverting gives an approximate transform-limited pulse duration of 120fs, which is comparable to the pulses obtained from the latest compact femtosecond lasers [6, 7]. Such lasers have recently been demonstrated as a WDM source, offering a total capacity of 1.36 Tb/s [8]. This highlights the application of a phase-locked FCG as a compact source

8. Conclusions & Further Work

for optical communications. With improvements to the system design and dispersion compensation a further increase to the comb width can be expected, potentially offering shorter pulse widths and greater data transfer rates.

An interesting question now arises as to whether a pulsed output is an efficient mode of operation for the OPO, regardless of the comb generation particulars. The key issue lies with the fact that the pump is CW, whilst the signal and idler consists of a pulse circulating within the cavity. In an OPO with a single or double pass pump, such as the one used by Diddams [1], the pump will only be depleted in the short amount of time that it takes for the signal/idler pulse to pass through the nonlinear crystal. Since in the parametric process there is no equivalent to the upper state lifetime and hence no pump storage mechanism, most of the pump energy will be wasted. This implies that pulsed output with a CW pump is not an efficient process. However, now consider the case of the pump enhanced OPO, as utilised by the frequency comb generator described in this thesis. Here, there is a mechanism for pump storage via the circulating field within the pump cavity. The lifetime of this storage mechanism would be comparatively short, being determined by the photon lifetime within the resonant cavity. Nevertheless, the ability to store pump energy for 10 – 20 round trips of the cavity suggests that a pulsed signal and idler might be a favourable mode of operation. Therefore, it seems that mode-locked operation is much more likely in an OPO-FCG system that employs pump enhancement.

Given the previous comparisons between comb generation and FM lasers, it seems prudent to see if the equations and parameters relating to the latter can be applied to the FCG results of chapter 7. Recalling chapter 2, section 2.5, the most important parameter is the modulation index of FM oscillation and is given by:

$$\Gamma = \frac{\delta \nu_{FSR}}{\pi \Delta \nu} \quad (8.1)$$

Given that the modulation range over which comb generation occurred was around 10kHz, an upper limit of 5kHz can be placed on $\Delta \nu$, the detuning of the modulation frequency from the cavity FSR. This results in a value of roughly 16300 for the modulation index of the comb generation process. Bearing in mind that Γ is also a good approximation to the number of modes under the comb envelope, the calculated

8. Conclusions & Further Work

value is in good agreement with the number of modes determined experimentally. From Γ , the spectral width of FM oscillation can be calculated using:

$$\Delta\nu_{FSW} = 2\Gamma f_m \quad (8.2)$$

When applied to the comb generation results, equation (8.2) gives a bandwidth that is twice the observed value. The factor of 2 suggests that there is more to this than simply calculation and experimental errors. Quite possibly, it highlights some of the differences between FM lasers and OPO-FCG that were mentioned in chapter 2. Further experimentation, at different modulation depths and frequency detunings, will be required to reach a definitive conclusion.

In terms of pulsed operation, there are two FM laser systems in particular that are comparable to the OPO-FCG described in this thesis, one based on a dye laser and the other on a T:S oscillator [9, 10]. To find the closest match, it is necessary to compare the storage times for the pump energy. The upper state lifetimes of both Ti:S and dye based compounds are well documented as 3.2 μ s and 2 - 5ns respectively [11]. In the case of the OPO-FCG, storage time is given by the photon lifetime in the pump cavity. This can be calculated using equation (8.3) below:

$$\tau_{cav} = \frac{2L}{\beta c} \quad (8.3)$$

Here, L is the optical length of the pump cavity and b is the total loss per round trip, including input coupling and parasitic. Using the loss figures calculated in chapter 4, section 4.6, the photon lifetime comes to around 3ns. Hence, the FM dye laser is the closest comparison to the OPO-FCG in terms of pump storage time.

Pulsed operation was observed in the FM dye laser for a detuning between modulation frequency and cavity FSR of <100 kHz. For the dispersion compensated FCG, the maximum allowed detuning given in chapter 7, section 7.4, was 10 kHz, well within this range. If the similarities between FM lasers and frequency comb generation hold, this implies that the dispersion compensated FCG was operating in the phase-locked regime. To determine if this is the case, a simple experiment is planned. The fast photodiode used to detect beat frequencies should have a sufficient detection bandwidth to observe a pulsed output at a repetition rate of ~515 MHz, should it exist.

8. Conclusions & Further Work

A sufficiently fast spectrum analyser will also be required to display the signal from the photodiode and attempts are currently underway to acquire such a device. Once in place, this experiment should provide some definitive answers as to the temporal behaviour of the dispersion compensated FCG.

8.3) Concluding Remarks

This project described in this thesis has proved a success in many ways. Frequency comb generation has been achieved in a pump-enhanced OPO, with an optimum pumping level accessible to single-mode diode lasers. This paves the way for a compact and efficient system, suitable for telecoms applications. Additionally, a large volume of theory has been developed and explored, leading to a greater understanding of the comb generation process and operation of the OPO. Finally, the implementation of dispersion compensation, whilst not considered at the inception of the project, has provided a wealth of information as well as fulfilling its intended aims. It has led to the development of novel cavity designs and alignment techniques, shown a new operating regime for the OPO and significantly extended the width of the frequency comb. It is hoped that the results and conclusions herein can lead to further development of the device and the fulfilment of its potential in the field of optical communications.

References

1. Diddams, S.A., et al., *Broadband Optical Frequency Comb Generation with a Phase-Modulated Parametric Oscillator*. Optics Letters, 1999. **24**(23): p. 1747-1749.
2. <http://www.blueskyresearch.com/index.htm>
3. Casperson, L.W., *Mode Stability of Lasers and Periodic Optical Systems*. IEEE Journal of Quantum Electronics, 1974. **QE-10**(9): p. 629-634.
4. Kogelnik, H. and T. Li, *Laser Beams and Resonators*. Proceedings of the IEEE, 1966. **54**(10): p. 1312-1329.
5. Spurr, M.B. and M.H. Dunn, *Euclidean Light*. Optics & Photonics News, 2002. **13**(8): p. 40.

8. Conclusions & Further Work

6. Brown, C.T.A., et al., *Compact Laser-Diode-based Femtosecond Sources*. New Journal of Physics, 2004. **6**: p. art. no.-175.
7. Hopkins, J.M., et al., *Highly Compact and Efficient Femtosecond Cr:LiSAF Lasers*. IEEE Journal of Quantum Electronics, 2002. **38**(4): p. 360-368.
8. Chai, Y.J., et al., *1.36-Tb/s Spectral Slicing Source based on a Cr⁴⁺-YAG Femtosecond Laser*. Journal of Lightwave Technology, 2005. **23**(3): p. 1319-1324.
9. Kane, D.M., S.R. Bramwell, and A.I. Ferguson, *FM Dye-Lasers*. Applied Physics B - Photophysics and Laser Chemistry, 1986. **39**(3): p. 171-178.
10. Curley, P.F. and A.I. Ferguson, *Frequency-Modulated Operation of a Ti-Sapphire Laser*. Optics Communications, 1991. **83**(1-2): p. 85-91.
11. Svelto, O., *Principles of Lasers*. 3rd ed. 1989: Plenum Press. 351.

Appendix I: Publications & Conference Proceedings

I.1 – Journal Publications

- Spurr, M. B. & Dunn, M. H., *Euclidean Light*. Optics & Photonics News, 2002. **13**(8): p. 40.

I.2 – Conference Proceedings

- Spurr, M. B., Lindsay, I. D. & Dunn, M. H., *Low Threshold Frequency Comb Generator for 1600nm based on a Pump-Enhanced Optical Parametric Oscillator*. Conference on Lasers & Electro-Optics 2003, **CthG6**. Baltimore, USA (June 2003).
- Spurr, M. B. & Dunn, M. H., *Low Threshold Frequency Comb Generation at 1600nm in a Pump-Enhanced Optical Parametric Oscillator*. PREP 2004, **OP14**. University of Hertfordshire, UK (April 2004).

Appendix II: Derivation of Optimisation Equations for PE-SRO

This appendix serves to provide the derivation of the optimisation equations for a PE-SRO, referred to in chapter 3, section 3.4 as equations (3.28) – (3.31). A schematic of a PE-SRO is shown in figure 1 below.

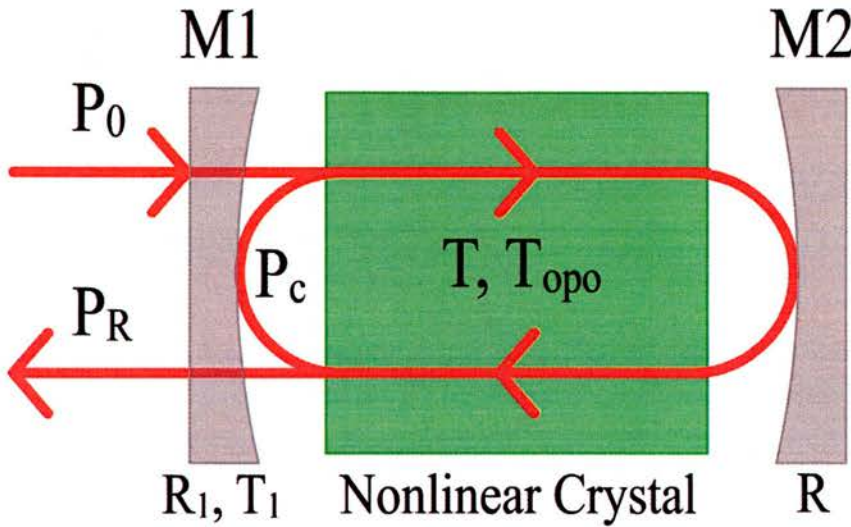


Figure 1 – Schematic of a PE-SRO

In the above diagram, the nonlinear crystal is situated in a two-mirror cavity. Mirror M1, with reflectivity, R_1 , and transmission, T_1 , serves as an input coupler for the incident pump wave, whose power is P_0 . M2 has reflectivity, R , and the nonlinear crystal has two effective pump transmissions. The first, T , is due to parasitic losses such as scattering and absorption, whilst the second, T_{oppo} , is due to the nonlinear loss associated with parametric downconversion. By combining M2 and the nonlinear crystal, an effective reflectivity can be defined as

$$R_m = (TT_{oppo}R) \tag{1}$$

The circulating power, P_c , can be obtained by summing the electric fields after consecutive round trips of the cavity. The method is virtually identical to that used in chapter 3, section 3.3 to derive an expression for the pump enhancement factor. Once

Appendix II: Derivation of Optimisation Equations for PE-SRO

the total electric field has been found, the expression is squared to give the circulating power or intensity i.e.

$$P_c = \frac{T_1 P_0}{\left[1 - \sqrt{(R_1 R_m)}\right]^2} \quad (2)$$

Note the similarity between the above equation and equation (3.14) from chapter 3. The main differences are the replacement of R_e with R_m to account for losses at the pump due to downconversion and the assumption that the cavity in figure 1 is on resonance. Note that the above expression also assumes that the circulating power throughout the cavity is constant. This was also one of the main issues in chapter 3, section 3.4, when determining whether the equations derived in this appendix could be applied to a PE-DRO.

At and above OPO threshold, the gain for the downconverted waves is equal to the internal cavity loss. This means that the circulating pump power is clamped to its threshold value i.e. $P_c = P_{th}$. For a fixed input pump power, the downconverted power is simply equal to the reduction in circulating pump power due to the nonlinear loss,

$$P_{DC} = (1 - T_{OPO}) P_{th} \quad (3)$$

Using equation (3) to substitute for T_{OPO} in equations (1) and (2), the following expression for the downconverted power can be obtained:

$$P_{DC} = P_{th} \left\{ 1 - (R_1 R T)^{-1} \left[1 - \sqrt{\left(\frac{T_1 P_0}{P_{th}} \right)} \right]^2 \right\} \quad (4)$$

If it is assumed that M1 is perfect and exhibits no absorption at the pump (i.e. $R_1 + T_1 = 1$), then equation (4) can be differentiated with respect to T_1 to find the optimum transmission for M1. This gives the optimum input coupling condition,

$$T_1^{opt} = \frac{P_0}{P_{th}} \quad (5)$$

Appendix II: Derivation of Optimisation Equations for PE-SRO

Note that this expression also results from setting $R_m = R_1$ in equation (2), the condition for zero back-reflection derived in chapter 3, section 3.3. Hence, the condition of optimum input coupling corresponds to an impedance matched pump cavity.

Substituting for T_1 in equation (4) produces an expression for the downconverted power produced under the optimum input coupling condition.

$$P_{DC}^{opt} = P_{th} \left[1 - (RT)^{-1} \left(1 - \frac{P_0}{P_{th}} \right) \right] \quad (6)$$

Therefore, to obtain the optimum downconverted power in a PE-SRO, the transmission of the pump input mirror should be set as close as possible to the ratio of the input pump power and the threshold power.

If there were no parasitic loss experienced by the pump, either via transmission at M2 or linear losses on transmission through the crystal, the product RT would equal 1. In this case, equation (6) above would reduce to:

$$P_{DC}^{opt} = P_0 \quad (7)$$

Equation (7) shows that, in the absence of parasitic losses and under optimum input coupling conditions for the pump, the downconverted power becomes equal to the input pump power. In other words, the PE-SRO exhibits 100% conversion efficiency between the pump and downconverted waves.

Since it is generally difficult to achieve the exact input mirror transmission determined by equation (5) for a fixed input pump power, a more common procedure is to find the optimum pump power for a certain level of input coupling. This will occur when the pump cavity is impedance matched and the back-reflected pump power is at or very close to zero. In figure 1, the back-reflection is represented by P_R , which can be obtained in a similar way to P_c (see method in chapter 3, section 3.3):

$$P_R = P_0 \left[\frac{\sqrt{R_1} - \sqrt{R_m}}{1 - \sqrt{R_1 R_m}} \right]^2 \quad (8)$$

Appendix II: Derivation of Optimisation Equations for PE-SRO

This equation confirms that the condition for zero back-reflection and impedance matching is $R_1 = R_m$, as discussed previously.

From the preceding derivations, the important equations in the context of PE-SRO optimisation are (2), (3), (4) and (8). Additionally, equations (5) and (6) show that 100% downconversion efficiency is possible under optimum conditions.

Appendix III: MathCAD Programs

In this appendix, listings are given for the MathCAD programs used for various modelling purposes within this thesis.

III.1 – Used to model phasematch bandwidths for LiNbO₃ and MgO:LiNbO₃ in chapter 4, section 4.1.

Phasematch Bandwidth for PPLN

Calculates phasematching bandwidth for PPLN using programmed numerical method and based upon our requirements

OPO Equations

$\lambda_p := 0.8$ pump wavelength (μm), assumed constant $T := 192.5$ crystal temp. ($^{\circ}\text{C}$)

$x := 0, 1.. 850$ scaling parameter $l := 20000$ crystal length (μm)

$\lambda_{s_x} := \frac{x + 950}{1000}$ variable signal wavelength (0.95 - 1.6 μm) i.e
from degeneracy to transparency limit of idler

$\lambda_i(\lambda_s) := \frac{\lambda_s \cdot \lambda_p}{\lambda_s - \lambda_p}$ idler wavelength (μm), depends on signal due to energy conservation

$a_1 := 5.35583$

$a_2 := 0.100473$

$a_3 := 0.20692$

$a_4 := 100$

$a_5 := 11.34927$ Sellmeier coefficients for LN

$a_6 := 1.5334 \cdot 10^{-2}$

$b_1 := 4.629 \cdot 10^{-7}$

$b_2 := 3.862 \cdot 10^{-8}$

$b_3 := -0.89 \cdot 10^{-8}$

$b_4 := 2.657 \cdot 10^{-5}$

$f := (T - 24.5) \cdot (T + 570.82)$ temperature parameter

$$n(\lambda) := \left[a_1 + b_1 \cdot f + \frac{a_2 + b_2 \cdot f}{\lambda^2 - (a_3 + b_3 \cdot f)^2} + \frac{a_4 + b_4 \cdot f}{\lambda^2 - a_5^2} - a_6 \cdot \lambda^2 \right]^{\frac{1}{2}}$$
 temperature dependant
Sellmeier equation for
refractive index

Frequency Conversion

$c := 299792458$ speed of light (m/s)

$$v(\lambda) := \frac{c}{10^{-6} \cdot \lambda} \quad \text{conversion from wavelength to frequency}$$

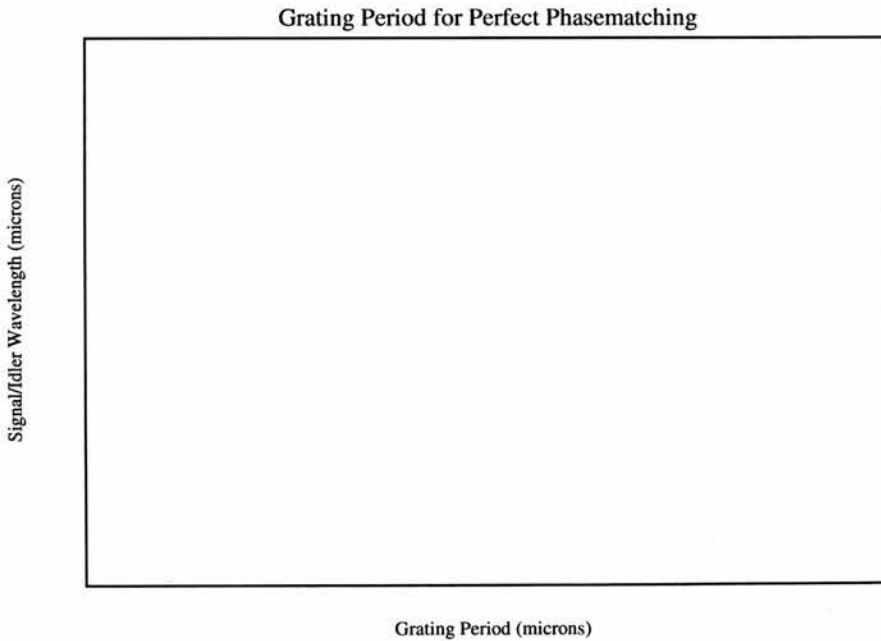
$$\Delta v_{pm}(\Delta \lambda_{pm}, \lambda) := \frac{c}{10^{-6} \lambda^2} \cdot \Delta \lambda_{pm} \quad \text{conversion from wavelength bandwidth to frequency bandwidth with correct SI units}$$

Tuning with Grating Period

$$\Lambda(\lambda_s, \lambda_i) := \left(\frac{n(\lambda_p)}{\lambda_p} - \frac{n(\lambda_s)}{\lambda_s} - \frac{n(\lambda_i)}{\lambda_i} \right)^{-1} \quad \text{grating period required for perfect phasematching}$$

$$\text{idler}_{x,0} := \lambda_i(\lambda_{s_x}) \quad \text{idler wavelengths corresponding to signal wavelengths via energy conservation of pump}$$

$$\text{Grating}_{x,0} := \Lambda(\lambda_{s_x}, \text{idler}_{x,0}) \quad \text{grating periods}$$



Numerical Evaluation of PMB

```

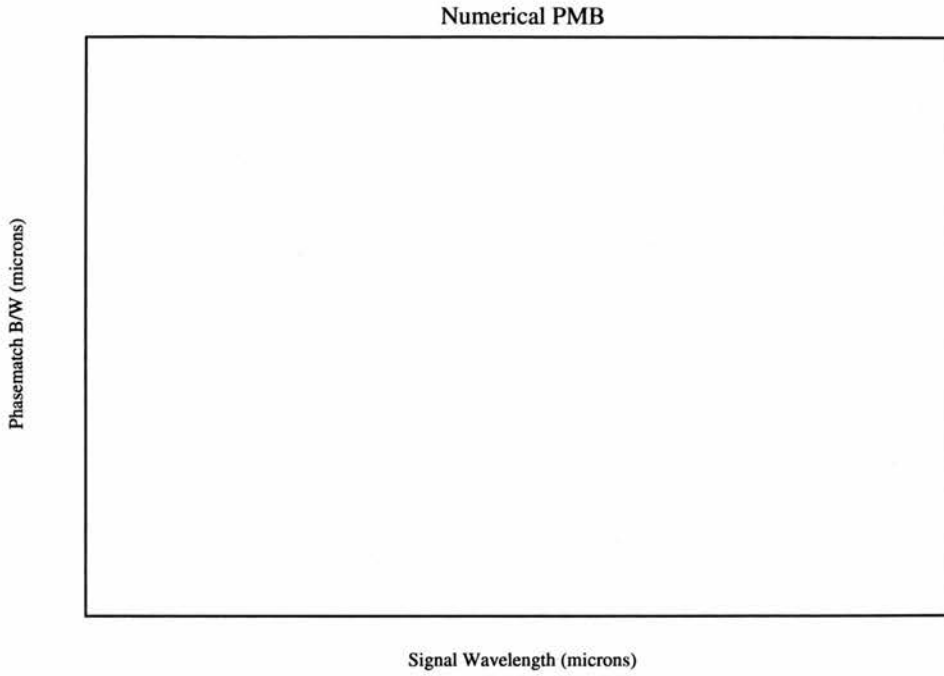
Δλpm(λp, λs, λi) := | tol ← 0.00001      minimum tolerable difference between Δk and π/L
                    | step ← 0.01      step size for changing λs
                    | Λperf ← ( (n(λp)/λp - n(λs)/λs - n(λi)/λi) )-1  grating period required for perfect
                    |                                       phasematching at λs
                    | λcent ← λs      λs is centre wavelength of phasematching curve
                    | Δk ← 2·π·( | (n(λp)/λp - n(λs)/λs - n(λi)/λi - 1/Λperf) | )  phase mismatch
                    |                                       calculated
                    |                                       for grating period which
                    |                                       perfectly phasematches λs
                    | diff ← (π/1 - |Δk|) / (π/1)  determines how close calculated Δk is to π/L limit
                    | dir ← diff / |diff|  determines whether Δk is above or below π/L limit
                    | while |diff| ≥ tol  whilst difference between Δk and π/L is
                    |                                       greater than the tolerance level,
                    |                                       decreases λs by step size (unless above
                    |                                       degeneracy), calculates corresponding
                    |                                       λi and hence determines new Δk
                    |   | λs ← λs - step  if λs < 1.6
                    |   | λs ← λs + step  otherwise
                    |   | λi ← (λs·λp) / (λs - λp)
                    |   | Δk ← 2·π·( | (n(λp)/λp - n(λs)/λs - n(λi)/λi - 1/Λperf) | )
                    |   | diff ← (π/1 - |Δk|) / (π/1)  if Δk has gone past π/L, step size is halved and
                    |   |                                       signal is increased or decreased accordingly,
                    |   |                                       allowing the program to iterate Δk around π/L
                    |   |                                       until it is within the tolerance limit
                    |   | newdir ← diff / |diff|
                    |   | step ← step·(-0.5)  if newdir ≠ dir
                    |   | dir ← newdir
                    | λwidth ← λs  sets wavelength at half width to be λs at which Δk = π/L
                    | pmb ← 2·|λcent - λwidth|  full bandwidth is twice the width from the
                    | pmb  centre wavelength to the wavelength at which
                    |                                       Δk = π/L

```

NOTE: Need to **decrease** λ_s initially, otherwise obtain **very large bandwidth just before degeneracy**. This is due to the fact that, close to degeneracy, the phasematching curves of the signal and idler **overlap**. At a certain signal wavelength, the overlap point will have $\Delta k > \pi/L$ and hence the program will continue on to the **idler phasematch curve** until it finds $\Delta k = \pi/L$. This produces a **false value** for the bandwidth which is **significantly larger than at degeneracy**. By decreasing λ_s , the program moves in the opposite direction to the overlap point and reaches $\Delta k = \pi/L$ on the **signal phasematch curve**. This situation is reversed **above degeneracy** and therefore need to **increase** λ_s above 1600nm.

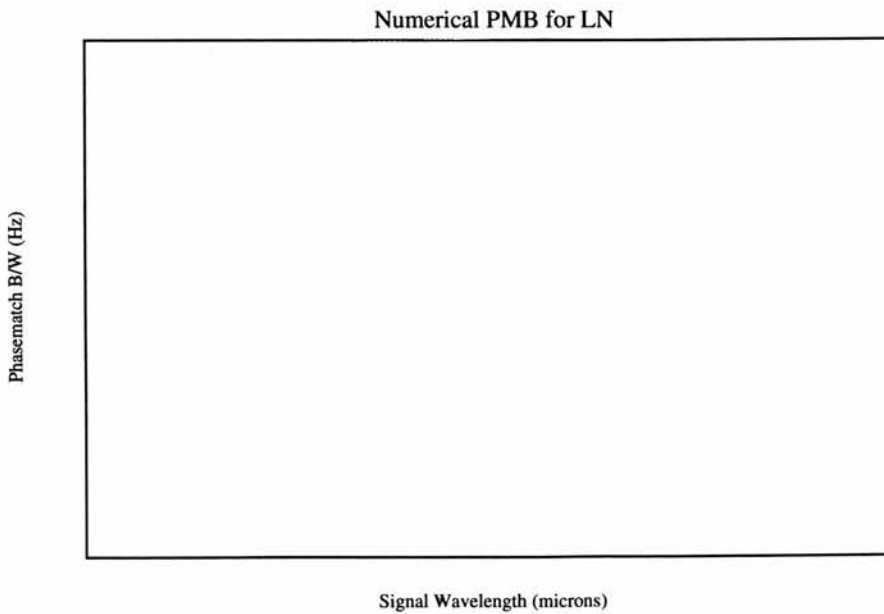
Wavelength Bandwidth

$\text{Bandwidth}_{x,0} := \Delta\lambda_{\text{pm}}(\lambda_p, \lambda_{s_x}, \text{idler}_{x,0})$ phasematching bandwidth for each λ_s



Frequency Bandwidth

$\text{Bandwidth}_{x,1} := \Delta\nu_{\text{pm}}(\text{Bandwidth}_{x,0}, \lambda_{s_x})$ phasematching bandwidth for each λ_s



Internal Loss from Dip in Back-Reflection

$$A := \min R \cdot R1 \cdot R2 - R2$$

$$B := 2 \cdot \sqrt{R1} \cdot \sqrt{R2} - \min R \cdot 2 \cdot \sqrt{R1} \cdot \sqrt{R2}$$

$$C := \min R - R1$$

First, calculate $e^{-2\alpha}$ (represented by x) using standard quadratic formula. This comes from rearranging the equation for cavity reflectivity at resonance (see notes).

$$x := \text{if} \left(\text{Coupling} = 1, \frac{-B + \sqrt{B^2 - 4 \cdot A \cdot C}}{2 \cdot A}, \frac{-B - \sqrt{B^2 - 4 \cdot A \cdot C}}{2 \cdot A} \right)$$

Calculates internal loss depending on coupling condition

$$\alpha := \frac{-\ln(x)}{2} \quad \text{Intra-cavity single-pass amplitude loss}$$

$$\text{PowerLoss} := 2\alpha$$

$$\text{PowerLoss} = \blacksquare$$

Intra-cavity single-pass power loss (i.e. loss due to scattering, absorption and off-axis reflection).

Internal Loss from FWHM of Back-Reflection

Provides a check for value calculated previously. Method is similar to that above, again utilising the quadratic formula (see notes for full derivation).

$$a := \frac{1}{2 \cdot \sqrt{R1} \cdot \sqrt{R2}}$$

$$b := \cos(\text{FWHM}) - 2$$

$$c := \frac{\sqrt{R1} \cdot \sqrt{R2}}{2}$$

$$y := \frac{-b + \sqrt{b^2 - 4 \cdot a \cdot c}}{2a}$$

$$\text{PowerLoss2} := \ln(y)$$

$$\text{PowerLoss2} = \blacksquare$$

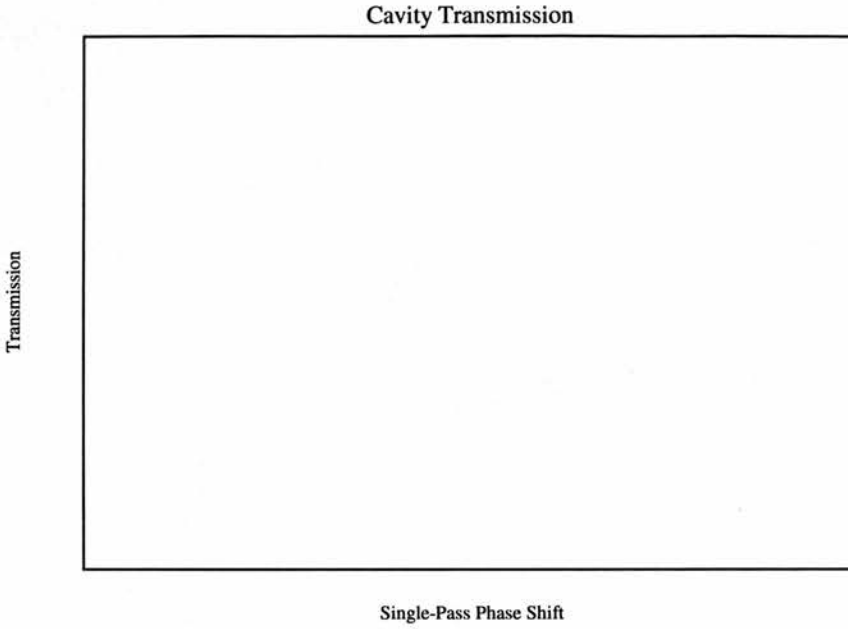
Same as PowerLoss above, but calculated using FWHM of back-reflection. Small differences likely due to error in measurement of FWHM.

Cavity Transmission

$$\text{Trans}(\Phi) := \frac{T1 \cdot T2}{e^{2\alpha} + R1 \cdot R2 \cdot e^{-2\alpha} - 2 \cdot \sqrt{R1} \cdot \sqrt{R2} \cdot \cos(2\Phi)}$$

Function for cavity transmission (i.e. transmission through output coupler). Derived using standard method for Fabry Perot cavities (see notes).

$$\text{CavTi} := \text{Trans}(\Phi_i)$$

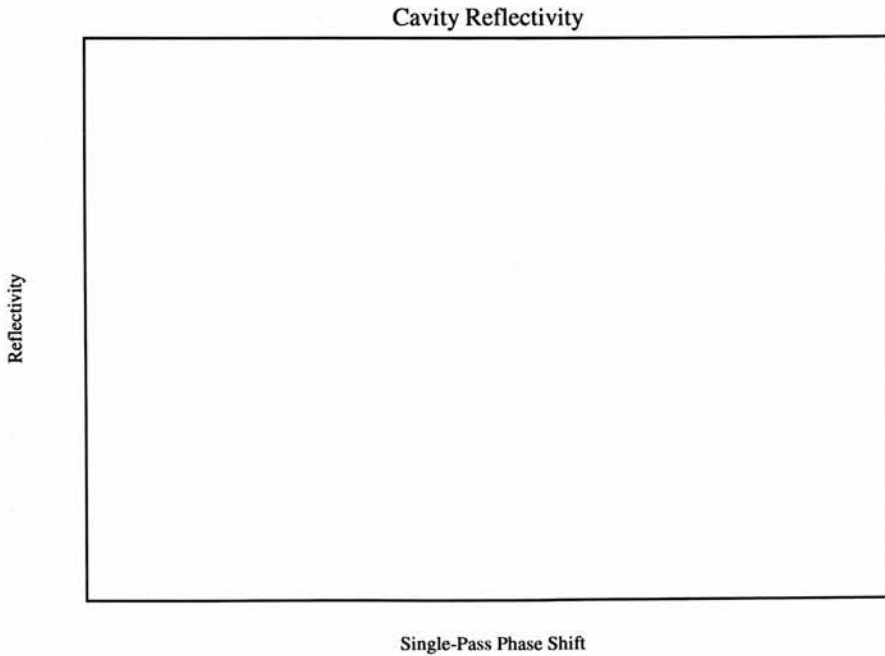


Cavity Reflectivity

$$\text{Refl}(\Phi) := \frac{R1 + R2 \cdot e^{-4\alpha} - 2 \cdot \sqrt{R1} \cdot \sqrt{R2} \cdot e^{-2\alpha} \cdot \cos(2 \cdot \Phi)}{1 + R1 \cdot R2 \cdot e^{-4\alpha} - 2 \cdot \sqrt{R1} \cdot \sqrt{R2} \cdot e^{-2\alpha} \cdot \cos(2\Phi)}$$

Function for cavity reflectivity (i.e. reflection from input coupler). Again, standard derivation for Fabry-Perot cavities was used (see notes).

$$\text{CavR}_i := \text{Refl}(\Phi_i)$$



Enhancement Factor

$$EF := \frac{T1}{e^{2\alpha} + R1 \cdot R2 \cdot e^{-2\alpha} - 2 \cdot \sqrt{R1} \cdot \sqrt{R2}}$$

EF =

Pump enhancement factor - ratio of circulating power inside cavity to power incident on input coupler.

Pcirc := EF · Po Power circulating in cavity (W)

Pcirc =

Pout := Pcirc · T2 Power transmitted through cavity (W)

Pout =

III.3 – Used to model the spectral behaviour of the OPO-FCG and determine oscillating mode pairs in chapter 6, section 6.2.

Cavity Modes

Calculates position of all modes within a specified bandwidth for OPO-FCG cavity, taking into account dispersion in nonlinear and EOM crystals. Determines which mode pairs will oscillate and how this changes with cavity length detuning.

Constants

c := 299792458 speed of light in vacuo (m/s)

Sellmeier Data

a1 := 5.35583

B1 := 0.6961663

a2 := 0.100473

B2 := 0.4079426

a3 := 0.20692

B3 := 0.8974794

a4 := 100

Sellmeier coefficients for LN

Λ1 := 0.0684043

Sellmeier coefficients for fused silica

a5 := 11.34927

Λ2 := 0.1162414

a6 := 1.5334 · 10⁻²

Λ3 := 9.896161

b1 := 4.629 · 10⁻⁷

b2 := 3.862 · 10⁻⁸

b3 := -0.89 · 10⁻⁸

b4 := 2.657 · 10⁻⁵

f(T) := (T - 24.5) · (T + 570.82) temperature parameter

Appendix III: MathCAD Programs

$$n(\lambda, T) := \left[a1 + b1 \cdot f(T) + \frac{a2 + b2 \cdot f(T)}{\lambda^2 - (a3 + b3 \cdot f(T))^2} + \frac{a4 + b4 \cdot f(T)}{\lambda^2 - a5^2} - a6 \cdot \lambda^2 \right]^{\frac{1}{2}}$$

temperature dependant Sellmeier equation for refractive index of LN (λ in μm)

$$nlens(\lambda) := \left[1 + \frac{B1}{\Lambda1^2 \cdot \left(\frac{1}{\Lambda1^2} - \frac{1}{\lambda^2} \right)} + \frac{B2}{\Lambda2^2 \cdot \left(\frac{1}{\Lambda2^2} - \frac{1}{\lambda^2} \right)} + \frac{B3}{\Lambda3^2 \cdot \left(\frac{1}{\Lambda3^2} - \frac{1}{\lambda^2} \right)} \right]^{\frac{1}{2}}$$

Sellmeier equation for refractive index of fused silica (λ in μm)

$$n1(v, T) := n\left(10^6 \cdot \frac{c}{v}, T\right)$$

allows Sellmeier equation for LN to be used with frequency rather than wavelength

$$nlens1(v) := nlens\left(10^6 \cdot \frac{c}{v}\right)$$

allows Sellmeier equation for fused silica to be used with frequency rather than wavelength

$$n2(\omega, T) := n1\left(\frac{\omega}{2\pi}, T\right)$$

allows Sellmeier equation for LN to be used with angular frequency

$$nlens2(\omega) := nlens1\left(\frac{\omega}{2\pi}\right)$$

allows Sellmeier equation for fused silica to be used with angular frequency

Equations & Conversions

$$v(\lambda) := \frac{c}{\lambda} \quad \lambda(v) := \frac{c}{v}$$

conversions between frequency and wavelength

$$vi(vp, vs) := vp - vs$$

idler frequency defined by energy conservation

$$\Delta k(vp, vs, T, \Lambda) := 2\pi \left(\frac{vp \cdot n1(vp, T)}{c} - \frac{vs \cdot n1(vs, T)}{c} - \frac{vi(vp, vs) \cdot n1(vi(vp, vs), T)}{c} - \frac{1}{\Lambda} \right)$$

phase mismatch

Free spectral range for signal modes

$$FSRs(vs, T_{NL}, T_{EOM}, L_{cav}, L_{crys}) := \frac{c}{2 \cdot \left[\left(n1(vs, T_{NL}) - 1 \right) L_{crys} + \left(n1(vs, T_{EOM}) - 1 \right) L_{crys} + \dots \right] + \left[\left(nlens1(vs) - 1 \right) \cdot 0.004 + L_{cav} \right]}$$

Free spectral range for idler modes

$$FSRi(vs, vp, T_{NL}, T_{EOM}, L_{cav}, L_{crys}) := \frac{c}{2 \cdot \left[\left(n1(vi(vp, vs), T_{NL}) - 1 \right) L_{crys} + \dots \right] + \left[\left(n1(vi(vp, vs), T_{EOM}) - 1 \right) L_{crys} + \dots \right] + \left[\left(nlens1(vi(vp, vs)) - 1 \right) \cdot 0.004 + L_{cav} \right]}$$

Appendix III: MathCAD Programs

Input Data

$\lambda_p \equiv 800 \cdot 10^{-9}$ $v_p := v(\lambda_p)$ pump wavelength & frequency
 $\lambda_{\text{centre}} \equiv 1600 \cdot 10^{-9}$ $v_{\text{centre}} := (v(\lambda_{\text{centre}}))$ initial centre frequency set to degeneracy
 $\Delta L \equiv 5 \times 10^{-8}$ cavity length detuning

Corresponding change in mode frequency

$$\Delta v(v, T_{\text{NL}}, T_{\text{EOM}}, L_{\text{cav}}, L_{\text{crys}}, \Delta L) := \frac{-v}{\left[\frac{(n1(v, T_{\text{NL}}) - 1)L_{\text{crys}} + (n1(v, T_{\text{EOM}}) - 1)L_{\text{crys}} + \dots}{+ [(n_{\text{lens1}}(v) - 1) \cdot 0.004 + L_{\text{cav}}]} \right]} \cdot \Delta L$$

$L_{\text{cav}} \equiv 0.1997$ length of cavity

$L_{\text{crys}} \equiv 0.02$ length of crystals in cavity

$T_{\text{NL}} \equiv 170$ temperature of nonlinear crystal

$T_{\text{EOM}} \equiv 25$ temperature of EOM crystal

$\Lambda \equiv 19.6 \cdot 10^{-6}$ poling period of nonlinear crystal for QPM

Bandwidth $\equiv 7 \cdot 10^{12}$ bandwidth over which model runs

Position Of Modes

In this section, the position of all signal and idler modes over the specified bandwidth is calculated, using the centre frequency as a reference point.

```

modes := | m ← 0                               sets mode number to 0 initially
          | vs0 ← vcentre                       sets first signal and idler modes
          | vi0 ← vcentre                       equal to centre frequency
          | fsrs0 ← FSRs(vs0, TNL, TEOM, Lcav, Lcrys)   sets first FSR for signal and idler
          | fsri0 ← FSRi(vi0, vp, TNL, TEOM, Lcav, Lcrys)   equal to FSR at centre frequency
          | diff ← 0                             sets difference between current signal and idler
          | while diff < Bandwidth               frequencies equal to zero initially
          |   | vsm+1 ← vsm + fsrsm           whilst difference between
          |   | vim+1 ← vim - fsrim           current signal and idler modes
          |   | fsrsm+1 ← FSRs(vsm+1, TNL, TEOM, Lcav, Lcrys)   is less than user specified
          |   | fsrim+1 ← FSRi(vsm+1, vp, TNL, TEOM, Lcav, Lcrys)   bandwidth, adds/subtracts
          |   | diff ← vsm+1 - vim+1           corresponding FSR to obtain
          |   | m ← m + 1                         next signal/idler mode and
          |   |                                   calculates next FSR
          |   |                                   calculates new difference between current signal and
          |   |                                   idler modes and increases mode number by 1
          | for j ∈ 0, 1.. m
          |   | modesj,0 ← j                     puts signal and idler
          |   | modesj,1 ← vsj + Δv(vsj, TNL, TEOM, Lcav, Lcrys, ΔL)   modes into a single
          |   | modesj,2 ← vij + Δv(vij, TNL, TEOM, Lcav, Lcrys, ΔL)   array to be outputted by
          |   |                                   program (note: 1 =
          |   |                                   signal modes, 2 = idler
          |   |                                   modes)
          | modes
  
```

Oscillating Mode Pair

In this section the oscillating mode pair is obtained by overlapping the signal and idler mode combs to satisfy energy conservation and looking for the pair with the greatest overlap.

```

oscillating := | m ← modes1,0           start with first signal & idler mode pair
                | n ← modes1,0
                | a ← 0
                | b ← 0
                | smallest_diff ← vp      set smallest difference between pump
                |                                     frequency and sum of signal & idler modes
                |                                     equal to pump frequency initially
                | for j ∈ 1, 2..last(modes(0))
                |   | a ← j - 20
                |   | a ← 1 if j - 20 < 1      sets up range of idler modes over which current
                |   | b ← j + 20              signal mode is compared to find best overlap
                |   | b ← last(modes(0)) if (j + 20) > last(modes(0))
                |   | for k ∈ a..b
                |   |   | overlap ← modesj,1 + modesk,2  takes each mode pair and sums their
                |   |   |                                     frequencies, then calculates difference
                |   |   | diff ← |vp - overlap|           between sum and pump frequency
                |   |   | if diff < smallest_diff
                |   |   |   | m ← modesj,0               if difference is less than smallest difference,
                |   |   |   | n ← modesk,0               difference and mode numbers are stored
                |   |   |   | smallest_diff ← diff
                |   | oscillating0,0 ← m
                |   | oscillating0,1 ← n                outputs mode numbers, signal & idler frequencies
                |   | oscillating0,2 ← modesm,1        and difference between sum and pump frequency
                |   | oscillating0,3 ← modesm,2        for mode pair with greatest overlap (smallest
                |   | oscillating0,4 ← smallest_diff     difference)
                | oscillating
    
```

oscillating = ■

last(modes⁽⁰⁾) = ■

$\lambda(\text{oscillating}_{0,2}) = \blacksquare$

vp = ■

v_{centre} = ■

$\lambda(\text{oscillating}_{0,3}) = \blacksquare$

$$\frac{\lambda(\text{oscillating}_{0,3}) - \lambda(\text{oscillating}_{0,2})}{10^{-9}} = \blacksquare$$